MODELLING THE TRANSPORT OF NANOPARTICLES ACROSS THE BLOOD-BRAIN BARRIER USING AN AGENT-BASED APPROACH

Gavin James Matthew Fullstone

Submitted for the Degree of Doctor of Philosophy

Faculty of Mathematical and Physical Sciences, Department of Chemistry

University College London

DECLARATION OF AUTHORSHIP

I, Gavin Fullstone, confirm that the work presented in this thesis is my own. Where information has been derived from other sources, I confirm that this has been indicated in the thesis.

TABLE OF CONTENTS

DECLARATION OF AUTHORSHIP 2

TABLE OF CONTENTS 3

ABSTRACT 8

ACKNOWLEDGEMENTS 9

PUBLICATIONS, CONFERENCES AND AWARDS 10

LIST OF FIGURES 12

LIST OF ABBREVIATIONS 18

CHAPTER 1: INTRODUCTION 20

1.1 CLINICAL MOTIVATION 20

1.1.1 The Central Nervous System 20

1.1.2 Burden of Disease 21

1.1.3 Drug Delivery into the Central Nervous System 22

1.2 ANATOMY OF THE CENTRAL NERVOUS SYSTEM 23

1.2.1 Interstitial Fluid 24

1.2.2 Cerebrospinal Fluid 25

1.3 BARRIERS OF THE CENTRAL NERVOUS SYSTEM 26

1.3.1 Blood Cerebrospinal Fluid Barriers 27

1.3.2 Arachnoid Membranes 29

1.3.3 Blood Brain Barrier 30

1.4 TRANSPORT AT THE BLOOD BRAIN BARRIER 34

1.4.1 Small Molecule Transport 34

1.4.2 Immune Cell Migration 36

1.4.3 Vesicular Transport 36

1.5 METHODS FOR THE STUDY OF THE BLOOD BRAIN BARRIER 38

1.5.1 *In vitro* Models of the Blood-Brain Barrier 38

1.5.2 *In vivo* Models of the Blood-Brain Barrier 40

1.5.3 *Ex vivo* Models of the Blood Brain Barrier 40

1.5.4 *In silico* and Mathematical Models of the Blood Brain Barrier 41

1.6 COMPUTATIONAL FLUID DYNAMICS 41

1.6.1 Discretisation of the Navier-Stokes Equations 43

1.6.2 Lattice-Boltzmann Method 44

1.7 COMPUTATIONAL FLUID DYNAMICS AND THE BLOOD 44
1.7.1 Blood Vessel Architecture 44
1.7.2 Properties of the Blood and Vasculature 46
1.8 CEREBROVASCULATURE STRUCTURE AND FLOW REGULATION 46
1.8.1 Cerebral Pressure Autoregulation 46
1.8.2 Neurovascular Coupling and Functional Hyperaemia 47
1.8.3 Cerebrovascular Abnormalities in Disease 49
1.9 AGENT-BASED MODELLING 51
1.9.1 Agent-based Modelling for System Analysis 51
1.9.2 Parallel Computing 52
1.9.3 The Flexible Large-scale Agent-based Modelling Environment 53
1.9.4 Agent-based Modelling for Biology 56
1.10 NANOTECHNOLOGY 58
1.10.1 Nanotechnology for Drug Delivery 58
1.10.2 Nanoparticle Toxicology 59
1.10.3 Drug Retention and Release 60
1.10.4 Nanoparticle Half-life and Bio-distribution 60
1.10.5 Achieving Specificity 63
1.10.6 Nanotechnology for Central Nervous System Delivery 63
1.10.7 Lrp1-Targeted Polymersomes for Central Nervous System Delivery 66
1.11 CHEMOTAXIS 70
1.11.1 Chemotaxis 70
1.11.2 Designing a Nanoscale Chemotactic Particle: Mechanisms of Particle Motion 71
1.11.3 Designing a Nanoscale Chemotactic Particle: Rotational Diffusion 73
1.11.4 Chemotactic Polymersomes 77
1.12 AIMS AND OBJECTIVES 80
CHAPTER 2: MATERIALS AND METHODS 82
2.1 THE FLEXIBLE LARGE-SCALE AGENT-BASED MODELLING ENVIRONMENT 82

2.1.1 FLAME: Generating Initial States 83
2.1.2 FLAME: Serial Compilation and Execution 83
2.1.3 FLAME: Parallel Compilation and Execution 84
2.1.4 FLAME: Data Processing and Visualisation 85
2.2 POLYMERSOME ANALYSIS FOR AGENT-BASED MODELLING 85
2.2.1 Size Analysis 85
2.2.2 Calculating Polymer Number from Polymersome Size 87
2.2.3 Calculating Ligand Density from Polymersome Size 91
2.3 COMPUTATIONAL FLUID DYNAMICS 92
2.3.1 Incompressible Form of the Navier-Stokes Equations 92
2.3.2 Execution of the Galerkin/Least Squares Method in Comsol Multiphysics 93
2.3.3 Geometry 94
2.3.4 Meshing 96
2.3.5 Fluid Properties 97
2.3.6 Boundary Conditions 99
2.3.7 Execution of a Laminar Flow Model in FLAME 102
2.4 SIMULATION OF BROWNIAN MOTION 102
2.5 SIMULATION OF ROTATIONAL DIFFUSION 104
2.6 SIMULATION OF A DIRECTIONALLY BIASED NANOPARTICLE 106
2.7 CONSIDERATION OF BOUNDARIES 107
2.8 SIMULATION OF RECEPTOR BINDING 108
2.9 SIMULATION OF CELL TRAFFICKING 112
2.10 SIMULATION OF FENESTRATIONS 112
2.11 STATISTICAL ANALYSIS 113
CHAPTER 3: RESULTS AND DISCUSSION I 114
Agent-based Modelling of Nanoparticle Behaviour under Blood Flow: Insights into Distribution and Targeting Tumours
3.1 INTRODUCTION 114
3.1.1 Blood Flow in Capillaries 114
3.1.2 Blood Flow and Brownian Motion in Capillaries 115
3.1.3 Red Blood Cells and Blood Flow 115

3.1.4 Transport at the Vessel Wall 116
3.2 AIMS AND OBJECTIVES 116
3.3 RESULTS AND DISCUSSION 117
3.3.1 Building an Agent-based Model of Blood Flow 117
3.3.2 Agent-based Modelling of Brownian Motion 123
3.3.3 Parallelisation of the Capillary Blood Flow Model 126
3.3.4 Brownian Forces become the Dominant Force at the Vessel Wall Interface 128
3.3.5 Red Blood Cells enhance Nanoparticle Dispersion 131
3.3.6 Nanoparticle Size Selectively Targets Delivery to Tumour Tissues 139
3.4 CONCLUSIONS 149
CHAPTER 4: RESULTS AND DISCUSSION II 151
Modelling Nanoparticle Binding at the Blood-Brain Barrier: Insights into Improving General and Specific Delivery to the Central Nervous System
4.1: INTRODUCTION 151
4.1.1 Controlling Transcytosis Efficiency by Affinity 151
4.1.2 Controlling Nanoparticle Affinity 153
4.1.3 Shear Flow and Nanoparticle-Cell Binding 156
4.2 AIMS AND OBJECTIVES 159
4.3 RESULTS AND DISCUSSION 159
4.3.1 Building a Transwell Model of Nanoparticle Transcytosis 159
4.3.2 Improving Specificity by Adapting Nanoparticle Properties 167
4.3.3 Improving Transcytosis Efficiency by Adapting Nanoparticle Properties 172
4.3.4 Building a Capillary Model of Nanoparticle Binding 176
4.3.5 The Effect of Functional Hyperaemia on Nanoparticle Binding 181
4.4 CONCLUSIONS 194
CHAPTER 5: RESULTS AND DISCUSSION III 196
Modelling the Chemotaxis Properties of Nanoparticles
5.1 INTRODUCTION 196
5.2 AIMS AND OBJECTIVES 197

5.3 RESULTS AND DISCUSSION 197
5.3.1 Building an Agent-based Model of Particle Propulsion 197
5.3.2 Accumulation of Particles undergoing Propulsion at Interfaces 203
5.3.3 Propulsion and Blood-Tissue Transport 204
5.3.4 Chemotaxis 209
5.4 CONCLUSIONS 222
CHAPTER 6: CONCLUSIONS AND FUTURE DIRECTIONS 223
6.1 GENERAL CONCLUSIONS 223
6.2: FUTURE PERSPECTIVES 227
6.2.1 Validation and Refinement 228
6.2.2 Application to Large-scale Modelling 228
6.2.3 Towards Personalised Medicine 229
BIBLIOGRAPHY 231
APPENDIX 254
I: APLEY PRIZE SUBMISSION 254
II: MODEL OF BROWNIAN MOTION 258
III: FLAME MODEL OF BROWNIAN MOTION 261
IV: TRANSCYTOSIS EFFICIENCY OF ANGIOPEP-2 FUNCTIONALISED POLYMERSOMES 265
V: DELIVERY OF CHEMOTACTIC NANOPARTICLES INTO THE CNS OF RATS 266

ABSTRACT

Diseases affecting the Central Nervous System (CNS), consisting of the brain and spinal cord, will account for an estimated 11.84% of all deaths by 2015, with few effective treatment options. This is partly a consequence of poor penetrance of blood-borne molecules, including almost all therapeutics, into the CNS. This is due to the existence of a blood-brain barrier, severely limiting potential therapeutic intervention. Nanoparticles are diverse nanoscale particles that have recently been demonstrated to be able to improve drug penetrance across the blood-brain barrier, by targeting endogenous transport systems. However, further methods to improve their general delivery to the CNS and specific delivery to different regions of the CNS are required.

Here, agent-based modelling has been utilised to simulate blood flow in a capillary at the blood-brain barrier. This modelling approach has demonstrated the importance of a number of biological, physiological and physical factors that affect nanoparticle uptake to the CNS. This model was used to demonstrate how the fluid dynamics in capillaries enhances nanoparticle distribution to the vessel wall interface. These simulations have demonstrated that by tuning nanoparticle properties, including ligand density, receptor-ligand affinity and size, general delivery by transcytosis can be improved. Moreover, particular nanoparticle formulations can target high levels, but not low levels, of receptor expression at the blood-brain barrier thus providing a method to improve specific delivery into particularly CNS regions. Furthermore, nanoparticles can be formulated to stabilise nanoparticle binding under different flow conditions. In particular during regional blood flow increases, called functional hyperaemia, which aid access of nutrients to that region of the CNS. It is predicted from these simulations that this could be harnessed to further improve specificity of delivery. Finally, chemotactic nanoparticles are shown to have an improved distribution to the vessel wall interface and penetration through the CNS tissue.

ACKNOWLEDGEMENTS

This project was initially funded by a BBSRC doctoral training grant at the University of Sheffield and then continued with funding provided by the Faculty of Mathematical and Physical Sciences, University College London. I thank both my funders for giving me the opportunity to undertake this project. There are many people who deserve thanks for the contribution to this thesis. I'd like to start with my three supervisors, Giuseppe Battaglia, Jonathan Wood and Mike Holcombe for their input and guidance.

I'd like to take the opportunity to thank those people that contributed to my work and training within the lab. I'd like to start with David Rhodes and Simon Coakley for training and technical support in the use of the FLAME software. Furthermore, I'd like to thank Russell Pearson for his help and introduction to the Battaglia lab. Moreover, I'd like to thank James Robertson and Milagros Avila Olias for providing the DLS data used in simulating polydisperse nanoparticle populations. I thank Anna Puiggalí Jou for providing her hard-earned Nanosight data. I also give thanks to Xiaohe (Joe) Tian and Sophie Nyberg for providing *in vitro* and *in vivo* data for my work. Thanks to Silvia Bianco for providing some of the graphics.

I'd like to thank many of the people who have made my time during the course of this project so enjoyable. To Guy Yealland and Milagros Avila Olias from the Battaglia group, for accompanying me on my aspiration to visit the Galapagos Islands and Ecuador, I am very grateful for getting to share such a brilliant experience with you both. I would also like to thank others from the Battaglia group, past and present, with particular mentions for James Robertson, Monika Magon, Anna Puiggali Jou, Priyalakshmi Viswanathan, Sophie Nyberg, Eloise Morecroft, James Hindley, Luca Chierico, Carla Pegoraro, Dan Little and Silvia Bianco. Finally, thank you to my family and friends, particularly Ami Gell, Rebecca Armstrong, David Armstrong, Dean Winfield, Kathryn Evans, Marc Winfield, Michael Pirrie, Thomas Mutton and William Vittery, for their support.

PUBLICATIONS, CONFERENCES AND AWARDS

LIST OF PUBLICATIONS

Gavin Fullstone, Jonathan Wood, Mike Holcombe, Giuseppe Battaglia.
Modelling the Transport of Nanoparticles under Blood Flow using an Agent-based Approach.
Scientific Reports, **5**, doi:10.1038/srep10649

Gavin Fullstone, Sophie Nyberg, Xiaohe Tian, Giuseppe Battaglia
Chapter 2: From the Blood to the Central Nervous System, a Nanoparticle's Journey through the Blood-Brain Barrier by Transcytosis
Nanotechnology and the Brain
Elsevier
Pre-publication Stage

LIST OF CONFERENCES

Oral Presentations

- 2nd United Kingdom and Ireland Early Career Blood Brain Barrier Conference. Liverpool, United Kingdom
  23rd November 2012
- 2nd Global American Society for Mechanical Engineering (ASME) Conference for Nano-engineering for Medicine and Biology. Boston, United States of America
  4th-6th February 2013
- Société d'Etude des Interfaces entre le Sang et le Cerveau (SEISC) Joint UK-France-Belgian Conference on Blood Brain Barriers. Arras, France
  15th-17th May 2013
- 3rd United Kingdom and Ireland Early Career Blood Brain Barrier Conference. Cambridge, United Kingdom
  22nd November 2013

Poster Presentations

- Institute of Physics (IOP) Conference for The Physics of Soft and Biological Matter. Cambridge, United Kingdom
  14^{th}-16^{th} April 2014

Organised and Chaired Conferences

- 4^{th} United Kingdom and Ireland Early Career Blood Brain Barrier Conference. London, United Kingdom
  21^{st} November 2014
  Organised with Sophie Nyberg, Silvia Bianco and Giuseppe Battaglia
  Chaired with Giuseppe Battaglia

LIST OF AWARDS

- Outstanding Paper award at the American Society for Mechanical Engineering (ASME) Conference of Nano-engineering for Medicine and Biology
  6^{th} February 2013
- Apley Prize for Best Thesis Abstract from the Department of Chemistry, University College London, 23^{rd} September 2014 (Appendix I)

LIST OF FIGURES

Figure 1.1: Cells of the Central Nervous System 21

Figure 1.2: Relative Global Deaths for Selected Neurological Disorders..... 22

Figure 1.3: Structure of the Central Nervous System and Ventricular System 26

Figure 1.4: Structure of Tight Junctions at the Blood Brain Barrier..... 27

Figure 1.5: Organisation of the Blood-Cerebrospinal Fluid Barriers 28

Figure 1.6: The Arachnoid Barrier..... 30

Figure 1.7: Structure of the Neurovascular Unit..... 31

Figure 1.8: Structure of Endothelium 32

Figure 1.9: Function of the Blood-Brain Barrier 33

Figure 1.10: Transport at the Blood-Brain Barrier..... 35

Figure 1.11: Methods to Study the Blood-Brain Barrier 38

Figure 1.12: Diagram of Transwell..... 39

Figure 1.13: The Retinal Vasculature 45

Figure 1.14: Mechanism of Functional Hyperaemia 48

Figure 1.15: Serial and Parallel Computing for Agent-based Applications 52

Figure 1.16: Parallelisation of Agent-based Models using FLAME Message Boards 55

Figure 1.17 Dependency Graph and FLAME Scheduler for a Simple Receptor Binding Model..... 56

Figure 1.18: Aggregation of PDPA Diblock Copolymers driven by changes in pH 67

Figure 1.19: Cargo Release of pH-sensitive Polymersomes 68

Figure 1.20: Biodistribution of Functionalised and non-Functionalised POEGMA-PDPA 70

Figure 1.21: Motion of Suspended Particles. 72

Figure 1.22: Run and Tumble Model of Chemotaxis 73

Figure 1.23: Effects of Diffusion Time on Sustaining Direction during a Run 74

Figure 1.24: Chemotaxis of Peritrichous Flagellated Bacteria by Run and Tumble 75

Figure 1.25: Relationship between Particle Diameter, Rotational and Translational Diffusion Coefficients 76

Figure 1.26: Structure of a 9:1 Ratio PMPC-PDPA/PEO-PBO Hybrid Polymersome 78

Figure 1.27 Proposed Mechanism of Propulsion for a Hybrid PMPC-PDPA/PEO-PBO Polymersome 79

Figure 2.1: Creating an Agent-based Application using FLAME 83

Figure 2.2: Simulation of DLS Distributions 87

Figure 2.3: Anatomy of a Polymersome 88

Figure 2.4: Creating the Vessel Geometry in Comsol Multiphysics 94

Figure 2.5: Creating the Red Blood Cell Geometry in Comsol Multiphysics .. 95

Figure 2.6: Setting the Difference in Geometry in Comsol Multiphysics 96

Figure 2.7: The Vessel Geometry in Comsol Multiphysics 96

Figure 2.8: Meshing the Geometry in Comsol Multiphysics 97

Figure 2.9: Meshed Geometry in Comsol Multiphysics 97

Figure 2.10: Setting Blood Material Properties in Comsol Multiphysics 98

Figure 2.11: Setting the Material in which to Solve Laminar Flow in Comsol Multiphysics 98

Figure 2.12: Setting the No Slip Boundary in Comsol Multiphysics 99

Figure 2.13: Setting the Moving Boundaries in Comsol Multiphysics 100

Figure 2.14: Setting the Inlet Conditions in Comsol Multiphysics 100

Figure 2.15: Setting the Outlet Conditions in Comsol Multiphysics 101

Figure 2.16: Configuring the Stationary Iterative Solver in Comsol Multiphysics 101
Figure 2.17: Schematic of a Chemotactic Polymersome 106
Figure 2.18: Reflective Boundaries 108
Figure 3.1: Laminar Flow in a Pipe 115
Figure 3.2: Flow Diagram of Model Functions 118
Figure 3.3: Model Summary Schematic 121
Figure 3.4: Testing the Implementation of the Polar Box-Muller Transformation 124
Figure 3.5: Validation of the Random Walk in 3D 125
Figure 3.6: Nanoparticle Traces of Simulated Nanoparticle and Tracked Nanoparticle Motion 126
Figure 3.7: Parallelisation of the Capillary Blood Flow Model 127
Figure 3.8: Heat Mapping of Laminar Forces 128
Figure 3.9: Balance of Brownian to Laminar Forces 130
Figure 3.10: FLAME State and Process Order Graphs of the Core Model .. 132
Figure 3.11: The Relationship between Haematocrit and Viscosity 133
Figure 3.12: The Effect of Haematocrit on Nanoparticle Distribution 134
Figure 3.13: The Effect of Haematocrit on Nanoparticle Velocity 135
Figure 3.14: The Effect of Haematocrit on Dispersion 137
Figure 3.15: The Effect of Haematocrit on Fluid Dynamics in a Capillary 138
Figure 3.16: Morphology of Fenestrations in Normal and Tumour Vessels . 140
Figure 3.17: FLAME State and Process Order Graphs of the Fenestration Model 141
Figure 3.18: Simulating Polydisperse Nanoparticle Distributions from Dynamic Light Scattering Data 142
Figure 3.19: Polydisperse Nanoparticle Populations 143

Figure 3.20: Uptake of Nanoparticles across Normal and Tumour Capillaries 144

Figure 3.21: Filtration Effect of Fenestrations and Polydisperse Nanoparticles 147

Figure 3.22: Uptake of Mono *versus* Poly -disperse Populations by Number and by Volume 148

Figure 4.1: Stages of Transcytosis 152

Figure 4.2: Effect of Binding Affinity on Transcytosis Efficiency 153

Figure 4.3: Controlling the Interfacial Surface Area by Changing Size and Morphology 154

Figure 4.4: Effect of Ligand Density on Nanoparticle-Cell Adhesion 155

Figure 4.5: Effect of Receptor Density on Nanoparticle-Cell Adhesion..... 156

Figure 4.6: Forces acting on Nanoparticles under Shear Flow 157

Figure 4.7: Dimensions of a Polycarbonate Transwell..... 160

Figure 4.8: Simulation of Transcytosis States..... 165

Figure 4.9: FLAME State and Process Order Graphs of the Transwell Receptor Binding Model 166

Figure 4.10: Nanoparticle Binding in an *in silico* Transwell Model of the Blood Brain Barrier without Transport..... 169

Figure 4.11: Specificity of Nanoparticle Binding in an *in silico* Transwell Model of the Blood Brain Barrier without Transport..... 170

Figure 4.12 Number of Bonds *per* Nanoparticle for Binding in an *in silico* Transwell Model of the Blood Brain Barrier without Transport 172

Figure 4.13: Nanoparticle Transcytosis in an *in silico* Transwell Model of the Blood Brain Barrier 173

Figure 4.14: Nanoparticle Binding to the Basolateral Side of an *in silico* Transwell Model of the Blood Brain Barrier 174

Figure 4.15: Nanoparticle Release in an *in silico* Transwell Model of the Blood Brain Barrier 176

Figure 4.16: FLAME State and Process Order Graphs of the Capillary Receptor Binding Model 179

Figure 4.17: Dislodging Force as a Function of Particle Size 180

Figure 4.18: Shear Stress under Normal Flow and Functional Hyperaemia 182

Figure 4.19: Normalised Number of Particles Transiting through a Vessel under Normal Flow and Functional Hyperaemia 182

Figure 4.20: Efficiency of Nanoparticle Binding in a Capillary Model of Normal Flow and Functional Hyperaemia 184

Figure 4.21: Effect of Functional Hyperaemia on Nanoparticle Binding 186

Figure 4.22: Specificity of Nanoparticles for increased Receptor Expression under Shear Flow 187

Figure 4.23: Average Number of Bonds per Nanoparticle in a Capillary Model of Normal Flow and Functional Hyperaemia..... 189

Figure 4.24: The Combined increased Specificity from induction of Functional Hyperaemia and increased Receptor Density 190

Figure 5.1: The Average Mean Squared Displacement of a Population of Nanoparticles *versus* Time 200

Figure 5.2: The Mean Squared Displacement of a Population of Nanoparticles versus Time 201

Figure 5.3: Nanoparticle Motion Traces with varying Size and Propulsion Velocity 202

Figure 5.4: Nanoparticle Motion Traces with varying Size and Propulsion Velocity 204

Figure 5.5: Nanoparticle Motion Traces with varying Size and Propulsion Velocity inside a Capillary..... 206

Figure 5.6: Binding of Nanoparticles undergoing Propulsion in a Simple Model of a Capillary..... 207

Figure 5.7: Binding of Chemotactic Nanoparticles in a Capillary 208

Figure 5.8: Substrate-dependent Reaction Velocity..... 211

Figure 5.9: Chemotaxis Simulation Set up..... 212

Figure 5.10: Chemotaxis Efficiency of Chemotactic Particles under different Gradients 214

Figure 5.11: Polar Run and Tumble of different Particles 215

Figure 5.12: Enzyme and Substrate Concentration dependent Propulsion Velocity 216

Figure 5.13: Chemotaxis Efficiency of Chemotactic Particles under different Gradients with different Enzyme Encapsulation 217

Figure 5.14: Polar Run and Tumble of different Particles with different Enzyme Encapsulation 218

Figure 5.15: Group Behaviour of Self-Diffusiophoretic Particles..... 219

Permission for the reproduction of Figures 1.3, 1.4 and 1.10 has been granted under License Number 3647080588637.

Permission for the reproduction of Figure 1.8 has been granted under License Number 3650151303698.

The International Society for Optics and Photonics (SPIE) has granted permission for the reproduction of Figure 1.13.

Permission for the reproduction of Figure 1.24 has been granted under License Number 3650150393527.

LIST OF ABBREVIATIONS

Ang	Angiopep-2
CCW	Counter Clockwise
CFD	Computational Fluid Dynamics
CNS	Central Nervous System
CPU	Central Processing Unit
CSF	Cerebrospinal Fluid
CVO	Circumventricular Organ
CW	Clockwise
DLS	Dynamic Light Scattering
DMEM	Dulbecco's Modified Eagle Medium
DPI	Dual Polarisation Interferometry
ECF	Extracellular Fluid
EPR	Enhanced Permeability and Retention
FEM	Finite Element Method
FLAME	Flexible Large-Scale Agent-based Modelling Environment
FLOPS	Floating Point Operations *per* Second
fMRI	Functional Magnetic Resonance Imaging
GFAP	Glial Fibrillary Acidic Protein
GLS	Galerkin/Least Squares
GMRES	Generalised Minimal Residual Method
HBMEC	Human Brain Microvascular Endothelial Cell
HPLC	High Performance Liquid Chromatography
IPF	Interstitial Fluid Pressure
ISF	Interstitial Fluid
ITC	Isothermal Titration Calorimetry
LDL	Low Density Lipoprotein
Lrp1	Low Density Lipoprotein Receptor Related Protein 1
MPI	Message Passing Interface
MPS	Mononuclear Phagocyte System

MRI	Magnetic Resonance Imaging
MRP	Multidrug Resistance Protein
MSD	Mean Squared Displacement
MT	Microscale Thermophoresis
NTA	Nanosight Tracking Analysis
OpenMP	Open Multi-Processing
PBO	Poly [Butylene Oxide]
PDE	Partial Differential Equation
PDPA	Poly [2-(Diisopropylamino) Ethyl Methacrylate]
PEG	Poly [Ethylene Glycol]
PEO	Poly [Ethylene Oxide]
PET	Positron Emission Tomography
Pgp	P-Glycoprotein
PMPC	Poly [(2-Methylacryloyl) Ethyl Phosphorylcholine]
PNS	Peripheral Nervous System
POEGMA	Poly [Oligo (Ethylene Glycol) Methyl Methacrylate]
PSA	Polar Surface Area
QSAR	Quantitative Structure Activity Relationship
RBC	RBC
RES	Reticuloendothelial System
SAXS	Small Angle X-Ray Scattering
SPECT	Single Photon Emission Computer Tomography
SPR	Surface Plasmon Resonance
TEER	Trans-Endothelial Electrical Resistance
TEM	Transmission Electron Microscopy
TRAIL	Tumor Necrosis Factor Related Apoptosis Inducing Ligand
vSMC	Vascular Smooth Muscle Cells
XMML	X-Machine Markup Language

CHAPTER 1: INTRODUCTION

1.1 CLINICAL MOTIVATION

1.1.1 The Central Nervous System

The nervous system is a network of cells that are involved in rapid communication around the body. It is split into two major parts, the peripheral nervous system (PNS) and the central nervous system (CNS). The PNS consists of the sensory neurones and motor neurones. Sensory neurones detect certain stimuli and relay messages to the CNS. The motor neurones distribute instructions from the CNS to peripheral tissue to affect activity, for example, cause a muscle to contract. The CNS consists of the brain and spinal cord. Its major function is in processing information from the PNS and co-ordinating the activity of the body. It is responsible for many of the higher functions of humans and animals including, consciousness, memory, learning and language. It is a highly complex organ with different regions having specific functions. The CNS contains a number of different cells that contribute to CNS function in various ways, as summarised in *Figure 1.1*.

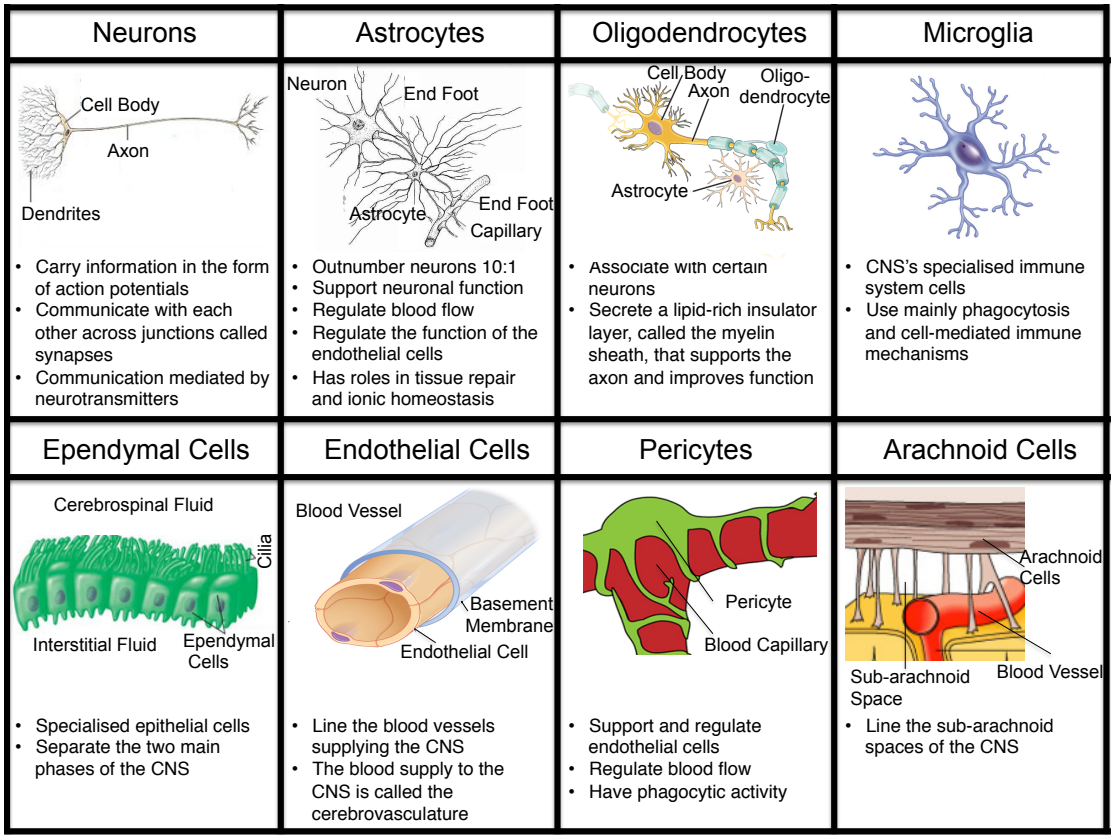

Figure 1.1: Cells of the Central Nervous System. A summary of the functions of different CNS cells.

1.1.2 Burden of Disease

The CNS is a highly delicate tissue and has a reduced reparative and regenerative capacity compared to many other tissues (Fawcett and Asher, 1999). Therefore diseases of the CNS, generally, have a high morbidity and mortality rate. It is estimated that ~1 billion worldwide individuals have a neurological disease with diverse presentations from migraines to fatal neurodegenerative diseases. Furthermore, neurological diseases are responsible for 12% of global deaths with current projections suggesting that the burden of such diseases will increase by the year 2030 (WHO, 2007). This is because many CNS diseases tend to affect older individuals and global life expectancies are increasing. Neurological diseases are numerous and highly diverse, they can be broadly characterised as cerebrovascular diseases, neurodegenerative diseases, neurodevelopmental psychiatric diseases and

infectious diseases. A summary of the relative impact of selected neurological diseases is given in *Figure 1.2*.

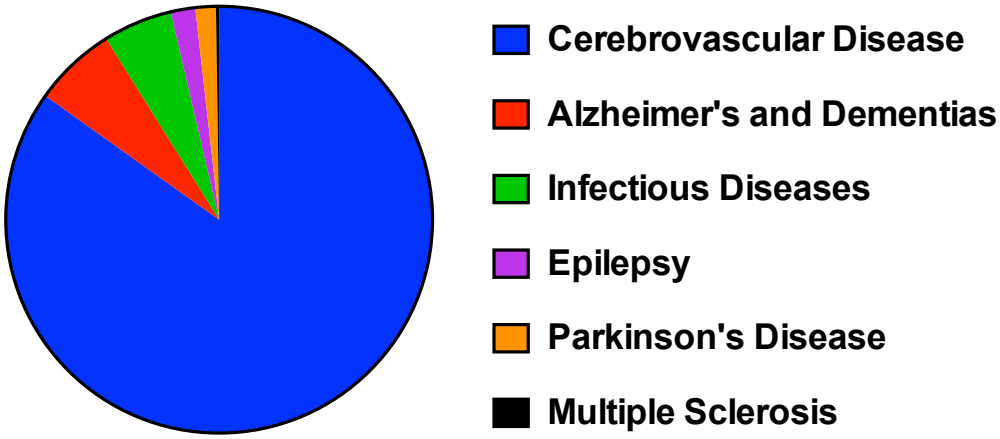

Figure 1.2: Relative Global Deaths for Selected Neurological Disorders. (WHO, 2007)

Cerebrovascular diseases refer to diseases that adversely affect the function of the vasculature supplying the CNS. This includes haemorrhages, where blood vessels rupture and leak blood into the CNS tissue itself, and ischaemia where blood supply to the tissue is insufficient. These two diseases often result in damage to the underlying neurological tissue causing a neural insult known as a stroke (Lipton, 1999, Fewel et al., 2003). Neurodegenerative diseases are characterised by neural cell death causing partial or complete loss of certain CNS functions, these include disease such as Alzheimer's and Parkinson's disease. The neurodevelopmental diseases are caused by abnormalities in CNS development and include schizophrenia and autism spectrum disorders.

1.1.3 Drug Delivery into the Central Nervous System

There are very few current effective treatment options for most CNS disorders, this is a consequence of several key factors. Firstly, the understanding of both molecular and tissue level factors that cause pathogenesis in most CNS disorders is relatively poor. Secondly, whilst

classical animal *in vivo* models can give some insights into pathogenesis in these disorders, compared to many other non-neurological models of disease, these models do not correlate as well with the clinical manifestations in humans (Markou et al., 2009). Thirdly, diagnosis of neural disease usually occurs after the onset of clinical symptoms, which often occur long after initial damage and at a point where intervention efficacy will be vastly reduced (Dekosky and Marek, 2003). However, one of the most important factors in the lack of adequate treatment options is the exclusion of many potential therapeutic molecules from the CNS tissue. It is believed that over 98% of small molecular weight therapeutics and nearly all of large molecular weight therapeutics are unable to penetrate into the CNS. This is due to the evolution of blood-brain barriers, which act to tightly regulate exchange of molecules between the blood and the CNS tissue (Abbott et al., 2010, Pardridge, 2005). In order to improve general treatment strategies aimed at the CNS, novel methods to deliver a wider range of molecules to the CNS are needed. The following sections introduce the anatomy, physiology and biology of the CNS and the barriers. The knowledge of these features is vital for understanding how molecules can be delivered to the CNS, can be distributed to targets within the CNS and are cleared from the CNS.

1.2 ANATOMY OF THE CENTRAL NERVOUS SYSTEM

The CNS is made up of two phases, a cellular phase bathed in interstitial fluid (ISF) and an acellular phase filled with cerebrospinal fluid (CSF). The fluid of these two phases can freely interact across a layer of specialised epithelial cells known as the ependyma. Dynamics of these two fluid phases and their interaction together are important for the understanding of how the CNS is able to distribute molecules to their required location and remove unwanted molecules from the CNS (Davson and Segal, 1995, Abbott, 2004).

1.2.1 Interstitial Fluid

The ISF contains all of the cells that are responsible for the specialised CNS function. These include, but are not limited to, neurones, astrocytes, microglia, oligodendrocytes and pericytes. Therefore delivery of potential therapeutics into the ISF is essential for having any positive therapeutic effect. The ISF is mainly produced by the extensive blood-brain barrier that is discussed later in Section 1.3.1. Transport through the ISF has been shown to involve diffusion, bulk flows and more recently through astrocyte-mediated convection called the glymphatic pathway (Abbott, 2004, Mendelsohn and Larrick, 2013, Iliff et al., 2013). The CNS, despite its high metabolic activity and high sensitivity to toxic compounds lacks an extensive lymphatic system. It was believed that the CNS completely lacked a lymphatic system, however recently it was demonstrated to be present lining the dural sinus in the meninges (Louveau et al., 2015). The lymphatic system in peripheral tissue is responsible for the drainage and removal of toxic materials, trafficking the waste back for degradation by the liver *via* the blood. Abbott and colleagues described pathways of least resistance through the ISF. These typically occurred in the perivascular space around larger blood vessels and in astrocyte lined tracks along neuronal axons. Both of these mechanisms would result in a relatively inefficient mechanism of transport of material through the ISF (Abbott, 2004), as it relies on diffusion alone. However recent work has demonstrated a new system, termed the glymphatic system, which appears to explain this apparent discrepancy (Iliff et al., 2013, Mendelsohn and Larrick, 2013). Fluid from the CSF influxes through the para-arterial space, a space formed between the outside of arteries and astrocytic endfeet that surround the arteries. This fluid flows out of the para-arterial space by a convective flow maintained by astrocytes through the water channel aquaporin 4. The convective flow continues across the ISF towards the para-venous space, a space surrounding the cerebral veins. The para-venous space effluxes to the lymphatic system of the neck, eventually reaching the liver for degradation *via* the blood. This convective flow therefore washes away waste products forming an effective waste removal mechanism (Yang et al., 2013,

Nedergaard, 2013, Xie et al., 2013, Mendelsohn and Larrick, 2013). However, since this system is hypothesised to be a major route for toxic protein clearance, it may be impaired in neurodevelopmental disorders or ageing, contributing to the build up of protein plaques and tangles (Mendelsohn and Larrick, 2013).

1.2.2 Cerebrospinal Fluid

The CSF is an acellular fluid contained within a series of interlinked fluid sacs called ventricles and in the subarachnoid spaces (See *Figure 1.3*). Studies have shown that the bulk of the fluid is produced at the various choroid plexuses within the brain (Davson and Segal, 1995). The CSF then flows through the ventricular system, entering the subarachnoid spaces before draining out at the arachnoid membranes. The CSF offers the brain mechanical protection in response to trauma, buoyancy (Carpenter et al., c.1976), a route for waste clearance to venous blood and a source of non-neuronal signalling (Milhorat and Hammock, 1983, Rapoport, 1976). Gupta and colleagues were the first group to look extensively at the fluid dynamics throughout the entire system using computational modelling based on magnetic resonance imaging (MRI) data. One of the most interesting findings was that in certain regions of the CNS, fluid dynamics approached simple diffusion. These regions corresponded particularly to specific locations within the CNS. It was hypothesised that these regions would permit increased ISF-CSF interaction than areas where CSF flow is higher. Therefore CSF-borne molecules may be selectively accrued in these regions (Gupta et al., 2010).

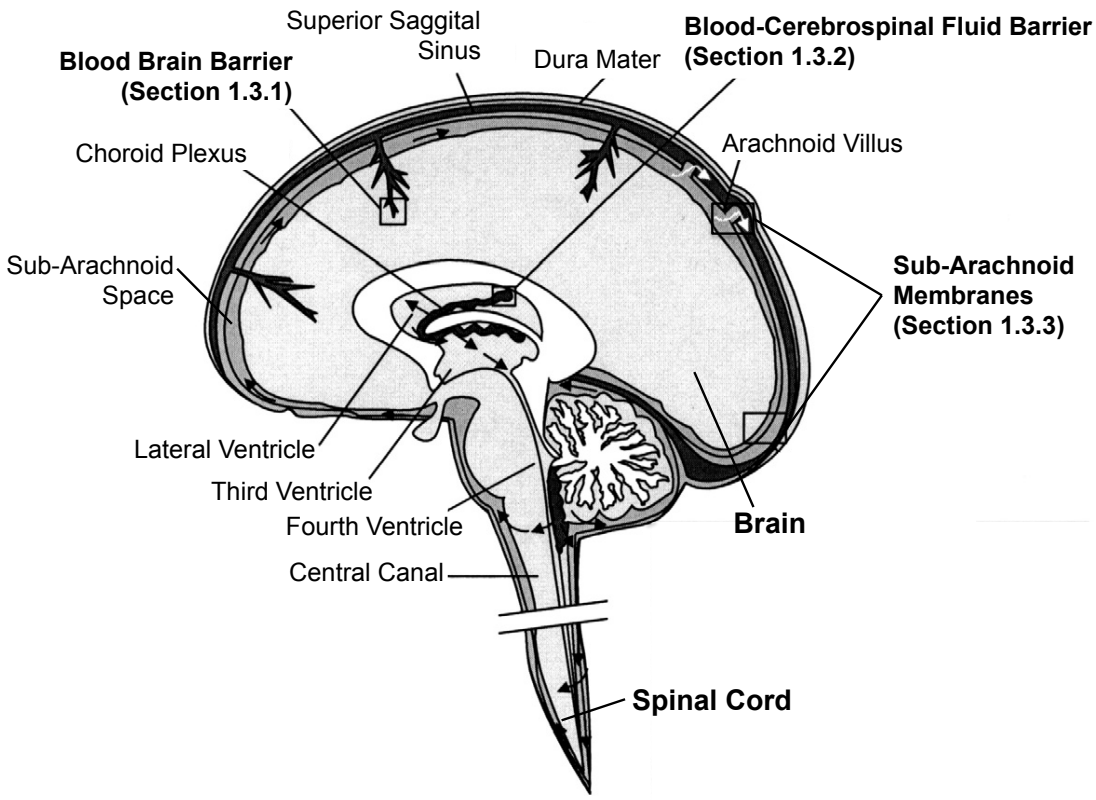

Figure 1.3: Structure of the Central Nervous System and Ventricular System. The CNS consists of the brain and spinal cord. There are three major barriers indicated, the blood-brain barrier that feeds the ISF, the blood cerebrospinal fluid barriers that feed the CSF in the ventricular system and the sub-arachnoid membranes where CSF leaves the sub-arachnoid spaces to return to the blood. Flow of CSF is indicated by arrows from its origin in the choroid plexuses to the site of removal at the arachnoid villi. Adapted from (Abbott et al., 2010)

1.3 BARRIERS OF THE CENTRAL NERVOUS SYSTEM

There are a number of barriers of the CNS, these are the blood-brain barrier, the blood-cerebrospinal fluid barriers and the arachnoid membranes. These barriers share a common function in the regulation of transport between the periphery and the CNS. The barriers vastly reduce the ability of most molecules freely diffusing between adjacent cells, known as by the paracellular route. This is through the presence of specialised intercellular junctions, called tight junctions, between neighbouring cells of the barrier (*Figure 1.4*). In the absence of the paracellular route, cells mediate the exchange of substances through the intracellular route. These barriers can, therefore, act as the gatekeepers of the CNS. Consequently, understanding

their biology is integral to achieving improved CNS delivery systems (Abbott, 2005, Abbott et al., 2010, Pardridge, 2005).

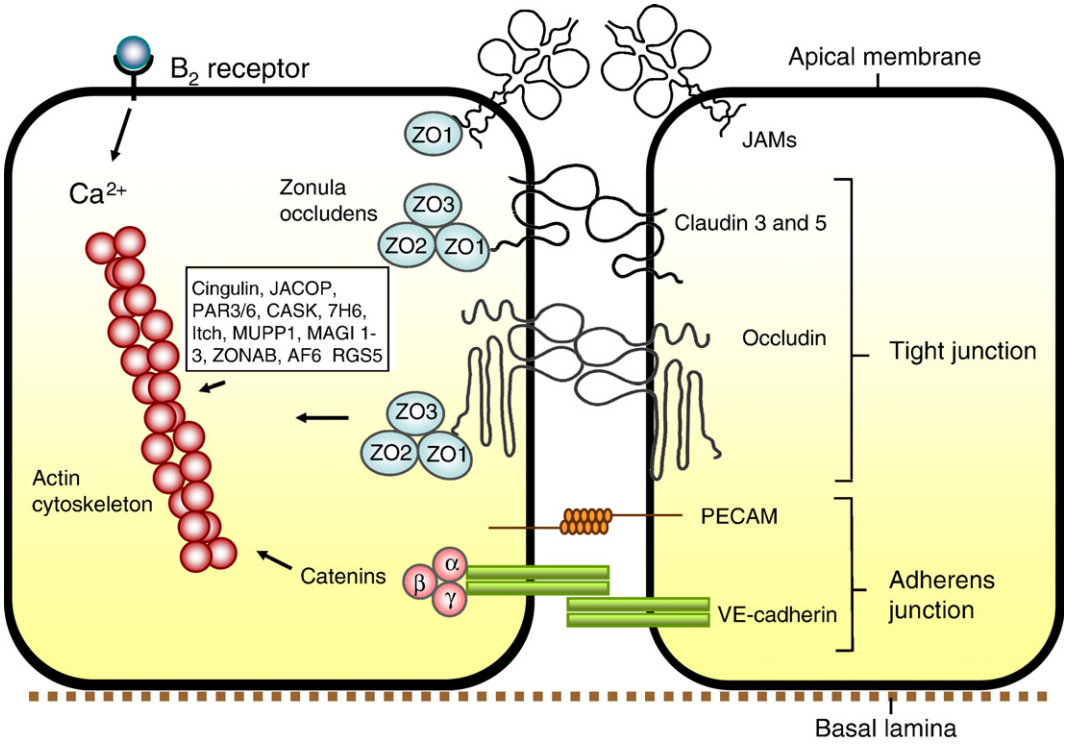

Figure 1.4: Structure of Tight Junctions at the Blood Brain Barrier. Adhesion junctions are formed between adjacent cells using adheren proteins that link to the cell cytoskeleton. Tight junction proteins confer tight junction properties and are present in addition to adheren proteins (Abbott et al., 2010).

1.3.1 Blood Cerebrospinal Fluid Barriers

The blood-cerebrospinal fluid barriers are found within two distinct structures, the choroid plexuses and the circumventricular organs (CVOs) (Langlet et al., 2013, Davson and Segal, 1995). These structures are both characterised by a high density of fenestrations (controlled pores through endothelial cells) and the lack tight junctions, thus permitting free exchange of material from the blood to the tissue. However barrier function instead occurs at the specialised ependyma that interface the extracellular fluid (ECF) of the choroid plexus to the CSF. The choroid plexus's main function is in generating the CSF. The ependymal cells that make up the blood-cerebrospinal fluid barrier perform this function. However, the ependymal cells also have tight intercellular

junctions and therefore form the essential barrier function at the choroid plexus, as demonstrated in *Figure 1.5* (Abbott, 2005, Langlet et al., 2013).

The CVOs function in communicating between the CNS and peripheral blood. They can be secretory, secreting signals in response to neural activity, or sensory, signalling to the CNS in response to peripheral blood signals. The mediators of these signals are cells called tanycytes that sit within the ependymal layer. This layer forms the barrier properties at the CVOs and makes the tanycytes ideally placed to interface between the blood and the CNS, *via* the CSF, as demonstrated in *Figure 1.5*.(Abbott, 2005, Langlet et al., 2013). Interestingly the function of the CVOs would require highly efficient CSF-ISF crosstalk in the local region, therefore these regions are likely to favour exchange of molecules, as reported by Kurtcuoglu and co-workers (Kurtcuoglu et al., 2007).

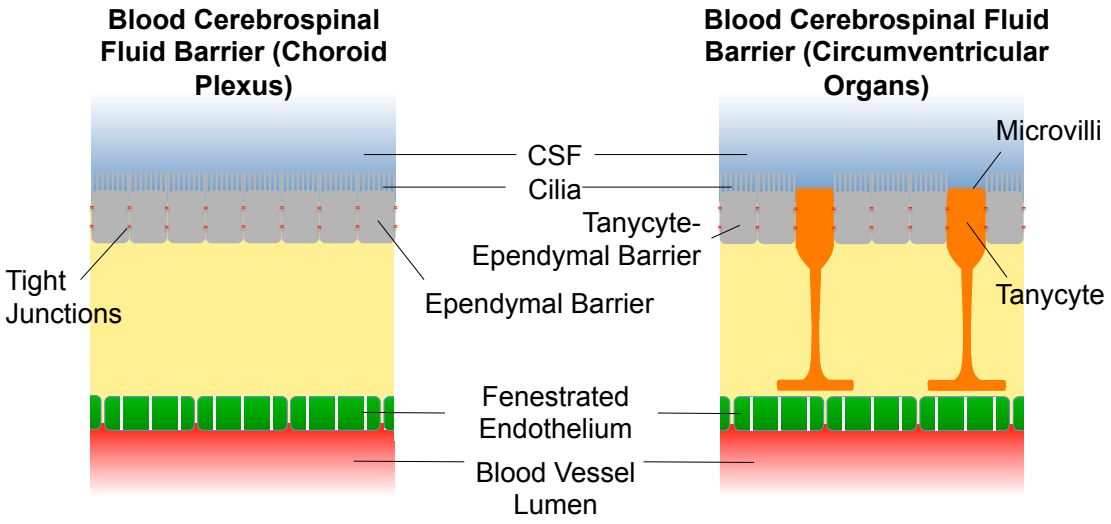

Figure 1.5: Organisation of the Blood-Cerebrospinal Fluid Barriers. Structure of the blood cerebrospinal fluid barriers at both the choroid plexus and the circumventricular organs. The endothelium is fenestrated at both barriers and therefore freely permeable between tissue and blood. However the barrier function is formed by the ependymal cells in both barriers. In the CVOs, tanycytes are interspersed in the ependymal barrier but still form tight junctions thus maintaining barrier integrity between the perivascular space of the CVOs and the CSF.

The blood cerebrospinal fluid barriers are generally regarded as a poor way to deliver therapeutics to the CNS. This is because it relies on the CSF flow and ISF exchange to reach potential targets. The work by Gupta and co-workers raises the intriguing prospect that using the choroid plexus may favour delivery into specific regions of the CNS (Gupta et al., 2010). The CVOs however may present a far more interesting site for delivery of therapeutics as they are optimised to interact between the blood and particular regions of the CNS, for example the median eminence CVO and the proximal CNS tissue in the hypothalamus (Langlet et al., 2013). Moreover, delivery of effector molecules to tanycytes potentially could be used to influence tanycyte signals to the CNS, thus effecting specific CNS functions (Langlet, 2014).

1.3.2 Arachnoid Membranes

The arachnoid membranes border the CSF-filled subarachnoid spaces. Tight junctions are formed by a layer of arachnoid cells to provide a physical barrier between the sub-arachnoid space and venous blood of the sagittal sinus (*Figure 1.6*). Interspersed within the arachnoid membranes are arachnoid granulations or villi that permit the drainage of CSF into the venous blood. Since it is mainly a drainage point, the arachnoid membranes don't present a practical access point for therapeutic delivery. Furthermore, to penetrate key areas of the brain would require the ability to move against the bulk flow of the CSF (Abbott, 2005, Abbott et al., 2010).

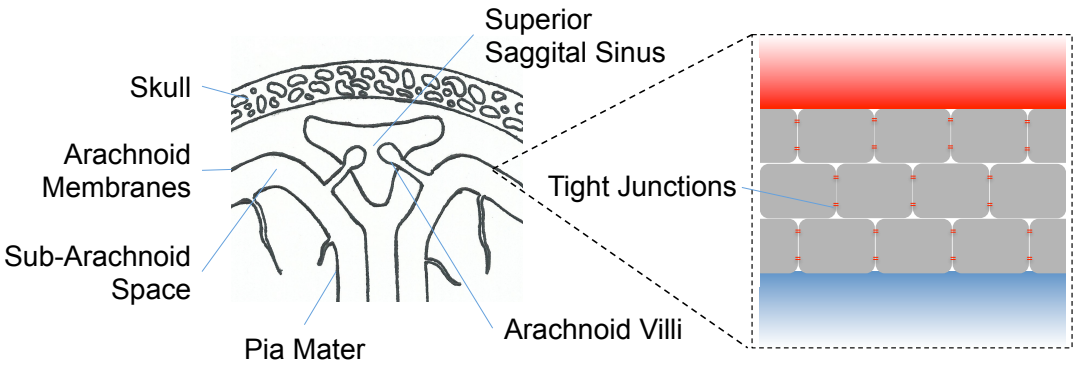

Figure 1.6: The Arachnoid Barrier. The arachnoid barrier is present underneath the skull, the CSF in the sub-arachnoid spaces can cross into the venous blood, such as the superior sagittal sinus, through arachnoid villi. The arachnoid cells provide barrier function.

1.3.3 Blood Brain Barrier

The most important and well studied of the barriers is the blood-brain barrier. The blood-brain barrier constitutes a surface area of 20 m^2, thus making it the largest interface between the blood and the CNS. Moreover the barrier sits directly between the blood and the ISF, providing the shortest route from entry point to target (Pardridge, 2005). The barrier function occurs at the level of the endothelial cells that constitute the blood vessel walls supplying the CNS tissue, but is regulated by a number of associated cells including pericytes, astrocytes, microglia and neurones, which collectively form the neurovascular unit, as demonstrated in *Figure 1.7* (Abbott et al., 2010).

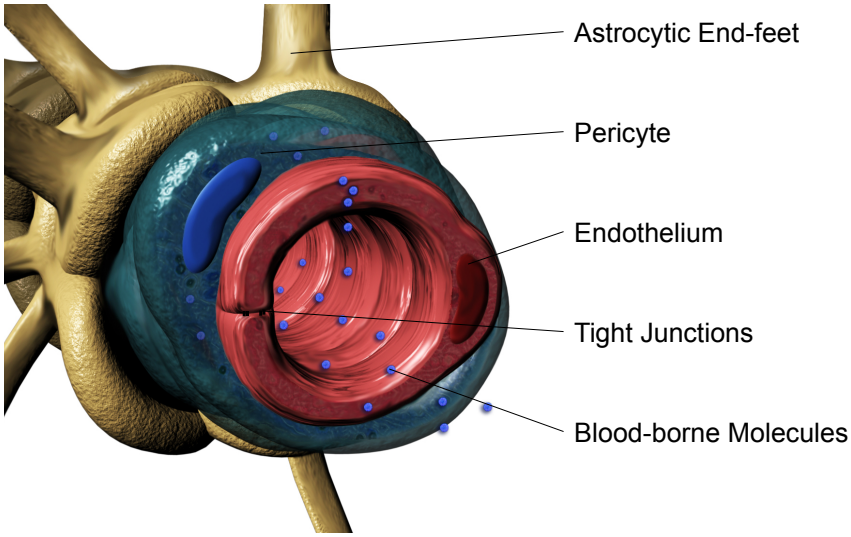

Figure 1.7: Structure of the Neurovascular Unit. Endothelial cells constitute the vessel walls of blood vessels. Tight junction proteins form tight inter and intracellular junctions. Pericytes surround the endothelial layer, sharing a basal lamina with the endothelial cells. Projections from astrocyte cells contact the vessel at end-feet structures. Graphic produced by Silvia Bianco based on the image by Miller (Miller, 2002) and initial sketches provided by Gavin Fullstone and Giuseppe Battaglia.

The barrier functions to vastly reduced the unregulated exchange of molecules between the blood and the CNS. It achieves this by the lack of fenestrations (see *Figure 1.8*), and tight junctions between neighbouring cells. This 'physical barrier' restricts the passage of almost all molecules with the exception of small lipophilic molecules including oxygen. Moreover, potentially harmful molecules that have the correct physical and chemical properties to permit passage across the blood brain barrier may be subject to broad-specificity efflux transport or metabolic degradation. These are known as the 'transport barrier' and 'metabolic barrier' properties of the blood brain barrier respectively (Abbott et al., 2010, Pardridge, 2005, Zlokovic, 2008).

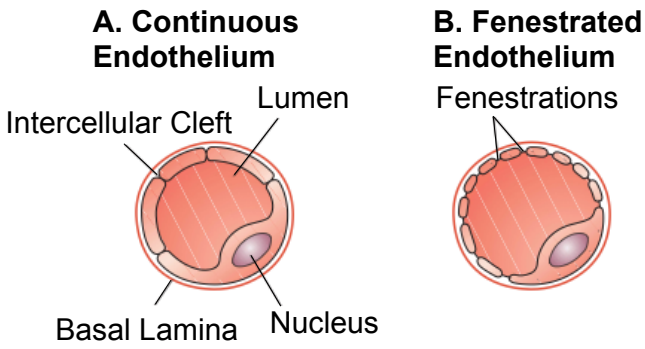

Figure 1.8: Structure of Endothelium. Cross-sections of continuous endothelium (A) found at the blood-brain barrier compared to fenestrated endothelium found in other tissues, such as the kidney and the choroid plexus (B). (Cleaver and Melton, 2003).

The almost universal exclusion of vital molecules for basic function of the CNS, such as glucose, amino acids and nucleotides, by passive diffusion mechanisms means that the endothelium must transport essential molecules from the blood to the CNS and *vice versa* by active transport or facilitated diffusion. These mechanisms of transport are discussed in more detail in section 1.4. A summary of the blood brain barrier's structure and function is presented in *Figure 1.9*.

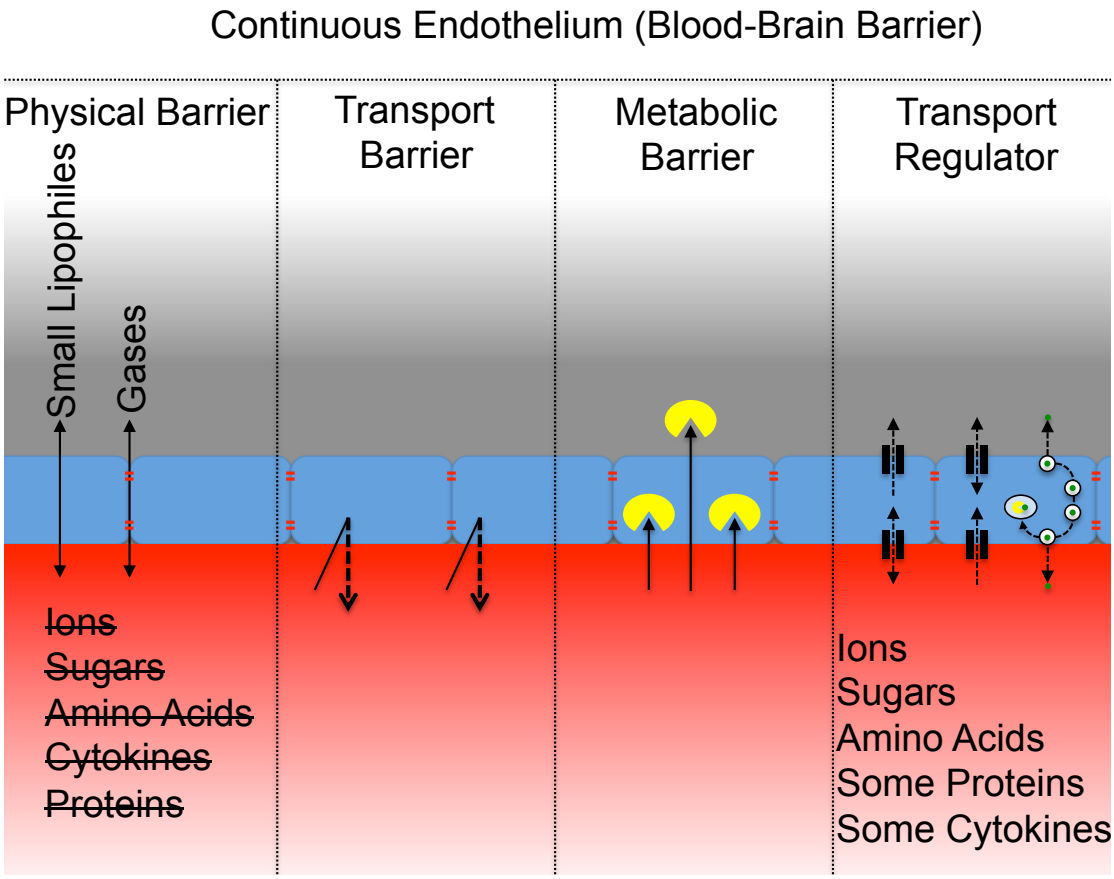

Figure 1.9: Function of the Blood-Brain Barrier. The blood-brain barrier consists of continuous endothelium that lacks fenestrations and has tight junctions between cells, thus presenting a physical barrier to the free exchange of most molecules. Some molecules that cross are removed by efflux transporters (transport barrier) or by degradation by enzymes (metabolic barrier). In order to obtain necessary molecules, the blood-brain barrier regulates transport through the cell.

The blood-brain barrier is generally cited as the best access point to the CNS for therapeutic delivery, as it permits short transit time to targets and has the potential to reach all areas of the CNS. However, being able to access all areas of the CNS could lead to potential off-target effects and given the fragile nature of the CNS this may be catastrophic. Whilst the blood-brain barrier presents an interesting site for delivery, methods to achieve specific delivery at certain points of the barrier are necessary for future progression of CNS therapeutic design. In the remainder of this thesis, methods to improve general and specific delivery across the blood-brain barrier directly into the ISF are explored.

1.4 TRANSPORT AT THE BLOOD BRAIN BARRIER

1.4.1 Small Molecule Transport

There are a number of different transport mechanisms that occur at the blood-brain barrier, as demonstrated in *Figure 1.10*. The simplest is that of passive diffusion, where molecules with particular properties are able to diffuse across the barrier in a concentration dependent manner. Molecules that can passively diffuse across the barrier are generally small (<500Da) and lipid soluble (Pardridge, 2005). More recently, improved methods for analysing the relationships between structural and chemical properties with brain penetrance have been used. The most thorough is that of Quantitative Structure Activity Relationship (QSAR) analysis, which uses training libraries of molecules with known penetrance properties to predict the likelihood of candidate molecules penetrating the CNS. Several such studies have been performed with the most commonly studied variables being, polar surface area (PSA), octanol-water partition coefficient (logP) and the number of hydrogen bond acceptors/donors. The PSA is the sum of the surface area of all polar atoms and generally needs to be <90 $Å^2$ to breach the blood-brain barrier. logP is a measure of hydrophobicity and correlates with increase in blood-brain barrier permeation, the optimal range has been found to be 1.5-2.7. The use of such analysis may be of aid in modifying potential candidate molecules for improved CNS penetrance or eliminating poor candidates from high-throughput screening studies. However, in all these studies, the small training libraries used have limited the accuracy of prediction. Moreover, such an approach still limits the scope of therapeutic molecules to a small subset of molecules (Clark, 2003, Zhang et al., 2008b).

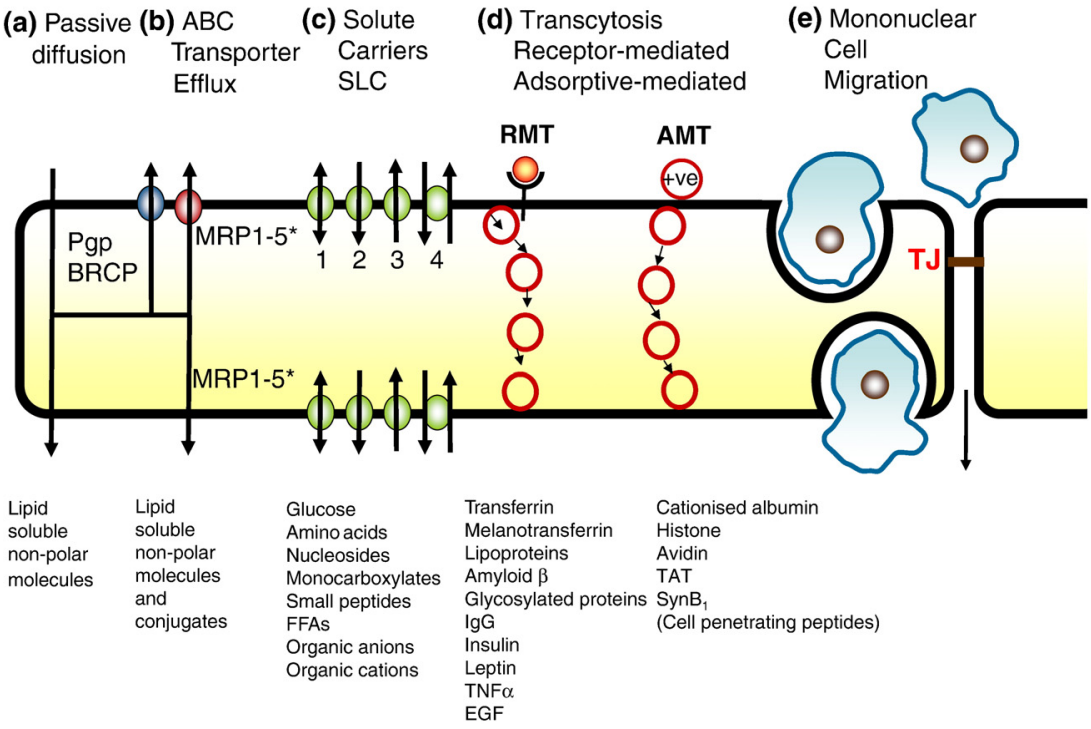

Figure 1.10: Transport at the Blood-Brain Barrier. Examples of the major transport systems across the blood-brain barrier and cargo that utilise them (Abbott et al., 2010)

The majority of transport occurs through molecular transporters, membrane proteins that shuttle the molecule across the cell membrane. These include broad-specificity efflux transporters that remove molecules from the CNS and several metabolite transporters. The broad-specificity of efflux transporters leads to the removal of many potential therapeutic molecules from the CNS, thus decreasing penetrance. The most widely studied of these are P-glycoprotein (Pgp) and the multidrug resistance proteins (MRPs) (Abbott et al., 2010, Pardridge, 2005). Inhibition or knockout of Pgp, coupled with application of molecules that are a substrate of Pgp has been demonstrated to permit improved delivery of potentially therapeutic molecules to the CNS (Sadeque et al., 2000, Mayer et al., 1996, Schinkel et al., 1995, Schinkel et al., 1994).

1.4.2 Immune Cell Migration

The blood-brain barrier is also the site where immune cells can migrate into the CNS. Generally the CNS is regarded as a largely immune system privileged area, with immune function being predominantly provided by the resident microglia (Hanisch and Kettenmann, 2007, Kreutzberg, 1996). Small-scale entry of immune cells from the blood for non-pathological surveillance of the CNS does occur, but large-scale migration of immune cells into the CNS is generally the hallmark of diseases such as multiple sclerosis (Hickey et al., 1991, Ransohoff et al., 2003). In order to use this entry portal to effectively deliver molecules to the CNS tissue requires delivering to the immune cells, migration across the barrier and release unaltered into the CNS.

1.4.3 Vesicular Transport

In addition to solute and immune cell transport, there are some endocytic or vesicular based transport mechanisms. These transport systems involve the invagination of the membrane around the substrate that buds off from the plasma membrane to create a spherical membrane structure around the cargo, known as a transport vesicle. These vesicles are then sorted for recycling, degradation *via* the endocytic pathway or for transport to the opposite membrane, a process known as transcytosis (Mellman, 1996, Broadwell et al., 1988). Vesicular transport mechanisms at the blood-brain barrier are believed to occur at a reduced frequency compared to other continuous endothelium in other tissues. In skeletal muscles, for example, there are 4-5 times as many vesicular structures (Claudio et al., 1989, Reese and Karnovsky, 1967).

Transcytosis can be both receptor-mediated or adsorptive-mediated. Adsorptive-mediated transcytosis occurs as a result of a strong interaction between a cargo molecules (or molecules) and the endothelial wall. Cargo molecules of adsorptive transcytosis are usually strongly cationic to induce the necessary strong interaction with the negatively charged glycocalyx and cell membrane of the endothelium (Hervé et al., 2008). Receptor-mediated

transport has gained wide interest as it provides the capability to control uptake across the blood-brain barrier by tagging cargo with specific ligands. A number of different cargo molecules are known to be able to induce transcytosis, including transferrin, lactoferrin, melanotransferrin, apolipoproteins and insulin (Abbott et al., 2010). The best studied is that of transferrin, a protein that transports iron to tissue. Transferrin is an 80kDa protein that can induce both endocytosis and transcytosis at the blood-brain barrier. The transferrin receptor is expressed only on the apical side of the endothelial barrier. The exact mechanisms for triggering the transcytosis or endocytosis route are poorly understood. In endocytosis the receptor-transferrin complex is recycled intact but after the loss of its iron ions, unlike in most cases where the ligand-receptor complex is broken prior to receptor recycling (Yamashiro et al., 1984, Hopkins, 1983). Interestingly, transferrin has a major role in myelination of neurones, therefore it is possible that due to the increased transferrin demand the receptor expression at the barrier may be increased in white matter (high abundance of myelinated neurones) regions of the brain compared to grey matter (absence of myelinated neurones) (Monteros et al., 1999, Todorich et al., 2009).

Lrp1 (low density lipoprotein receptor-related protein 1) and its ligands are the second mostly widely studied of the receptor-mediated transcytosis systems at the blood-brain barrier. Lrp1 transports a number of low density lipoproteins (LDLs) across the blood-brain barrier (Herz and Marschang, 2003). Lrp1 is expressed on both the apical and basolateral sides of the blood-brain barrier and by most of the cells of the CNS including pericytes, astrocytes, neurones, microglia and oligodendrocytes (Urmoneit et al., 1997, Gaultier et al., 2009, Herz and Marschang, 2003). In the other cells of the CNS, Lrp1 is involved in signalling and endocytosis. Targeting Lrp1, due to its wide expression throughout the CNS, confers the capability to deliver to all cells within the CNS but will inevitably lead to off-target effects.

1.5 METHODS FOR THE STUDY OF THE BLOOD BRAIN BARRIER

The blood-brain barrier function can be studied in a number of ways including *in vivo*, *in vitro*, *ex vivo* and theoretical approaches. This is summarised in *Figure 1.11*, with more detail on each method provided in the remainder of this section.

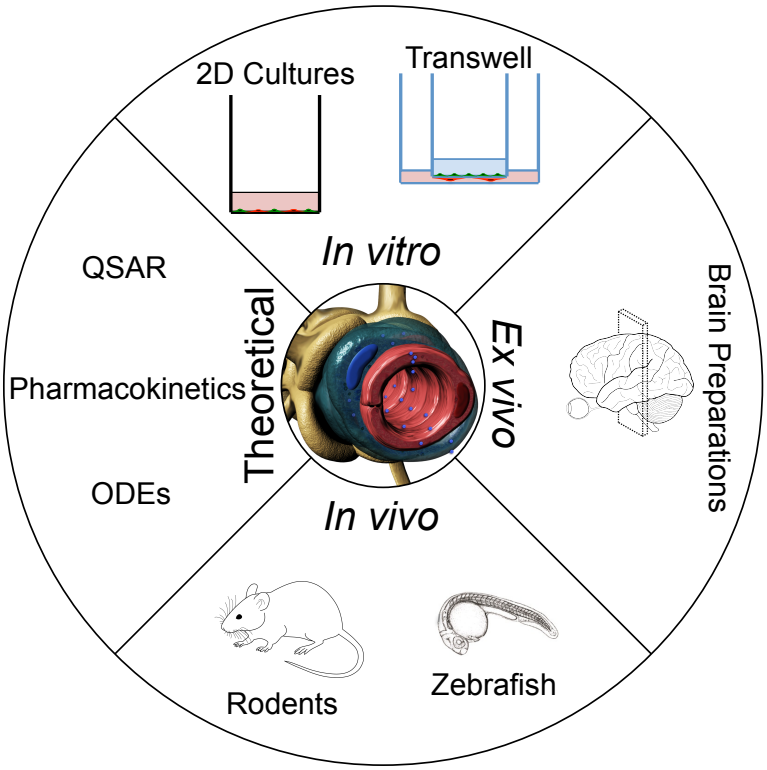

Figure 1.11: Methods to Study the Blood-Brain Barrier.

1.5.1 *In vitro* Models of the Blood-Brain Barrier

The easiest method to study the blood-brain barrier is using *in vitro* methods, culturing endothelial cells alone or co-culturing with other regulatory cells such as pericytes and astrocytes. Many studies of the blood-brain barrier require the endothelial cells to be polarised, where cells distinguish between the two sides of the cell (the tissue or basolateral side and the blood or apical side). These studies routinely use a semi-permeable insert, called a transwell, which can be placed within a standard culture plate (see *Figure 1.12*).

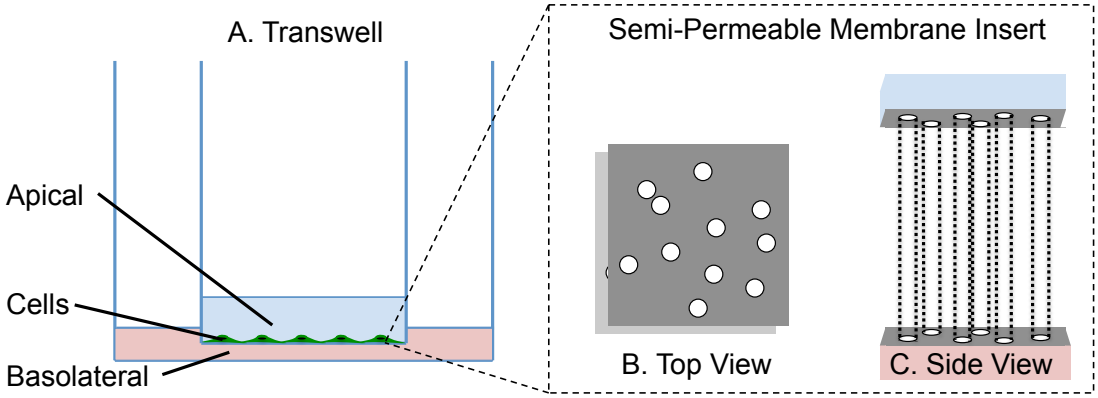

Figure 1.12: Diagram of Transwell. The transwell (A) cultures endothelial cells on a semi-permeable membrane, thus allowing definition of the apical and basolateral sides of the cell. A section of the semi-permeable membrane insert is shown with pores from the top (B) and from the side (C).

In addition to the endothelial layer, supporting cells such as astrocytes and pericytes can be grown on the bottom of the media dish or the reverse side of the transwell insert. The physical barrier properties of the endothelial layer can be assessed using permeability studies, typically sucrose or dextrans, or by measurement of the trans-endothelial electrical resistance (TEER), which measures the resistance of ionic movement across the cell layer in units of Ω cm^{-2}. These models permit a facile method for large-scale screening and pharmacokinetic studies. However, the lack of physiologically accurate arrangement of cells, the absence of flow, the differences between *in vivo* and *in vitro* cells and a reduced tightness of the barrier limit this methods utility. Previously, several attempts have been made to address some of these issues. The most frequent measure of barrier tightness is the TEER that is compared to the *in vivo* values. Butt and colleagues measured the TEER in anaesthetised rats and demonstrated TEER values up to 5900 Ω cm^{-2} with an average of ~1400 Ω cm^{-2} (Butt et al., 1990). Most of the *in vitro* transwell models made with immortalised cell lines reach a maximum of ~200 Ω cm^{-2}. Patabendige and co-workers have developed transwell models from primary porcine endothelial cells with a mean TEER value of ~800 Ω cm^{-2}, still significantly lower than that of the *in vivo* TEER (Patabendige et al., 2013). Introduction of flow in transwell models and similar models also increases the

TEER values in a variety of different cell lines (Cucullo et al., 2013, Griep et al., 2013, Cucullo et al., 2008, Neuhaus et al., 2006). The introduction of flow has achieved a maximum of >700 Ω cm^{-2} for the human brain microvascular endothelial cell (*HBMEC*) line (Cucullo et al., 2013, Griep et al., 2013). Although all these methods are useful for screening, different cell lines and culture techniques also vary other properties of the barrier such as transporter expression (Poller et al., 2008).

1.5.2 *In vivo* Models of the Blood-Brain Barrier

The most biologically relevant methods for studying the blood-brain barrier are by using *in vivo* animal models. The most commonly used animal models of the blood-brain barrier are mice (*Mus musculus*) and rats (*Rattus norvegicus*). The development of the barrier has been well characterised in these organisms and has close functional and structural agreement with the human barrier. However, *in vivo* studies are limited by poor quantitation of CNS delivery and by the cost and complexity of utilising live imaging techniques on these animals. Recently, the presence a blood-brain barrier has been demonstrated in the small teleost zebrafish (*Danio rerio*) early in embryogenesis by dye permeability studies, expression of tight junction proteins and association of other cells of the neurovascular unit. The zebrafish embryo offers optical clarity making it highly suitable for *in vivo* live imaging using light and confocal microscopy. Whilst it can be expected that zebrafish would have reduced translational benefit to humans than rodents, it offers capabilities that make it ideal for high throughput *in vivo* screening to complement rodent studies (Eliceiri et al., 2011, Fleming et al., 2013, Jeong et al., 2008).

1.5.3 *Ex vivo* Models of the Blood Brain Barrier

Along with animal studies, testing on human or rodent *ex vivo* tissue can be used (Abbott et al., 2006, Dallaire et al., 1991, Joo and Karnushi.I, 1973). The use of human tissue has a major advantage in improving translational work

from animal models to humans. However *ex vivo* tissue can be considerably more difficult to elucidate biological mechanisms than *in vitro* systems due to the added complexity of slices (Abbott et al., 2006, Dallaire et al., 1991, Joo and Karnushi.I, 1973). Furthermore, blood-brain barrier studies using *ex vivo* slices are limited by the lack of blood flow and the frequent complete collapse of blood vessels due to the loss of blood pressure.

1.5.4 *In silico* and Mathematical Models of the Blood Brain Barrier

The previous sections describe classical biological approaches to the study of the blood-brain barrier. However, modelling approaches increasingly are being used to understand and predict various functions of the blood-brain barrier. These modelling approaches include mathematical descriptions of pharmacokinetics and prediction of molecule permeability. Pharmacokinetics uses equations or a series of equations to describe the clearance, transport and distribution of molecules within the CNS. A number of groups have successfully produced CNS focused pharmacokinetic models of various scales from just the barrier itself, to the whole circulatory system (Westerhout et al., 2012, Badhan et al., 2014, Wong et al., 2013). In *Section 1.2.4* the use of QSAR modelling, a method that predicts permeability of molecules based on physical and chemical properties, was described. In the next sections two methods of *in silico* modelling, which have been used with success in other fields, are discussed. This work aims to apply these methods to study the transport across the blood-brain barrier,

1.6 COMPUTATIONAL FLUID DYNAMICS

Transport from the blood to the CNS across the blood-brain barrier is reliant on distribution through the circulatory system. Therefore, understanding the dynamics of blood flow is important for study of distribution and uptake at the blood-brain barrier. The dynamics of a fluid can be described by three coupled partial differential equations, collectively known as the Navier-Stokes equations. These are the conservation of mass, the conservation of

momentum and the conservation of energy. The conservation of momentum is given in its general form as:

$$\boldsymbol{\rho}\left(\frac{\partial \boldsymbol{v}}{\partial \boldsymbol{t}} + \boldsymbol{v}\cdot\boldsymbol{\nabla}\boldsymbol{v}\right) = -\boldsymbol{\nabla}\boldsymbol{p} + \boldsymbol{\nabla}\cdot\boldsymbol{\tau} + \boldsymbol{F} \qquad (1.1)$$

where $\boldsymbol{\rho}$ is the density, $\boldsymbol{t}$ is time, $\boldsymbol{\nabla}$ is the del operator, $\boldsymbol{v}$ is the velocity, $\boldsymbol{p}$ is the pressure, $\boldsymbol{\tau}$ is the 2nd order stress tensor and $\boldsymbol{F}$ is the force. The conservation of mass is given as:

$$\frac{\partial \boldsymbol{\rho}}{\partial \boldsymbol{t}} + \boldsymbol{\nabla}\cdot\boldsymbol{\rho}\boldsymbol{v} = \boldsymbol{0} \qquad (1.2)$$

and finally the conservation of energy is:

$$\boldsymbol{\rho C_p}\left(\frac{\partial \boldsymbol{T}}{\partial \boldsymbol{t}} + (\boldsymbol{v}.\boldsymbol{\nabla})\boldsymbol{T}\right) = -(\boldsymbol{\nabla}.\boldsymbol{q}) + \boldsymbol{\tau}\!:\boldsymbol{S} - \frac{\boldsymbol{T}}{\boldsymbol{\rho}}\frac{\partial \boldsymbol{\rho}}{\partial \boldsymbol{T}}\Big|_{\boldsymbol{p}}\left(\frac{\partial \boldsymbol{p}}{\partial \boldsymbol{t}} + (\boldsymbol{v}.\boldsymbol{\nabla})\boldsymbol{p}\right) + \boldsymbol{Q} \qquad (1.3)$$

where $\boldsymbol{C_\rho}$ is the specific heat capacity at constant pressure, $\boldsymbol{T}$ is the absolute temperature, $\boldsymbol{q}$ is the heat flux vector, $\boldsymbol{S}$ is the rate of strain tensor and $\boldsymbol{Q}$ is the heat sources.

Computational fluid dynamics (CFD) is the use of computational methods to solve or reconstitute these equations in set conditions and geometry. The ultimate goal in CFD methods is to solve the equation for conservation of momentum (*Equation 1.1*), whilst simultaneously satisfying *Equation 1.2* and *1.3*. The complexity of the equations and the non-linearity of many of the terms mean that exact solutions are rare and limited to a number of specific cases where the non-linear terms are eliminated or do not need to be considered such as in Poiseuille's flow or Stoke's flow. Where exact solutions are not available, a number of techniques have been developed to find a solution to the equations with good concordance with flow measurements.

Many of these focus on breaking down the geometry into smaller segments and solving in each segment to obtain a solution for the whole geometry. This is known as discretisation of the Navier-Stokes equations.

1.6.1 Discretisation of the Navier-Stokes Equations

There are many different methods for finding a solution to the Navier-Stokes equations, the oldest is that of the finite difference method. The finite difference method uses a uniform square mesh grid and the differential or strong form of the Navier-Stokes equations to solve fluid flow. The reliance on such a mesh structure makes it inadequate for solving blood flows within complex geometry. Subsequently, two further methods were developed to increase the capacity of CFD methods to deal with complex multi-dimensional geometry and particularly curvature. These methods are the finite volume and finite element methods. These methods use the integral or weak form of the Navier-Stokes equations to iteratively assess flow in more complex geometry.

The finite volume method solves the weak form of the Navier-Stokes equations at discrete mesh points. The finite volume refers to a small but finite volume at each mesh point. The finite volume method evaluates flux at the surface of the finite volume under the *proviso* that the flux entering a given volume is the same as the volume exiting an adjacent volume, as a result the conservation of mass is preserved and therefore the finite volume method is referred to as a conservative method.

The finite element method (FEM), like the finite volume and finite difference method, uses a mesh of the whole geometry and evaluates the fluid dynamics at each discrete subdomain, called an element. The finite element method is particularly adept at approximating partial differential equations across a domain with set boundary conditions. For example, a stationary wall of a pipe would be said to be a no slip boundary, therefore at elements located on this boundary the fluid velocity is equal to 0 (Ferziger and Perić, 2002).

1.6.2 Lattice-Boltzmann Method

The CFD methods presented in the previous section are methods of discretisation of a problem across a large-domain by breaking the domain up into smaller components. The lattice-Boltzmann method is an alternative method for evaluating fluid flow over large domains. However, rather than being based on discretisation of macroscopic scale partial differential equations (the Navier-Stokes equations), the lattice-Boltzmann method is based on a series of models of particles kinetics at the micro- and meso-scopic scale that produce a collective flow model over a large domain that conforms to the macroscale Navier-Stokes equations. One of the major advantages of the lattice-Boltzmann method is its ease of scalability onto parallel high performance computing systems (Chen and Doolen, 1998).

1.7 COMPUTATIONAL FLUID DYNAMICS AND THE BLOOD

The vasculature system is a series of interconnected blood vessels that act to carry nutrients and signals to tissues whilst simultaneously removing waste products from tissues. Blood flow through the vascular system is driven by a pressure gradient from contraction of the heart. CFD methods have been successfully applied to modelling various aspects of the vasculature and the behaviour of the blood. These approaches have improved insight into angiogenesis (the formation of new blood vessels from existing ones) (Bernabeu et al., 2014, Bentley et al., 2008), atherosclerosis (Krams et al., 1997, Steinman et al., 2002) and transport (Korin et al., 2012, Liu et al., 2012). However a number of important considerations are required when modelling the blood using such methods.

1.7.1 Blood Vessel Architecture

Blood vessels are highly heterogeneous in architecture and function. The major vessels are arteries and veins, large vessels that carry blood to and away from the tissues respectively. Arteries deliver blood from the heart and feed the microvasculature, vessels that distribute the blood throughout the

tissue to maximise transport to the entire tissue. The veins then remove blood from the microvasculature and return it back to the heart. The microvasculature contains three major vessel types, arterioles, capillaries and venules. The arteries directly feed arterioles that supply the most numerous vessels, the capillaries (Alberts et al., 2002). Capillaries are the major site of transport between blood and tissue and can vary greatly in size from a few micrometres to tens of micrometres in diameter. Their small diameter is crucial to capillary function in maximising the surface area of the wall to the volume of the blood. Capillaries feed into venules that remove the blood from the tissue and return it to the veins. Architecture of the microvasculature is complex as vessels branch into the capillary bed, as can be seen in the image of the retinal vasculature in *Figure 1.13*.

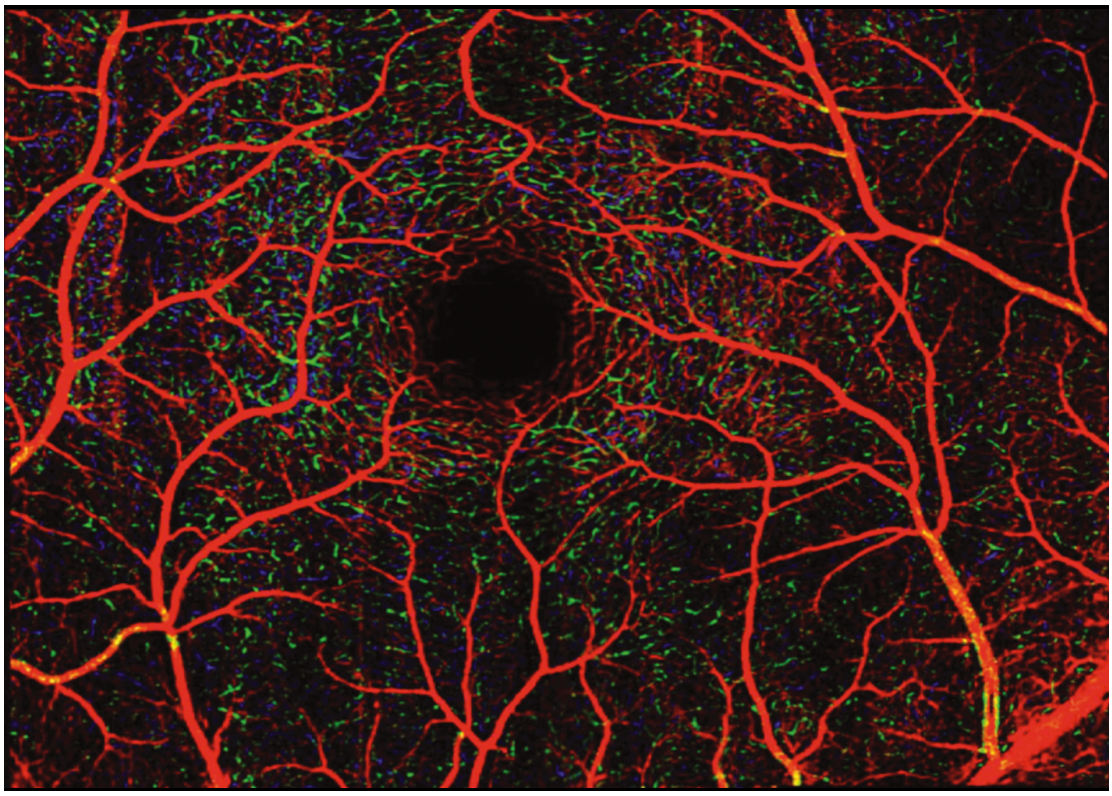

Figure 1.13: The Retinal Vasculature. Depth Coloured Image of the Retinal Vasculature using Ultrahigh Sensitive Optical Microangiography. Red = Ganglion Cell Layer, Green = Inner Plexiform Layer, Blue = Outer Plexiform Layer. Adapted from (An et al., 2011)

1.7.2 Properties of the Blood and Vasculature

The blood itself has a number of fluid properties that make it complex to model using CFD methods. Firstly, the blood is a non-Newtonian fluid, which means that the viscosity of the blood changes according to shear stress in a non-linear fashion. This is a result of the particulate nature of the blood as cells or cell fragments make up 40-45% (*v/v*) of the blood, a measure known as the haematocrit (Baskurt and Meiselman, 2003). The vast majority of the cells are RBCs (RBCs), also known as erythrocytes, however the immune system's white blood cells and platelets are also present. The non-cellular fluid within blood is known as plasma and is a Newtonian fluid. The presence of cells alters the density and viscosity properties of blood, key terms used within CFD methods. Furthermore, in the microvasculature, blood cells are similar to the diameter to the vessel wall and therefore have a high influence on properties of flow within the blood (Baskurt and Meiselman, 2003, McWhirter et al., 2009, McWhirter et al., 2011, Schmid-Schönbein et al., 1969). The Fåhræus-Lindqvist effect is one such property where the apparent viscosity of the blood decreases as the capillary diameter decreases. This is the result of RBCs congregating at the centre of the capillary leaving an acellular or cell-free phase at the vessel walls. This cell-free phase has a lower viscosity than the rest of the blood providing a path of least resistance for blood flow (Fahraeus and Lindqvist, 1931).

1.8 CEREBROVASCULATURE STRUCTURE AND FLOW REGULATION

In order to improve delivery across the blood-brain barrier from the blood, it is important to understand specific aspects of flow regulation in the cerebral vasculature. Two distinct mechanisms, autoregulation and neurovascular coupling carry out regulation of cerebral blood flow.

1.8.1 Cerebral Pressure Autoregulation

The cerebral blood flow is integral to maintaining CNS homeostasis, as low blood flow would result in ischaemia of the brain and high pressure would lead

to increased intracranial pressure. Therefore the CNS has evolved a system to regulate the cerebral blood flow and keep it at a constant level regardless of changes to systemic blood pressure. This mechanism is known as autoregulation and the exact mechanism is poorly understood (Peterson et al., 2011, van Beek et al., 2008). However, it is known to involve changes in vascular tone and is attenuated in blood vessels 'denuded' of endothelial cells, suggesting an integral role of the endothelium itself (Harder, 1987, Rubanyi et al., 1990). Other mechanisms have been proposed including specific roles for vascular smooth muscle cells (vSMCs), suggesting a more complex regulatory system.

1.8.2 Neurovascular Coupling and Functional Hyperaemia

The CNS has the highest energy demand of the organs in the body. It is believed to contribute 20% of the total energy expenditure of the body, despite contributing to just 2% of its total mass. This demand for energy is the result of the aerobic respiration that must occur to feed the active transport required in undertaking neuronal signalling, particularly in repolarisation after an action potential (~47% of total energy consumption) and active uptake of neurotransmitters from synapses (~34% of total energy consumption) (Attwell and Laughlin, 2001). In order to reduce wastage of energy and improve efficiency, the CNS has developed a feedback system to increase delivery to regions of the CNS that are active. This feedback mechanism is called neurovascular coupling and acts by increasing the local cerebral blood flow, known as functional hyperaemia (Attwell and Laughlin, 2001, Roy and Sherrington, 1890). The detection of this increase in blood flow is the basis for using functional magnetic resonance imaging (fMRI), to associate certain stimuli or tasks with regional CNS activity (Villringer and Dirnagl, 1995).

Functional hyperaemia is mediated through dilation of the vSMCs that regulate dilation and constriction of the arterioles in the microvasculature. The dilation of the arterioles increases blood flow entry from the arteries into the arteriole. Consequently blood flow is increased throughout the rest of the

connected microvasculature network, as seen in *Figure 1.14* (Attwell et al., 2010).

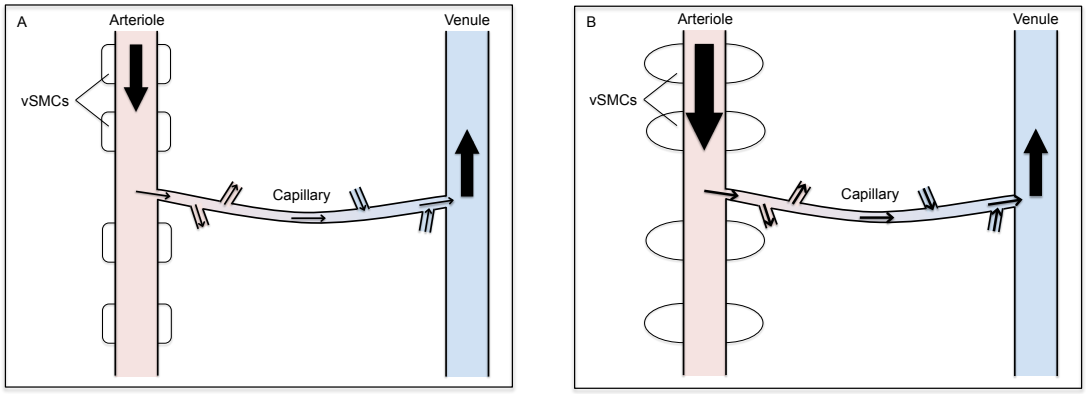

Figure 1.14: Mechanism of Functional Hyperaemia. In the absence of local neural stimulation, vSMCs contract and constrict the arteriole (A). After neural stimulation, the vSMCs dilate, allowing more blood flow to pass through the arteriole and the downstream microvasculature network (B).

The traditional pathway of neurovascular coupling shown is mediated by neuronal and astrocytic control, using a variety of different signalling pathways. Recently, the release of the neurotransmitter glutamate has been demonstrated to contribute majorly to the regulation of the functional hyperaemia response, with the response being propagated through both neurones (Busija et al., 2007, Ma et al., 1996) and astrocytes (Gordon et al., 2008, Metea et al., 2007, Peng et al., 2002, Peng et al., 2004, Porter and McCarthy, 1996).

It has been known since the work of Dore that pericytes express contractile proteins (Dore, 1923). Recently this has gained renewed interest due to the concept that pericytes may contribute to neurovascular coupling by altering capillary diameter. Furthermore, they have distinct features that make them ideal for this role, particularly their proximity to neurones compared to arterioles and their ideal location to work in syndicate with blood vessels and neurones. This would suggest pericytes have the capacity to regulate capillary diameter and therefore blood flow through capillaries. A number of *in vitro*, *ex*

vivo and *in vivo* experiments have demonstrated that pericytes can contract when stimulated with electrical and chemical stimuli (Hamilton et al., 2010). Peppiatt and colleagues were the first group to observe contraction of pericytes in capillaries *in vivo*, however the method of induction and degree of constriction led to questioning of whether this occurs in more physiological conditions as it led to almost complete occlusion of the capillary (Peppiatt et al., 2006). This conclusion was supported by the work of Stefanovic and colleagues who used two-photon laser scanning microscopy to find a dilation of the capillary bed of 10.9±1.2% that contributed an estimated 18% of the functional hyperaemia response in rats (Stefanovic et al., 2008). In contrast, Fernandez-Klett and co-workers used a similar methodology and found that although pericytes were contractile *in vivo*, the functional hyperaemia response was mediated by the arterioles in mice (Fernandez-Klett et al., 2010). The different findings of these studies may suggest a differential regulation of functional hyperaemia in rats and mice. However, Hall and co-workers have more recently demonstrated that pericytes can dilate *in vivo*, in both rat and mice models, in response to glutamate and that this pericyte-mediated mechanism of functional hyperaemia occurs prior to arteriole dilation and may contribute more to the overall observed changes in blood flow (Hall et al., 2014). What appears to be unanimous between these studies is that pericytes are contractile *in vivo* and that this does seem to be a contributing component of the functional hyperaemia response, though the relative significance and mechanisms of regulation still require further study. It is a distinct possibility that the pericyte mechanism acts in a rapid temporal capacity prior to the arteriole-mechanism and/or to fine tune arteriole-mediated functional hyperaemia at the capillary level. Pericytes may also contribute towards flow autoregulation.

1.8.3 Cerebrovascular Abnormalities in Disease

The previous sections give details on regulation of blood flow in normal conditions. However, changes in blood vessel architecture and blood flow

regulation itself have been demonstrated in a number of diseases and ageing. In many instances, it is unclear whether these changes are causative or consequential factors of the disease, but are often considered to be contributing factors to the pathological progression of the disease. For example, it may be considered in ischaemia, where blood flow is insufficient for CNS function, the ischaemia may contribute to neuronal or glial damage. However, initial neuronal and glial damage may likewise reduce the effectiveness of neurovascular coupling and therefore lead to a breakdown of the functional hyperaemia response and consequently result in ischaemia. Changes in blood flow in specific diseases may affect design of therapeutics in order to maintain sufficient delivery to the site of action within the CNS. Here, the cerebrovascular changes, observed in several diseases and during normal ageing, are described.

Alzheimer's has one of the best-characterised links with cerebral blood flow changes. Several reports have even shown neurovascular response defects in high-risk individuals carrying the important risk *APOE4* allele before the onset of clinical manifestations of the disease itself (Bookheimer et al., 2000, Ruitenberg et al., 2005, Sheline et al., 2010, Smith et al., 1999a). Furthermore, Bell and colleagues have demonstrated structural differences in the cerebral vasculature of the hippocampus in apoe-/- mice stably transfected with the human risk allele *APOE4*, compared to the control and non-risk human *APOE2* or *APOE3* transfected mice. In the *APOE4*-mice the length of the microvasculature measured was significantly shorter than in the control or *APOE2* and *APOE3* mice (Bell et al., 2012).

Vascular degeneration has also been observed in brain slices of Parkinson's disease patients. Overall, capillaries were significantly less abundant, reduced in length, larger in diameter and with a reduced number of branching events when compared with normal brain slices (Guan et al., 2013). Derejko and colleagues have also demonstrated differences and deficiencies in the general cerebral blood flow of Parkinson's patients and furthermore a significant deficiency in blood flow to the parietal and temporal lobe of

Parkinson's patients with dementia when compared to those without a clinical dementia manifestation (Derejko et al., 2006).

Decline of cerebral blood flow has been demonstrated to occur in ageing with particular reductions in the limbic and associated cortices being proposed to being causative of the cognitive decline associated with ageing (Martin et al., 1991). In cat models, functional hyperaemia has been demonstrated to be impaired in ageing due to alterations in the microvasculature (Li and Freeman, 2010). Furthermore, structural changes in the cerebral microvasculature have been observed in the ageing rat along with loss and morphological changes of pericytes (Hughes et al., 2006). The loss of pericytes may contribute to reduction in functional hyperaemia response in ageing individuals.

1.9 AGENT-BASED MODELLING

1.9.1 Agent-based Modelling for System Analysis

Agent-based modelling is a type of modelling specifically designed for systems analysis. It deconstructs a system into components, known as agents, and assigns mathematical expressions to describe their behaviour. Subsequently, by combining the different agents together in simulations, through agent-agent and agent-environment interactions, emerging systems behaviour can be observed. Biological systems are highly complex involving many components, across many different scales, from single molecules through to whole cells, tissues, whole organisms and populations of organisms. Moreover, they are inherently dynamic and often contain complex and spatially heterogeneous features. Manipulation of single components within biological systems, by traditional experimental methods, is often difficult due to their inherent complexity. Traditional differential equation methods are limited by their poor representation of dynamic and spatially complex systems. Agent-based modelling is based on rules obtained, directly or indirectly, from experimental methods. Agents within agent-based simulations can be given spatial identifiers, providing more rigorous modelling of spatially complex systems than by other modelling methods. Furthermore, it allows facile

manipulation of parameters inaccessible through more conventional techniques to provide system level trends, to complement traditional experimental approaches.

1.9.2 Parallel Computing

Agent-based simulations, though powerful in terms of predictive capabilities, are often limited in simulation size by the CPU (Central Processing Unit) power and memory availability. This can be addressed by utilising distributed computing, distributing work and memory across several CPUs, commonly referred to as cores. This creates an entire new problem, how to efficiently access data from agents or functions operating on non-self cores. There are several different ways to approach this issue and to optimise this process to achieve maximum 'speed up' of the simulation. Most of these methods focus on using the message passing interface (MPI), a communication system that can send data between cores (See *Figure 1.15*).

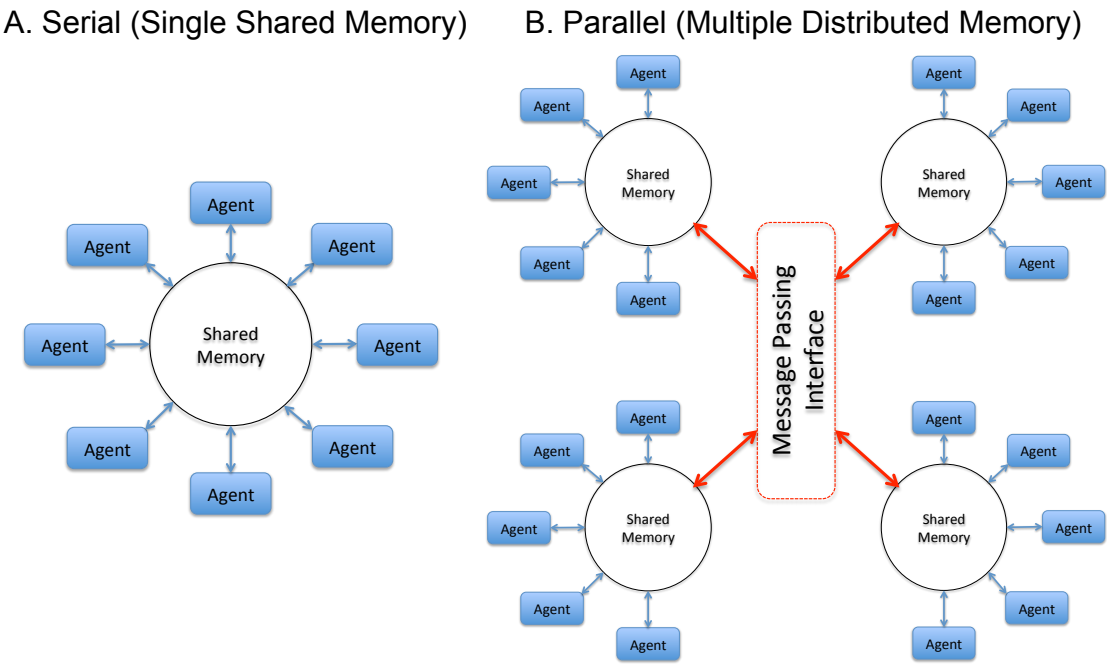

Figure 1.15: Serial and Parallel Computing for Agent-based Applications. Agents exchange data through a shared memory in serial computing (A). However in parallel computing (B), each core contains a separate memory, cores must communicate with each other through the message passing interface.

The speed of the simulation is usually limited on how long these communications take to send to the relevant cores. The speed of communication depends on the 'interconnect' between cores. MPI coding requires specialist knowledge and needs extensive optimisation to minimise 'overheads' of parallelisation. Moreover, small changes to the code may necessitate the repeating of the optimisation steps, limiting flexibility in reusing sections of code for different applications.

1.9.3 The Flexible Large-scale Agent-based Modelling Environment

A wide variety of agent-based modelling platforms are available, many of which provide established toolkits for agent-based simulations. The most popular platforms include, but are not limited to, Repast, SWARM and MASON. However, one of the major drawbacks of most of the available platforms is their programming in Java. Java is a highly accessible language that performs well in web-based platforms. However, it is not an optimal language for use on high-performance computing systems. FLAME (Flexible Large-scale Agent-based Modelling Environment) is a generalised agent-based modelling platform designed in collaboration between the University of Sheffield's Department of Computer Science and the Science and Technology Facilities Council's Rutherford Appleton Laboratory in 2003. FLAME is designed to permit the building of both serial (non-distributed computing) and parallel (distributed computing) agent-based models without any change in the user input code. It has been used to study non-biological systems such as the European economy (Deissenberg et al., 2008) and biological systems such as keratinocyte colony formation (Sun et al., 2008, Sun et al., 2007), development of the epidermis (Adra et al., 2010, Sun et al., 2009, Li et al., 2013) and *Escherichia coli's* oxygen response (Bai et al., 2014). Its design was particularly tailored for large-scale simulations on high performance computers in a number of ways. Firstly, it utilises the C language that has been used extensively in high performance computing and has many

established tools such as Open Multi-processing (OpenMP) and the MPI. These two tools represent the most prominent parallel programming tools in use on high performance computers. Secondly, the normal prerequisite of knowledge of MPI programming is not necessary for building parallel applications using FLAME, as FLAME builds the MPI simulation code from non-MPI functions programmed by the user. FLAME therefore allows a greater range of users to utilise high performance computing for agent-based modelling. Finally, FLAME contains an inherent method for optimising parallel agent-based models that reduces the requirement for repeated optimisation by the user (Chin et al., 2012).

In FLAME, the user defines agents; their respective memory variables; their respective functions to carry out and data access requirements for those functions, from other functions. This is achieved in a basic form using XMML (X-Machine Markup Language). The functions themselves are then coded in a separate function file or files coded in the C language. FLAME utilises these two user-generated codes to construct an iterative-based executable model in either serial or parallel.

FLAME uses message boards for communications between agents. The XMML file declares these message boards and the variables stored on them. Functions that require data on the message boards read through all the messages on a particular message board and by using filtering can access the required data. In serial, agents can read and write to this board rapidly as it is maintained in the local memory. However, in parallel each core has its own message board that must be synced with the other boards. When a function adds data to a message board, a message is generated to update the other message boards (as seen in *Figure 1.16*).

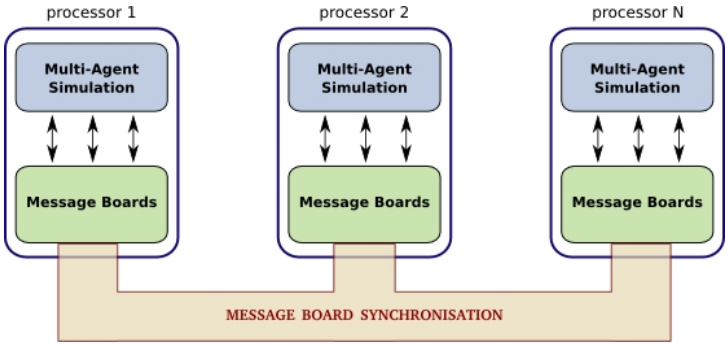

Figure 1.16: Parallelisation of Agent-based Models using FLAME Message Boards. (Chin et al., 2012)

Whilst messages are in transit, no function can read data from the message board. FLAME's approach to parallelisation uses a scheduler that prioritises work that will generate communications between cores. Whilst the messages are sent in the background, it will then perform all possible work not dependent on those communications, in order to reduce overhead times associated with parallelisation (as demonstrated in *Figure 1.17*).

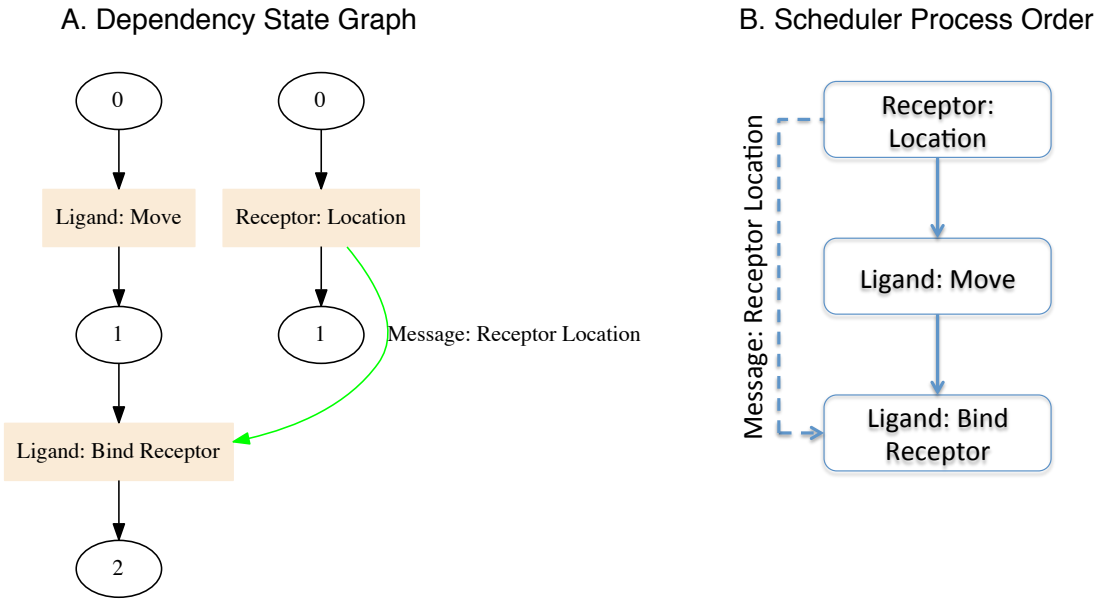

Figure 1.17 Dependency Graph and FLAME Scheduler for a Simple Receptor Binding Model. In the dependency graph (left), 3 functions are displayed, the function 'Ligand: Bind Receptor' is dependent on the carrying out of the preceding function 'Ligand: Move' and also the message 'Receptor Location.' The message is generally limiting to the speed of the process, therefore the scheduler (right) prioritises the function that generates the message, 'Receptor: Location.' Whilst the message is transferring in the background, the scheduler will perform the function 'Ligand: Move' as it is not dependent on the message. This reduces the lag time that the message-dependent function 'Ligand: Bind Receptor' must wait to receive the message before it can use it to perform useful work.

The use of distinct functions in FLAME also allows the capability to easily add functions to and remove functions from a simulation, whilst still providing the inherent parallelisation optimisation described. This enables the user to systematically include and exclude certain functions and agents, thus giving profound flexibility in simulation to best answer the research question.

1.9.4 Agent-based Modelling for Biology

Agent-based modelling has far reaching applications, from the economy to crowd behaviour. However, recently its use for biological modelling has gained interest. Biological systems are characterised by their inherent complexity and more traditional methods such as *in vitro* or *in vivo*

approaches are not always adequate for understanding how a highly complex system operates. Agent-based modelling can give unique insight and predicative capabilities as it relies on a bottom up approach, therefore complementing more traditional methods. Moreover, the advance in and increasing accessibility of high performance computing systems means there is more power for accurate modelling of such complex systems. Agent-based modelling has been used successfully across many different scales in biological systems, in the remainder of this section we summarise some of these.

The NFκB pathway is an immune system pathway that has been implicated in atherosclerosis and cancer. Molecular scale agent-based modelling was utilised to demonstrate that after activation of the NFκB pathway, a pool of spatially sequestered NFκB inhibitor, IκB, bound to the actin cytoskeleton could be released and aid the rapid temporal resolution of the NFκB response (Pogson et al., 2008).

Sprouting angiogenesis is the process by which new blood vessels sprout from existing vessels. This process involves complex cell selection dynamics into tip cells and sprout cells. Agent-based modelling was utilised to demonstrate how this selection occurs in response to vascular endothelial growth factor (VEGF-A) by Notch-Delta-like Ligand 4 lateral inhibition (Bentley et al., 2008, Jakobsson et al., 2010).

Multiple sclerosis is a brain disorder characterised by the breakdown of the blood-brain barrier leading to immune cell migration into the brain tissue. Pennisi and colleagues, used a multi-scale agent-based model of the blood-brain barrier during multiple sclerosis to model the efficacy of treatment strategies that aid blood-brain barrier repair against those that protect the blood-brain barrier against further damage. They demonstrated that treatments that encourage repair are often less effective than treatments that reduce further damage (Pennisi et al.).

Jackson and colleagues used agent-based modelling to investigate the foraging behaviour of the Pharaoh ant, *Monomorium pharaonis*. The Pharaoh

ant is a blind tropical ant that lives in large colonies formed of a number of smaller interlinked colonies. A key aspect to their survival is the ability to locate food and co-ordinate the foraging of new food sources to be collected and brought back to the colony. Agent-based modelling, using ants as individual agents, elucidated a complex co-ordination mechanism involving the deposition of pheromone trails to food source. Ants joining these trails can orientate towards the nest by a system of bifurcations, thus allowing individual ants to both forage for new food sources and return to the nest effectively (Jackson et al., 2004, Jackson et al., 2007, Robinson et al., 2005).

1.10 NANOTECHNOLOGY

1.10.1 Nanotechnology for Drug Delivery

Nanotechnology is a greatly emerging field with wide-range of potential clinical applications, including in diagnostics, imaging agents and controlled therapeutic delivery. A particular area of interest is the use of nanoscale particles, called nanoparticles, to deliver a wide-range of potential therapeutic cargo molecules to specific locations within the body by modification of nanoparticle properties. Nanotechnology in drug delivery is a relatively young technology in application to drug delivery and therefore it is rapidly evolving to create more sophisticated nanoparticles for drug delivery applications.

Nanoparticles can be split into two major categories, “hard” and “soft”, based on the chemistry of their formation. Hard nanoparticles describes nanoparticles formed by strong covalent, metallic or ionic bonds. These include metal nanoparticles such as gold or silver and carbon nanotubes. These particles are often defined by their rigid structure and lack of flexibility. Soft nanoparticles describe nanoparticles formed by numerous weaker interactions such as hydrophobicity, hydrogen bonding and Coulombic forces. These include, lipid-based liposomes, polymer-based polymersomes and protein nanoparticles. Soft nanoparticles offer much more flexibility and reduced rigidity compared to their hard counterpart and are more reminiscent

of the soft interfaces of cell membranes. Hybrid nanoparticles containing a hard nanoparticle core but a soft outer surface also exist.

Nanoparticle properties such as size, shape and surface chemistry can be modified for particular properties depending on the application. Fine-tuning these properties can aid nanoparticle interactions with the host system. Generally there are several key properties that need to be addressed:

- Toxicology
- Drug retention and release
- Half-life
- Bio-distribution
- Biodegradation and clearance

1.10.2 Nanoparticle Toxicology

Nanoparticles for use in drug delivery must be able to be used effectively without causing harmful side effects to the patient. Nanotoxicology is a complicated field due to the dependence on properties such as drug retention, half-life and bio-distribution, discussed later in this section. Nanoparticles are often designed based on chemicals or bulk materials with a known toxicological or biological profile. However, when changing the arrangement of these materials into nanoparticles, the size, shape and surface chemistry are vastly different to the original material, which may alter how they interact in a biological system, compared to the individual components. For example, gold in its bulk form is highly inert but in a nanoparticle becomes much more reactive and can be used in catalysis of certain reactions. This is a result of the small size increasing the surface area to volume ratio (Haruta, 2003). Generally, cationic nanoparticles are regarded as having a higher cytotoxicity than anionic nanoparticles because of their increased ability to penetrate cellular membranes (Goodman et al., 2004, Chen et al., 2009).

1.10.3 Drug Retention and Release

A major consideration in utilising nanoparticles for drug delivery is in what you want to deliver and how the nanoparticle formulation must be adapted to deliver the therapeutic agent effectively and intact. For example, a nanoparticle designed to deliver a small hydrophobic drug may be quite different than one designed to deliver a large hydrophilic antibody. The most common way to carry drugs is through “complexing” and “encapsulating” the drug(s). Complexing involves forming a direct interaction with the drug such as covalent or ionic bonding to the nanoparticle. However, this requires creating an interaction that is either stable but maintains the drug in an active form or stable only until the desired point of release. Encapsulating a drug involves incorporating the therapeutic agent within the structure of the nanoparticle itself. Ideally, encapsulating therapeutic agent protects the drug from exposure until the desired target is reached.

In order to release drugs from nanoparticles at the site of action requires careful design of nanoparticles. One of the most common methods of drug release is through stimuli-responsive nanoparticles that release their cargo in response to particular stimuli such as pH, light, temperature and chemical modification (Ganta et al., 2008). The idea being to find a particularly stimulus present at the site of action, for example, pH or temperature changes in tumour tissues (Gerweck and Seetharaman, 1996), pH-changes in the endocytic pathway (Cain et al., 1989) or chemical modification by tissue-specific enzymes.

1.10.4 Nanoparticle Half-life and Bio-distribution

Regardless of the route of administration, nanoparticles must be able to traverse biological barriers in order to enter and persist within the body until the target site is reached. The body has evolved a number of sophisticated barriers to prevent the free access of foreign material to the body. One of the most critical is that of the immune system. The immune system is responsible for maintaining whole body homeostasis, particularly in eradication of foreign

material and repair of cellular or tissue damage. It is adept at recognition of non-self entities, triggering their subsequent destruction. Furthermore, after exposure to a foreign-body, “immunity” is developed so that the foreign body is more rapidly recognised and destroyed in future. Nanoparticles, to persist within the body, must be able to circumvent this defence mechanism. Most nanoparticles are sequestered by part of the immune system called the reticuloendothelial system (RES), also known as the mononuclear phagocyte system (MPS), a system of immune cells resident in tissues including the spleen, liver, lungs, bone marrow and lymph nodes (Van Furth, 1982, Owens and Peppas, 2006).

“Immune stealth” describes the stages of designing nanoparticles to have a reduced interaction with the immune system. Size, shape and surface chemistry have all been demonstrated to be able to modulate immune cell interactions. Perhaps the best studied is surface modification of nanoparticles to prevent immune cell interactions. Surface charge of nanoparticles is known to affect the non-specific binding of soluble factors in the body forming a hydrated layer called the “corona.” Binding of soluble factors leads to a process called opsonisation where the particle is more readily recognised by the immune system and tagged for destruction (Storm et al., 1995). Reduction of surface charges or the inclusion of polymers like poly [ethylene glycol] (PEG) on the outer surface reduces nanoparticle elimination by the immune system. PEG and similar polymers have a highly favourable interaction with water and thus recruit a protective water sheath around the nanoparticle consequently lowering non-specific interactions with other materials and cells (Gref et al., 2000, Owens and Peppas, 2006). The consequent reduction in “protein fouling” to the nanoparticle corona is believed to be responsible for the reduced clearance of PEG-coated nanoparticles. Hamad and colleagues demonstrated that the molecular weight of PEG was a key factor in its interaction with the complement system of the immune system (Hamad et al., 2008). The complement system is a collection of soluble inactive circulatory proteins that when activated trigger an innate immune response. They found that higher molecular weight PEGs increased activation of the alternative

complement pathway, leading to opsonisation of the PEG molecules. Michel and co-workers likewise established that the architecture of PEG affected its protein adsorption properties (Michel et al., 2005). Recently, it has been demonstrated that PEG exposure can result in the production of anti-PEG antibodies (Ishida et al., 2007, Wang et al., 2007, Środa et al., 2005). This consequently was responsible for an increased blood clearance rate. Moreover, repeated administration demonstrated an antibody-led immunity to PEG-based nanoparticles, potentially reducing their effectiveness in subsequent future administration (Środa et al., 2005). It is estimated that approximately 1 in 4 healthy people now have anti-PEG antibodies, a 100-fold increase across the previous 20 years, thus demonstrating a future reduction in the efficacy of this strategy (Garay et al., 2012).

Size is the next best-studied property for the clearance of nanoparticles. It has been shown systemically administered nanoparticles, greater than 200 nm in size, will readily accumulate in the Kuppfer cells of the liver and also in the spleen (Maeda et al., 2000, Owens and Peppas, 2006). Size also impacts the filtration properties of the nanoparticles from the blood. Small sized nanoparticles, of less than 6 nm, are susceptible to filtration by the kidneys and removal *via* excretion of urine (Choi et al., 2007). Larger nanoparticles, up to 40-60 nm in size, may be subject to blood extravasation, the leakage through pores in the endothelial wall in discontinuous/sinusoidal or fenestrated endothelium. It has been mooted, as a consequence of these clearance profiles, that nanoparticles of a size range of 40-100 nm should have improved half-lives within the systemic circulation and therefore are more suitable for general drug delivery systems (Alexis et al., 2008).

Shape has also been shown to aid evasion of the immune system, the Discher group have previously used tubular micelles to compare the half-life of different shaped nanoparticles. They concluded that the half-life can reach a maximum of 5 days for poly [ethyleneglycol]-poly [ethylethylene] tubular micelles, much greater than half-life exhibited for the same chemistry in a spherical vesicle morphology or indeed for any spherical morphology in the literature (Geng et al., 2007).

1.10.5 Achieving Specificity

The previous section described nanoparticle design strategies to evade non-specific off-target delivery. However, the ultimate goal is to achieve specificity for the tissue of interest. The easiest method of developing specificity for a therapeutic target is through the enhanced permeability and retention (EPR) effect. The vasculature of tumour tissues has a higher permeability than other tissues. Furthermore, tumour tissue often lacks the extensive lymphatic drainage systems prevalent in other tissues. Therefore, nanoparticles in the blood naturally accrue in tumour tissues more favourably than in other tissues. The specificity can be achieved by modulating nanoparticle size, an effect explored in more detail in *Chapter 3* (Bogdanov et al., 1997, Iyer et al., 2006).

The most common way to achieve specificity for desired tissue is through the targeting of unique or overexpressed receptors on the target tissue. Nanoparticles, adorned with such targeting moieties, ideally would enter the tissue of interest more readily than other tissues. Complications arise in finding uniquely expressed receptors and achieving delivery only to tissues where the receptor is overexpressed, with some off-target delivery to other tissues that express the receptor, even if it's a comparatively reduced amount. The latter has been addressed by the work of the Frenkel group, who hypothesised that specific binding of nanoparticles to cells overexpressing a specific receptor can be controlled through a combination of high avidity and low affinity (Martinez-Veracoechea and Frenkel, 2011). This concept and other methods of achieving specific delivery will be explored in *Chapter 4* and *Chapter 5*.

1.10.6 Nanotechnology for Central Nervous System Delivery

The previous sections describe general facets of drug delivery using nanoparticles, with particular reference to physical and chemical attributes. One of the major applications for this technology is in improving the general penetrance of a multitude of potential therapeutics to the CNS. Most nanotechnology approaches for CNS delivery focus on crossing the blood-

brain barrier. Here, some of the existing approaches to crossing the blood-brain barrier using nanoparticles are discussed.

The most studied nanoparticle composition for CNS delivery is poly [butyl cyanoacrylate] coated with polysorbate 80. Kreuter and colleagues used this formulation to deliver the analgesics Dalargin or Loperamide and found a greater analgesic response when formulated together than the drug and carrier administered together but without direct binding of the drug to nanoparticle (Kreuter et al., 1995, Alyautdin et al., 1997). In their later work they ascertained the entry of the nanoparticle was dependent on adsorption of Apolipoproteins B and E, through a likely mechanism of receptor-mediated endocytosis and consequent diffusion of the drug or transcytosis (Kreuter et al., 2002, Alyautdin et al., 1997). A similar study by Schröder and Sabel validated that this formulation could successfully increase CNS penetrance of Dalargin (Schröder and Sabel, 1996). Gao and Jiang used the same formulation to test the effect of size on CNS delivery of methotrexate. They concluded that delivery of methotrexate was more efficient for nanoparticles of 70 nm than with 170 nm, 220 nm and 345 nm nanoparticles (Gao and Jiang, 2006).

In studies of gold nanoparticle bio-distribution, several groups have reported that small nanoparticles of size 10-20 nm accumulate in the brain tissue. Hun and colleagues demonstrated that 20 nm gold nanoparticles were able to permeate the blood retinal barrier, analogous in function to the blood brain barrier, with no toxicity to the retinal tissue (Jeong Hun et al., 2009). De Jong and colleagues in bio-distribution studies also found that 10 nm gold nanoparticles could be located in the brain, but not 50 nm, 100 nm or 250 nm gold nanoparticles, suggesting that size is key to their passage across the barrier (De Jong et al., 2008).

In subsequent studies, focus has shifted to target particular systems of transcytosis, most notably the transferrin-receptor mediated and the Lrp-1-mediated routes. Monoclonal antibodies to the transferrin receptor have been found to increase blood-brain barrier penetrance. Ox26 is one such antibody

that was shown to increase brain penetrance of methotrexate conjugated to the antibody (Pardridge et al., 1991, Friden et al., 1991). Ox26 functionalised poly [glycerol]-conjugated poly[lactic-*co*-glycolic acid] nanoparticles encapsulating the analgesic endomorphins had an improved analgesia effect in rat models than controls (Bao et al., 2012). Gosk and colleagues used Ox26 conjugated to liposomes to increase CNS delivery. However, they concluded that these liposomes were co-localised with brain capillary endothelial cells, rather than entering the parenchyma itself (Gosk et al., 2004). Further work by the Zhu group found that an optimal surface density of Ox26 improved delivery of poly[ethylene glycol]-poly[ε-caprolactone] polymersomes to the CNS, suggesting multiple Ox26-transferrin receptor binding events effected transcytosis efficiency. Niewoehner and co-workers studied this principle by comparing monovalent and bivalent antibodies to the transferrin receptor. They found improved transcytosis efficiency with the monovalent antibody. Moreover, the bivalent antibodies were taken through the endocytic pathway to the lysosome compartments, further evidence that multivalent targeting of the transferrin receptor can reduce delivery (Niewoehner et al., 2014). In addition to avidity, affinity has been shown to be integral to transcytosis efficiency. It has been demonstrated that high affinity antibodies to the transferrin receptor, such as Ox26, co-localised with the brain endothelial cells. However, reducing the affinity allowed improved transcytosis efficiency into the CNS tissue itself (Yu et al., 2011). The Davis group used a combination of size and avidity to fine-tune the interactions of gold nanoparticles with the brain endothelium. They concluded that high avidity nanoparticles remained attached to the brain endothelium on the CNS side, whilst lower avidity nanoparticles can successfully bind on the blood side and unbind on the CNS side to improve efficiency (Wiley et al., 2013). In the study of transferrin receptor targeted nanoparticles it is clear that efficient transcytosis is more complex than simply binding the correct receptor. This may be due to triggering different transport mechanisms by cross-linking receptors or by strong binding. However this process may be as simple as requiring a sufficiently strong initial binding to trigger initial transcytosis, but

simultaneously a weak enough binding to allow unbinding on the other side of the barrier. The strength of binding of a nanoparticle is regulated through, the interfacial contact surface area between nanoparticle and cell (related to size), the number of bonds formed (related to ligand and receptor density) and the individual strength of each of those bonds (related to affinity). This concept will be discussed in more detail in *Chapter 4*.

More recently, targeting Lrp1-mediated transcytosis has become an increasingly popular mechanism for CNS delivery across the blood-brain barrier. Demeule and colleagues identified a family of peptides, called Angiopeps, based on the Kunitz protease inhibitor domain of Lrp-receptor family substrates. Angiopep-2, particularly, has been shown to stimulate highly efficient transcytosis across the blood-brain barrier by Lrp1-receptor mediated transcytosis (Demeule et al., 2008b, Demeule et al., 2008a). The high expression of Lrp-1 on glial cells has led to the widespread use of this peptide to target gliomas with anti-tumour agents. Functionalisation of poly[ethylene glycol]–poly[ε-caprolactone] nanoparticles, PEG-modified poly[amidoamine] dendrimers and PEG-modified multi-walled carbon nanotubes, with Angiopep-2 was able to increase the delivery and anti-tumour activity of drugs including doxorubicin, docetaxel and the TRAIL (tumor necrosis factor-related apoptosis-inducing ligand) gene construct against gliomas (Gao et al., 2014, Huang et al., 2011, Ren et al., 2012). These studies demonstrate that angiopep-2 can successfully improve delivery of a diverse range of nanoparticles across the blood-brain barrier for potential therapeutic intervention.

1.10.7 Lrp1-Targeted Polymersomes for Central Nervous System Delivery

In the Battaglia group, a pH-sensitive polymersome system has been developed for CNS delivery (Tian et al., Submitted). Polymersomes consist of amphiphilic diblock copolymers that possess a hydrophilic and hydrophobic block. Polymersomes are formed by the self-assembly of these copolymers

into vesicle structures in an aqueous environment. The Battaglia group utilise a pH-sensitive hydrophobic block, poly[2-(diisopropylamino)ethyl methacrylate] (PDPA) that in acidic environments, of pH less than the pKa of 6.4, is protonated and therefore hydrophilic. At pH 6.5 or above, the PDPA block loses its proton, becoming hydrophobic (Lomas et al., 2007). This permits control of the self-assembly process by adjusting the pH (See *Figure 1.18*).

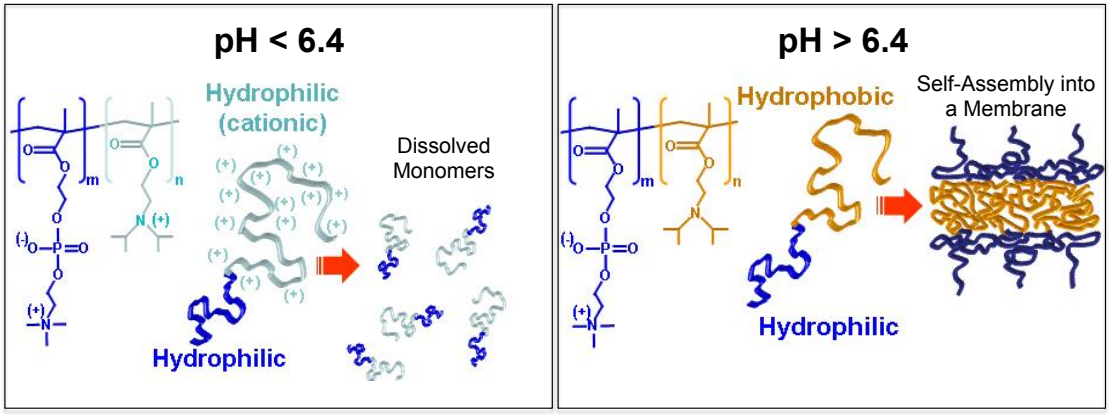

Figure 1.18: Aggregation of PDPA Diblock Copolymers driven by changes in pH. The tertiary amine of PDPA is protonated at a pH of below 6.4 (light blue). This makes the PDPA block hydrophilic and therefore the monomers are soluble. At a pH above 6.4, this proton is lost and the PDPA becomes hydrophobic (orange), in an aqueous solution this leads to the formation of bilayer membrane structure formed of many aggregated monomers.

Moreover, the pH-sensitivity provides an intracellular cargo release mechanism when taken up by cells through endocytosis. The endocytosis pathway culminates in endosomal compartments with a characteristic low pH. During the progression through the pathway, the acidification leads to the disassembly of the polymersomes into many monomers. This creates an osmotic shock that induces transient pores within the endosomal membrane, thus allowing the cargo to leave the endosome and enter the cell cytoplasm for hydrophilic molecules or a membrane for hydrophobic/amphiphilic molecules, as summarised in *Figure 1.19* (Lomas et al., 2007, Lomas et al., 2008, Massignani et al., 2009).

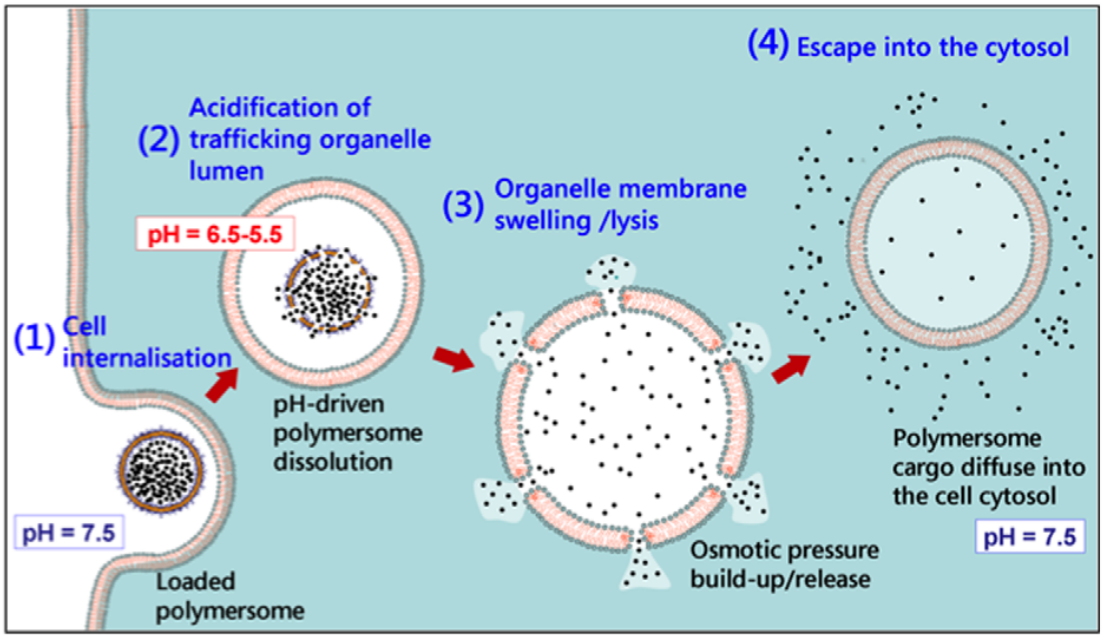

Figure 1.19: Cargo Release of pH-sensitive Polymersomes. Polymersomes are internalised from a physiological environment of pH of ~7.5 (1), they are trafficked through the endocytic pathway characterised by gradual acidification (2). At pH of below 6.5, polymersomes start to disassemble into monomers causing an osmotic shock (3). Cargo can escape into the cytosol, through transient pores that then reseal when back when osmotic balance is restored (4) (Massignani et al., 2010).

In combination with the PDPA hydrophobic block, the Battaglia group utilise different hydrophilic blocks, based on their cellular interactions. Poly[oligo(ethylene glycol) methyl methacrylate] (POEGMA) is one such polymer that contains ethylene glycol oligomers off a methyl methacrylate backbone. The ethylene glycol oligomers give POEGMA PEG-like properties of immune stealth. In CNS delivery the POEGMA-PDPA polymersomes are functionalised with Angiopep-2 to create Ang-POEGMA-PDPA polymersomes (Demeule et al., 2008b). These polymersomes have been successfully shown to be transcytosed across *in vitro* transwell models of the blood-brain barrier more efficiently than non-functionalised POEGMA-PDPA polymersomes. Moreover, the transcytosis event does not involve acidification or any apparent co-localisation with traditional markers of the endosomal pathway (Tian et al., Submitted). When astrocytes are cultured on the bottom of the

transwell system, Ang-POEGMA-PDPA polymersomes accumulate in the astrocytes. This is hypothesised to be through an Lrp1-mediated endocytosis mechanism. Furthermore, IgG encapsulated into these polymersomes co-localises with both the neural marker NeuN and the astrocyte marker Glial Fibrillary Acidic Protein (GFAP) when injected intravenously in the mouse tail. This demonstrates that Ang-POEGMA-PDPA polymersomes can deliver large macromolecules to cells of the CNS across the blood-brain barrier. In biodistribution studies, when compared to non-functionalised POEGMA-PDPA, CNS uptake of Ang-POEGMA-PDPA is indeed improved (*Figure 1.20*). However, the CNS uptake is still much reduced compared to other organs, particularly those associated with the RES such as the liver, spleen and bone marrow. It is also apparent that some sort of CNS clearance is occurring with peak signal at 2 hours, slowly reducing to near baseline levels. It is apparent from this work and that of others from section 1.10.6, that CNS delivery can be achieved but that it is still highly inefficient and more work is required to improve this uptake.

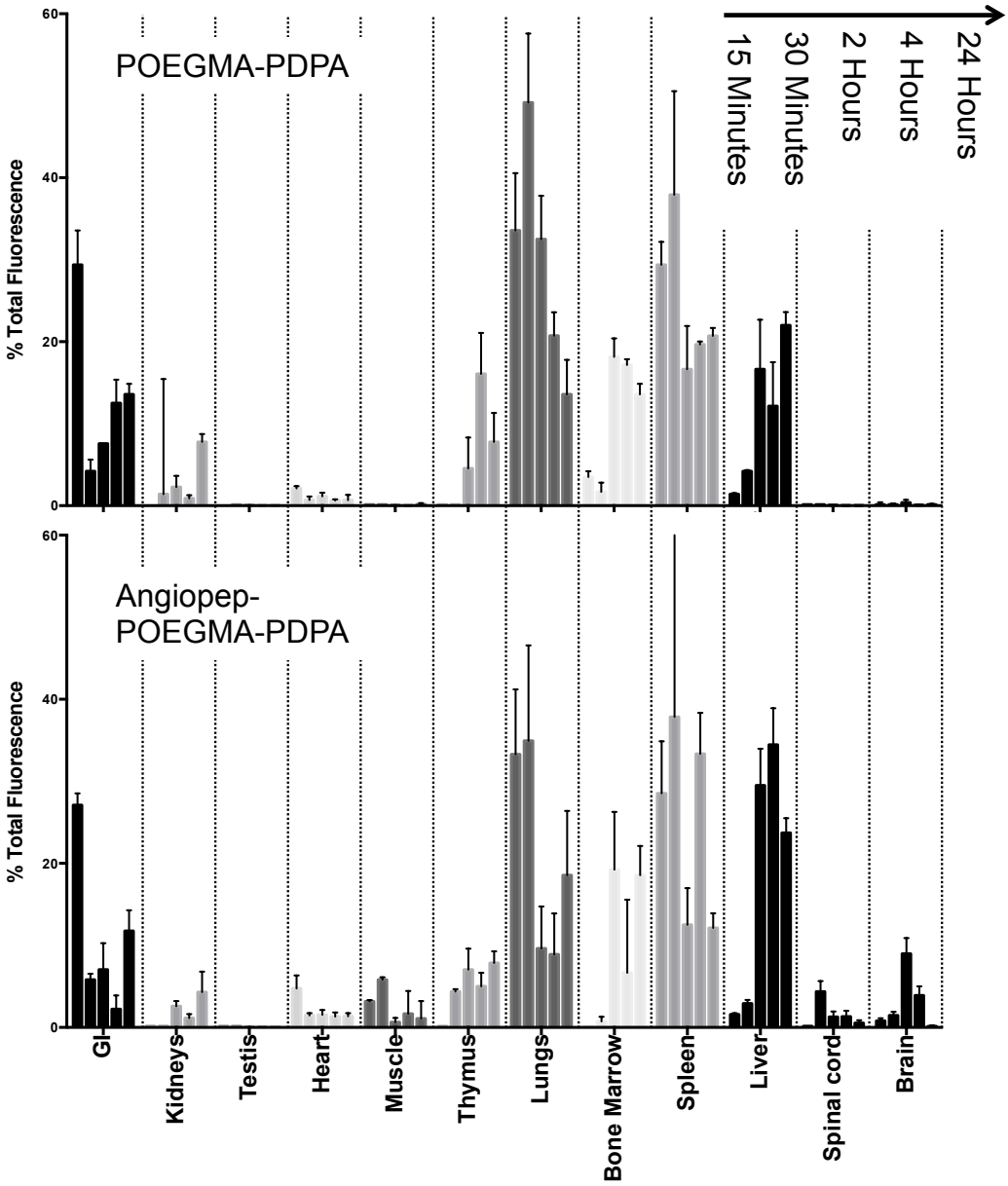

Figure 1.20: Biodistribution of Functionalised and non-Functionalised POEGMA-PDPA. Uptake of the two formulations of POEGMA-PDPA at 15 minutes, 30 minutes, 2 hours, 4 hours and 24 hours post intravenous injection into the tail vein of mice, obtained through *in vivo* imaging systems (IVIS) spectrum. Mean ± standard error of the mean. (Tian et al., Submitted).

1.11 CHEMOTAXIS

1.11.1 Chemotaxis

Chemotaxis is the process whereby a cell or entity is able to detect and respond to a concentration gradient by alterations in motility. This motility can be towards higher concentrations of a certain stimulus or stimuli

(chemoattractants) or away from certain stimuli (chemorepellants). This phenomenon is key to bacteria finding favourable environments (Adler, 1966, Zigmond, 1977), developmental processes in multicellular organisms and immune system function (Zigmond, 1977). More recently, inorganic micro- and nano-scale particles with chemotactic properties have been explored. Since chemotaxis confers the potential to target particular cells or tissues by following concentration gradients of appropriate signals, these particles may have interesting applications therapeutically. This section explores the theory for designing and optimising such a system for biological applications.

1.11.2 Designing a Nanoscale Chemotactic Particle: Mechanisms of Particle Motion

Although microscale chemotactic systems have been developed, nanoscale systems are far more favourable for *in vivo* applications due to improved clearance profiles, particularly between sizes of 40 and 100 nm (as covered extensively previously in this chapter). Whilst nanoscale chemotactic particles are highly desirable, serious complexities arise when designing particles at this scale. “Molecular motors,” appendages or molecular machines that generate mechanical force, can actively drive the motion of microscale particles. The most famous molecular motor is the bacterial flagellum that generates thrust through the proton-driven rotation of a helical appendage called a flagellum (Silverman and Simon, 1974). There are a number of other molecular motors such as cilia, however they all operate at the microscale. In order to produce chemotaxis at the nanoscale, other phoretic mechanisms of colloidal movement must be explored.

Diffusiophoresis is the long known phenomenon that when suspended colloidal particles are exposed to a substrate concentration gradient, they spontaneously move in a directionally biased manner either towards or away from the gradient (See *Figure 1.21*). This is driven by an unbalanced interfacial tension on the particle surface, generating a slip velocity across the particle (Derjaguin, 1987). Osmophoresis is similar process, involving a fluid-

filled vesicle surrounded by a semi-permeable membrane. However, osmophoresis is driven by asymmetric osmotic pressure across the particle membrane as a result of the difference in substrate concentration (Gordon, 1981).

Diffusiophoresis and osmophoresis are both driven by the imposed substrate concentration gradient. Self-diffusiophoresis and self-osmophoresis describe particles that are able to generate their own local concentration gradient and therefore create controlled motion (Golestanian et al., 2007). Local concentration gradients can be generated by the asymmetric catalysis of a reaction (see *Figure 1.21C*).

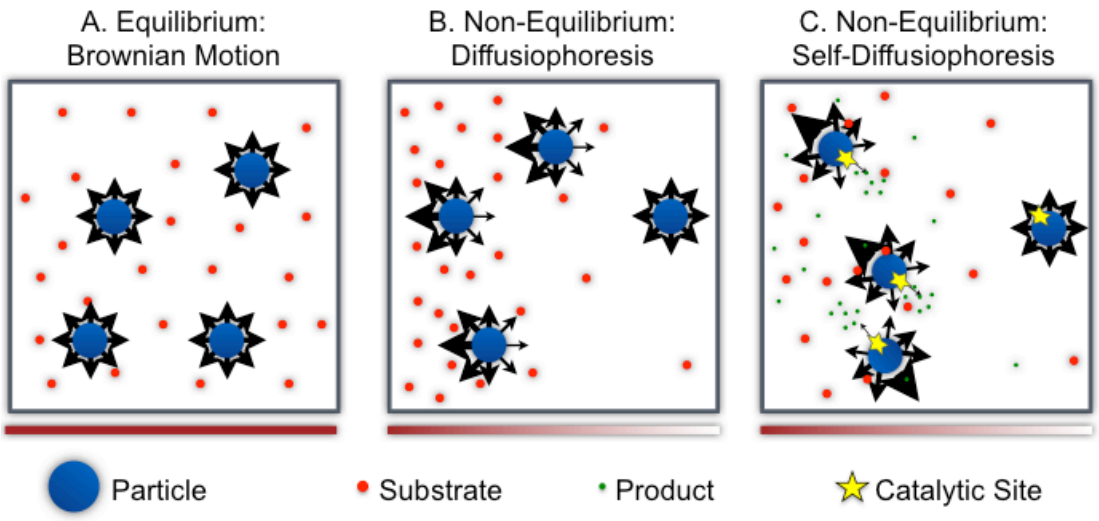

Figure 1.21: Motion of Suspended Particles. In a system at equilibrium, suspended particles move in a directionally non-biased manner called Brownian motion (A). However, when a substrate concentration gradient is applied, suspended particles begin to move in a directionally biased manner towards or away from the source of substrate, this is known as diffusiophoresis (B). Distal to the source of substrate where the concentration is minimal, suspended particles still move according to Brownian motion. Suspended particles that are able to generate their own concentration gradients, by catalytic conversion of substrates into products, move in directionally biased manner according to the axis of symmetry, called self-diffusiophoresis (C). Particles not exposed to substrate undergo Brownian motion, due to the lack of catalytic activity.

In self-diffusiophoretic or self-osmophoretic mechanisms, the direction of travel is controlled by the axis of symmetry, rather than the substrate concentration gradient. Instantaneously this may result in motion away from the source of substrate as direction is assumed random (Ebbens and Howse, 2010, Golestanian et al., 2005). However, over longer time frames particles can undertake controlled chemotaxis by a 'run and tumble' mechanism, similar to that used by bacteria, as demonstrated in the schematic in *Figure 1.22*.

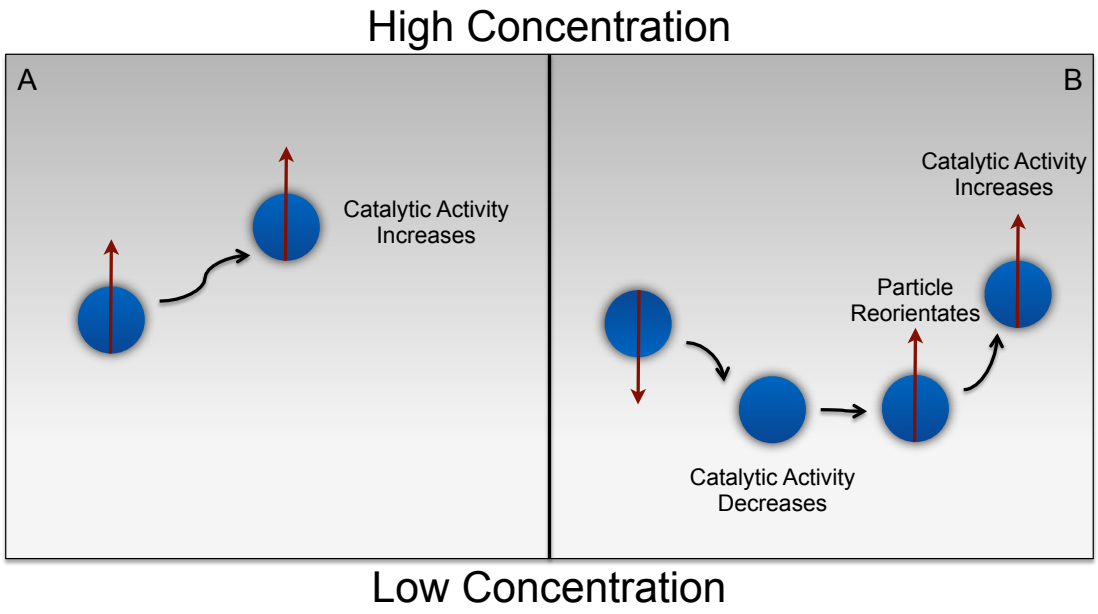

Figure 1.22: Run and Tumble Model of Chemotaxis. In these two scenarios, the substrate gradient decreases from top to bottom. In scenario A, a particle moves by self-diffusiophoresis towards the source of substrate. As the substrate availability increases, the catalytic activity increases and this motion is reinforced into a "run". However, in B, the particle moves away from the substrate, therefore catalytic activity will decrease and the particle will move slower, tending towards Brownian motion. This is called a "tumble" event, which occurs until the particle is randomly orientated in such a way that the particle is now driven towards the substrate, in a "run."

1.11.3 Designing a Nanoscale Chemotactic Particle: Rotational Diffusion

Suspended particles undertake a process called rotational diffusion, where particles rotate in a random and non-directionally biased manner. One of the

major complications in the design of chemotactic particles is the contradictory requirements of rotational diffusion for successful chemotaxis. Effective chemotaxis requires being able to follow a trajectory for a sustained time when on a run, whilst being able to rapidly re-orientate during a tumble. For the former, a slow rotational diffusion time is desirable because otherwise during a run the particle will 'forget' its initial trajectory (as demonstrated in *Figure 1.23*).

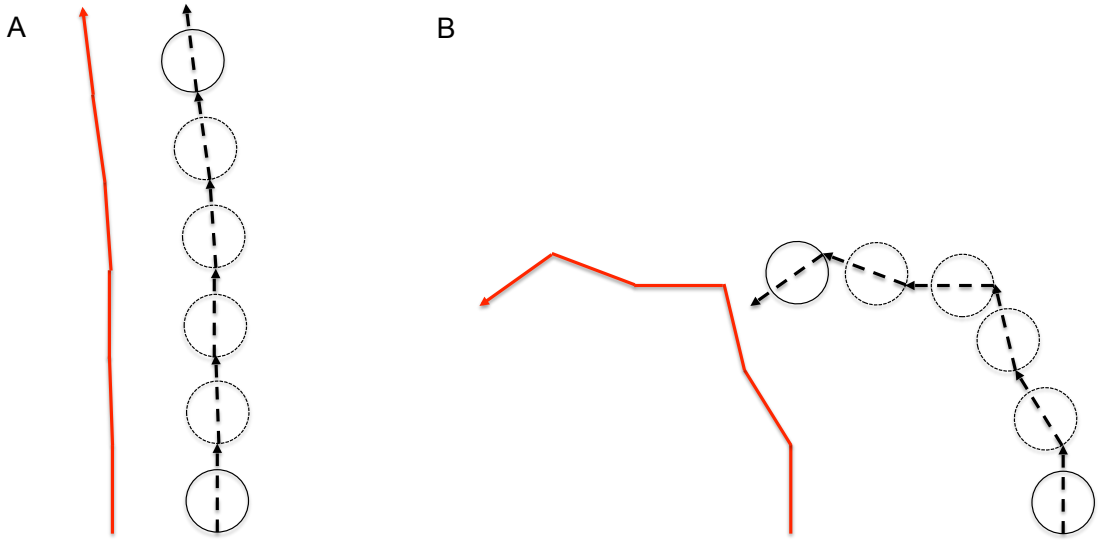

Figure 1.23: Effects of Diffusion Time on Sustaining Direction during a Run
Schematic of a particle undertaking a run with long (A) and short (B) rotational times.

A fast rotational diffusion time, however, is favourable for reorientation. *Escherichia coli* and other species of bacteria have evolved to solve this problem by sustaining a run for only a few seconds before tumbling, regardless of concentration gradient (Berg and Brown, 1972). This timescale allows it to follow a trajectory up until rotational diffusion times start to become significant enough to sufficiently alter the original direction. Furthermore, it is possible that rotational times during tumbles are accelerated by switching the direction of the flagella rotation, as opposed to stopping rotation altogether. In a run, the flagella rotate counter-clockwise (CCW) which, due to the helical nature of the flagellum, allows them to come together to form a single rotating

bundle (*Figure 1.24A*). During a tumble, instead of the stopping rotating altogether the flagella rotate in the opposite, clockwise (CW), direction. This leads to the bundle falling apart and the flagella re-orientate themselves, as seen in *Figure 1.24B*. The rotation of flagella significantly increases the force acting upon the cell, but unlike in a run, this force is symmetrical distributed so consequences in little directed translational movement. However it could increase the rotational time, allowing for more rapid reorientation for the next run stage.

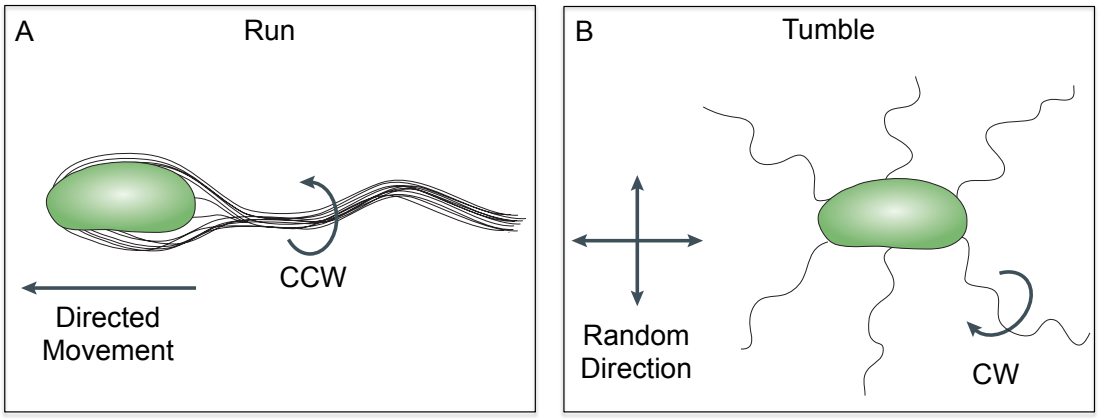

Figure 1.24: Chemotaxis of Peritrichous Flagellated Bacteria by Run and Tumble. In a run, the flagella rotate in a counter clockwise manner allowing them to form a single rotating bundle. In a tumble the flagella rotate in a clockwise manner, causing the flagella to separate (Butler and Camilli, 2005).

Nanoscale chemotactic particles are generally considered poor at long-range chemotaxis because of their incredibly high rotational diffusion. Rotational diffusion ($\boldsymbol{D_r}$) is calculated from the particle size using the equation:

$$\boldsymbol{D_r} = \frac{\boldsymbol{k_B T}}{\boldsymbol{8\pi\eta r^3}} \qquad (1.4)$$

where $\boldsymbol{k_B}$ is the Boltzmann constant, $\boldsymbol{T}$ is the absolute temperature, $\boldsymbol{\eta}$ is viscosity and $\boldsymbol{r}$ is the particle radius. As the particle size decreases, the

rotational diffusion coefficient increases relative to the radius to the power of three. *Figure 1.25* demonstrates the relationship between nanoparticle size and rotational diffusion coefficient for a spherical particle.

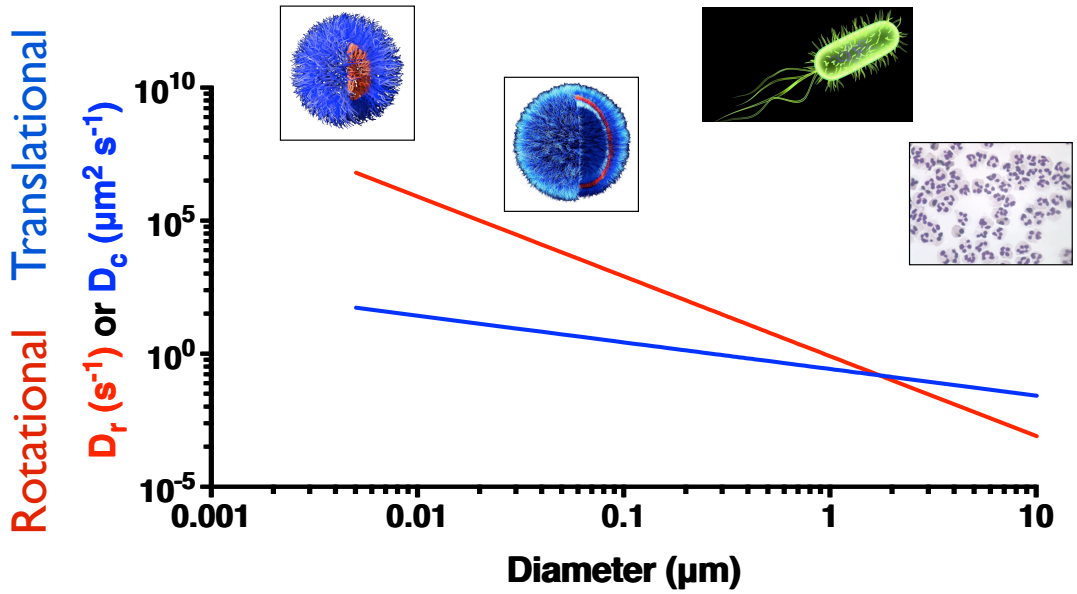

Figure 1.25: Relationship between Particle Diameter, Rotational and Translational Diffusion Coefficients. T=310K, η=0.0017 Pa.s. Pictures (left to right): Micelle ~10 nm, polymersome ~50-150 nm, bacteria ~1-2 μm and neutrophils ~10-15 μm. Image of primary neutrophils provided by James Robertson. Micelle and vesicle images provided by Silvia Bianco.

The rotational diffusion of nanoscale particles, of 100 nm in size, means that a particle will be essentially randomly orientated in ~0.4 ms. Therefore, nanoparticles cannot sustain effective chemotaxis over long time scales unless either a change occurs in rotational times or without other considerations coming into play. The Golestanian group have recently suggested that chemotactic particles actively align to the substrate concentration gradient, thus reducing the apparent rotational times (Saha et al., 2014). They have also previously observed such a reduction in rotational times for platinum-coated microscale polystyrene Janus particles (Howse et al., 2007). If such an alignment could be replicated at the nanoscale, it raises the intriguing possibility of being able to regulate both translational and rotational mobility to produce strong chemotaxis. The Golestanian group also propose a number of other mechanisms of chemotaxis in addition to the

alignment effect. They postulated that particles would naturally accrue in areas of low enzymatic activity, as they would be eventually driven away from highly concentrated regions due to the consequent high enzymatic activity, this they refer to as the “polar run and tumble”. However, they also describe the net motion of such a particle towards a substrate by the traditional run and tumble method, referred to as “apolar run and tumble.” In any population of particles a combination of the alignment, polar run and tumble, apolar run and tumble and diffusiophoresis/osmophoresis may be acting simultaneously giving complex phoretic behaviour in response to a substrate concentration gradient. Moreover, through interactions of multiple particles moving by such mechanisms, emergent collective behaviour may occur (Saha et al., 2014).

1.11.4 Chemotactic Polymersomes

In recent work within the Battaglia group, the aforementioned principles were used in the design and testing of chemotactic polymersomes. In order to generate the asymmetry required for self-diffusiophoresis or self-osmophoresis to occur, polymersomes were made from blending two different copolymers, poly[(2-methacryloyl)ethyl phosphorylcholine]-poly[2-(diisopropylamino)ethyl methacrylate] (PMPC-PDPA) and poly[ethylene oxide]-poly[butylene oxide] (PEO-PBO). The polymers within the hybrid polymersomes, over time, phase separate into distinct domains (LoPresti et al., 2011). The phase separation of these two copolymers creates “mushroom-like” polymersomes at a ratio of 9:1 PMPC-PDPA to PEO-PBO, as demonstrated in *Figure 1.26* (Cecchin et al., Submitted).

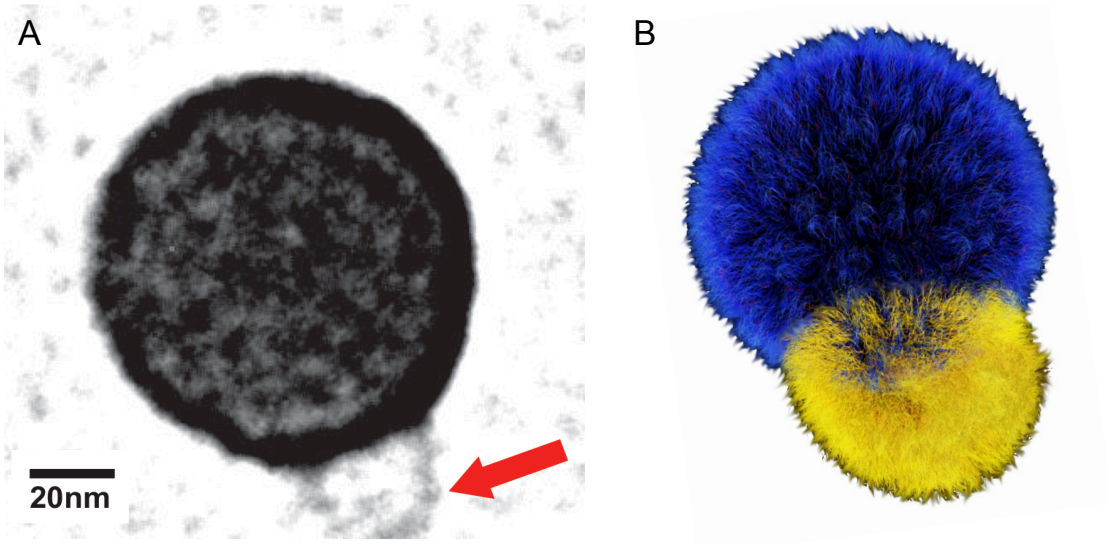

Figure 1.26: Structure of a 9:1 Ratio PMPC-PDPA/PEO-PBO Hybrid Polymersome. Transmission electron micrograph of a hybrid PMPC-PDPA/PEO-PBO polymersome forming the indicated mushroom domain of PEO-PBO (A). Schematic of the hybrid polymersome with PMPC-PDPA as blue and PEO-PBO as yellow (B). Micrograph taken from (Cecchin et al., Submitted). Graphic produced by Silvia Bianco.

The PEO-PBO copolymer forms more permeable membrane structures than PMPC-PDPA (Battaglia et al., 2006). Consequently, the efflux of products from an enzymatic reaction, performed in the aqueous core, will occur more favourably through the PEO-PBO domain, thus generating the concentration gradient required for self-diffusiophoresis or self-osmophoresis, as summarised in *Figure 1.27*.

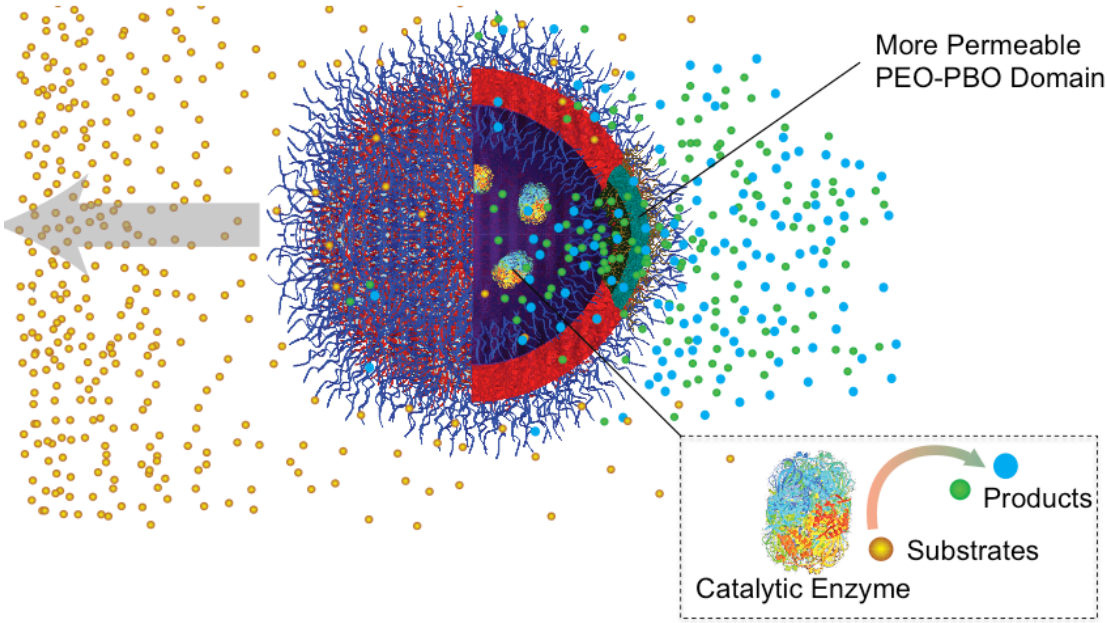

Figure 1.27 Proposed Mechanism of Propulsion for a Hybrid PMPC-PDPA/PEO-PBO Polymersome. Hybrid polymersomes that encapsulate a catalytic enzyme favourable expel the additional products from the reaction through the more permeable PEO-PBO domain, thus generating a concentration gradient across the polymersome for self-diffusiophoresis and self-osmophoresis (Cecchin et al., Submitted).

The PMPC-PDPA/PEO-PBO polymersomes have been demonstrated to be chemotactic in several tests, using different enzyme-substrate combinations (Cecchin et al., Submitted). The two enzyme-substrate combinations used were catalase enzyme with hydrogen peroxide substrate and glucose oxidase enzyme with glucose substrate. When assayed for single particle chemotaxis, by Nanosight® tracking analysis, the hybrid polymersomes demonstrated clear directional propulsion towards the substrate source, with no directional bias observed in symmetric pristine PMPC-PDPA polymersomes, symmetric pristine PEO-PBO polymersomes, or asymmetric hybrid polymersomes minus enzyme. Furthermore, long-range chemotaxis behaviour was observed in a bulk chemotaxis assay that measured movement of the nanoparticle population by fluorescence intensity across a 10 cm Petri dish. Moreover, the strength of chemotaxis to glucose could be increased by co-encapsulation glucose oxidase and catalase, which forms a cascade reaction, as hydrogen peroxide is a product of glucose oxidase. This demonstrates that hybrid

polymersomes are chemotactic in response to different substrates across length scales orders of magnitude greater than the polymersome. Furthermore, the chemotactic activity over long distances and time scales and calculated rotational times of up to 10000 times slower than expected would suggest that this system is able align itself to the external concentration gradient as discussed in the previous section (Cecchin et al., Submitted).

1.12 AIMS AND OBJECTIVES

Increasingly, nanoparticles are being utilised as novel delivery vectors across the blood brain barrier. Generally, these approaches are limited by their still relatively poor and non-specific delivery. Therefore, the overall aim of this work is to utilise computational methodologies to investigate methods to ultimately improve the general and specific delivery of nanoparticles across the blood brain barrier. Incorporated in this overall aim are a number of key aims:

Aim: To produce an agent-based model of nanoparticle behaviour under blood flows.

Hypothesis: It is hypothesised that by combining FLAME's agent-based modelling framework and CFD methods, a highly flexible model of nanoparticle behaviour under blood flow can be developed that can be used for further study of nanoparticle interaction with the blood-brain barrier at both the individual particle and system levels.

Aim: To demonstrate how modification of receptor-ligand mediated nanoparticle-endothelial interactions can result in improved general and specific transcytosis efficiency across the blood-brain barrier.

Hypothesis: Manipulating nanoparticle properties such as size, ligand density (avidity) and receptor-ligand affinity can alter the nanoparticle-endothelial interaction. Tailoring these interactions for certain scenarios such

as different receptor expression and different shear flows can improve general and specific delivery across the blood-brain barrier.

Aim: To determine whether chemotactic nanoparticles are able to improve delivery to target cells and delivery across the blood-brain barrier

Hypothesis: Chemotactic nanoparticles are able to follow gradients of specific chemical stimuli. Fine-tuning and use of chemotactic nanoparticles will allow nanoparticles to follow appropriate chemical signals to the cell or tissue that releases them. Furthermore, this may also be utilised to introduce greater dispersive activity of nanoparticles within the blood stream that may increase delivery.

CHAPTER 2: MATERIALS AND METHODS

2.1 THE FLEXIBLE LARGE-SCALE AGENT-BASED MODELLING ENVIRONMENT

FLAME is an open source software package written in C. The FLAME framework is not an agent-based modelling application itself but generates an agent-based executable for serial or parallel architectures from user input files. FLAME consists of two major components, the parser executable, (*Xparser*) and the message board communication libraries (*Libmboard*). The source code for these were downloaded from the FLAME website (www.flame.ac.uk).

The FLAME framework requires three input files for an executable model:

- *Model.xml*: This file is written in XMML using the FLAME XMML schema located at http://flame.ac.uk/schema/xmml_v2.xsd. This file declares agents, memory variables for each agent, functions to undertake by each agent, the process order for each function, input and output messages required for each function, messages and memory variables for each message.
- *Functions.c*: This file is written in the C language, it must include all the functions declared in the *Model.xml* file. The functions have full read and write capabilities for the given agent's memory variables. It may also read or write message board variables if declared appropriately as an input or output within the relevant function in the *Model.xml* file.
- *0.xml*: This file is an XMML file containing the information for the initial states of the model. It declares the memory variables for each agent at time 0 in the given simulation.

The FLAME *Xparser* uses the *Model.xml* and *Functions.c* files to generate the simulation code using the FLAME XMML schema templates. The compiler then is used to generate the executable using the *Libmboard* library. The executable requires an input of initial states (*0.xml*) to run the simulation. A

diagrammatic summary of producing an agent-based model using FLAME is demonstrated in *Figure 2.1*.

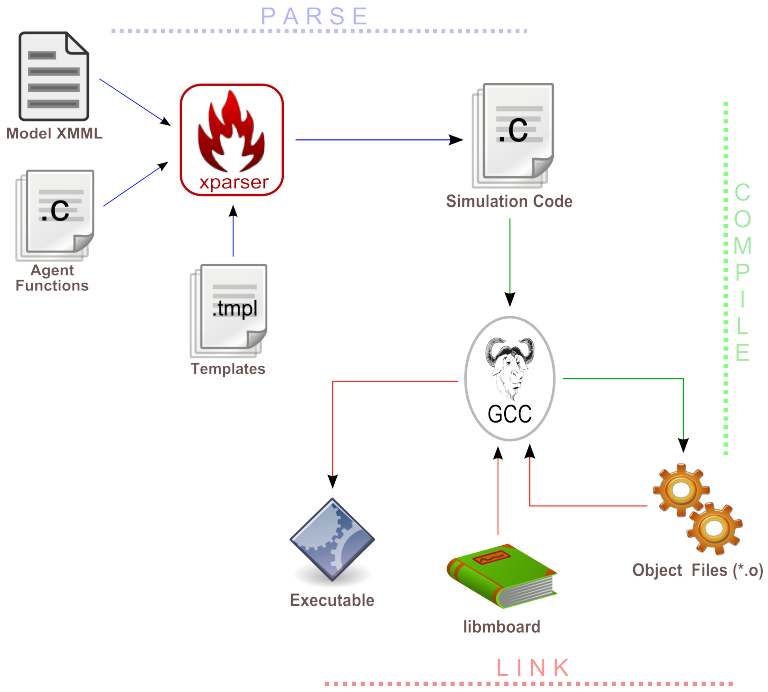

Figure 2.1: Creating an Agent-based Application using FLAME. Illustration of the two phases of creating a FLAME executable from user input files. Parsing, creating the simulation code from the XMML and C input files. Compilation and linking, compilation of the simulation code into the final executable model (Chin et al., 2012).

2.1.1 FLAME: Generating Initial States

The initial states, *0.xml*, files were created using MATLAB® and Statistics Toolbox Release 8.2.0.701 (2013b), The MathWorks, Inc., Natick, Massachusetts, United States. Software license number 910950.

2.1.2 FLAME: Serial Compilation and Execution

FLAME, by default, creates serial applications for execution on a single CPU. Simulation scripts were written and compiled, in serial, for testing using Xcode® 5 and executed on a MacBook Pro running OS X 10.8.

2.1.3 FLAME: Parallel Compilation and Execution

FLAME can generate parallel applications by the inclusion of the argument '-p' during parsing. Applications were compiled and executed, in parallel, on the Iceberg high performance computing facility (https://www.shef.ac.uk/wrgrid/iceberg) based at the University of Sheffield. Iceberg runs a 64-bit Redhat-based Linux operating system with 1544 CPUs that run at a collective performance of ~15 teraflops (Floating-point Operations *Per* Second). Parallel applications on Iceberg were compiled using the GNU compiler collection with OpenMPI 1.8.3 and run across multiple Intel® cores using an InfiniBand® interconnect.

Parallel models must partition data across the available cores. Achieving maximum speed-up ideally locates communicating agents on the same core. FLAME offers in-built methods for partitioning agents when executed in parallel, *round robin* or *geometric* partitioning:

Round robin Partitioning: This is the simplest partitioning method that distributes one agent at a time to each core in turn. It is implemented by the inclusion of a '-r' argument to the simulation executable. Although this method is the simplest, it does not consider the function of the agent, which may impact model performance

Geometric Partitioning: This partitioning method considers the spatial variables (x, y and z co-ordinates) of each agent to allocate agents to cores based on similar location. It is implemented by the inclusion of '-g' argument to the simulation executable. This method is based on the rationale that spatially proximal agents are more likely to communicate than distal agents. Therefore, partitioning using this method often improves the speed up of parallelisation.

Geometric partitioning offers a greater speed up for simulations where changes in x, y and z co-ordinates are consistent between agents and sufficiently small. However, in the simulations presented in this thesis, generally, this is not the case. Furthermore, *geometric* partitioning can give

unbalanced loading between nodes, reducing performance. Therefore, *round robin* partitioning is used throughout this work.

2.1.4 FLAME: Data Processing and Visualisation

Data processing of model output was performed using self-designed C scripts or visualised using the FLAME visualiser developed previously by Dr Simon Coakley (downloadable from www.flame.ac.uk). State graphs and process order graphs, generated in the dotty language by FLAME, were visualised using the open-source software Graphviz, available from http://www.graphviz.org.

2.2 POLYMERSOME ANALYSIS FOR AGENT-BASED MODELLING

This section is dedicated to the conversion of the physical chemistry of nanoparticles, particularly polymersomes, into usable data within agent-based models.

2.2.1 Size Analysis

The models presented in this thesis are based around spherical nanoparticles. Therefore the major physical variable of these particles is size. In many *in silico* studies, size populations are given homogeneously as particles of a given size. However, most samples contain a distribution of sizes, known as a polydisperse population. These can be further filtered and separated into different sized subpopulations. These are then analysed by a number of different methods. The most commonly employed analytical techniques used within the Battaglia laboratory are dynamic light scattering (DLS), transmission electron microscopy (TEM) and Nanosight tracking analysis (NTA). TEM and NTA give particle-by-particle measurements of particle size and therefore can be directly used to create simulated particles of the measured sizes. However this can be limiting when simulating larger or smaller populations than that measured. DLS does not use individual particle

measurements, but rather measures scattering patterns of the population. The correlation of scatter patterns with the original measurement changes over time according to the rate of movement (Brownian motion) of the particles. This is then used to determine the size distribution through the Stokes-Einstein equation that relates size to particle diffusion (Einstein, 1905).

DLS distribution curves are generated by the sorting of particle size into size classes by the Zetasizer® software package. In order to achieve a single method for generating nanoparticle populations from size data, simple tools to place NTA and TEM data into the same size classes as output by Zetasizer® have been developed using MATLAB. The resultant size distributions are then used to generate simulated samples that fit the given distribution. First, the simulated nanoparticle agents are assigned to a size class based on probabilities calculated from the cumulative frequency data (See *Figure 2.2A* and *2B*). The absolute size is then assigned by weighting the probability of sizes within the class by the neighbouring classes. *Figure 2.2* demonstrates distributions of different sized polydisperse nanoparticles from DLS analysis (*Figure 2.2C*) and their respective simulated distributions (*Figure 2.2D*).

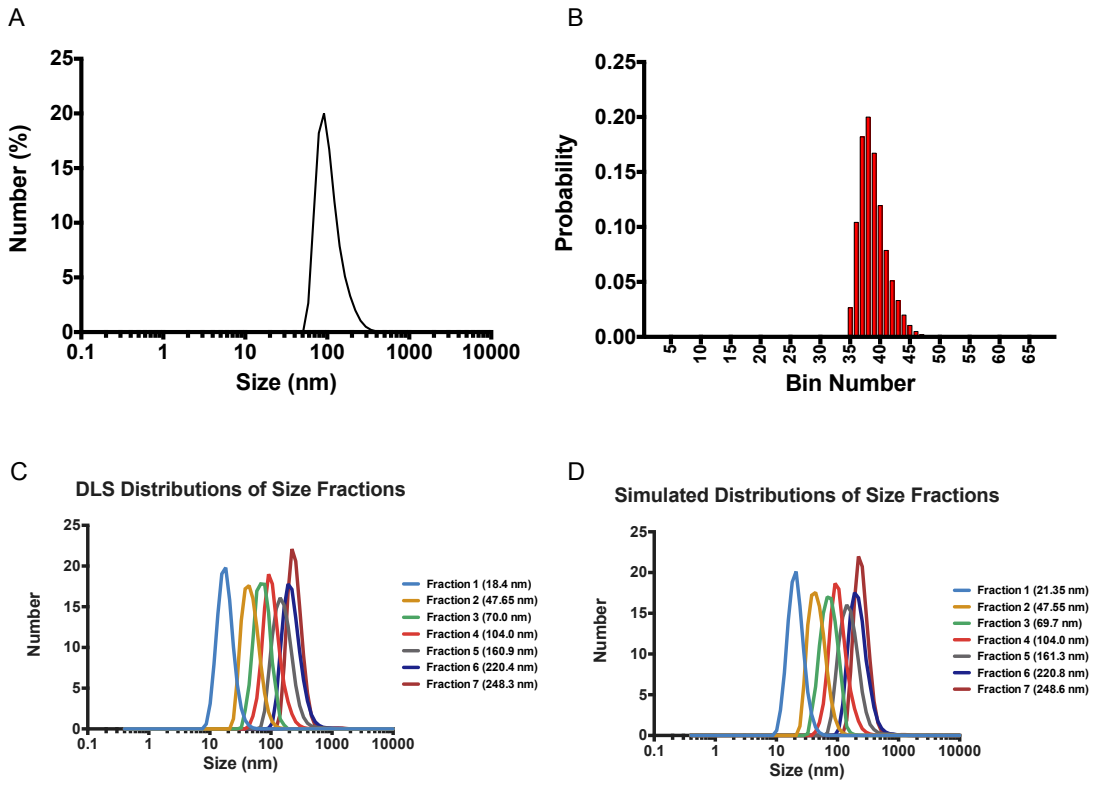

Figure 2.2: Simulation of DLS Distributions. Distribution of a nanoparticle population obtained by DLS analysis (A). Bar graph of probability of a given particle being within each size class (B). Distributions of multiple nanoparticle populations obtained from DLS analysis (C). and their simulated equivalent populations (D). DLS distribution data provided by Dr James Robertson and Dr Milagros Avila-Olias of the University of Sheffield, based on size separation of $PMPC_{25}$-$PDPA_{70}$ polymersomes.

2.2.2 Calculating Polymer Number from Polymersome Size

An estimate of the number of polymers ($\boldsymbol{N_{agg}}$) *per* polymersome can be calculated from the hydrated particle radius ($\boldsymbol{r}$), monomer molecular weight ($\boldsymbol{Mw_{POLYMER}}$), polymer chain lengths ($\boldsymbol{L_{POLYMER}}$), polymer density ($\boldsymbol{\rho_{POLYMER}}$), particle membrane thickness ($\boldsymbol{M_{NP}}$) and the particle brush length ($\boldsymbol{B_{NP}}$). The membrane and brush are demonstrated in the anatomy of a polymersome in *Figure 2.3*.

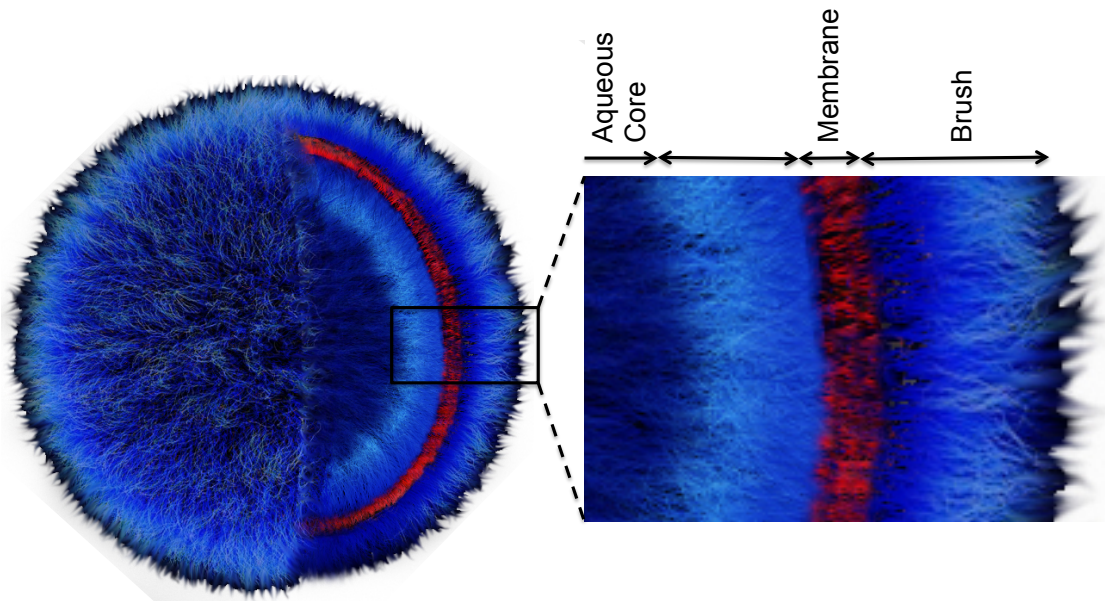

Figure 2.3: Anatomy of a Polymersome. The graphic that this figure is adapted from was provided by Silvia Bianco.

Density ($\boldsymbol{\rho}$)

The density of polymers in an aqueous environment is difficult to determine due to the association with water in a hydrated form. Packing of the membrane and the pH-sensitive nature of PDPA polymer further complicate this. This is because the hydrophilic properties of PDPA are governed by its ionisation state. Given that the densities of polymers are usually similar to water, they can be estimated as having a density tending towards that of water (1.0 g·cm^{-3}). Therefore density for PMPC and PDPA are considered as:

$\boldsymbol{\rho_{PMPC}}$ = 1.0 g·cm^{-3} (1000.0 kg·m^{-3})

$\boldsymbol{\rho_{PDPA}}$ = 1.0 g·cm^{-3} (1000.0 kg·m^{-3})

Molecular Volume ($\boldsymbol{Mv_{POLYMER}}$)

The molecular volume of a polymer can be calculated from the polymer density and the molecular weight of the polymer:

$$\boldsymbol{Mv_{POLYMER}} = \frac{\boldsymbol{Mw_{POLYMER}}}{\boldsymbol{\rho_{POLYMER} N_{AVAGADRO}}} \quad (2.1)$$ (Battaglia and Ryan, 2005, Smart et al., 2009)

MPC and DPA have a molecular weight of 295.5 g·mol^{-1} and 213.3 g·mol^{-1} respectively. Therefore, for a standard formulation of $PMPC_{25}$-$PDPA_{70}$ ($\boldsymbol{L_{PMPC}}$ = 25 and $\boldsymbol{L_{PDPA}}$ = 70), you obtain the following molecular volumes:

$\boldsymbol{Mv_{PMPC}}$ = 1.23×10^{-20} cm^3

$\boldsymbol{Mv_{PDPA}}$ = 2.36×10^{-20} cm^3

For the purpose of the later calculations, it is easier to convert the units to nm^3 by multiplying by 10^{21}.

$\boldsymbol{Mv_{PMPC}}$ = 12.3 nm^3

$\boldsymbol{Mv_{PMPC}}$ = 23.6 nm^3

Membrane Thickness (T_{NP}) and Brush Length (B_{NP})

The membrane thickness and brush length have been previously measured for polymersomes from transmission electron microscope (TEM) images and small angle x-ray scattering (SAXS) (Smart et al., 2009, Pearson et al., 2013) Battaglia JACS 2005). It was demonstrated that the membrane thickness scales with the molecular mass according to a power law with a 2/3 exponent:

$$\boldsymbol{M_{NP}} = \boldsymbol{0.359}(\boldsymbol{L_{PDPA}})^{\frac{2}{3}} \quad (2.2)$$

The constant 0.359 is derived from the membrane thickness ($\boldsymbol{M_{NP}}$) of 6.1 nm measured for an $\boldsymbol{L_{PDPA}}$ of 77 in Pearson and colleagues by $\frac{6.1}{77^{\frac{2}{3}}} = 0.359$ (Pearson et al., 2013).

The hydrophilic brush thickness scales linearly with the number of repeating units in the hydrophilic block, according to a dense brush configuration. For $PMPC_{25}$-$PDPA_{70}$ polymersomes, the membrane thickness can be experimentally measured using TEM to be 6.1 nm. The POEGMA brush can be calculated assuming a fully stretched configuration, where a C-C bond is 0.247 nm, giving a brush length of 6.187 nm (from 25×0.247).

Polymer Chains per Polymersome ($\boldsymbol{N_{agg}}$)

The number of polymer chains per vesicle of radius $\boldsymbol{r}$ can be calculated by first calculating the membrane volume ($\boldsymbol{Mv_{NP}}$):

$$\boldsymbol{Mv_{NP}} = \frac{\boldsymbol{4}}{\boldsymbol{3}}\boldsymbol{\pi}((\boldsymbol{r_{NP}} - \boldsymbol{B_{NP}})^{\boldsymbol{3}} - (\boldsymbol{r} - \boldsymbol{B_{NP}} - \boldsymbol{M_{NP}})^{\boldsymbol{3}}) \qquad (2.3)$$

Assuming a packing factor of 1, *Equation 2.3* can be divided by the molecular volume of PDPA, thus giving:

$$\boldsymbol{N_{agg}} = \frac{\frac{\boldsymbol{4}}{\boldsymbol{3}}\boldsymbol{\pi}((\mathrm{r}_{\boldsymbol{NP}} - \boldsymbol{B_{NP}})^{\boldsymbol{3}} - (\boldsymbol{r} - \boldsymbol{B_{NP}} - \boldsymbol{M_{NP}})^{\boldsymbol{3}})}{\boldsymbol{Mv_{PDPA}}} \qquad (2.4).$$

This is the method presented by Wang and colleagues (Wang et al., 2012). This is similar to the method presented by Massignani and colleagues, however their calculation is based on the surface area of the vesicle and area *per* molecule of the hydrophilic block as opposed to the volume (Massignani et al., 2009).

2.2.3 Calculating Ligand Density from Polymersome Size

The number of polymer chains in the outer leaflet, particularly in smaller vesicles, is expected to be greater than in the inner leaflet. This can be explained by the ratio ($\boldsymbol{R_{SA}}$) of the exterior membrane surface area ($\boldsymbol{E_{SA}}$) and the interior membrane surface area ($\boldsymbol{I_{SA}}$):

$$\boldsymbol{R_{SA}} = \frac{\boldsymbol{E_{SA}}}{\boldsymbol{I_{SA}}} \qquad (2.5)$$

For a vesicle this is equal to:

$$\boldsymbol{R_{SA}} = \frac{(\boldsymbol{r}-\boldsymbol{B_{NP}})^2}{(\boldsymbol{r}-\boldsymbol{B_{NP}}-\boldsymbol{Mb_{NP}})^2} \qquad (2.6)$$

As the polymersome size increases and $\boldsymbol{r}$ becomes larger, this ratio tends towards 0. To estimate the difference in the number of chains between the inner and outer leaflet, a similar calculation was made using the inner volume of the membrane and the outer volume of the membrane, therefore:

$$\boldsymbol{N_{agg-inner}} = \frac{\frac{4}{3}\boldsymbol{\pi}((\boldsymbol{r}-\boldsymbol{B_{NP}}-\frac{\boldsymbol{M_{NP}}}{2})^3-(\boldsymbol{r}-\boldsymbol{B_{NP}}-\boldsymbol{M_{NP}})^3)}{\boldsymbol{Mv_{PDPA}}} \qquad (2.7)$$

$$\boldsymbol{N_{agg-outer}} = \frac{\frac{4}{3}\boldsymbol{\pi}((\boldsymbol{r}-\boldsymbol{B_{NP}})^3-\left(\boldsymbol{r}-\boldsymbol{B_{NP}}-\frac{\boldsymbol{M_{NP}}}{2}\right)^3)}{\boldsymbol{Mv_{PDPA}}} \qquad (2.8)$$

Ligands are covalently attached to the end of the polymer chains. The percentage of polymers used in formation is known from chemical analysis by high performance liquid chromatography (HPLC) and controlled by blending functionalised and non-functionalised polymers. Therefore using the estimate of the number of polymer chains in the outer leaflet ($\boldsymbol{N_{agg-outer}}$) and the

percentage of functionalised polymer ($P_{\%}$), the ligand density (L_D) can be estimated:

$$L_D = \frac{N_{agg-outer} \times \frac{P_{\%}}{100\%}}{4\pi r^2} \qquad (2.9)$$

2.3 COMPUTATIONAL FLUID DYNAMICS

2.3.1 Incompressible Form of the Navier-Stokes Equations

The Navier-Stokes equations refer to three coupled partial differential equations (PDEs) with the vector equation for the conservation of momentum being:

$$\rho\left(\frac{\partial u}{\partial t} + v \cdot \nabla v\right) = -\nabla p + \nabla \cdot \tau + F \qquad (2.10)$$

where ρ is the density, t is time, ∇ is the del operator, v is the velocity, p is the pressure, τ is the total stress tensor and F is the force. The continuity equation describing the conservation of mass can be expressed as:

$$\frac{\partial \rho}{\partial t} + \nabla \cdot \rho u = 0 \qquad (2.11)$$

while the equation for conservation of energy is:

$$\rho C_p\left(\frac{\partial T}{\partial t} + (v.\nabla)T\right) = -(\nabla.q) + \tau : S - \frac{T}{\rho}\frac{\partial \rho}{\partial T}\Big|_p\left(\frac{\partial p}{\partial t} + (v.\nabla)p\right) + Q \qquad (2.12)$$

where C_ρ is the specific heat capacity at constant pressure, T is the absolute temperature, q is the heat flux vector, S is the rate of strain tensor and Q is the heat sources.

In order to simplify the solutions to the Navier-Stokes equations, RBCs are treated as separate objects that influence flow by creating transient moving wall boundaries. Acellular blood (plasma) is a Newtonian fluid and therefore the fluid flow has been treated as Newtonian. Blood flow is incompressible, thus meaning the density of the fluid remains unchanged, such that:

$$\frac{\partial \rho}{\partial t} = \mathbf{0} \qquad (2.13)$$

Therefore, by substituting *Equation 2.13* into *Equation 2.10* and *Equation 2.11* the incompressible Newtonian form for the conservation of momentum (*Equation 2.14*) and incompressible form of the continuity equation (*Equation 2.15*) is achieved:

$$\boldsymbol{\rho}\left(\frac{\partial \boldsymbol{v}}{\partial t} + \boldsymbol{v} \cdot \boldsymbol{\nabla v}\right) = -\boldsymbol{\nabla p} + \boldsymbol{\eta \nabla^2 v} + \boldsymbol{F} \qquad (2.14)$$

where $\boldsymbol{\eta}$ is the dynamic viscosity and $\boldsymbol{\nabla^2}$ is the Vector Laplacian. The incompressible form of the continuity equation is:

$$\boldsymbol{\rho \nabla \cdot v} = \mathbf{0} \qquad (2.15).$$

Equation 2.13 also leads to decoupling of the energy *Equation 2.12* from *Equation 2.14* and *Equation 2.15*.

2.3.2 Execution of the Galerkin/Least Squares Method in Comsol Multiphysics

In order to find a solution to the Navier-Stokes equations the laminar flow package in the Comsol® Multiphysics software (License number 7074209) was used. Comsol Multiphysics uses a Galerkin/Least Squares (GLS) method

to resolve the Navier-Stokes equations. The GLS method is a variation of the FEM. The next section describes how the model was produced in Comsol.

2.3.3 Geometry

The vessel geometry was created using a regular cylinder of specified radius and height (*Figure 2.4*).

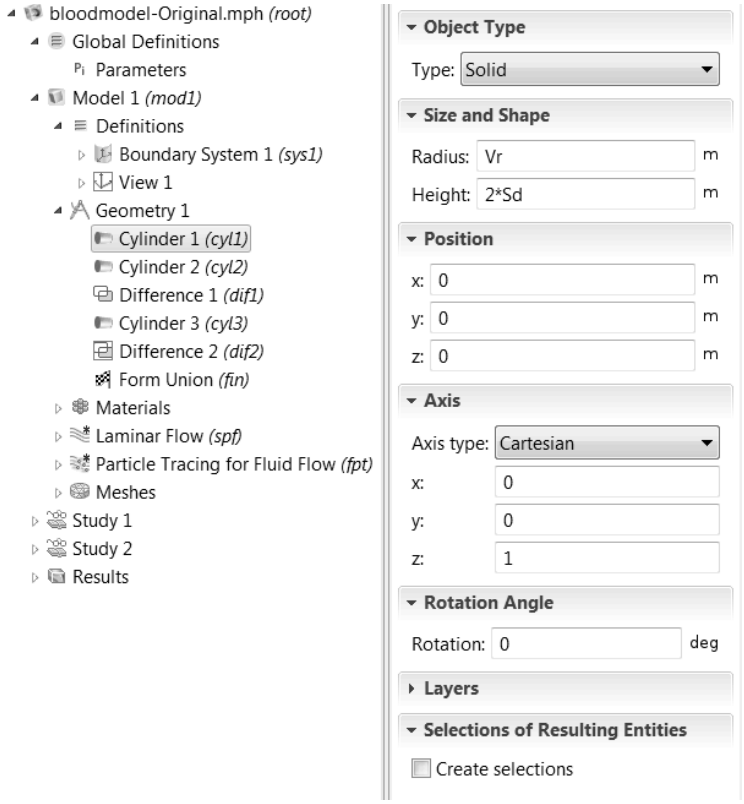

Figure 2.4: Creating the Vessel Geometry in Comsol Multiphysics.

The RBCs were placed at intervals dictated by the haematocrit, as cylinders with a radius and height of a RBC in a parachute conformation (*Figure 2.5*).

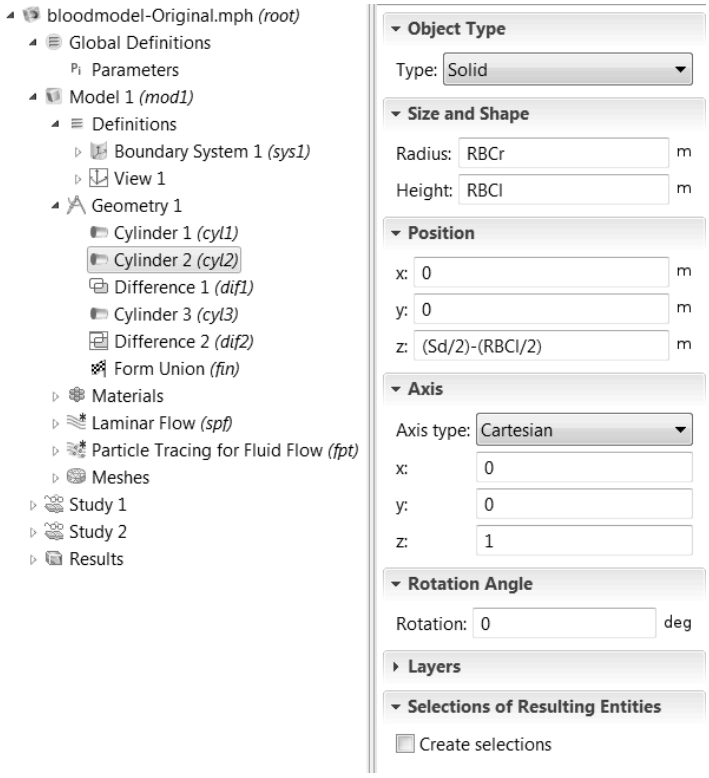

Figure 2.5: Creating the Red Blood Cell Geometry in Comsol Multiphysics.

The vessel and RBCs are declared as separate entities by the 'difference' setting (*Figure 2.6*).

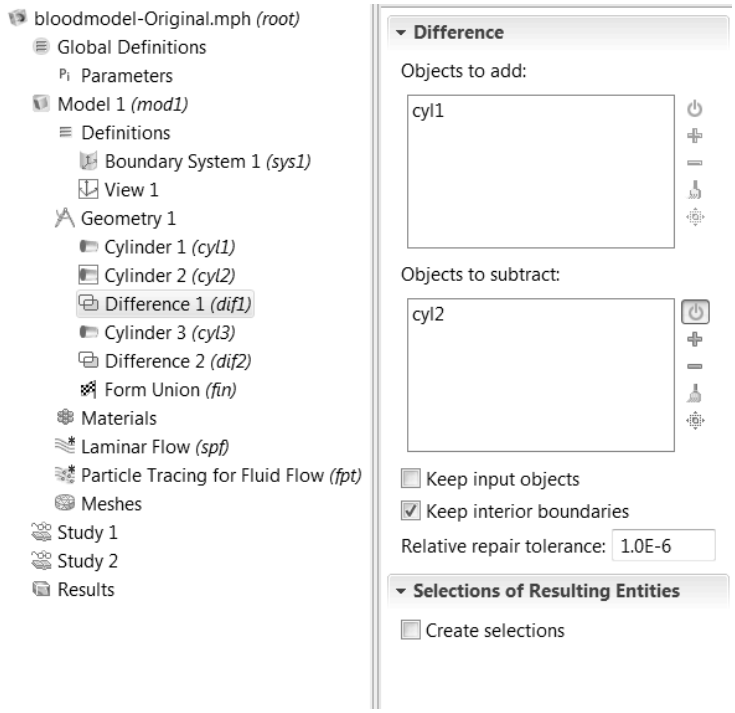

Figure 2.6: Setting the Difference in Geometry in Comsol Multiphysics.

The resulting geometry is visualised in *Figure 2.7*.

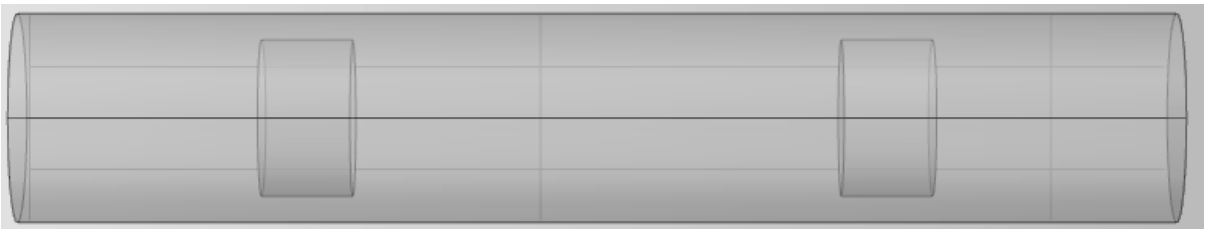

Figure 2.7: The Vessel Geometry in Comsol Multiphysics. A shortened section of the geometry in Comsol Multiphysics.

2.3.4 Meshing

In order to produce the finite elements within the geometry, the tetrahedral meshing setting was used with a 'fine' mesh setting, giving approximately 45 elements·μm^{-3} depending on haematocrit levels (*Figure 2.8*).

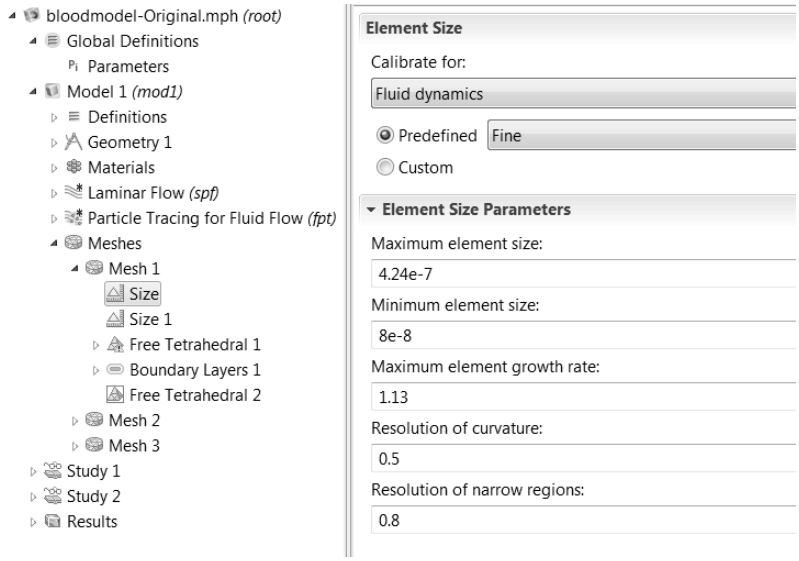

Figure 2.8: Meshing the Geometry in Comsol Multiphysics.

The resulting meshed geometry was visualised as *Figure 2.9*.

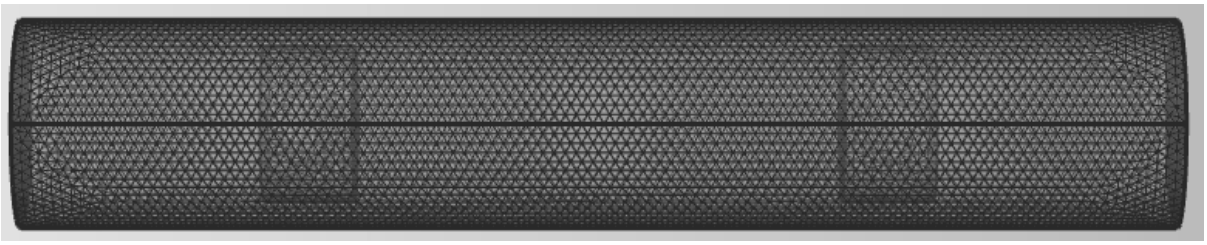

Figure 2.9: Meshed Geometry in Comsol Multiphysics.

2.3.5 Fluid Properties

Blood plasma was treated as a Newtonian fluid with a variable viscosity related to the haematocrit and a density of 1060 kg·m^{-3} (*Figure 2.10*).

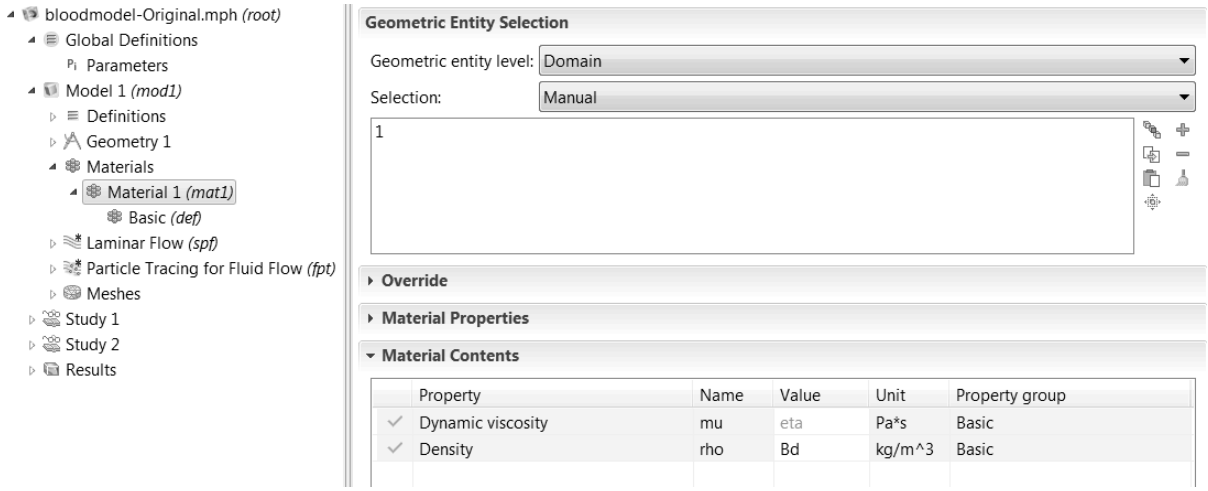

Figure 2.10: Setting Blood Material Properties in Comsol Multiphysics.

The Navier-Stokes equations were applied to the fluid domain or blood plasma using the vessel and RBCs to create boundary conditions (*Figure 2.11*).

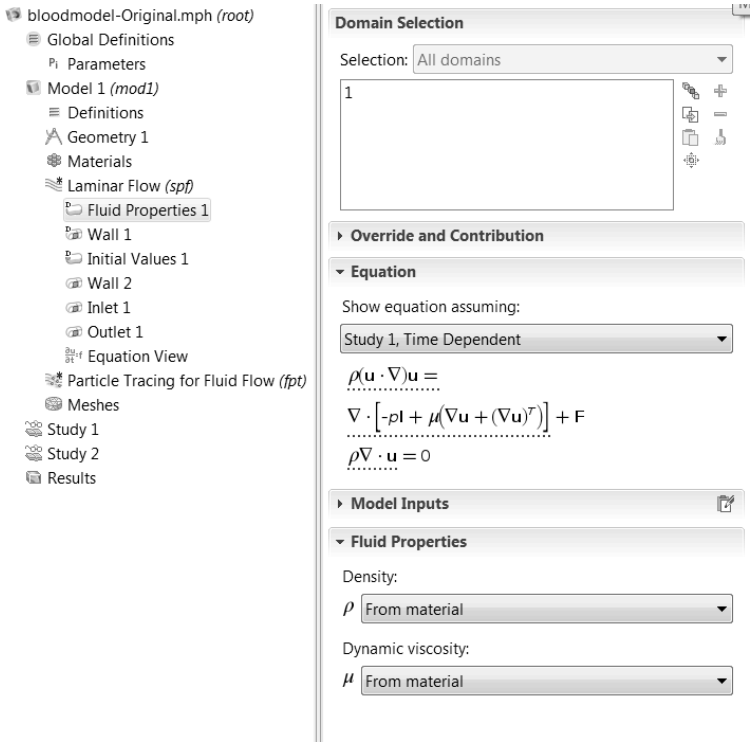

Figure 2.11: Setting the Material in which to Solve Laminar Flow in Comsol Multiphysics.

2.3.6 Boundary Conditions

There are four main boundaries used within the laminar flow model presented in this thesis. The vessel walls were declared as non-slip boundaries with a velocity of 0 (*Figure 2.12*).

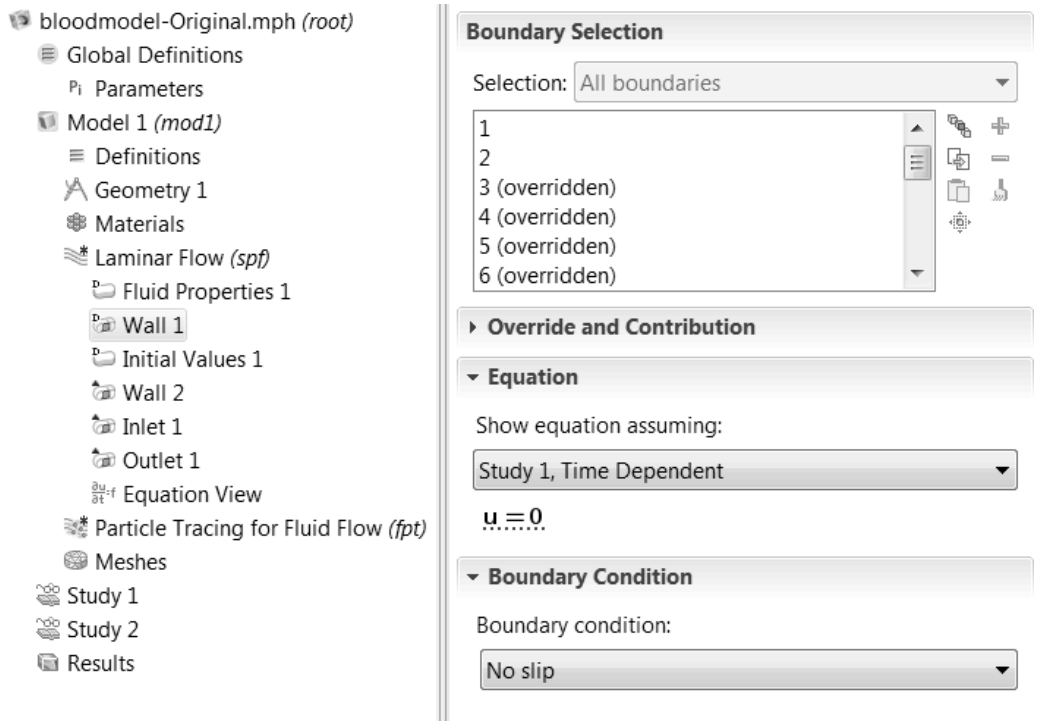

Figure 2.12: Setting the No Slip Boundary in Comsol Multiphysics.

The RBC walls were treated as moving boundaries at a rate of 60 $\mu m \cdot s^{-1}$ for normal conditions and 80 $\mu m \cdot s^{-1}$ for functional hyperaemia conditions (*Figure 2.13*).

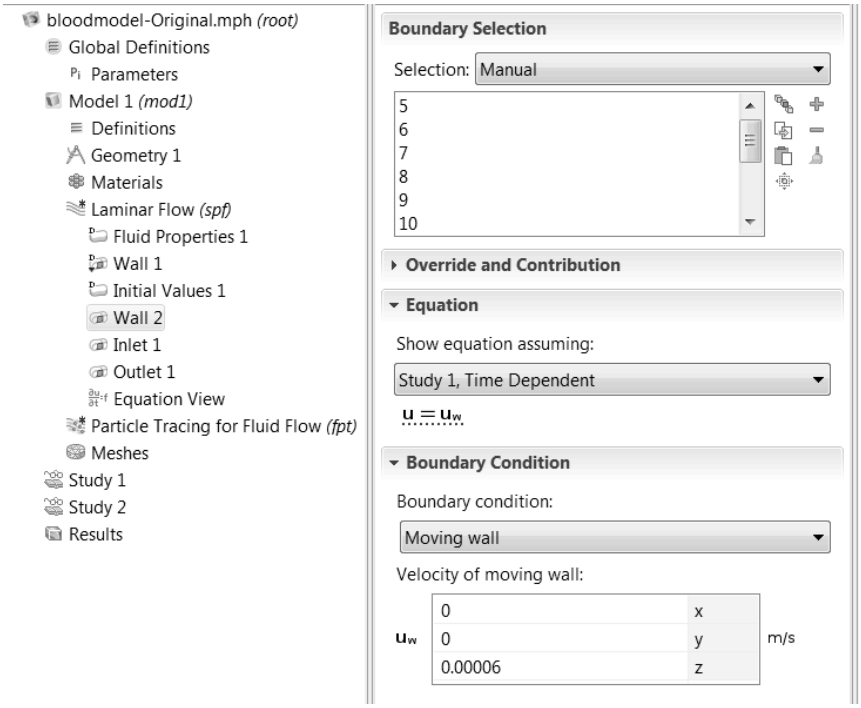

Figure 2.13: Setting the Moving Boundaries in Comsol Multiphysics.

One end of the vessel was designated the inlet (*Figure 2.14*) and the other the outlet (*Figure 2.15*). The inlet and outlet were specified by pressure values.

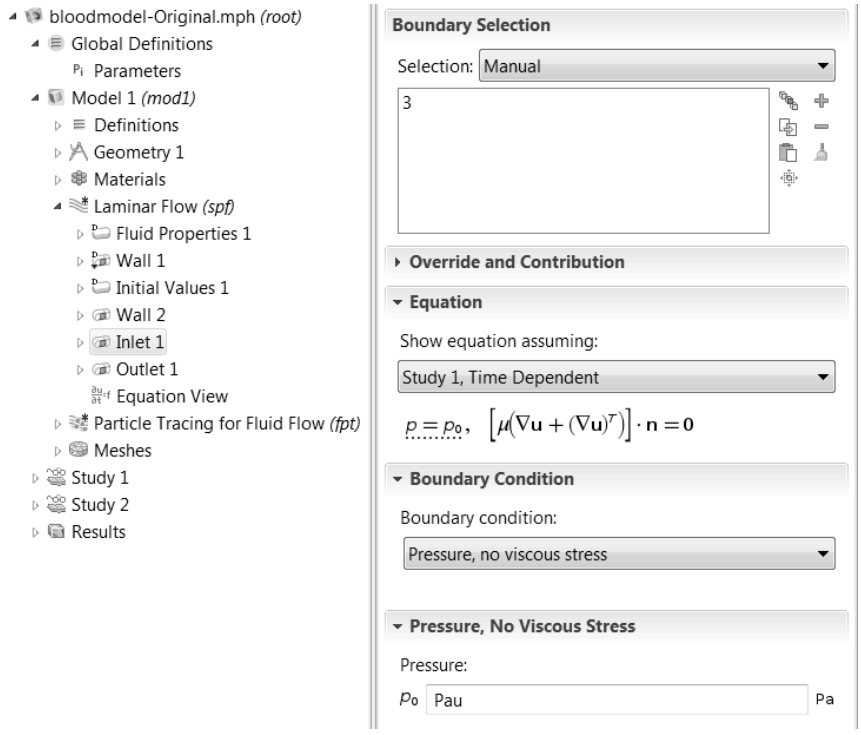

Figure 2.14: Setting the Inlet Conditions in Comsol Multiphysics.

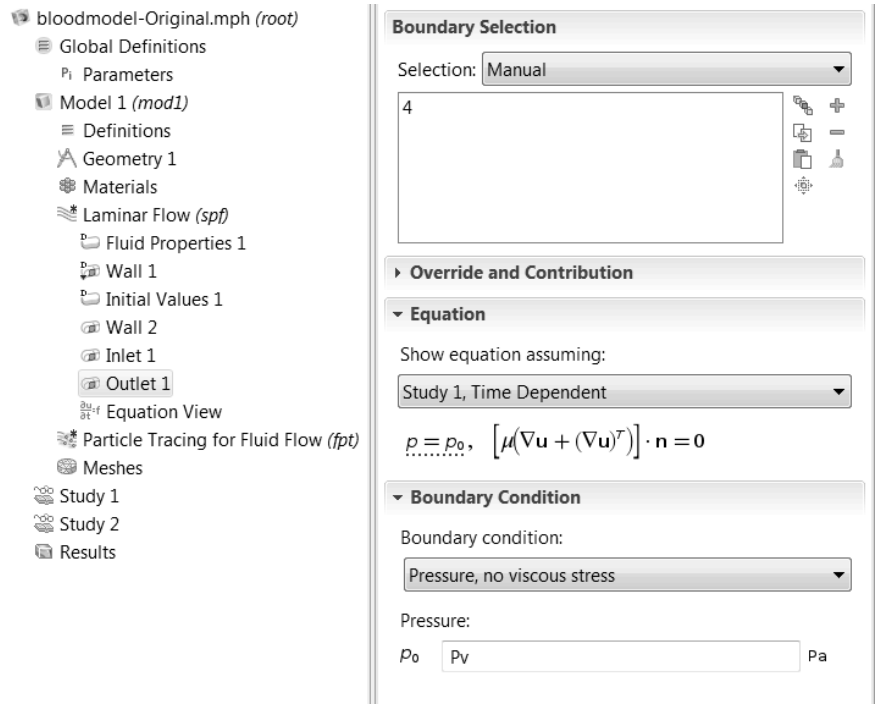

Figure 2.15: Setting the Outlet Conditions in Comsol Multiphysics.

Comsol Multiphysics uses the weak form of the Navier-Stokes equation and the generalised minimal residual method (GMRES) to solve flow within the defined geometry. GMRES is an iterative method of obtaining an approximate solution to the given problem (*Figure 2.16*).

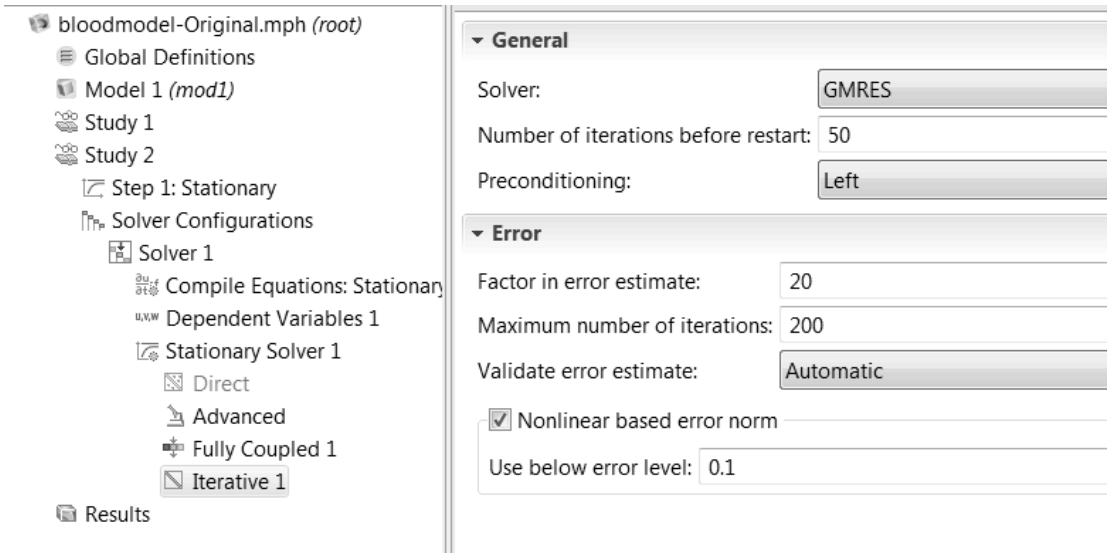

Figure 2.16: Configuring the Stationary Iterative Solver in Comsol Multiphysics

2.3.7 Execution of a Laminar Flow Model in FLAME

The meshing from the Comsol Multiphysics solution for the Navier-Stokes equations was exported with co-ordinates (x, y, z), velocity in all three planes (V_x, V_y, V_z), total velocity (V_{Total}) and the shear stress (τ_s). The MATLAB initial states generator used these values to build the mesh as a FLAME XMML file for implementation. In order to allow RBCs to move and not require re-meshing, the nodes updated their location each iteration by the same distance traversed by the RBCs. This allowed a simple parallelisation of an FEM solution for laminar flow.

Nanoparticle motion was given by Newton's second law according to the velocity of the nearest element:

$$\boldsymbol{m}\frac{\boldsymbol{\partial^2 x}}{\boldsymbol{\partial t^2}} = \boldsymbol{F}(\boldsymbol{t}, \boldsymbol{x}, \frac{\boldsymbol{\partial x}}{\boldsymbol{\partial t}}) \qquad (2.16)$$

where $\boldsymbol{m}$ is the mass, $\frac{\boldsymbol{\partial^2 x}}{\boldsymbol{\partial t^2}}$ is the acceleration in x, $\boldsymbol{F}$ the force, $\boldsymbol{t}$ the time and x the x-coordinate.

2.4 SIMULATION OF BROWNIAN MOTION

A simulation of the random walk, known as Brownian motion, can be achieved from environmental and particle specific properties as outlined by Andrews and Bray (Andrews and Bray, 2004). Using the Stokes-Einstein equation the diffusion coefficient ($\boldsymbol{D_c}$) can be calculated by:

$$\boldsymbol{D_c} = \frac{\boldsymbol{k_B T}}{\boldsymbol{6\pi\eta r}} \qquad (2.17)$$

where $\boldsymbol{k_B}$ is the Boltzmann constant, $\boldsymbol{T}$ is the absolute temperature, $\boldsymbol{\eta}$ is the dynamic viscosity and $\boldsymbol{r}$ is the particle radius.

Andrews and Bray described methods to convert the diffusion coefficient into a standard deviation ($\boldsymbol{\sigma}$) that can be used to plot a normalised distribution:

$$\boldsymbol{\sigma \equiv \sqrt{2D_c \Delta t}} \qquad (2.18)$$

where $\boldsymbol{\Delta t}$ is the time step. Thus giving the Gaussian for probability ($\boldsymbol{P}$) of a change in x-coordinate of $\boldsymbol{\Delta x}$:

$$\boldsymbol{P \equiv \frac{1}{\sigma\sqrt{2\pi}} e^{\left(-\frac{\Delta x^2}{2\sigma^2}\right)}} \qquad (2.19)$$

Then by generating random numbers that fit the normalised distribution, a random walk in the x-plane can be achieved. Random numbers that fit to a normalised distribution can be given by the Box-Muller transformation and variations of this method (Box and Muller, 1958). The polar method presented below is an adaptation of this method by Bell and Knop (Knop, 1969). It has advantages in its improved computational efficiency and robustness when used for stochastic modelling. Firstly two random numbers ($\boldsymbol{d_1}$ and $\boldsymbol{d_2}$) are generated that satisfy the following:

$$\boldsymbol{-1 \leq d_1 \leq 1}$$

and $\boldsymbol{-1 \leq d_2 \leq 1}$

and $\boldsymbol{0 \leq {d_1}^2 {d_2}^2 \leq 1}$

Then two numbers ($\boldsymbol{G_1}$ and $\boldsymbol{G_2}$) are generated that satisfy a normal distribution with mean of 0 and standard deviation of 1 by the following:

$$\boldsymbol{G_1 = d_1 \sqrt{\frac{-2ln\left({d_1}^2 {d_2}^2\right)}{\left({d_1}^2 {d_2}^2\right)}}} \qquad (2.20)$$

$$G_2 = d_2\sqrt{\frac{-2\ln\left(d_1{}^2 d_2{}^2\right)}{\left(d_1{}^2 d_2{}^2\right)}} \qquad (2.21)$$

These numbers can be converted to fit the given distribution by the following translation:

$$\Delta \boldsymbol{x} = \boldsymbol{G\sigma} + \boldsymbol{\mu} \qquad (2.22)$$

where $\boldsymbol{\sigma}$ is the standard deviation previously calculated and $\boldsymbol{\mu}$ is the mean, which for the random walk should be 0. The resulting value is then used as the change in x-coordinate. The repeating of this for the y- and z- coordinates then gives a 3D simulation of the random walk. Simple example codes of this, in C and in FLAME, are given in the *Appendix II* and *III* respectively.

The random walk ($\boldsymbol{F_B}$) can be combined with the laminar flow ($\boldsymbol{F_L}$) model presented in the previous section by the addition of the movement vectors to give the total movement force ($\boldsymbol{F_{Total}}$):

$$\boldsymbol{F_{Total}} = \boldsymbol{F_L} + \boldsymbol{F_B} \qquad (2.23).$$

2.5 SIMULATION OF ROTATIONAL DIFFUSION

A simulation of rotational diffusion can be achieved by similar methods to translational diffusion as described in the previous section. Firstly the rotational diffusion coefficient ($\boldsymbol{D_r}$) is calculated:

$$\boldsymbol{D_r} = \frac{\boldsymbol{k_B T}}{\boldsymbol{8\pi\eta r^3}} \qquad (2.24)$$

where k_B is the Boltzmann constant, T is the absolute temperature, η is the dynamic viscosity and r is the particle radius. Then the standard deviation σ of Gaussian distribution is calculated:

$$\sigma \equiv \sqrt{2D_r \Delta t} \qquad (2.25)$$

where Δt is the time step. The probability (P) of a change in angle of theta ($\Delta\theta$) can then be calculated by:

$$P \equiv \frac{1}{\sigma\sqrt{2\pi}} e^{\left(-\frac{\Delta\theta^2}{2\sigma^2}\right)} \qquad (2.26).$$

Random numbers can be generated to fit this distribution by the polar form of the Box-Muller transformation described in the previous section.

Rotational diffusion is used to determine the location of points on the outer surface of the nanoparticle, such as receptors or an asymmetric patch. The new location of the point (x', y') can be calculated from the original point (x, **y**) and the angle of rotation (θ) by the rotation matrix:

$$\begin{bmatrix} x' \\ y' \end{bmatrix} = \begin{bmatrix} x \\ y \end{bmatrix} \begin{bmatrix} cos\,\theta & -sin\,\theta \\ sin\,\theta & cos\,\theta \end{bmatrix} \qquad (2.27)$$

therefore:

$$x' = x\cos\theta - y\sin\theta \qquad (2.28)$$

$$y' = x\sin\theta + y\cos\theta \qquad (2.29).$$

To achieve rotational diffusion, three angles are generated from the rotational diffusion coefficient, the angle around the z-axis (θ), around the x-axis (φ) and

around the y-axis ($\boldsymbol{\phi}$). The x, y and z co-ordinates of a point are then sequentially rotated around each angle to get the new co-ordinates.

2.6 SIMULATION OF A DIRECTIONALLY BIASED NANOPARTICLE

To simulate a directionally biased propelled particle, a point is assigned on the nanoparticle surface to act as the point of the asymmetric patch (x_{Assym}, y_{Assym}, z_{Assym}), with propulsion occurring in the opposite direction to that point. This is in order to fit with the hypothesis of action of the formulation designed within the Battaglia group (Cecchin et al., 2014), as demonstrated in *Figure 2.17.*

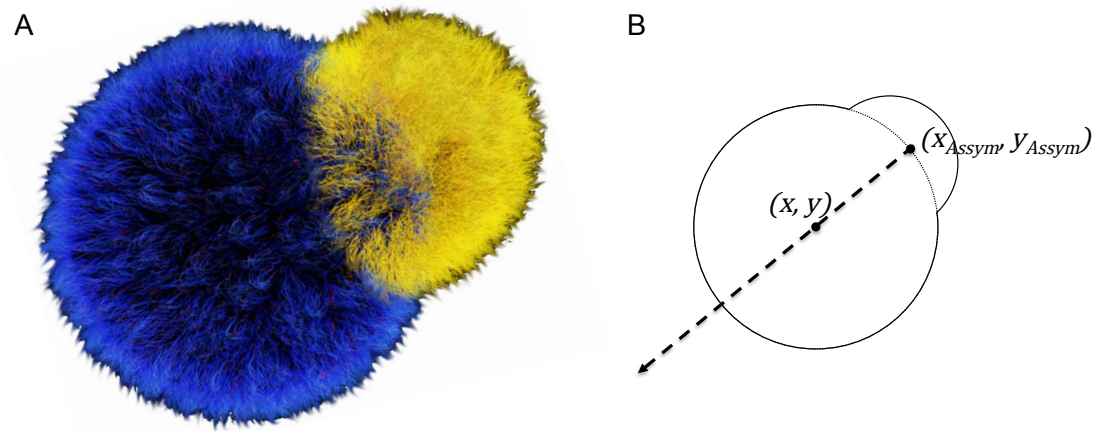

Figure 2.17: Schematic of a Chemotactic Polymersome. Graphic of a polymersome with an asymmetric patch (A) and a simple schematic of a modelled asymmetric point (B).

Rather than updating the x-, y- and z- coordinates of the asymmetric patch every iteration, the patch is originally set to (0, -$\boldsymbol{r}$, 0), where $\boldsymbol{r}$ is the particle radius. The angles of rotation (θ, φ and ϕ) of the whole particle are held within the memory and updated each iteration, the location of the patch is then calculated from these only when required using the original point in order to maximise computational efficiency.

The propulsion is then set in the opposite direction to the patch. The propulsion is given as a value in the positive y-direction (φ), thus given a propulsion vector of:

$$\begin{bmatrix} \mathbf{0} \\ \boldsymbol{P} \\ \mathbf{0} \end{bmatrix}.$$

This is rotated sequentially around the angles of rotation to give the final propulsion vector ($\boldsymbol{F_P}$). This is then added to the Brownian motion vector ($\boldsymbol{F_B}$) to give a total movement vector ($\boldsymbol{F_{Total}}$):

$$\boldsymbol{F_{Total}} = \boldsymbol{F_B} + \boldsymbol{F_P} \qquad (2.30).$$

Similarly the propelled particle simulation can be combined with the laminar force model by adding the laminar force vector:

$$\boldsymbol{F_{Total}} = \boldsymbol{F_L} + \boldsymbol{F_B} + \boldsymbol{F_P} \qquad (2.31).$$

2.7 CONSIDERATION OF BOUNDARIES

Motile particles will encounter boundaries due to the compartmentalised nature of biological systems. There are a number of ways to approach the interaction of particles and boundaries. The most common is the reflective boundary, particles that cross the plane of the boundary are simply reflected back into the compartment, as seen in *Figure 2.18*.

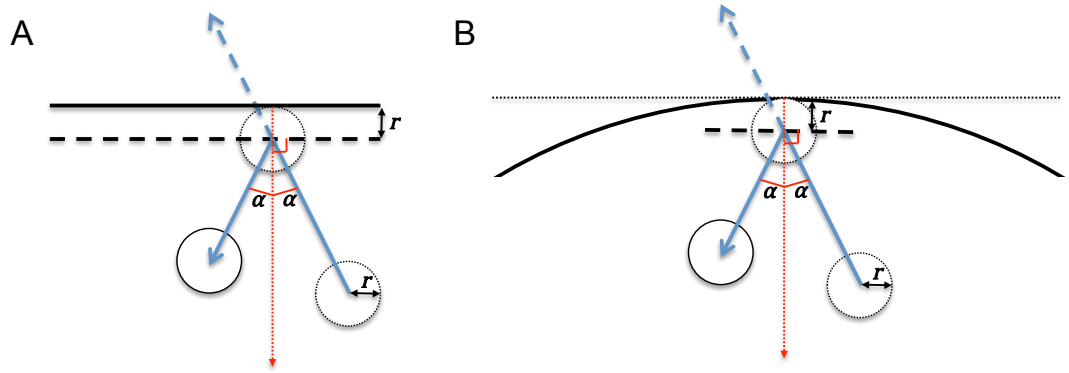

Figure 2.18: Reflective Boundaries. Particle reflections at a straight (A) and curved (B) boundary. The initial trajectory of the particle (blue line) is reflected in the line of incidence (black dashed line) that is set at a distance of the particle radius (r) from the boundary (black solid line) for A or from the tangent (black dotted line) at the point of intersection for B.

The reflective boundary is the most common type used within the simulations presented in this thesis, however the sticky boundary and deleting boundary are also used. Any particles that cross a sticky boundary are immobilised at the point of collision and can be quantitfied. The deleting boundary automatically deletes any agent that crosses it and is used at the exit of the vessel.

2.8 SIMULATION OF RECEPTOR BINDING

The binding and unbinding of a receptor was based on the model presented by Decuzzi and Ferrari with adaptations for agent-based modelling (Decuzzi and Ferrari, 2006). The probability ($\boldsymbol{P_{form}}$) of a ligand binding to a receptor is given by:

$$\boldsymbol{P_{form} \simeq 1 - e^{-R_D L_{A_c} k_a^0 \Delta t}} \qquad (2.32)$$

where $\boldsymbol{R_D}$ is the receptor density on the cell surface, $\boldsymbol{k_a^0}$ is the association constant at zero load per receptor-ligand pair, $\boldsymbol{L_{A_c}}$ is the contact area for a

ligand on the cell surface and $\boldsymbol{\Delta t}$ is the time step. The contact surface area for an individual ligand is given by:

$$\boldsymbol{L_{A_c} = \pi(B_L{}^2 - \delta_L{}^2)} \qquad (2.33)$$

where $\boldsymbol{\delta_L}$ is the distance from the ligand nanoparticle surface, to the cell surface.

The probability of a receptor-ligand bond rupturing ($\boldsymbol{P_{break}}$), when no shear flow is present is given by:

$$\boldsymbol{P_{break} \simeq 1 - e^{-k_D \Delta t}} \qquad (2.34)$$

where $\boldsymbol{k_D}$ is the dissociation constant, given as the inverse of the association constant.

In the presence of shear flow the probability of bond rupture can be given by:

$$\boldsymbol{P_{break} \simeq 1 - e^{-k_D \Delta t e^{\frac{B_L Fdis}{K_B T B_N}}}} \qquad (2.35)$$

where $\boldsymbol{B_L}$ is the characteristic bond length, $\boldsymbol{Fdis}$ is the dissociating force, $\boldsymbol{k_B}$ is the Boltzmann constant, $\boldsymbol{T}$ is the temperature and $\boldsymbol{B_N}$ is the number of bonds.

The total dissociating force is given by the addition of the drag force ($\boldsymbol{F_d}$) and half the torque force ($\boldsymbol{T_q}$):

$$\boldsymbol{F_{dis} = F_d + \frac{T_q}{2}} \qquad (2.36)$$

The drag force acting upon a spherical particle is related to the wall shear stress (S_μ), force as a function of aspect ratio (F^S), the particle radius (r) and the distance from the vessel wall and centre of nanoparticle mass (l):

$$F_D = 6\pi r l S_\mu F^S \qquad (2.37).$$

The force as a function of aspect ratio is given as:

$$F^S = 1 + (1.736 - 0.138\gamma + 0.128\gamma^2 + 0.09\gamma^3)e^{-\gamma} \qquad (2.38)$$

where γ is the aspect ratio of the nanoparticle (Pozrikidis, 1994). A spherical nanoparticle has an aspect ratio of 1, therefore:

$$F^S = 1.668 \qquad (2.39)$$

and thus the drag force can be estimated as:

$$F_D = 10\pi r l S_\mu \qquad (2.40).$$

The torque forces acting upon a nanoparticle can be similarly expressed as:

$$T = 4\pi r^3 S_\mu T^S \qquad (2.41)$$

where T^S is the force as a function of the aspect ratio, given as:

$$T^S = 1 + (-20.5 + 46.5\gamma - 35.1\gamma^2 + 8.95\gamma^3)e^{-\gamma} \qquad (2.42)$$ (Pozrikidis, 1994).

For a spherical nanoparticle ($\boldsymbol{\gamma = 1}$), this gives:

$$\boldsymbol{T^S = 0.945} \qquad (2.43)$$

and a simplified approximation of the torque as:

$$\boldsymbol{T = 3.78\pi r^3 S_\mu} \qquad (2.44).$$

The bond length in these studies was based on the bond length of the Lrp1-angiopep-2 interaction. There is limited availability of structural data for the Lrp1 protein, therefore the bond length was estimated from the molecular weight ($\boldsymbol{M_w}$) of the extracellular Lrp1β chain (85 kDa) and Angiopep-2 (2.3 kDa) as 6.5 nm using the methods presented by Erickson (Erickson, 2009, Martin et al., 2008). This method assumes that most proteins have a similar density of approximately 1.37 g·cm^{-3}. The density can be used to find the partial specific volume ($\boldsymbol{Pr_{SPV}}$) of proteins. The average partial specific volume is given as 0.73 cm^3·g^{-1}. This is then used to calculate the volume ($\boldsymbol{Pr_{Vol}}$) from the density:

$$\boldsymbol{Pr_{vol}(nm^3) = \frac{Pr_{SPV}(cm^3 \cdot g^{-1}) \times 10^{21}(nm^3 \cdot cm^{-3})}{6.023 \times 10^{23}(Da \cdot g^{-1})}} \qquad (2.45)$$

which simplifies to:

$$\boldsymbol{Pr_{vol}(nm^3) = [1.212 \times 10^{-3}(nm^3 \cdot Da^{-1})] \times M_w(Da)} \qquad (2.46).$$

Assuming the protein is a globular protein (spherical) this would give a length ($\boldsymbol{B_L}$) of:

$$\boldsymbol{B_L \approx 2\times\sqrt[3]{\frac{3Pr_{vol}}{4\pi}}} \qquad (2.47).$$

This method gives a rough estimate of the length of Lrp1 as 5.8 nm and Angiopep-2 as 0.87 nm. Therefore the bond length was estimated at 6.5 nm. However, it would be expected that the bond length would be larger than this as it is unlikely that a receptor protein is also globular. However there would also be some expected overlap of the ligand and receptor in order to form a bond. Although this method is a relatively crude estimation of the bond length, other studies have used arbitrary values ranging from 1 nm to 20 nm, which can significantly influence the results.

2.9 SIMULATION OF CELL TRAFFICKING

After initial binding, nanoparticle endocytosis, trafficking and exocytosis was performed using the timings elucidated by Xiaohe Tian. After binding, nanoparticles that remained bound to the apical membrane for 10 s were endocytosed. Endocytosed particles were unable to bind for a further 10 s, before being exocytosed on to the basolateral membrane (Tian and Battaglia, unpublished).

2.10 SIMULATION OF FENESTRATIONS

Fenestrations were treated as uniform cylindrical channels of 500 nm in length and 60 nm in diameter for normal tissue or 240 nm for tumour tissue. Fenestrations agents were added into simulations by randomly distributing the agents to a density of 16 μm^{-2} on the outside of the vessel in line with data obtained from the endothelium of the pancreas (Milici et al., 1985), ensuring that no two agents were within 60 nm or 240 nm, for normal or tumour models respectively, from the nearest fenestration. Entry into the fenestration pore was treated as a passage event for simplicity.

2.11 STATISTICAL ANALYSIS

Correlation of simulated and expected particle displacement was analysed through the two-tailed Pearson's rank coefficient. All other tests for significance were analysed by the t-test using the Holm-Sidak method. Significance analysis was performed in Prism version 6.0f for Macintosh OS X, GraphPad Software, La Jolla California USA, www.graphpad.com.

In *Chapter 4*, where ratios are calculated using the mean of nanoparticle binding events, the total error can be calculated as follows. When the ratio is:

$$\boldsymbol{R} = \frac{\overline{\boldsymbol{N_{xyz}}}}{\overline{\boldsymbol{N_{qrs}}}} \qquad (2.48)$$

where $\overline{\boldsymbol{N_{xyz}}}$ is the mean of values $\boldsymbol{x}$, $\boldsymbol{y}$ and $\boldsymbol{z}$ and $\overline{\boldsymbol{N_{qrs}}}$ is the mean of the values $\boldsymbol{q}$, $\boldsymbol{r}$ and $\boldsymbol{s}$. The total error $\boldsymbol{E}$ is calculated as:

$$\boldsymbol{E} = \boldsymbol{R}\sqrt{\frac{\sigma_x}{x} + \frac{\sigma_y}{y} + \frac{\sigma_z}{z} + \frac{\sigma_q}{q} + \frac{\sigma_r}{r} + \frac{\sigma_s}{s}} \qquad (2.49).$$

CHAPTER 3: RESULTS AND DISCUSSION I

AGENT-BASED MODELLING OF NANOPARTICLE BEHAVIOUR UNDER BLOOD FLOW: INSIGHTS INTO DISTRIBUTION AND TARGETING TUMOURS

3.1 INTRODUCTION

3.1.1 Blood Flow in Capillaries

Blood flow in the microvasculature affects the ability of blood-borne molecules to be distributed to the vessel walls and cross the endothelial wall into the tissue. Blood flow through capillaries is driven by the pressure difference between the pre-capillary pressurised arterioles and the post-capillary low-pressure venules. Capillary flow is laminar, as defined by the Reynold's number ($\boldsymbol{Re}$), the ratio between viscous and inertial forces:

$$\boldsymbol{Re} = \frac{\rho \overline{v} D_H}{\eta} \qquad (3.1)$$

where $\boldsymbol{\rho}$ is the density, $\overline{v}$ is the mean velocity, $\boldsymbol{D_H}$ is the hydraulic diameter and $\boldsymbol{\eta}$ the dynamic viscosity. Capillaries have a Reynold's number of 0.001, well below the range of transient flow of ~2400, due to their small length scales and high viscosity (Cho and Cho, 2011). Laminar flow is characterised by flow in parallel layers with no mixing. Flow at the vessel wall is vastly reduced due to friction with the stationary vessel wall, called a non-slip boundary, with the velocity increasing towards the centre of the vessel in a parabolic manner, as seen in *Figure 3.1*.

Figure 3.1: Laminar Flow in a Pipe. Longitudinal cross-section of laminar flow along a pipe.

3.1.2 Blood Flow and Brownian Motion in Capillaries

In addition to laminar forces, other forces also act upon nanoparticles within the blood. In particular, thermal fluctuations, also known as Brownian motion, cause random movement of particles in relation to the thermal energy of the system. The displacement of particles is related to the diffusion coefficient ($\boldsymbol{D_c}$), calculated from the system thermal energy and the Stokes' drag of the particles, by the Stokes-Einstein equation:

$$\boldsymbol{D_c} = \frac{\boldsymbol{k_B T}}{\boldsymbol{6\pi\eta r}} \qquad (3.2)$$

where $\boldsymbol{k_B}$ is the Boltzmann constant, $\boldsymbol{T}$ is the absolute temperature and $\boldsymbol{r}$ is the particle radius.

3.1.3 Red Blood Cells and Blood Flow

The blood contains a high density of blood cells and cell fragments, including RBCs, white blood cells and platelets. RBCs are the most numerate blood cell, constituting 38-46% of the volume of blood, a measure referred to as the haematocrit. White blood cells make up about 1% of blood volume and platelets <0.5% of blood volume. In capillaries, the haematocrit is reduced to 10-12%, reflecting the hydrostatic pressure (McWhirter et al., 2011). In its resting form, the RBC is a biconcave disk measuring ~7.8 µm in diameter, comparable to the size of capillaries. However, RBCs deform under shear stress into numerous conformations favourable for reduced resistance to flow

in restricted geometries (Skalak and Branemar.Pi, 1969, McWhirter et al., 2009). The presence of RBCs creates complications in obtaining accurate solutions to the Navier-Stokes equations. RBCs confer non-Newtonian properties to the fluid. This means that the viscosity will alter under shear stress in a non-predictable way. This can be explained by the dependence of viscosity on shear-rate, haematocrit, RBC conformation, RBC aggregation and plasma viscosity (Schmid-Schönbein et al., 1969, Wells and Merrill, 1962). These properties are also simultaneously related to the viscosity, therefore making complete solutions very difficult to obtain.

3.1.4 Transport at the Vessel Wall

At the vessel surface, nanoparticles can interact and traverse the endothelial layer in numerous ways. In many tissues, pores, called fenestrations, punctuate the microvasculature, which allows free exchange of many substrates. The structure, size and density of fenestrae differ from tissue to tissue depending on the function of the tissue itself. In early electron microscopy studies it was demonstrated that in the fenestrated endothelium of the pancreas, intestinal mucosa and kidneys, fenestrations were ~60 nm in diameter (Milici et al., 1985). Furthermore, these fenestrations can be considerably larger in vessels supplying tumours, with fenestrations reported from 200-1200 nm in size (Hobbs et al., 1998) (Alexis et al., 2008). However, in other tissues including at the blood-brain barrier, the vasculature is characterised by the lack of fenestrations (Abbott et al., 2010). The endothelial cells themselves can also regulate the exchange of numerous substrates between blood and tissue by receptor-mediated transport mechanisms and cellular trafficking.

3.2 AIMS AND OBJECTIVES

The aim of the work presented in this chapter was to implement an agent-based model, using FLAME, of blood flow within a capillary encompassing thermal fluctuations. The design of this model must be able to take advantage

of FLAME's intrinsic parallelisation optimisation to allow flexible addition and removal of specific functions in order to answer specific research questions, on top of the core blood flow functions. It is hypothesised that through the use of this model a further understanding of the fundamental role of capillary blood flow in distribution and uptake of nanoparticles can be gained. This model can then later be used to answer specific research questions related to nanoparticle transport at the blood-brain barrier.

3.3 RESULTS AND DISCUSSION

3.3.1 Building an Agent-based Model of Blood Flow

Agent-based modelling has previously proven to be a powerful tool for predictive biological modelling. Its integration with more classic CFD approaches allows great potential for testing the blood flow dependent behaviour of nanoparticles. Blood flow dynamics in capillaries is integral for distribution and subsequent uptake of blood-borne molecules. It was aimed to create a simple core model that simulates blood flow with the intention of studying a variety of other processes, including but not limited to, nanoparticle distribution studies, receptor binding dynamics, the effect of ligand density, and cellular trafficking, plus the effect of varying flow conditions on all of the aforementioned (*Chapters 4 and 5*). A summary of this is provided in the schematic in *Figure 3.2.* In this work, it was decided to use FLAME as the agent-based modelling platform. This was because of the ease of FLAME's scalability onto high performance computing systems. This is due to a number of factors, discussed in detail in Chapter 1, in summary the programming in C that is ideal for high performance computing architectures. Furthermore, the lack of required MPI coding from user allows increasing accessibility of the model to less specialised programmers. Finally, FLAME's ability to add and remove functions with ease to a core model with inherent speed up capabilities is a useful feature for the modelling work required in the whole of this thesis.

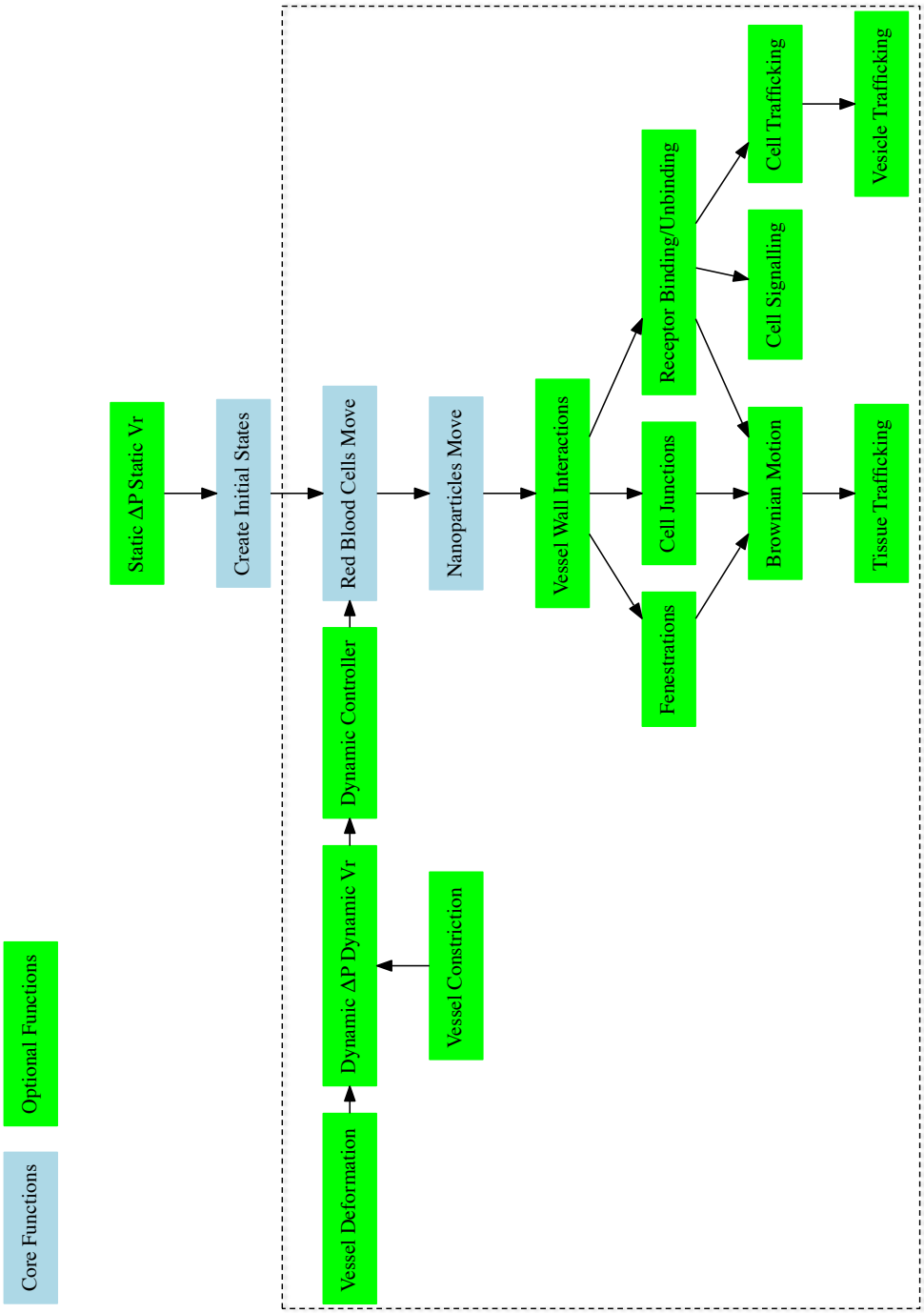

Figure 3.2: Flow Diagram of Model Functions. The flow diagram demonstrates the progression of functions in the model. Core functions that are conserved in all variations of the model are shown in blue, whilst optional functions that can be included in the model, at the user's discretion, are shown in green. The optional functions can be added in a variety of combinations into the core model, to allow flexibility in modelling approach to reflect the experimental question. The functions within the dashed box are performed iteratively, where a single iteration is equivalent to the discrete passage of a set time-step δt.

In the microvasculature, where RBC and capillary diameter are comparable, RBCs severely influence the fluid dynamics of blood flow. White blood cells and platelets are also present in the microvasculature; however, the reduced number of both cells compared to RBCs and the small size of platelets limits the influence of these cells. Therefore, this model concentrates on RBCs as the major driver of fluid dynamical changes in the microvasculature. Whilst inclusion of RBCs is important to flow modelling, direct modelling of RBC behaviours, such as deformation and aggregation, has been largely omitted. Previous studies have utilised several techniques, most notably immersed finite element methods, to incorporate RBC deformation and RBC interactions within flow models (Zhang et al., 2008a, Kaoui et al., 2009, Fedosov et al., 2014). Although a similar approach could be utilised within the model described, the additional computational burden required would limit the capabilities of the model to include much of the desired additional functionality. In these theoretical studies and experimental observations, a number of RBC conformations have been described, including, the slipper-like, the parachute, bullet-like and disk conformations. A number of these papers also produced phase-diagrams relating the conformation to other properties of the flow, such as shear stress, confinement and haematocrit (Fedosov et al., 2014, Kaoui et al., 2009). The slipper phase, according to the work of Fedosov and colleagues, occurs when both shear rates and confinement are low, however the shear rates and confinement parameters of these simulations favour the parachute conformation. Therefore the parachute conformation was adopted in consequent simulations.

Several studies have demonstrated that both specific and non-specific interaction with proteins can affect the nanoparticle residency in the blood (Cedervall et al., 2007, Lundqvist et al., 2008). Protein interactions are dictated by the surface chemistry and charge. A common solution to this is to use a coating that reduces protein adsorption such as PEG or similar (Vittaz et al., 1996). This generally improves the systemic half-life and reduces immune cell interaction properties, thus increasing the potential therapeutic load at target tissues (Otsuka et al., 2003, Owens and Peppas, 2006).

However, as discussed in *Chapter 1*, PEGylation is unable to completely prevent protein absorption leading to potential alterations in nanoparticle properties, including size, surface charge and immunogenicity. Furthermore, other factors such as PEG length and nanoparticle shape are also important in protein absorption to nanoparticles. However for simplicity, in subsequent simulations it is assumed that nanoparticles will be inert. In previous studies, it has been demonstrated that certain compositions of nanoparticles can interact with both themselves and RBCs, with varying effects on distribution and cellular interactions (Chambers and Mitragotri, 2007). However, these properties are likely to be individual to the nanoparticle formulation used and therefore have been omitted from the model, except for a simple rule that neither can occupy the same space. However, specific interactions are easily implementable within the model at a later stage if appropriate.

The laminar flow was evaluated by the Garlerkin/Least Squares FEM, using RBCs as moving boundaries at a rate of 60 $\mu m.s^{-1}$. A diagrammatic summary of the model built is provided in *Figure 3.3*. A table of variables for the model is included in *Table 3.1*.

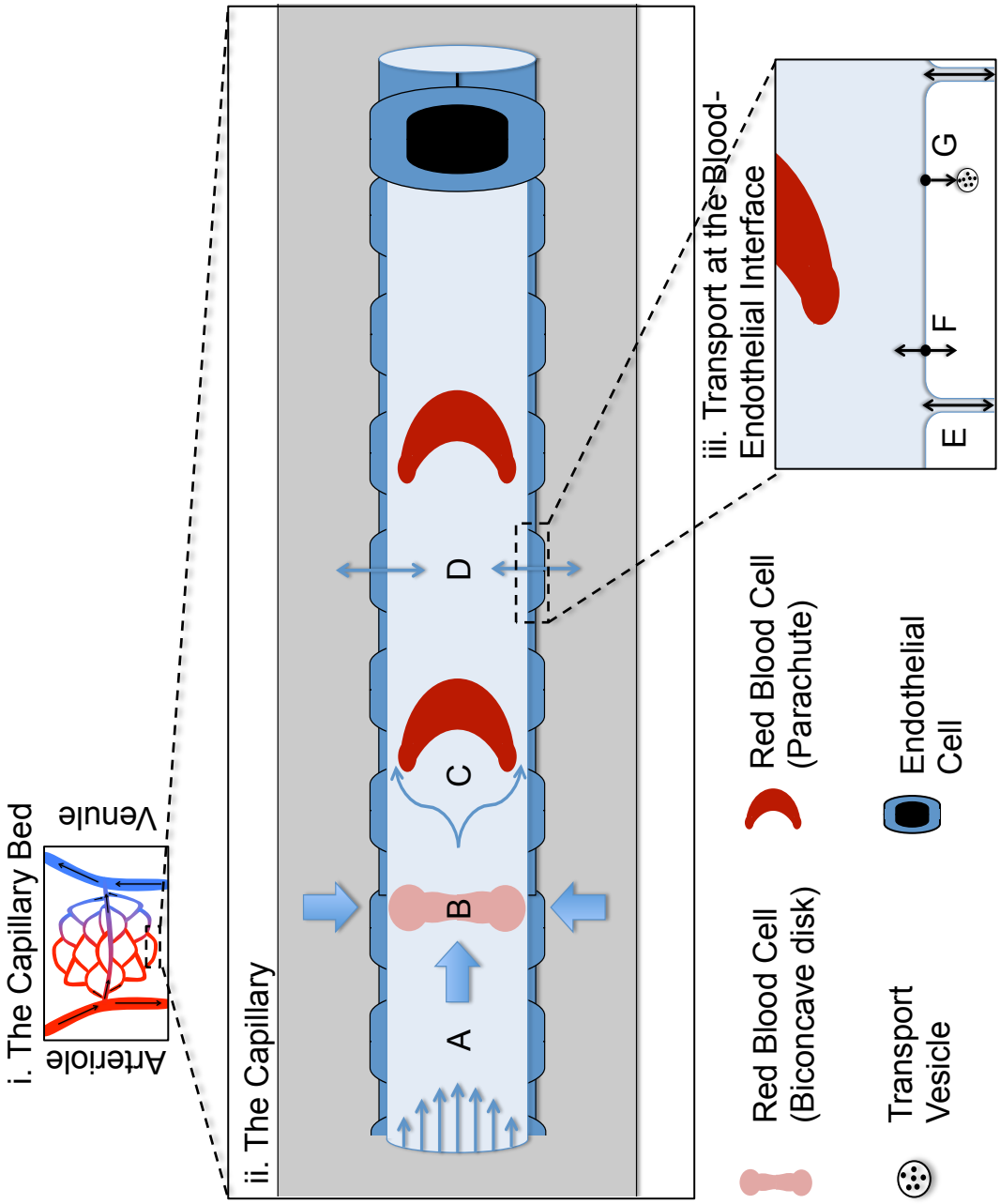

Figure 3.3: Model Summary Schematic. The model focuses on a single capillary (ii) taken from the capillary bed (i). The model includes the effect of laminar flow (A) on RBCs in their native biconcave disk shape (B), causing the deformation of RBCs into a parachute conformation (C). This subsequently affects distribution and fluid dynamics of particles in the fluid-phase of the blood, which will in turn affect interactions at the vessel wall (D). At the interface of blood and vessel wall (iii), particles proximal to the vessel wall can pass through cellular junctions between cells or fenestrations, if present, within cells and therefore freely exchange with the interstitial fluid according to the diffusion gradient (E). Particles may bind corresponding proximal receptors on the endothelial cells (F), they may then be released or internalised and subjected to various cellular trafficking systems (G).

Variable	Description	Symbol	Typical Value
Vessel Radius	Radius of the Capillary	V_r	4 µm
Vessel Length	Length of the Capillary	V_l	800 µm
RBC Radius	Radius of RBC	RBC_r	3.9 µm
RBC Width	Width of RBC	RBC_w	2.5 µm
Haematocrit	% RBCs/Blood (v/v)	$H_{\%}$	10-12 %
RBC Number	Number of RBC Agents to Reflect Haematocrit	RBC_n	
Nanoparticle Radius	Radius of Nanoparticle	r	10-200 nm
Arteriole Pressure	Pressure at Arteriole End of Capillary	p_a	1500-3000 Pa
Venule Pressure	Pressure at Venule End of Capillary	p_v	1000 Pa
Pressure Difference	Pressure difference from arteriole to venule end of the capillary	p_Δ	500-2000Pa
Dynamic Viscosity		η	See *Figure 3.10*
Temperature	Absolute Temperature	T	310 K
Boltzmann Constant		k_B	$1.381E^{-23}$ m^2 kg s^{-2} K^{-1}
Cartesian Coordinates		x, y, z	
Time Step	Time step per iteration	Δt	0.0001 (laminar) and 0.000001 (Brownian motion)
Velocity	Absolute velocity [in x y z]	v $[v_x, v_y, v_z]$	
Density	Density of Fluid	ρ	1060 kg m^{-3}
Stress Sensor	Shear Stress	τ	
Force	Force [Laminar, Brownian]	$F[F_L, F_B]$	
Dispersion Factor	Dispersion Factor, Average Dispersion Factor	$\vartheta_D, \overline{\vartheta_D}$	0 to 1
Element Number	Number of Elements for Finite Element Method	E_n	
Mass	Nanoparticle Mass	m	
Diffusion Coefficient		D_c	

Table 3.1: Names, Denotations and Typical Values of Key Values with the Model. Typical values are given, where appropriate, from information available in the literature.

3.3.2 Agent-based Modelling of Brownian Motion

Flow in capillaries is influenced by both laminar forces and thermal fluctuations referred to as Brownian motion. In order to create a model of the random walk characteristic of Brownian motion, the methods described by Andrews and Bray were used (Andrews and Bray, 2004). These methods utilise the diffusion coefficient of a particle to generate a Gaussian curve that describes the probability of a particle displacing a certain distance in a single plane in a discrete time step. The random walk in 1D can be achieved by generating random numbers that fit to the given Gaussian using the polar form of the Box-Muller transformation (Box and Muller, 1958, Knop, 1969). Repeating this for the extra dimensions can create 2D and 3D random walks (More details of this are included within *Chapter 2.*). To validate this method, 1000 random numbers that fit a Gaussian of mean 0 and standard deviation 1 were generated using the polar form of the Box-Muller transformation. This was used to generate the observed frequency of number ranges and plotted against the expected Gaussian, as seen in *Figure 3.4*. This demonstrated that this implementation of the polar form of the Box-Muller gave a highly significant agreement with the expected Gaussian, with a calculated Pearson's correlation coefficient (r_P) of 0.9998 and a P value of <0.0001.

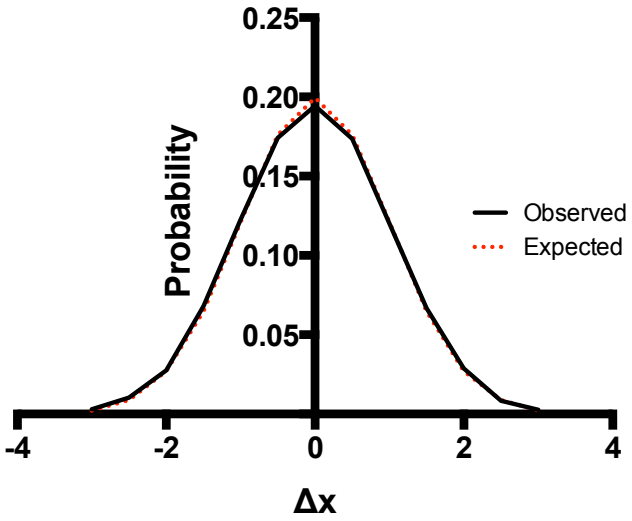

Figure 3.4: Testing the Implementation of the Polar Box-Muller Transformation. The frequency probabilities of the expected Gaussian curve of mean 0 and standard deviation 1 and that observed from the given implementation of the polar Box-Muller transformation.

This demonstrated that the Box-Muller transformation implementation could then be used to generate random normally distributed numbers for simulation of the random walk. To confirm that this method was suitable, the mean squared displacement (MSD) of particles over time ($\boldsymbol{t}$) was calculated using the equation:

$$\boldsymbol{MSD(t) = \langle q(t) - q(0) \rangle^2} \quad (3.3)$$

where $\boldsymbol{q(t)}$ is the position of the particle at time $\boldsymbol{t}$ and $\boldsymbol{q(0)}$ is the position of the particle at time 0. The MSD is related to the diffusion coefficient through the relationship:

$$\boldsymbol{MSD = kD_c} \quad (3.4)$$

where $\boldsymbol{k}$ is a constant of dimensionality of 2 for 1D, 4 for 2D or 6 for 3D. Therefore the calculated MSD can be compared to the expected displacement based on the particles diffusion coefficient, as demonstrated in *Figure 3.5*.

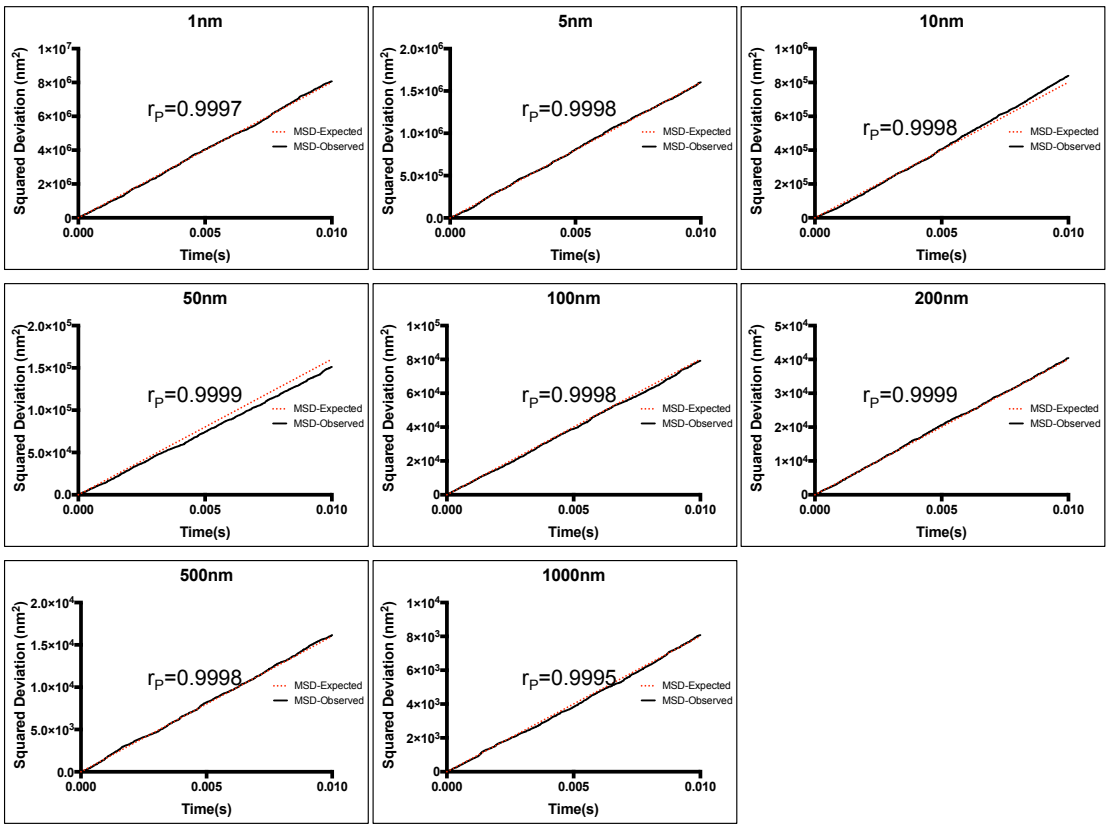

Figure 3.5: Validation of the Random Walk in 3D. The mean squared deviation of simulated particles of different diameters, compared to the expected mean squared deviation from the diffusion coefficient. All samples are significant as tested by the Pearson's rank correlation coefficient; the coefficient for each size is indicated (rP).

Figure 3.5 demonstrates that, for all sized particles tested, an excellent correlation is apparent between expected and observed mean squared deviations with correlation coefficients of all >0.9995 and P values < 0.0001. Furthermore, to demonstrate that the simulation of the random walk produced by the model is reflective of that of actual nanoparticles, particle traces were compared with those from similarly sized nanoparticles from Nanosight® tracking analysis, provided by Anna Puiggalí Jou (*Figure 3.6*).

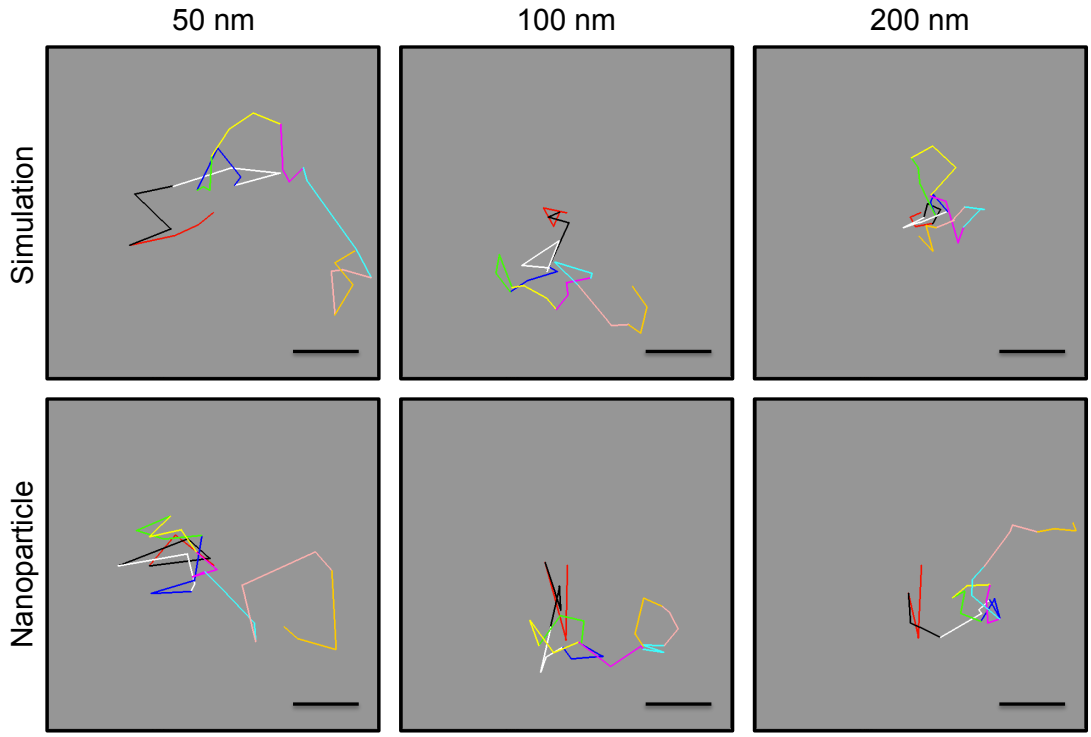

Figure 3.6: Nanoparticle Traces of Simulated Nanoparticle and Tracked Nanoparticle Motion. Comparison of simulated nanoparticles of different diameters with equivalent sized nanoparticles tracking using Nanosight Tracking Analysis. Scale bar=2 µm, $\boldsymbol{t}$=1.17 s, $\boldsymbol{\Delta t}$=0.039 s, $\boldsymbol{\eta}$=0.00069 Pa. s, $\boldsymbol{T}$=310 K.

Figure 3.6 demonstrates a good concordance of traces from the nanosight tracking analysis with the simulations of the random walk. Generally the distance travelled in each time step and across the whole time period gets shorter as particle size increases, due to the increased Stokes' resistance of the larger particles. The direction of each step is random in both the simulations and the tracking analysis, demonstrating that this method can be used for simulating the random walk.

3.3.3 Parallelisation of the Capillary Blood Flow Model

In order to test the parallelisation of the capillary model built using FLAME, a number of test simulations were run across different numbers of cores on the White Rose Grid Iceberg High Performance Computing Cluster at the University of Sheffield. Iceberg was chosen due to the ease of access, its use in developing FLAME and the extensive previous use of FLAME applications

on Iceberg (Kiran et al., 2011). It should be noted, however, that FLAME has also been tested on a large number of other architectures including SCARF, HAPU, NW-Grid, HPCx and bglogin2 (Chin et al., 2012). The runtimes were plotted in *Figure 3.7A* and demonstrates that the speed up is good up until 8-12 cores, thereafter the simulation time plateaus. Moreover, whilst the core hours used is efficient with a small number of cores (up to 16), thereafter the number of core hours used rises steadily until it is using 4.4-times the number of core hours for 16 cores and 5.7-times the number of core hours for 32 cores (*Figure 3.7B*). Therefore, all simulations were run across eight cores hereafter to obtain the lowest simulation time using the least computational resources. Furthermore, the use of 8 cores compared to ≥10 cores also reduced queuing time through the Son of Grid Engine queue system employed on Iceberg.

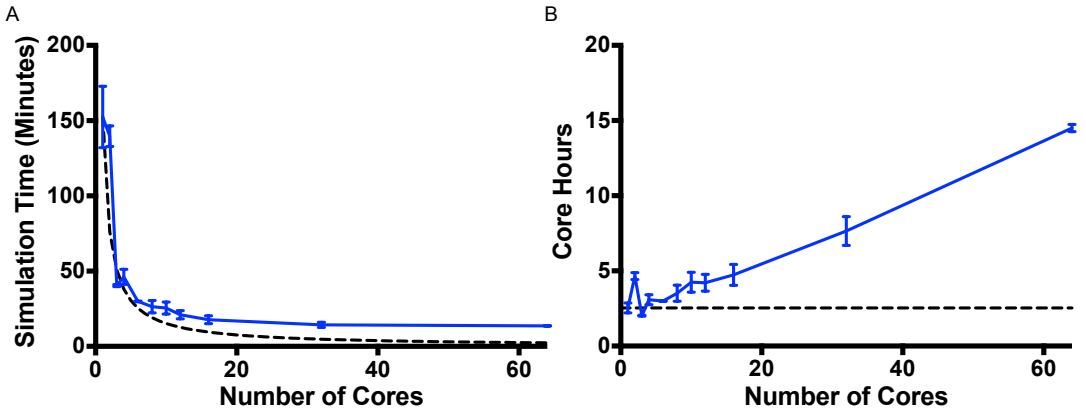

Figure 3.7: Parallelisation of the Capillary Blood Flow Model. The runtime of simulations (A) and the core hours (B) against the number of cores are plotted in blue (solid). The hypothetical runtime (A) and core hours (B) of simulations with maximum speed up is demonstrated in black (dashed). Each data point represents the mean ± standard deviation of three simulations (n=3).

3.3.4 Brownian Forces become the Dominant Force at the Vessel Wall Interface

To validate the correct operation of the finite element method used, heat maps were produced of flow velocity in longitudinal (*Figure 3.8A*) and latitudinal (*Figure 3.8B* and *3.8C*) vessel slices at a physiologically relevant haematocrit of 10.7% (McWhirter et al., 2011). The heat maps demonstrate a clear relationship between proximity to the vessel wall and a decrease in flow velocity (*Figure 3.8B*). In regions containing RBCs, flow velocity is increased around the cells as they move at slower rates than the fluid phase (*Figure 3.8C*).

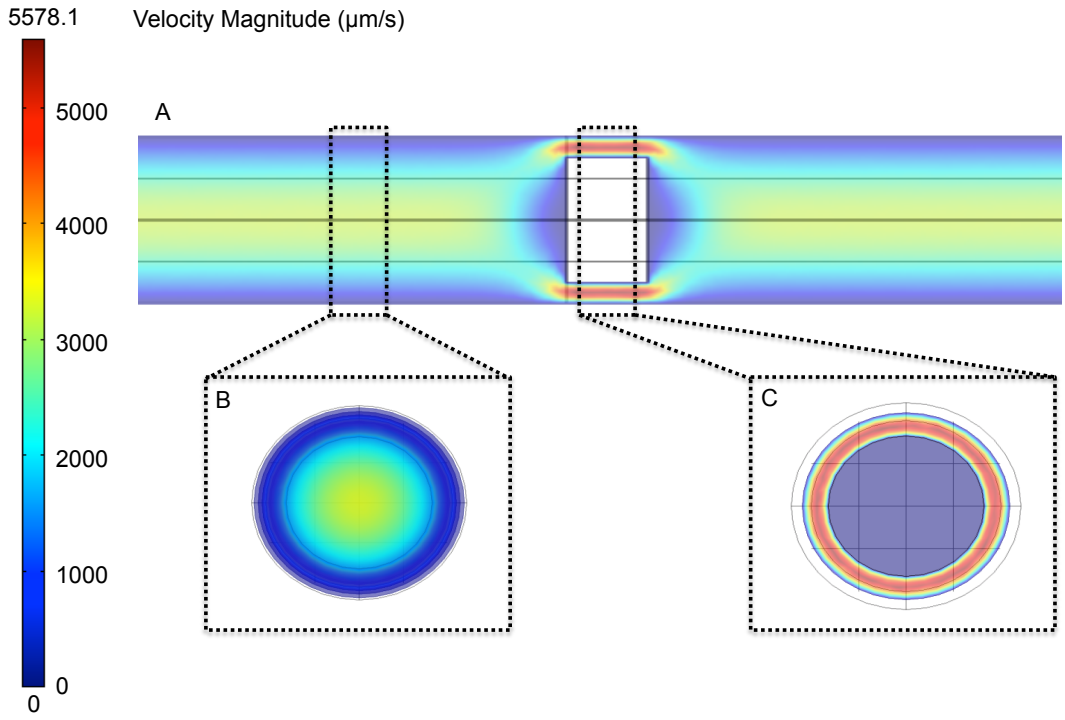

Figure 3.8: Heat Mapping of Laminar Forces. Longitudinal cross-section (A) demonstrating velocity of blood flow along the vessel, with latitudinal cross-sections proximal to the red blood (B) cell and distal to the RBC (C).

Next, a comparison of the various influences of Brownian motion and laminar flow on final nanoparticle movement was made in different regions of the vessel. Typical nanoparticle traces for Brownian motion (*Figure 3.9A* and *3.9B*) alone, laminar flow alone (*Figure 3.9C* and *3.9D*) and laminar flow with

Brownian motion (*Figure 3.9E-H*) are shown for a 100 nm nanoparticle at the centre of the vessel and the edge of the vessel. At the centre of the vessel, laminar forces are expected to be high ($v = 5500\ \mu m\ s^{-1}$) as it is furthest away from the non-slip boundary. The relative impact of Brownian forces (*Figure 3.9A*) is therefore consequently very small, relative to the laminar forces (*Figure 3.9C*), leading to only minor fluctuations from laminar flow (*Figure 3.9E* and *3.9G*). However at the vessel wall (*Figure 3.9D*), the flow velocity is vastly reduced ($v = 440\ \mu m\ s^{-1}$), thus making Brownian forces more significant to the displacement of the particle (*Figure 3.9B, 3.9F* and *3.9H*). This is summarised by the relative contributions of Brownian and laminar forces to the total MSD of nanoparticles at low and high shear flow (*Figure 3.9I*). At low laminar forces, Brownian forces contribute almost equally to laminar forces in the displacement of the particle, where as the relative contribution of Brownian forces at high laminar forces is negligible. The dominance of Brownian forces and reduction in laminar forces allows maximum contact time between potential substrates and the vessel wall interface. It also allows nanoparticles proximal to the vessel wall but not within binding range to diffuse closer to the vessel wall, thereby permitting binding. Although not included in the current model, the significance of Brownian forces at the vessel wall is likely to be further increased by the presence of a gel-like layer at the cell wall called the glycocalyx. This layer consists of glycosylated proteins (glycoproteins) and lipids (glycolipids) that can project 200-500 nm within the vessel. It can also regulate accessibility of various blood components to the wall based on particle properties such as charge and size (van den Berg et al., 2003).

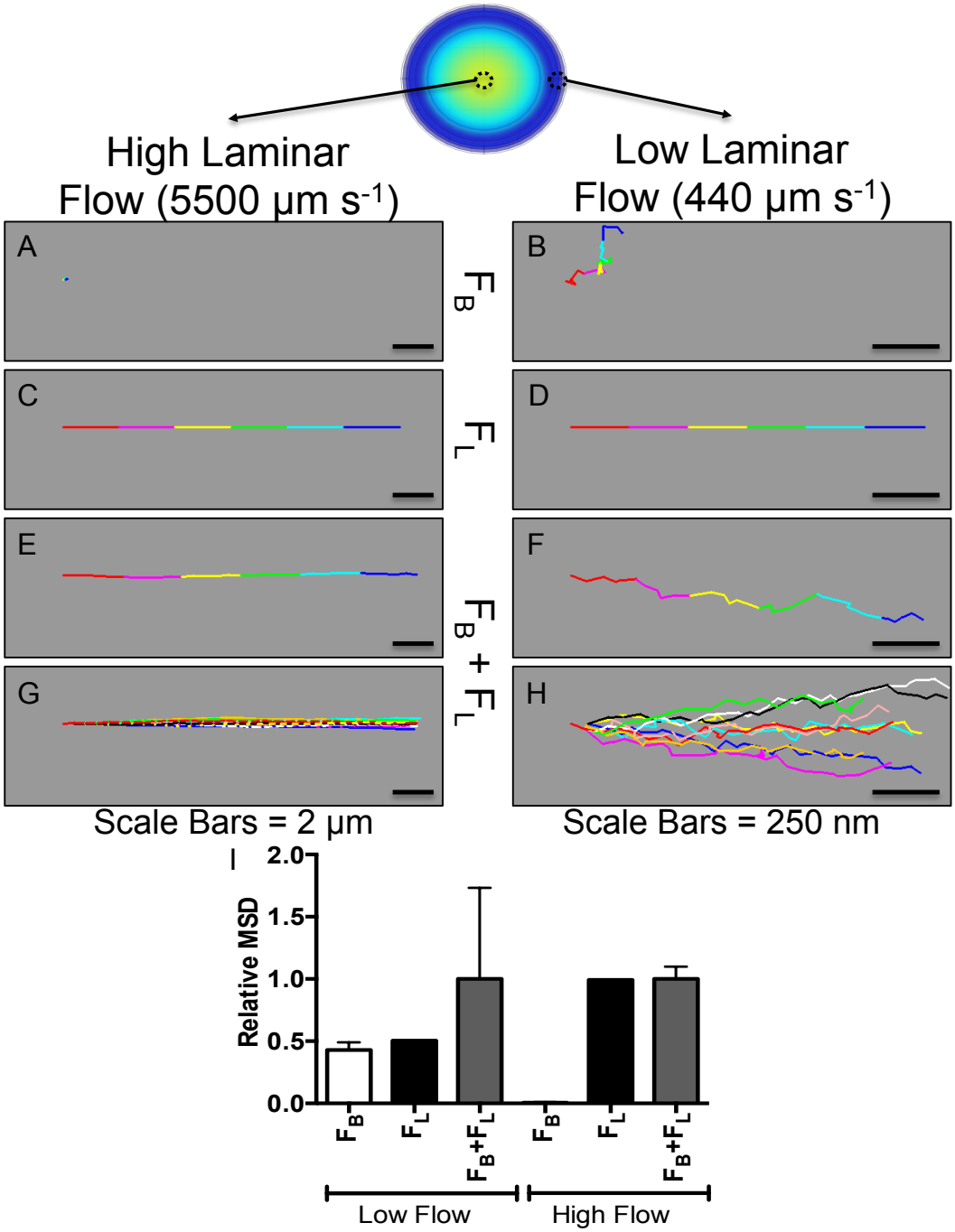

Figure 3.9: Balance of Brownian to Laminar Forces. 100 nm nanoparticle traces under only Brownian motion (A and B), only laminar flow (C and D) and both Brownian and laminar forces (E and F [single nanoparticle], G and H [ten nanoparticles]) at the edge (B, D, F and H) and centre (A, C, E and G) of the vessel. The relative contribution of laminar (FL) and Brownian (FB) forces to the mean squared displacement at low laminar and high laminar force is demonstrated (I). (Time = 0.003 s, Δt = 0.0001 s). Each data point represents the mean ± standard deviation of 10 simulations (n=10).

3.3.5 Red Blood Cells enhance Nanoparticle Dispersion

In order to see the effect that RBCs have on flow dynamics and subsequent nanoparticle dispersion, the behaviour of nanoparticles at varying haematocrits was studied. State and process order graphs, produced by FLAME, for the parallel execution of these simulations are provided in *Figure 3.10*.

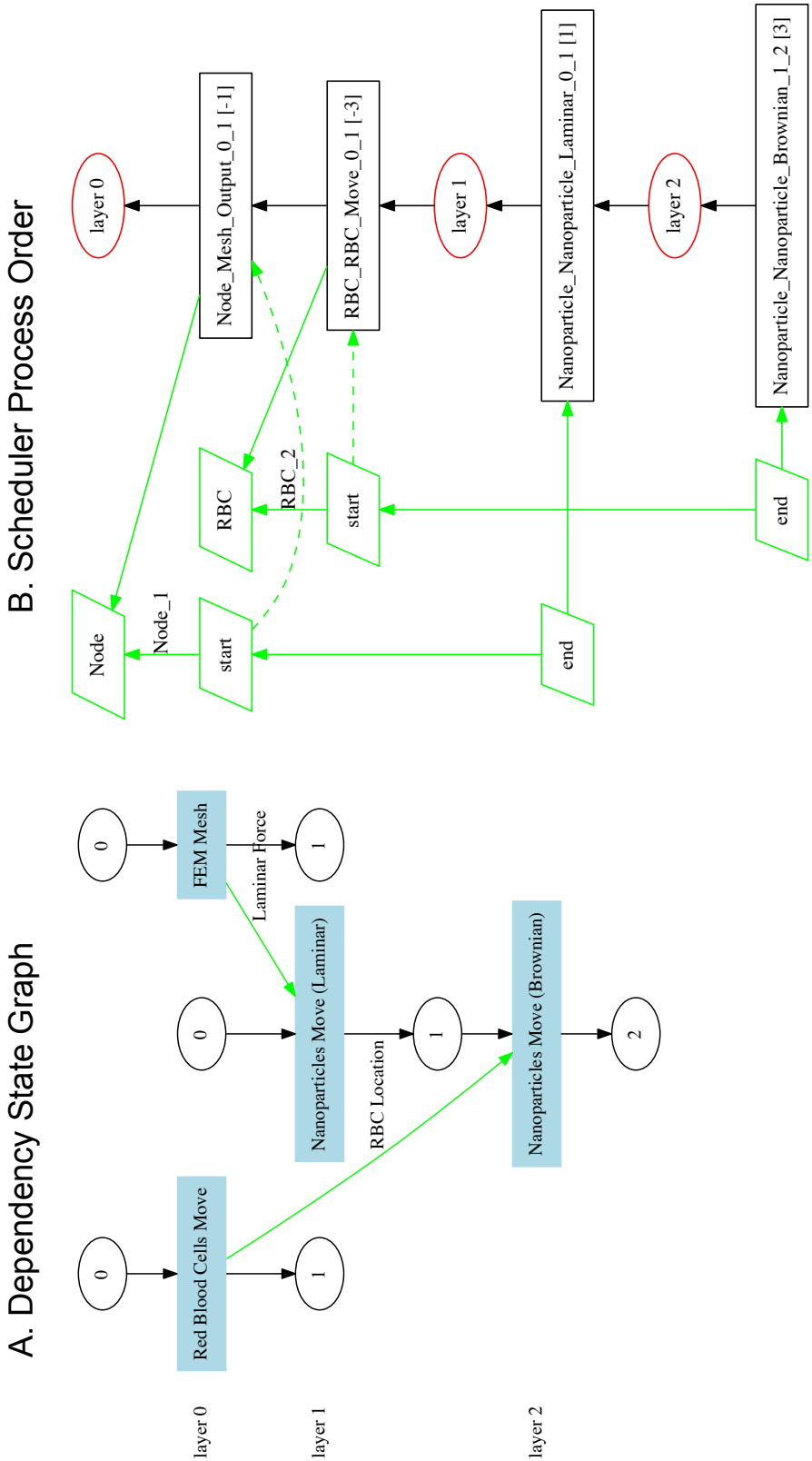

Figure 3.10: FLAME State and Process Order Graphs of the Core Model. The state graph (A) demonstrates the dependency of functions on both previous functions and messages for parallelisation of the core model. The process order graph (B) shows the order in which FLAME prioritises the functions to reduce the lag from using the message passing interface.

The haematocrit range used was from acellular (0%) to whole blood (45%), including a high density of simulations at the physiologically relevant range for a capillary (10-12%). The viscosity used in resolving the Navier-Stokes equations was related to the haematocrit in order to account for the non-linear increase in viscosity usually observed with higher haematocrit (*Figure 3.11*).

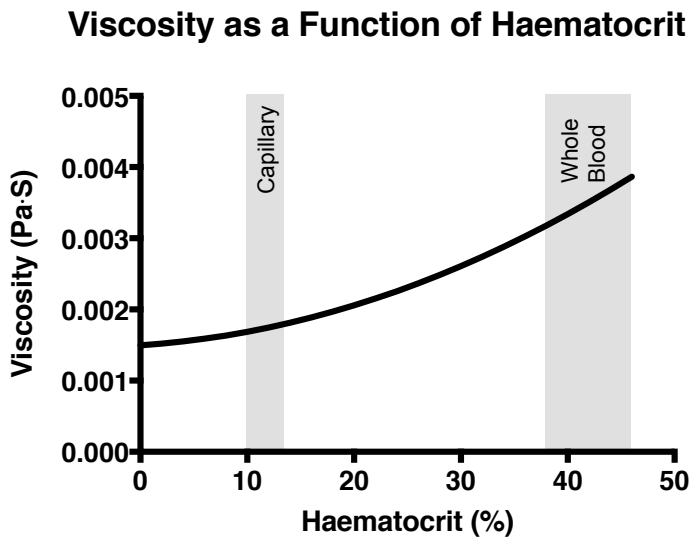

Figure 3.11: The Relationship between Haematocrit and Viscosity. The viscosity used in the models is given by a relationship between haematocrit and viscosity. Capillary and whole blood haematocrits are indicated.

Figure 3.12A shows the average position of a nanoparticle relative to the centre of a 4000 nm vessel, as a function of haematocrit. At haematocrits of 0%, an even dispersion of nanoparticles would be expected, giving a theoretical average of ~2700-2800 nm with a nanoparticle diameter of 100 nm. However, it would be expected that this value would increase due to volume exclusion with increasing number of RBCs located towards the centre of the vessel, as observed in *Figure 3.12A*. Furthermore, to correlate this with likelihood of increased delivery, the percentage of all nanoparticles that would be within a binding range of the vessel wall (*Figure 3.12B*), given as 20 nm from the proximal edge of the nanoparticle to the vessel wall, was quantified. A marked increase is observed with increasing haematocrit, particularly

across the physiologically relevant range, further demonstrating that RBCs aid the dispersion of nanoparticles to the vessel wall.

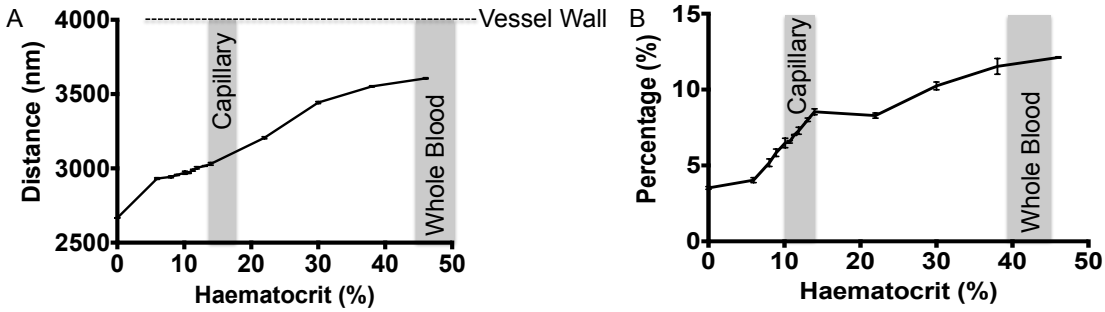

Figure 3.12: The Effect of Haematocrit on Nanoparticle Distribution. The increased dispersion of nanoparticles to the vessel edge as a function of increasing haematocrit is demonstrated by, the average distance from the centre of a 4000nm in radius capillary (A) and percentage of nanoparticles within 20 nm of the vessel wall (B). Capillary and whole blood haematocrit ranges are indicated. Each data point represents the mean ± standard deviation of three simulations (n=3).

The increase in haematocrit also had an effect on the average velocity of nanoparticles across the whole vessel (*Figure 3.13A*) and for nanoparticles within 20 nm of the vessel wall (*Figure 3.13B*). It can be expected that this would influence both the motion of particles at the vessel wall, as it alters the laminar-Brownian force ratio, and their subsequent transport at the vessel surface, due to increased wall shear stress.

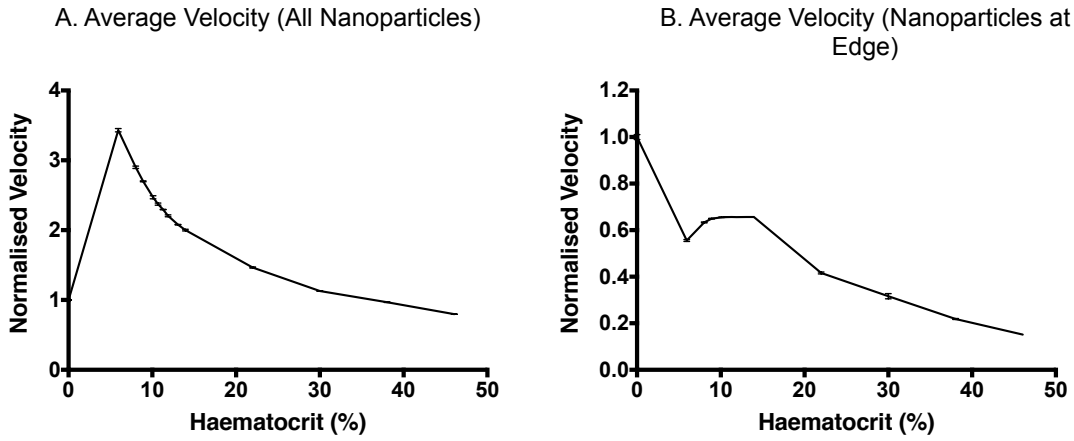

Figure 3.13: The Effect of Haematocrit on Nanoparticle Velocity. The average velocity of, all nanoparticles within the vessel (A) and only nanoparticles within 20 nm of the vessel wall (B), as a function of haematocrit. Mean ± standard deviation, n=3.

Similar conclusions, demonstrating improved nanoparticle distribution with higher haematocrit, were made by Tan and colleagues using both simulations and microfluidics as a method of validation (Tan et al., 2012). Whilst their conclusions are similar, they focus on scenarios in the presence or absence of RBCs, using a haematocrit of 38% (*in silico*) and 36% (microfludic experiments), which is considerably higher than the 10-12% expected in capillaries. Therefore, it is unclear from this work whether this observation would be as significant in more physiological conditions. Furthermore, the vessels used in their study were bigger than that described here (20 µm and 11 µm compared to 8 µm), making immediate comparison of data difficult.

To further study the flow dynamics with differing haematocrits, an average dispersion factor was calculated for vessels with varying haematocrit. The dispersion factor is the ratio between radial velocity (towards the vessel edge) and the longitudinal velocity (towards the end of the vessel) at a given element, with the radial velocity ($\boldsymbol{V_r}$) being:

$$\boldsymbol{V_r} = \sqrt{\boldsymbol{V_x}^2 + \boldsymbol{V_y}^2} \qquad (3.5)$$

where $\boldsymbol{V_x}$ is the velocity in the x-direction, $\boldsymbol{V_y}$ is the velocity in the y-direction. The Dispersion Factor ($\boldsymbol{\vartheta_D}$) can be thus defined as:

$$\boldsymbol{\vartheta_D} = \frac{\boldsymbol{V_r}}{\boldsymbol{V_z}} \qquad (3.6)$$

where $\boldsymbol{V_z}$ is the velocity in the z-direction, similarly the average dispersion factor ($\overline{\boldsymbol{\vartheta_D}}$) can be given as:

$$\overline{\boldsymbol{\vartheta_D}} = \frac{\sum \boldsymbol{\vartheta_D}}{\boldsymbol{E_n}} \qquad (3.7)$$

where $\boldsymbol{E_n}$ is the number of elements.

A dispersion factor of 0 would indicate that flow is parallel to the vessel wall, giving no dispersion, whereas, any increase in dispersion factor would show the presence of trajectories away from parallel to the vessel wall. *Figure 3.14* demonstrates an initial increase in the average dispersion factor as a function of haematocrit. However, above haematocrits of 20-25%, this then falls and tends back towards 0. This would indicate that an intermediate range of haematocrit could be better for allowing maximum dispersion of nanoparticles towards the edge of the vessel.

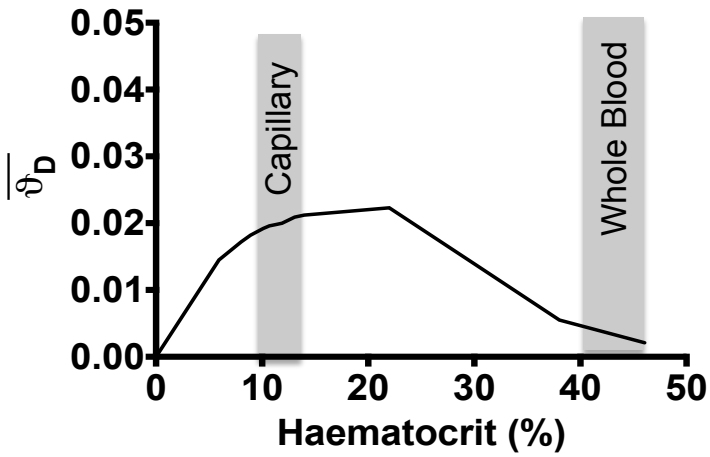

Figure 3.14: The Effect of Haematocrit on Dispersion. The average dispersion factor is shown as a function of increasing haematocrit. Capillary and whole blood haematocrit ranges are indicated. Each data point represents the average dispersion factor calculated from a single Comsol simulation (n=1).

To understand why the average dispersion factor shows increased dispersion from lower haematocrits to higher, further observation of flow dynamics was performed using heat mapping of the dispersion factor at individual elements. *Figures 3.15A, 3.15B* and *3.15C* are schematics of the three dominant flow streamlines observed throughout the simulations imposed on heat maps of the velocity in the y-axis (perpendicular to the vessel). In *Figure 3.15A*, in the absence of RBCs, flow can be considered to be a Poiseuille's flow and will result in an expected and observed average dispersion factor of 0. *Figure 3.15B* demonstrates that flow, in the presence of an intermediate haematocrit, will manoeuvre around the RBCs and will lead to the observed increase in average dispersion factor. However, at higher haematocrits, the space between RBCs is significantly reduced, and as such, two separate phases are formed (*Figure 3.15C*). A cellular-phase is formed where, due to the reduced space between RBCs, flow between RBCs occurs at the same velocity as that of the RBCs. A separate cell-free phase is created at the edge of the vessel; the flow of this phase occurs such that the cellular-phase resembles flow past a cylinder moving at a rate equal to the RBC velocity. Interaction between the two phases becomes minimal as the space between RBCs is reduced, consequently resulting in the decline of average dispersion factor observed

with increasing haematocrit above 20-25% in *Figure 3.14*. A similar but less defined pattern in flow is also apparent in the work of Tan and co-workers and McWhirter and colleagues (Tan et al., 2012, McWhirter et al., 2009).

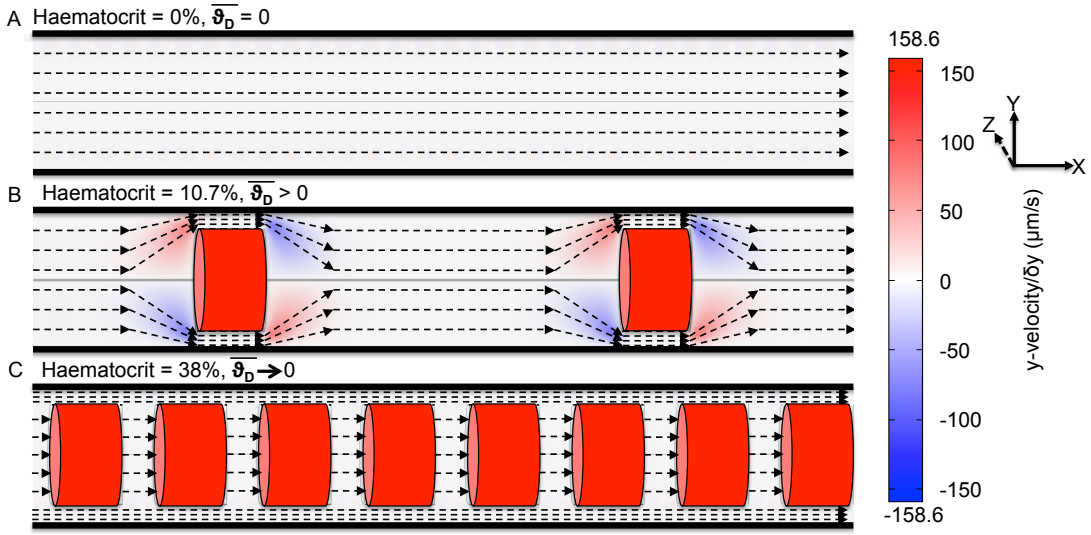

Figure 3.15: The Effect of Haematocrit on Fluid Dynamics in a Capillary. Streamlines of different types of flow observed and heat maps of the velocity in the y-plane are shown with respect to haematocrit, at no haematocrit ($H_{\%} = 0$) a one phase Poiseuille's flow (A), at 10.7% representative of intermediate haematocrits ($0 < H_{\%} < 20$) an interacting flow between cellular and cell-free layers (B) and at a haematocrit of 38% representative of high haematocrits ($H_{\%} > 20$) separate cellular and cell-free layers (C).

The consequence of a low average dispersion factor is that only nanoparticles already proximal to the vessel edge can be transported across the vessel wall. However with higher average dispersion factors, nanoparticles at the centre of the vessel will be transiently dispersed from the centre to the vessel edge and *vice versa* with flow. This permits a greater number of nanoparticles the opportunity to be transported at the vessel wall.

The effect of haematocrit on uptake from the blood hasn't been studied directly *in vivo*. However, in perfusion studies of the rat liver with different haematocrits both oxygen uptake and galactose elimination were reduced (Keiding et al., 1980). Though the reduction in the uptake of oxygen could be expected given the role of red blood cells in oxygen transport, the reduction in

galactose elimination may suggest that with reduced haematocrit there is reduced uptake of galactose from the blood, in line with the results of our simulations. However, it is important to note that as oxygen is important in metabolism, the galactose elimination reduction could be a secondary effect of the reduced oxygen uptake.

3.3.6 Nanoparticle Size Selectively Targets Delivery to Tumour Tissues

In order to demonstrate the flexibility and efficacy of the model in aiding the design of nanoparticles, the ability to increase specificity of nanoparticles for tumours was tested. A key factor in nanoparticle efficacy is their ability to selectively target the tissue of interest, whilst avoiding potential off-target effects at other tissues. The design of these simulations was to test the ability of different sized nanoparticles to traverse fenestrations with pore size corresponding to both normal vessels and tumour vessels. In line with the work of Milici and co-workers, a fenestration size of 60 nm for normal tissue was used and a relatively conservative size of 240 nm was used for tumours, in line with the values reported by Hobbs and colleagues (*Figure 3.16*) (Hobbs et al., 1998, Milici et al., 1985). It should be noted that tumour fenestrations can be considerably larger than that used in these simulations, however due to the heterogeneous nature of tumour fenestrations it was believed prudent to use a fenestration size towards the lower end of the range reported for this proof-of-principle study. In future work, use of more exact ranges for particular tumour types and the ability to account for heterogeneity in fenestration size could be included within the model.

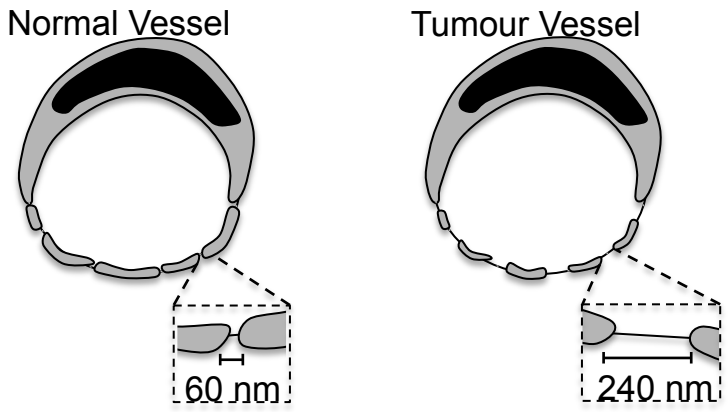

Figure 3.16: Morphology of Fenestrations in Normal and Tumour Vessels.

The core model described previously was utilised using a haematocrit of 10.7%, with the inclusion of a fenestration agent and function to add fenestrations to the vessel wall. The relevant state and process order graphs, generated by FLAME, for this model can be seen in *Figure 3.17*.

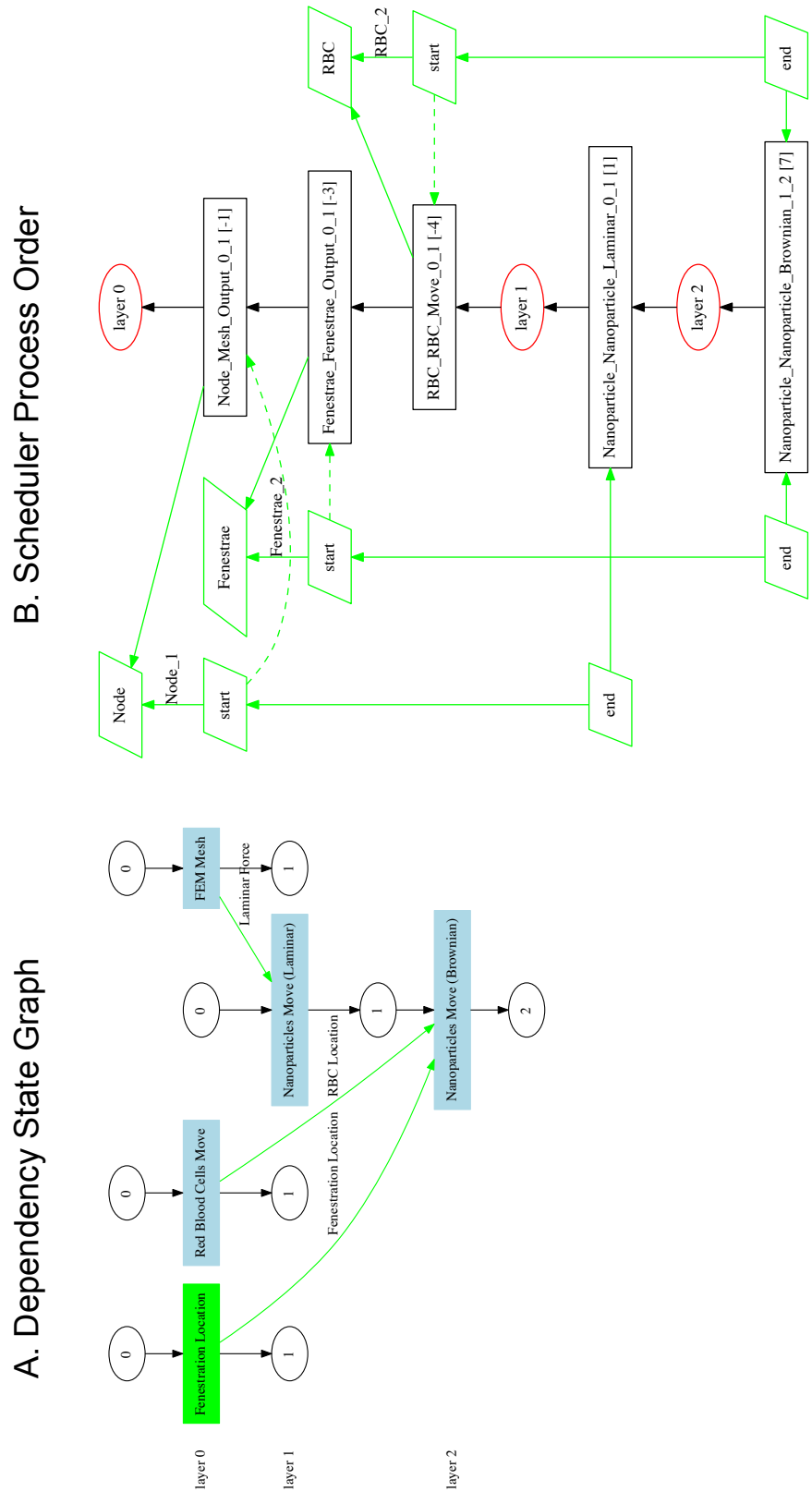

Figure 3.17: FLAME State and Process Order Graphs of the Fenestration Model. The state graph (A) demonstrates the dependency of functions on previous functions and messages for parallelisation of the fenestration model. The process order graph (B) shows the precise order in which FLAME prioritises the functions to reduce the lag from using the message passing interface.

Nanoparticle sizes used were 10 nm, 20 nm, 50 nm, 70 nm, 80 nm, 100 nm and 160 nm. Polydisperse samples were also generated to correspond to nanoparticle populations measured using dynamic light scattering analysis (see *Figure 3.18*).

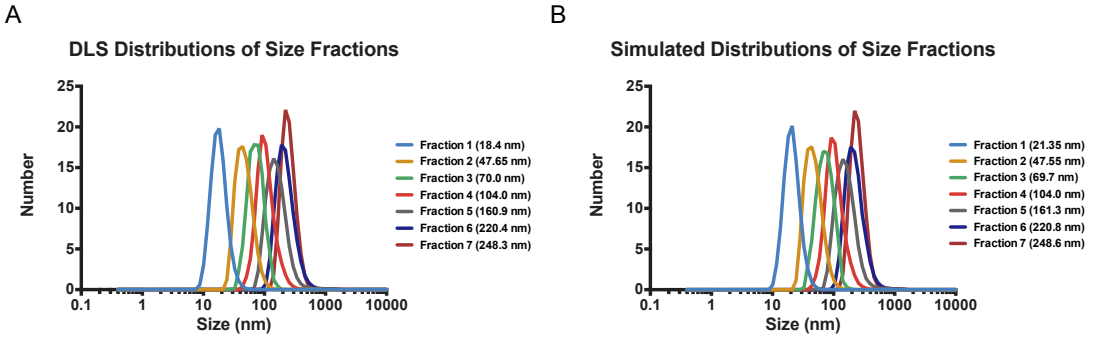

Figure 3.18: Simulating Polydisperse Nanoparticle Distributions from Dynamic Light Scattering Data. Size distributions from DLS Zetasizer software (A) and their corresponding simulated distributions (B) analysed and plotted in the same manner.

Polydisperse populations with an average diameter corresponding to 20 nm, 50 nm, 70 nm, 100 nm and 160 nm (*Figure 3.19*) were chosen to compare with the equivalent monodisperse samples and more importantly, with data expected from corresponding biological experiments.

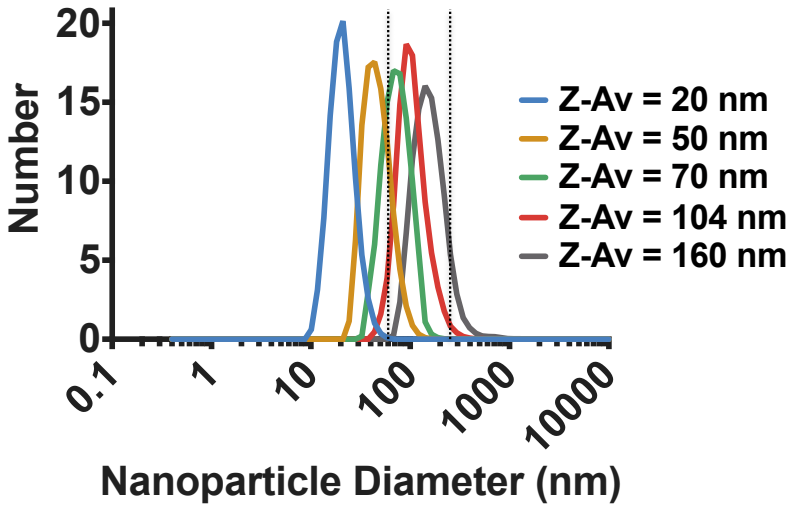

Figure 3.19: Polydisperse Nanoparticle Populations. Polydisperse nanoparticle populations generated from DLS size data were used alongside monodisperse populations of the average sizes, fenestration sizes are indicated by dashed lines.

Figure 3.20 demonstrates that across all size ranges, delivery across tumour vessel fenestrations is vastly increased compared to normal capillaries. Furthermore efficient delivery is still achieved with nanoparticles at 50 nm, 70 nm, 80 nm and 100 nm, where little or no delivery is achieved across normal fenestrations, suggesting that this size range can improve specific delivery to tumour tissue.

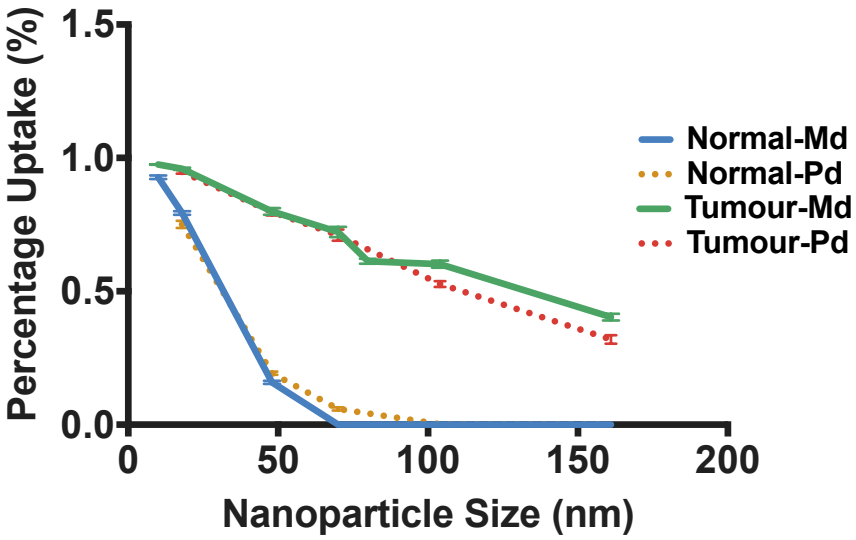

Figure 3.20: Uptake of Nanoparticles across Normal and Tumour Capillaries. The percentage uptake after 0.5 s is compared between normal fenestrations and tumour fenestrations for monodisperse (Md) and polydisperse (Pd) nanoparticle populations. Each data point represents the mean ± standard deviation of three simulations (n=3).

This concept, called the EPR effect or passive-targeting, has been proven previously in many studies (Bogdanov et al., 1997, Iyer et al., 2006). In these studies an important feature was the half-life of the nanoparticle, which is related to size, shape and surface chemistry. The EPR effect has been used, to good effect, to increase the tumour penetration of several well-known anti-cancer drugs including doxorubicin and Taxol. Gradishar and colleagues demonstrated that in Stage III clinical trials, administration of albumin-based 130 nm nanoparticles bound to Taxol performed signficantly better than Taxol controls (Gradishar et al., 2005). Sabbatini and co-workers, likewise, demonstrated an improved response in patients subjected to the higher molecular weight poly-$_L$-glutamic acid conjugated Taxol (~80000Da) (Sabbatini et al., 2004). Vasey and colleagues used *N*-2-(hydroxypropyl)methacrylamide conjugated doxorubicin (Mw= 30000 Da) and demonstrated anti-tumour activity in Phase I studies (Vasey et al., 1999). Doxil® is a commercially available liposome-encapsulated doxorubicin of size 87 nm. It is a PEGylated particle giving a half-life of 50-60 hours in human

blood (Soundararajan et al., 2009). A general feature of these studies was to raise the molecular weight above the rate of blood extravasation, thus improving blood circulation times, giving enhanced uptake in tumours in agreement with the data shown in this chapter. Generally sizes between 40-100 nm have previously been demonstrated to persist in the blood due to reduced loss caused by blood extravasation and filtration by the reticuloendothelial systems of the liver, spleen and kidneys (Maeda et al., 2000, Fang et al., 2011, Alexis et al., 2008). The results for specific delivery to a tumour fall within this range, thus making the data more significant with respect to translation from simulation to experimental data.

A comprehensive systematic study of the EPR effect, looking at characteristics such as size, shape and surface chemistry is lacking. However, the work of Meng and co-workers did look at factors including size and surface chemistry by studying the uptake of three composition of mesoporous silica nanoparticles, NP1, NP2 and NP3 (Meng et al., 2011). NP1 is a 100 nm nanoparticle that aggregates into large agglomerates in saline (520 nm) and media (306 nm in DMEM). NP2 is a smaller PEGylated nanoparticle of 70 nm that again aggregated in saline (597 nm). NP3, however, was a 77 nm nanoparticle that only swelled to 110 nm in saline. It was demonstrated that NP3, also based on PEG, accumulated significantly better in tumours *in vivo* than NP1 or NP2, reaching ~12% of injected dose. NP1 was sequestered, predominantly by the liver and spleen, consistent with removal of large particles by the RES. NP2 and NP3, however, demonstrated increased circulatory half-life, likely a result of the surface modification with PEG. NP2 demonstrated a reduced uptake in the tumour tissue, which may suggest that the large aggregates reduced these particles from crossing tumour fenestrations.

It should be noted that whilst irregular and larger fenestrations have been reported at tumour vasculature, fenestration density changes, irregular flow and poor cellular junction formation are also characteristic of tumour vasculature, inevitably influencing overall uptake into tumour tissues (Fang et al., 2011). As a consequence of the leaky vasculature and reduced lymphatic

system in tumour tissue, interstitial fluid pressure (IFP) is increased in tumour tissue. In normal tissue a convection flow occurs from the pressurised vessel to the non-pressurised tissue. However, the rise in IFP prevents this convective flow from the blood to tumour tissue, reducing extravasation to by diffusion only and as such partly negates the beneficial delivery of the EPR effect, causing a significant hurdle in cancer therapy (Jain and Stylianopoulos, 2010, Heldin et al., 2004, Wiig and Swartz, 2012). In the simulations presented in this chapter, convective flow across fenestrations is not considered, but would likely increase the uptake of nanoparticles into normal tissue, below the fenestration cut off, where the lack of IFP encourages uptake. This highlights the importance of using nanoparticles above the cut off range normal fenestrations but below that of tumour tissues. In future work, consideration for the IFP could be included within the model. However, as most of the work considered in this thesis focuses on the blood-brain barrier, where free exchange is vastly reduced, it has not been included in the model presented to reserve computational power for other functions.

In the analysis of polydisperse nanoparticle uptake, a marked difference in size between those entering fenestrations and those in the vessel was observed (*Figure 3.21*), with smaller sizes being taken up more readily as would be expected from the filtration effect observed in *Figure 3.20*.

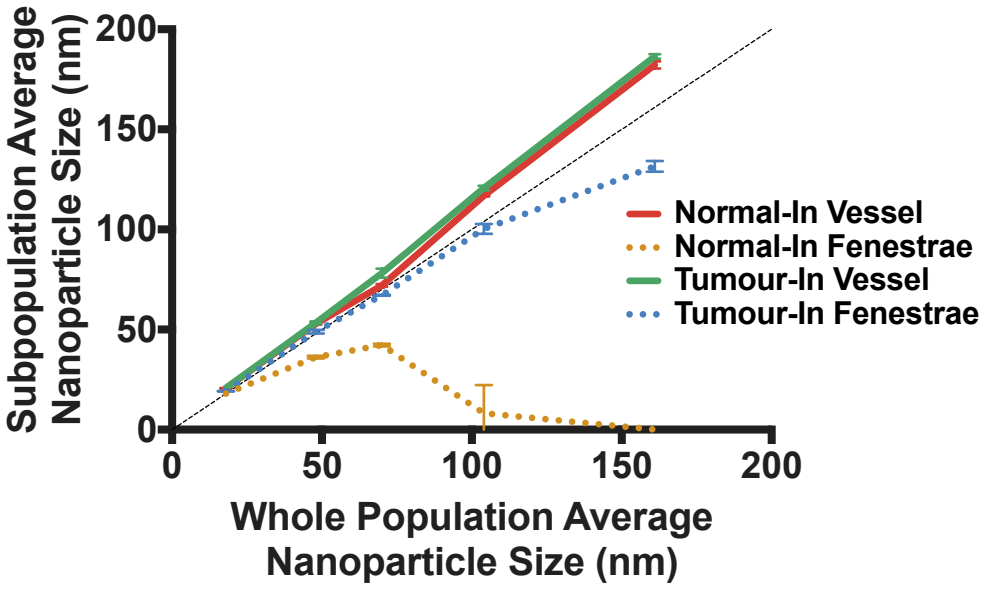

Figure 3.21: Filtration Effect of Fenestrations and Polydisperse Nanoparticles. A comparison was then made between the average size of the nanoparticles within fenestrations and those within the vessel for the polydisperse populations. Each data point represents the mean ± standard deviation of three simulations (n=3).

To quantify a potential effect of this on cargo delivery the number (*Figure 3.22A*) and volume of nanoparticles (*Figure 3.22B*) delivered was then compared between the polydisperse samples and their respective monodisperse samples, based on the assumption that the volume of a nanoparticle is directly related to the amount of cargo it can carry. Whilst a similar effect was demonstrated using both monodisperse and polydisperse populations, delivery of larger sizes, by number, was significantly ($P < 0.01$) reduced in the polydisperse samples, likely reflecting the presence of a minority of nanoparticles of greater size than the tumour vessel fenestrations as can be seen in the distributions in *Figure 3.19*. In parallel, in polydisperse populations corresponding to 70 nm, a small but critical increase is observed in the delivery to normal tissue ($P=0.00007$), reflecting presence of particles below the 60 nm cut off. Therefore, polydispersity is a key consideration in the design of nanoparticles for improved specificity using the EPR effect.

Furthermore, across all samples, the polydisperse populations delivered significantly less volume across the fenestrations (as much as 66% reduction

for the 160 nm population). This demonstrates that monodisperse nanoparticle populations, often used in computational simulations, may give poor correlation with observed experimental results, where delivery quantification will be directly related to the volume of the nanoparticle itself or the related volume of cargo. Whilst here the effects of polydispersity and size are considered for a specific scenario in nanoparticle delivery, size and therefore polydispersity also influence general nanoparticle properties such as immune system interaction, clearance, tissue penetration and diffusion rates.

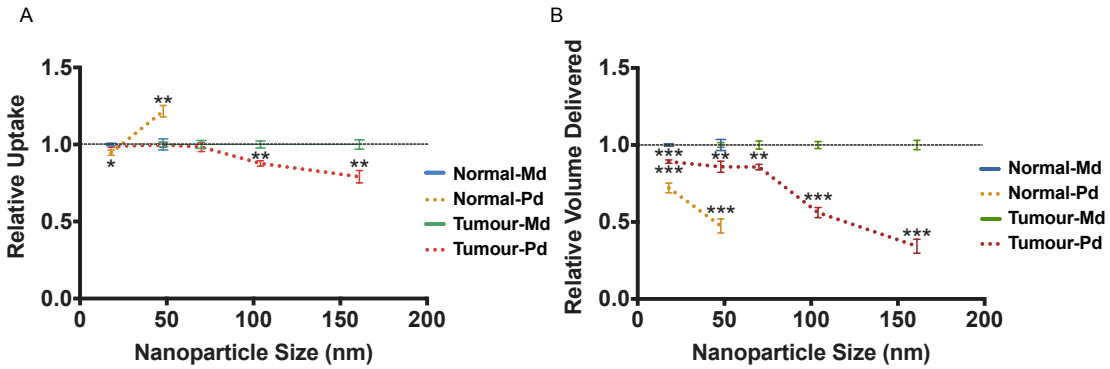

Figure 3.22: Uptake of Mono *versus* Poly -disperse Populations by Number and by Volume. Polydisperse populations (Pd) are compared to their size-matched monodisperse populations (Md) for uptake, by number, in fenestrations at 0.5 s; a dashed baseline for normalised monodisperse populations is included (A). The relative volume of nanoparticle mass delivered across fenestrations was then compared between polydisperse populations and their equivalent monodisperse population at 0.5 s; a dashed baseline for normalised monodisperse populations is included (B). Significance tested by the Holm-Sidak t-test, * $P < 0.01$, ** $P < 0.005$, *** $P < 0.001$. Each data point represents the mean ± standard deviation of three simulations (n=3).

Recently, the size cut off properties of fenestrations has gained new interest. It has been demonstrated that the fenestrations themselves, though sized around 60-65 nm, have a markedly lower size cut off (Sarin, 2010). For example, diaphragmed fenestrae such as those seen in glands have a cut off of 6-12 nm and non-diaphragmed fenestrae as seen in the kidney glomeruli has cut off of 15 nm. The low cut off kidney fenestrae is partially attributed to the actions of the glycocalyx layer, which has a pore size of ~20 nm (Squire et

al., 2001, Weinbaum et al., 2003). Interestingly, changes in the glycocalyx of tumour tissues has been reported and furthermore has been suggested to be important in the spread (metastasis) of cancer cells (Pavelka and Roth, 2010). The change in glycocalyx in tumours is important in understanding how the glycocalyx may influence the EPR effect, something not addressed within these simulations but a potential avenue for future study. The work of Sarin and others suggests that the permeability of fenestrated endothelium to ~60 nm macromolecules is attributable to vesicular-vacuolar organelles (Simionescu et al., 1974, Dvorak et al., 1996, Sarin, 2010). Furthermore, the work of Dvorak demonstrated the vesicular-vacuolar organelles transport more macromolecules in murine ovarian carcinoma models than in normal endothelium, suggesting a mechanism by which the EPR effect may occur independently of fenestrae (Dvorak et al., 1996). It is clear from this that the EPR effect may not be fully understood and better understanding of it may be used to improve future simulations.

The data provided in this section concentrates on the effect of size and polydispersity on simulated uptake of nanoparticles in tumour tissue compared to normal tissue. Although generally trends within this data match up well with the data provided in the literature, such as an increase in size improves specific tumour delivery, the simplicity of the model does not allow easy direct comparisons between the simulations and *in vivo* data. However, future further extrapolation to larger-scale simulations may address this issue.

3.4 CONCLUSIONS

In conclusion, a successful implementation of an agent-based model of nanoparticle behaviour under physiological blood flow has been demonstrated. This model has been designed to allow the facile inclusion of cellular interactions and trafficking. This model gives insight into the integral role of RBCs in the distribution of nanoparticles to the vessel walls. Furthermore, the model's successful application to aid nanoparticle design has been demonstrated by showing how larger size nanoparticles can

specifically target tumour tissues and how polydispersity is a key criterion to control delivery of nanoparticles. In the following chapters, this model is further adapted to study uptake of nanoparticles into the CNS across the blood-brain barrier.

CHAPTER 4: RESULTS AND DISCUSSION II

MODELLING NANOPARTICLE BINDING AT THE BLOOD-BRAIN BARRIER: INSIGHTS INTO IMPROVING GENERAL AND SPECIFIC DELIVERY TO THE CENTRAL NERVOUS SYSTEM

4.1: INTRODUCTION

4.1.1 Controlling Transcytosis Efficiency by Affinity

The blood-brain barrier is able to regulate the entry of large macromolecules, including certain proteins and lipoproteins, by transcytosis. Receptor-mediated transcytosis induces such a transport mechanism through the binding of a ligand to a receptor. In previous drug delivery approaches across the blood-brain barrier, hijacking this mechanism has been utilised to aid nanoparticle delivery to the CNS. However, methods to improve both the general delivery across the blood-brain barrier and specific delivery at different regions of the blood-brain barrier are needed to prevent off-target effects and improve therapeutic load. Delivery to specific regions of the CNS requires the targeting of heterogeneity in the blood-brain barrier. This concept is explored in this chapter by studying the process of transcytosis with different levels of receptor expression and different blood flows.

One of the most striking findings in studies of transcytosis across the blood-brain barrier was that low affinity antibodies to the transferrin receptor demonstrated improved transcytosis efficiency (Yu et al., 2014, Yu et al., 2011). Transcytosis involves five major stages, receptor binding, endocytosis, trafficking, exocytosis and receptor dissociation, as summarised in *Figure 4.1*.

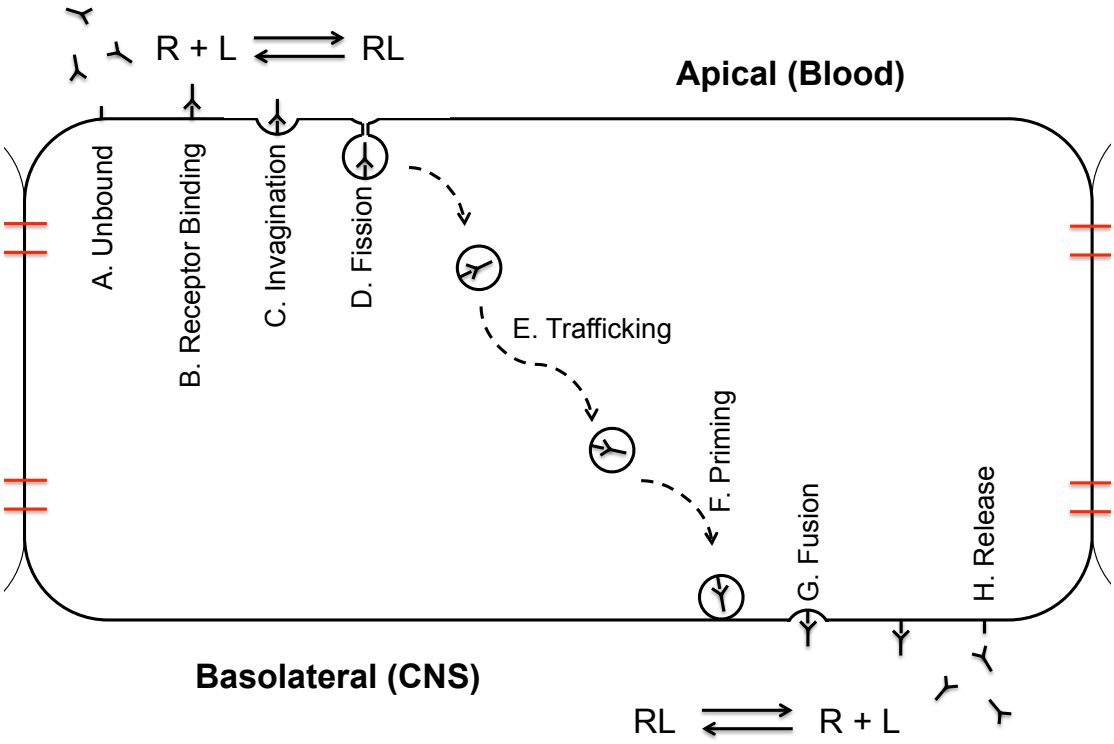

Figure 4.1: Stages of Transcytosis. Unbound cargo (A), upon receptor binding (B) can stimulate the endocytosis process that involves invagination (C), wrapping and fission (D) of a transport vehicle. The transport vehicle is trafficked across the cell (E) to the abluminal membrane where it is primed for exocytosis (F) and fuses with the membrane (G). The bound cargo is then released from the receptor into the abluminal compartment (H). Part B and H are both dependent on the same equilibrium reaction, $\boldsymbol{R} + \boldsymbol{L} \leftrightarrow \boldsymbol{RL}$. In transcytosis, part B requires the forward reaction and part H requires the reverse reaction.

It was hypothesised that the improved performance of lower affinity antibodies was a direct result of the need for both effective receptor binding and unbinding (Yu et al., 2011, Yu et al., 2014). High affinity antibodies are highly effective in receptor binding but highly ineffective at unbinding and therefore would fail to detach from endothelial cells. On the other hand, despite the improved unbinding capabilities of low affinity antibodies, the ability to form and maintain a stable bond for long enough to induce transcytosis is diminished, thus reducing transcytosis efficiency. Therefore, a balance is required to form and maintain sufficiently strong bonds to enable binding and endocytosis but also a sufficiently weak bond to allow unbinding and release, as seen in *Figure 4.2*.

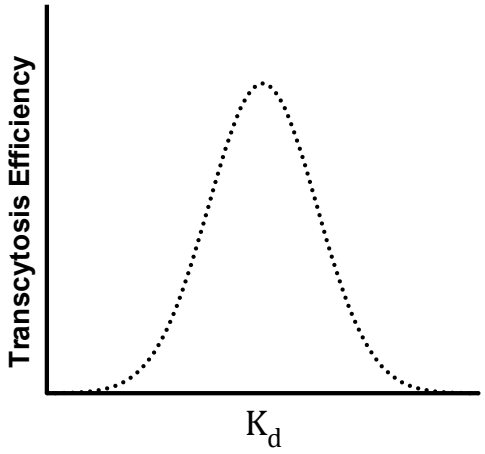

Figure 4.2: Effect of Binding Affinity on Transcytosis Efficiency. As affinity decreases and the dissociation constant (k_d) increases, the binding rate declines and simultaneously the unbinding rate increases. Transcytosis efficiency is optimal when both these rates are in balance at an intermediate dissociation constant.

4.1.2 Controlling Nanoparticle Affinity

Whilst similar principles may apply to nanoparticles, nanoparticle affinity is much more complex. Nanoparticles can form multiple receptor-ligand binding events between themselves and the interacting cell. Therefore, absolute binding affinity is dictated not only by the affinity of each receptor-ligand pair, but also by the number of bonds between the particle and host. The interfacial contact surface area (A_c), the receptor density (R_D) and the ligand density (L_D) dictate the number of bonds (B_N) between the particle and a cell. The target cell determines the receptor density whilst ligand density is an adaptable property of the nanoparticles. The interfacial surface area is the surface area of the nanoparticle that is within a set binding distance from the cell. The characteristic length of the receptor-ligand bond (B_L) dictates this distance. The interfacial surface area is thus dictated by the nanoparticle position, relative to the membrane, the size of the nanoparticle, the bond length and the curvature of the nanoparticle. In consequence, the interfacial surface area can be manipulated by altering the bond length, nanoparticle shape and nanoparticle size, as demonstrated in *Figure 4.3*.

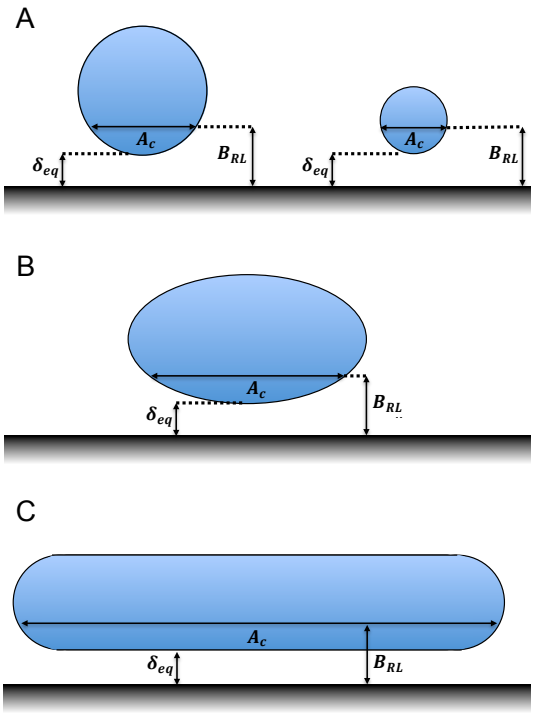

Figure 4.3: Controlling the Interfacial Surface Area by Changing Size and Morphology. The interfacial surface is dictated by the bond length (B_{RL}), nanoparticle size (A), nanoparticle shape (B and C) and the closest distance of the nanoparticle relative to the cell (δ_{eq}).

The ligand density affects the likelihood of new bond formation, with a higher density assumed to increase the probability of formation, as can be seen in *Figure 4.4*.

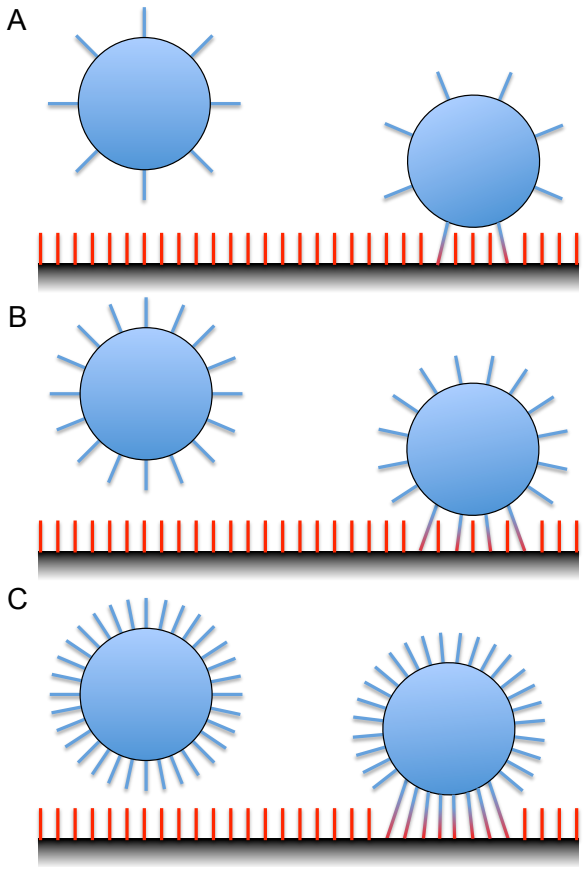

Figure 4.4: Effect of Ligand Density on Nanoparticle-Cell Adhesion. In A, the low ligand density reduces the number of bonds formed compared to B and C, where ligand density and number of bonds increases.

In addition to ligand density, receptor density is also important, as demonstrated in *Figure 4.5*. The probability of a spherical nanoparticle adhering ($\boldsymbol{P_a}$) to the cell membrane, in the absence of shear stress, can be given as:

$$\boldsymbol{P_a} \simeq \boldsymbol{R_D L_D k_a^0 A_c} \qquad (4.1)$$

where $\boldsymbol{k_a^0}$ is the association constant at zero load *per* receptor-ligand pair (Decuzzi and Ferrari, 2006). $\boldsymbol{k_a^0}$ can also be expressed as:

$$\boldsymbol{k_a^0} = \frac{\boldsymbol{k_f^0}}{\boldsymbol{k_r^0}} \qquad (4.2)$$

where k_f^0 and k_r^0 are the forward and reverse reaction rates at equilibrium distance respectively. Therefore, nanoparticle binding may be tailored for specific receptor expression levels by manipulation of the receptor-ligand bond strength (affinity), ligand density and nanoparticle size.

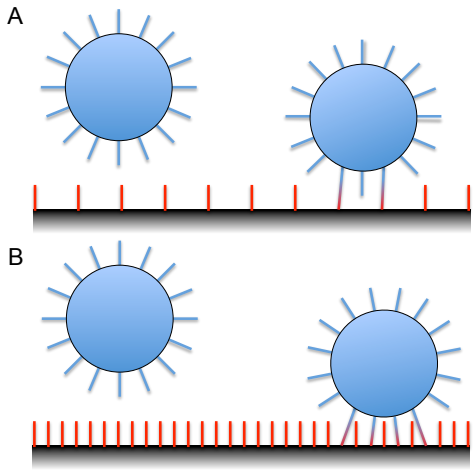

Figure 4.5: Effect of Receptor Density on Nanoparticle-Cell Adhesion. In A, the low receptor density reduces the number of bonds formed compared to B, where receptor density is greater.

4.1.3 Shear Flow and Nanoparticle-Cell Binding

Receptor binding of nanoparticles in the blood is affected by the blood flow. Blood flow creates a shearing force at the vessel walls that strains the receptor-ligand bonds and therefore increases the chances of bond rupture. However, multiple bonds help stabilise adhesion of nanoparticles to the endothelial wall. Nanoparticles adhered to the cell wall are subject to two major forces that will effect bond strain. The drag force (F_D) is the force exerted on the nanoparticle in the direction of flow, as seen in *Figure 4.6A*. The torque (T) is rotational force acting upon the nanoparticle, as seen in *Figure 4.6B*.

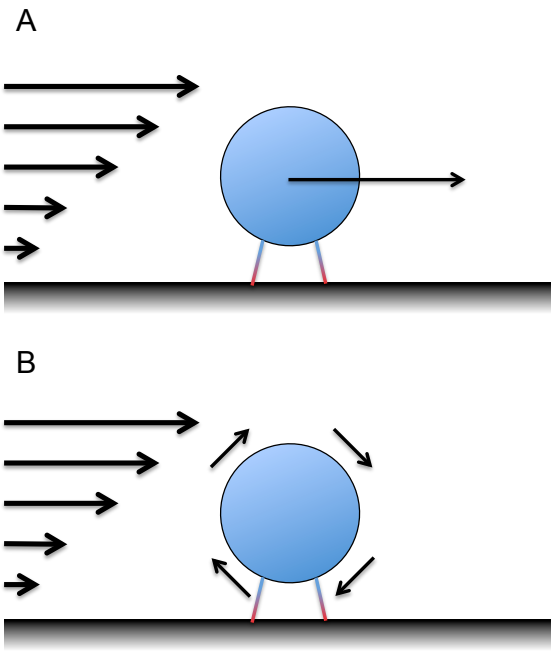

Figure 4.6: Forces acting on Nanoparticles under Shear Flow. There are two major forces acting on nanoparticles, the drag force (A) in the direction of flow and a rotating force called the torque (B).

The drag force and torque forces are both related to the particle radius ($\boldsymbol{r}$), particle aspect ratio ($\boldsymbol{\gamma}$) and wall shear stress ($\boldsymbol{S_\mu}$). The drag force can be defined as:

$$\boldsymbol{F_D = 6\pi r l S_\mu F^S} \qquad (4.3)$$

where $\boldsymbol{l}$ is the distance from the particle centre of mass to the cell membrane and $\boldsymbol{F^S}$ is the force as a function of aspect ratio which is equal to:

$$\boldsymbol{F^S = 1 + (1.736 - 0.138\gamma + 0.128\gamma^2 + 0.09\gamma^3)e^{-\gamma}} \qquad (4.4)$$ (Decuzzi and Ferrari, 2006, Bentley et al., 2008).

The torque can be given as:

$$T = 4\pi r^3 S_\mu T^S \quad (4.5)$$

where T^S is the torque force as a function of aspect ratio, given as:

$$T^S = 1 + (-20.5 + 46.5\gamma - 35.1\gamma^2 + 8.95\gamma^3)e^{-\gamma} \quad (4.6)$$ (Decuzzi and Ferrari, 2006, Bentley et al., 2008).

Therefore nanoparticle-cell adhesion is dependent on the fluid dynamics within the blood, in addition to the affinity, ligand-receptor densities, size and shape considerations from the previous section.

The fluid dynamics in the cerebrovasculature are generally maintained at a relatively constant level by autoregulation. However, transient local increases in blood flow, called functional hyperaemia, occur by the neurovascular coupling response. Functional hyperaemia is a natural mechanism for increasing the uptake of key molecules into the required area of the CNS, in response to local neural stimulation. Through a variety of techniques, particularly fMRI, we have been able to associate different parts of the CNS with their function. The knowledge of the function of distinct CNS regions means it may be possible to induce neural activity within a region of interest. For example, in rodents it is possible to reproducibly stimulate neural activity and consequent functional hyperaemia within the barrel cortex by whisker stimulation. Whilst, functional hyperaemia mechanism is mainly to increase access of important nutrients for ATP production, such as glucose and oxygen, it could be utilised to increase drug uptake into stimulated regions of the CNS. The increase of blood flow increases the overall number of nanoparticles that access the area, but may affect overall binding due to the increase in wall shear stress. Moreover, the size of a nanoparticle is significantly larger than a single glucose molecule (~1.5 nm). Therefore, given

the size components within *Equations 4.3* and *4.5*, it is apparent that the dislodging force will be significantly larger for a nanoparticle than a glucose molecule. However, a composition of nanoparticle could be designed to bind effectively under such conditions, allowing us to harness the inducible localised increase in blood flow in functional hyperaemia to give specific, controllable enrichment of nanoparticles delivered to distinct regions of the CNS.

4.2 AIMS AND OBJECTIVES

In this chapter, an agent-based model of nanoparticle-cell binding is built, based on the transwell *in vitro* models of the blood-brain barrier. This model will then be used to investigate how adapting the $\boldsymbol{k_a^0}$, ligand density and nanoparticle size can alter transcytosis efficiency. This will be used to establish optimal nanoparticle properties for different levels of receptor expression. These studies will be then extended to investigate the binding efficiency of nanoparticles under different shear flow conditions using the model from *Chapter 3*.

4.3 RESULTS AND DISCUSSION

4.3.1 Building a Transwell Model of Nanoparticle Transcytosis

Nanoparticles designed for their ability to cross the blood-brain barrier by receptor-mediated transcytosis are routinely pre-screened using *in vitro* transwell models of the blood-brain barrier. Therefore, to improve the translational utility of *in silico* approaches, an agent-based model was designed based on the geometry of the transwell insert used in the Battaglia laboratory (*Figure 4.7*).

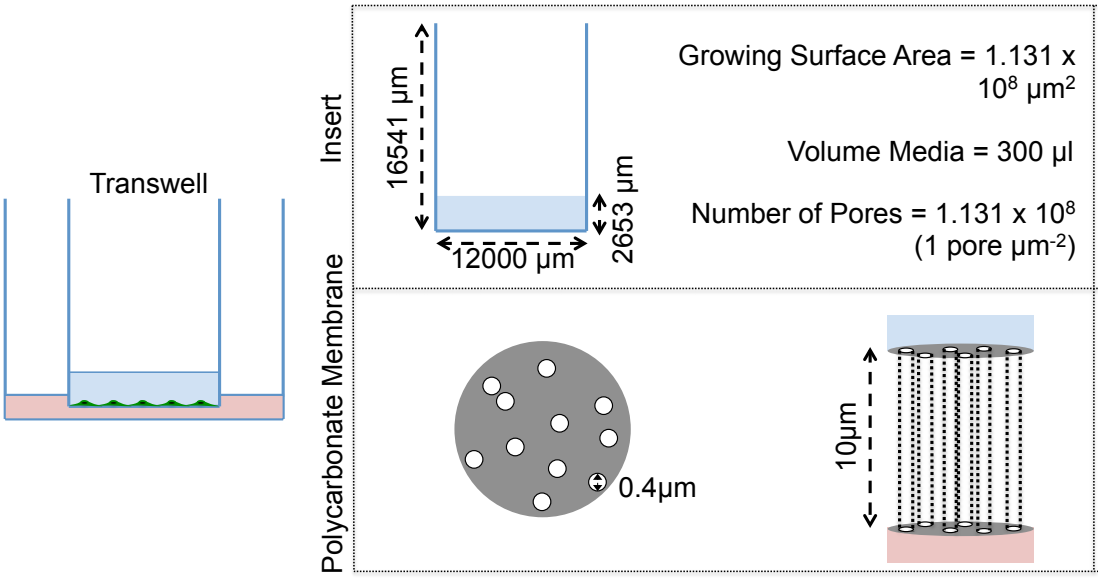

Figure 4.7: Dimensions of a Polycarbonate Transwell. The agent-based model was based on the polycarbonate transwell insert for a 6-well plate, using a media volume of 300 µl.

Cells were simulated as a uniform 2-µm thick layer at the bottom of the insert. Nanoparticles were randomly seeded within the aqueous phase in the starting states. Nanoparticles in the aqueous phase moved according to Brownian motion using the methods provided in *Chapter 3* with a time step ($\boldsymbol{\Delta t}$) of 0.00005 s. The dynamic viscosity was given as 0.00078 Pa·s, the viscosity of the cell medium Dulbecco's Modified Eagle Medium (DMEM) at a standard culture temperature of 37°C (310 K) (Bacabac et al., 2005). The boundaries of the transwell, the top of the aqueous phase and the edge of the cell layer were treated as reflective boundaries.

The Battaglia group's CNS-targeting nanoparticle is based on functionalising POEGMA-PDPA polymersomes with Angiopep-2 that targets the Lrp1 receptor (Tian et al., 2015). The characteristic length for Lrp1-Angiopep-2 was estimated as 6.5 nm based on the molecular weight of Lrp1β, the extracellular chain that forms part of the Lrp1 heterodimer, using the methods of Erickson (Alyaudtin et al., 2001, Schröder and Sabel, 1996). Nanoparticles in close enough proximity to the top of the cell layer ($\boldsymbol{\delta_{eq} < B_L}$) are able to form bonds with the cell. Temporary ligand agents were created randomly on the outside of these nanoparticles to the required density. It was adjudged that this

method would be computationally less expensive than adding in rotational diffusion and updating the positions of the ligands each iteration. Moreover, for the time step used for receptor binding (0.01 s) and the radii of the nanoparticles, the contact surface area is effectively randomised each iteration by rotational diffusion, so that re-creation of the ligands would not adversely effect the robustness of the model compared to incorporating full rotational diffusion.

Therefore this method was adapted to give a simulation of binding and unbinding across discrete steps. Decuzzi and Ferrari investigated the binding of nanoparticles in a static linear flow. They gave the probability of a nanoparticle adhering as:

$$\boldsymbol{P_a \simeq R_D L_D k_a^0 A_c e^{\left(-\frac{B_{RL} F_{RL}}{K_B T}\right)}} \qquad (4.7)$$

where $\boldsymbol{R_D L_D k_a^0 A_c}$ represents the likelihood of bond formation and $(-\frac{\boldsymbol{B_L F_{RL}}}{\boldsymbol{K_B T}})$ represents the total dislodging force. $\boldsymbol{F_{RL}}$ is the dislodging force *per* receptor-ligand pair. This is calculated from the total dislodging force divided by an approximation of bond number, derived from the receptor density and the contact surface area:

$$\boldsymbol{F_{RL} = \frac{F_{dis}}{R_D A_C}} \qquad (4.8)$$

The method Decuzzi and Ferrari does not have the capability to allow reversible binding and unbinding of nanoparticles, nor does it consider the exact number of bonds each particle makes. Therefore, this method was adapted to give a dynamic model of nanoparticle binding, where each available ligand is considered separately. A nanoparticle is bound if at least one ligand-receptor bond is formed. Therefore, adhesion occurs if:

$$\boldsymbol{B_N \geq 1} \qquad (4.9)$$

where $\boldsymbol{B_N}$ is the number of bonds which is equal to:

$$\boldsymbol{B_N = B_N + B_F - B_R} \qquad (4.10)$$

where $\boldsymbol{B_F}$ is the number of bonds formed and $\boldsymbol{B_R}$ is the number of bonds ruptured in a discrete passage of time ($\boldsymbol{\Delta t}$). For every individual ligand within bonding distance, the probability of forming a bond in a discrete passage of time was given as:

$$\boldsymbol{P_{form} \simeq 1 - e^{-R_D L_{A_c} k_a^0 \Delta t}} \qquad (4.11)$$ (Decuzzi and Ferrari, 2006, Hammer and Apte, 1992).

The contact surface area for an individual ligand ($\boldsymbol{L_{A_c}}$) is calculated by:

$$\boldsymbol{L_{A_c} = \pi(B_L{}^2 - \delta_L{}^2)} \qquad (4.12)$$

where $\boldsymbol{\delta_L}$ is the distance from the ligand nanoparticle surface, to the cell surface. In the absence of wall shear stress from flow, the probability of a ligand unbinding can be given from the dissociation constant ($\boldsymbol{k_D}$), the inverse of the association constant ($\boldsymbol{k_a^0}$). The probability of a bond rupturing in a discrete passage of time is given as:

$$\boldsymbol{P_{break} \simeq 1 - e^{-k_D \Delta t}} \qquad (4.13)$$

A bond is formed or ruptured accordingly if a randomly generated number is less than the calculated probability.

Timing of transcytosis remains a largely unexplored area, however timing of endocytosis has been much better studied, both theoretically and experimentally. Gao and colleagues used theoretically modelling to identify an optimal particle radius and wrapping time for particles. The optimal particle size was 54-60 nm in diameter, with an optimal wrapping time of 2-58 s (Gao et al., 2005). The timing of entry is dictated also in part by the pathway of entry and optimal size for each entry route. The most likely routes of entry for a nanoparticle to take are clathrin-mediated, caveolin-mediated or clathrin and caveolin-independent endocytosis. The optimal size of cargo for each route is 120 nm, 60 nm and 90 nm respectively (Conner and Schmid, 2003). Caveolin-mediated endocytosis is a slow process with a half-life of >20 minutes. However, clathrin and other caveolin-independent endocytosis mechanisms can be substantially quicker of the order of tens of seconds to minutes. In neural synapses a clathrin and caveolin-independent endocytosis mechanism has been timed of the order of milliseconds, much quicker than clathrin-dependent endocytosis (Watanabe et al., 2013, Artalejo et al., 2002). In addition to size, shape was also shown to be important in endocytosis mechanics as demonstrated by the work of Decuzzi and Ferrari. They demonstrated that with non-spherical particles, such as cylindrical particles or ellipsoid particles, the wrapping time is often slower, ranging from 41 s for an aspect ratio of nearly 1 and radius perpendicular to the cell membrane of 50 nm to 2105 s for an aspect ratio of 0.32 and radius perpendicular to the cell membrane of 500 nm (Decuzzi and Ferrari, 2008). In previous work in the Battaglia laboratory, based on live cell imaging of Lrp1-mediated transcytosis of polymersomes through *B.End3* brain endothelial cells, the timing of cellular trafficking has been tracked. Endocytosis occurs within 10 s from initial binding of polymersomes to the apical edge of the endothelial cell, within the realms of a clathrin-mediated or caveolin and clathrin-independent endocytosis process. Previously, LDLs and the transferrin receptor have been identified to utilise clathrin-mediated endocytosis but it is also possible other mechanisms could operate at the blood-brain barrier in place of or in conjunction with clathrin-mediated endocytosis (Schmid, 1997, Kibbey et al.,

1998). Trafficking and exocytosis is complete by 20 s after initial binding (Tian and Battaglia, unpublished). In the simulations of transcytosis similar timings were used. Bonds could be formed for 10 s after initial binding of the nanoparticle to the cell. Nanoparticles then entered a trafficking stage where no bonds were ruptured or formed for a further 10 s. Nanoparticles then undertook exocytosis and were placed on the basolateral side of the cell, where bonds can rupture once more (*Figure 4.8*). The state graph and process order graph for running the simulation of transwell nanoparticle binding, in parallel, is given in *Figure 4.9*.

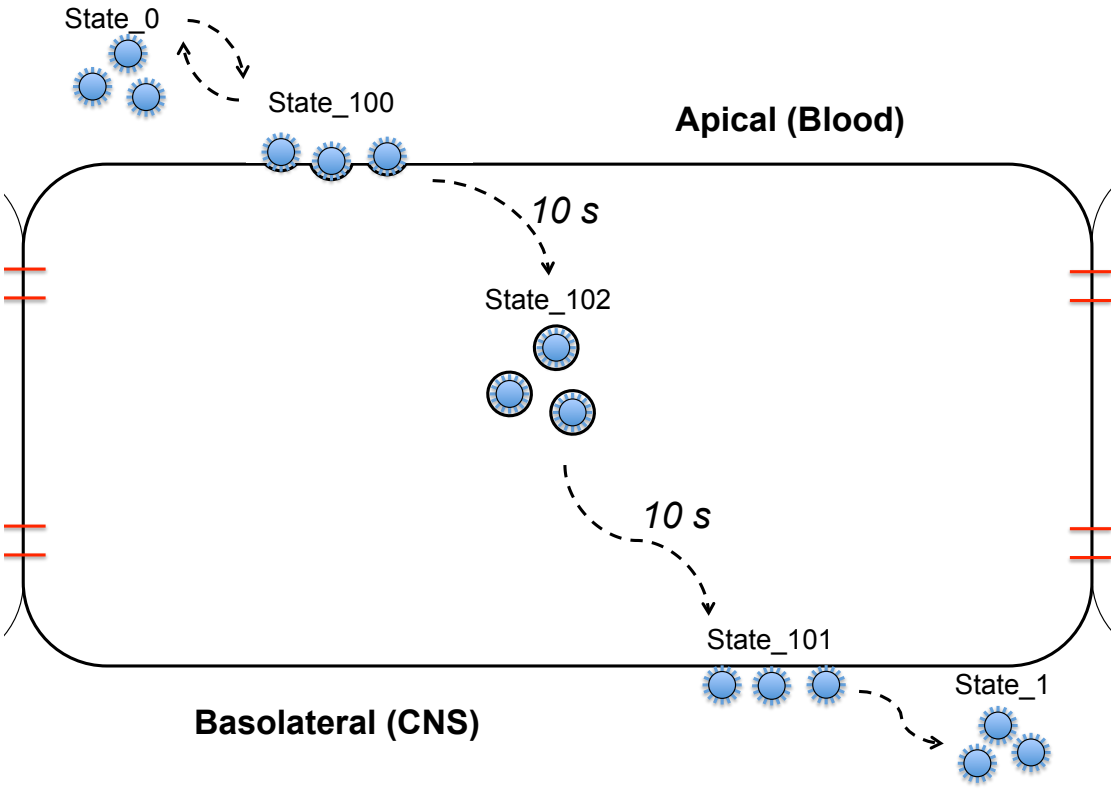

Figure 4.8: Simulation of Transcytosis States. Nanoparticles on the apical side are given the state variable 0. They are free to move by Brownian motion. When in close proximity to the vessel wall, state 0 nanoparticles can bind to the apical side of the cell. Successfully bound nanoparticles are given the state variable 100. They may form and break bonds, but are not subject to Brownian motion. If all bonds are broken the nanoparticle reverts to state 0. If it remains in state 100 for 10 s, then it is assigned the state variable 102. State 102 nanoparticles are unable to form or break bonds and are dormant for a further 10 s before entering state 101. State 101 nanoparticles are bound to the cell on the basolateral side, they may break bonds with the cell. If all bonds are broken, the nanoparticle is given a state variable of 1 and is released into the basolateral compartment.

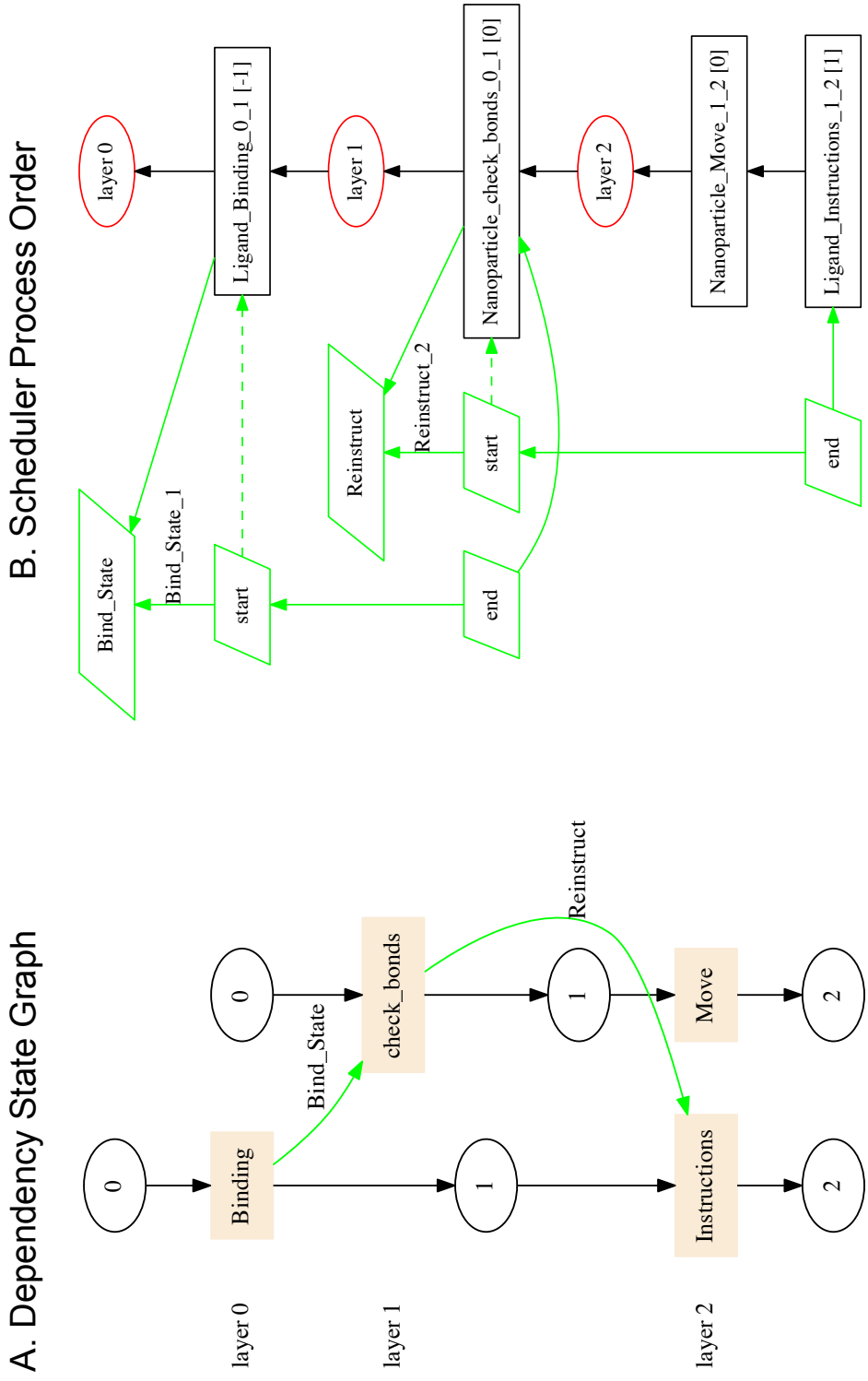

Figure 4.9: FLAME State and Process Order Graphs of the Transwell Receptor Binding Model. The state graph (A) demonstrates the dependency of functions on both previous functions and messages for parallelisation of the transwell receptor binding model. The process order graph (B) shows the order in which FLAME prioritises the functions to reduce the lag from using the message passing interface.

The simulation of transcytosis makes several assumptions. Firstly, that bond rupture does not occur during cellular trafficking. In transcytosis of transferrin, the receptor is usually recycled during the cellular trafficking in the early endosome, suggesting that most of the receptor unbinding occurs during this stage (Maxfield and McGraw, 2004). However, work within the Battaglia laboratory has determined that Lrp1 does not co-localise with endosomal markers and therefore receptor unbinding is less likely to occur at this stage in Lrp1-mediated transcytosis (Tian et al., 2015). Secondly, the simulations assume that no new binding events occur on the basolateral side. Lrp1 is expressed on both the apical and basolateral sides of the cell, this may allow binding to occur on the basolateral side and even basolateral to apical transcytosis events (Herz and Marschang, 2003). This has been omitted from the simulations and instead the simulation is performed for just 5 minutes, to discount the likelihood of basolateral to apical transcytosis events occurring in corresponding *in vitro* experiments. This method also assumes that each receptor-ligand binding event and each nanoparticle-cell binding event is independent. Steric effects can affect multiple receptor-ligand binding events. Multiple nanoparticle binding events have been demonstrated to effect events such as membrane wrapping and endocytosis (Abhishek et al., 2011). In observations of transcytosis in live cells, the lag time from when a particle binds to the apical membrane, until transport occurs, is correlated with an increased intensity in fluorescence from the nanoparticles (Tian and Battaglia, unpublished). This suggests that multiple particles are accrued and transported simultaneously, something not explored within these simulations.

4.3.2 Improving Specificity by Adapting Nanoparticle Properties

In order to test for optimal nanoparticle design, nanoparticles with different sizes, ligand densities and receptor-ligand affinities were evaluated in the transwell model of the blood-brain barrier. The nanoparticles were modelled as 40 nm and 100 nm spheres. This was in keeping with the optimal range for longevity in the blood. A number of different ligand densities were used in

simulations, these were 10^{14} m^{-2}, 5×10^{14} m^{-2}, 10^{15} m^{-2}, 2×10^{15} m^{-2} and 4×10^{15} m^{-2}. In previous studies of receptor-ligand binding for nanoparticle binding or in leukocyte rolling, a wide-range of $\boldsymbol{k_f^0}$ and $\boldsymbol{k_r^0}$ values has been used (Haun and Hammer, 2008, Mehta et al., 1998, Smith et al., 1999b, Tan et al., 2013). Substituting these values into *Equation 4.2* gives a range for $\boldsymbol{k_a^0}$ as 1-100000, therefore $\boldsymbol{k_a^0}$ values of 10, 100, 200, 500 and 1000 were used within the simulations. All the different combinations of nanoparticle composition were then trialled with receptor densities of 10^{15} m^{-2} and 5×10^{14} m^{-2}. 10^{15} m^{-2} was used in line with the work of Decuzzi and Ferrari. 5×10^{14} m^{-2} was used as it represents half the expression level of 10^{15} m^{-2} (Decuzzi and Ferrari, 2006).

In order to demonstrate the relative binding properties of each composition, 20000 nanoparticles were distributed in the transwell model and simulated for 5 minutes. Nanoparticles were permitted to bind and unbind, but transport was initially omitted, in order to study just the binding properties to the apical side of the barrier. *Figure 4.10* demonstrates that generally increasing the ligand density, receptor density and $\boldsymbol{k_a^0}$ improves nanoparticle binding. In *Figures 4.10C and D*, there is evidence of a plateau with high ligand densities and high $\boldsymbol{k_a^0}$. This is suggestive that binding becomes limited by the lower mobility of 100 nm nanoparticles compared to the 40 nm nanoparticles (*Figure 4.10A and B*) where such a plateau is less apparent. This limitation means 40 nm particles have the potential to perform better, reaching a maximum of 1.9% binding compared to ~1.5% for 100 nm nanoparticles. However binding at lower values of $\boldsymbol{k_a^0}$ and lower ligand densities is improved for 100 nm particles, demonstrating that their increased size gives stronger binding, likely due to the subsequent increased contact surface area between the nanoparticle and the cell membrane.

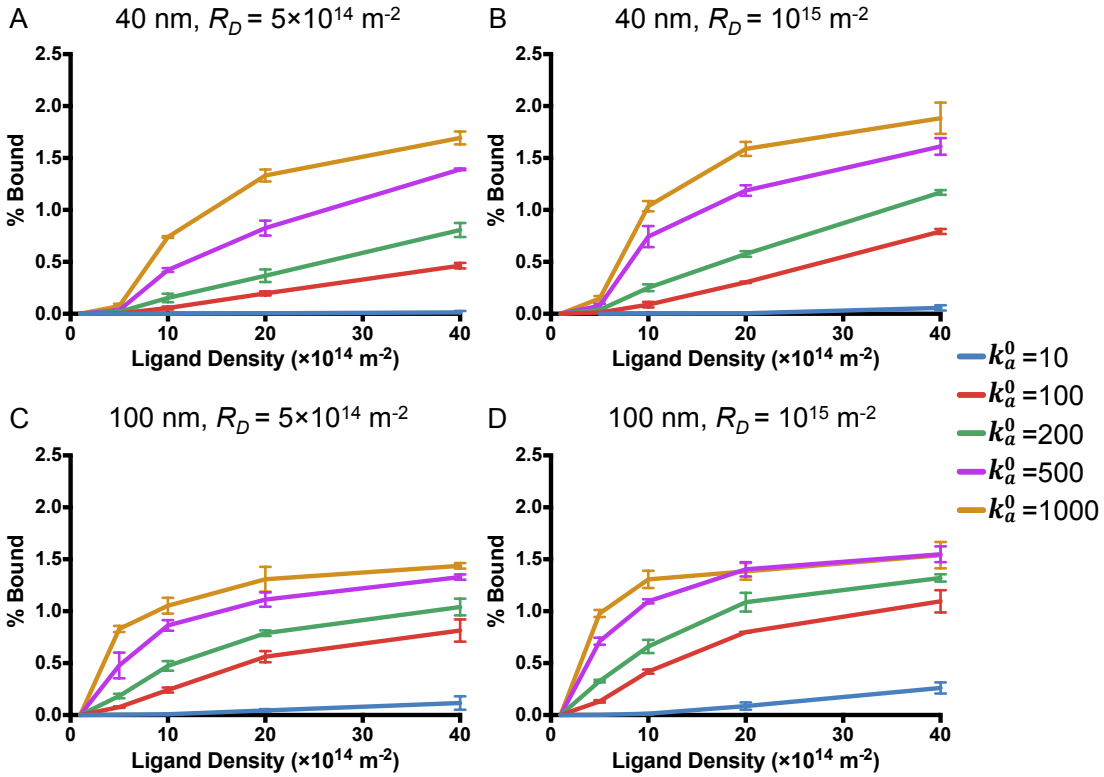

Figure 4.10: Nanoparticle Binding in an *in silico* Transwell Model of the Blood Brain Barrier without Transport. The percentage of nanoparticles bound to the barrier after 5 minutes for 40 nm particles with a receptor density of 5×10^{14} m^{-2} (A) or 10^{15} m^{-2} (B) and 100 nm particles with a receptor density of 5×10^{14} m^{-2} (C) or 10^{15} m^{-2} (D). Each data point represents the mean ± standard deviation of three simulations (n=3).

Generally there is an increase in the binding of nanoparticles to the higher density of receptor (*Figure 4.10B and D*) as compared to the lower density (*Figure 4.10A and C*). However, the difference is more distinct when the overall binding strength is reduced. For example, for a 40 nm particle with a ligand density of 4×10^{15} m^{-2}, a k_a^0 of 1000 gives a nominal 1.1-fold increase in binding to the higher receptor density, where as a k_a^0 of 100 gives a 1.7-fold increase. To investigate this further, the binding ratio of the mean binding to the higher density against the mean binding to the lower density was calculated for each nanoparticle formulation, along with the total error (calculated as described in *Section 2.11*), and plotted in *Figure 4.11*. Where

the total error was calculated to be >30% of the mean, the points were omitted:

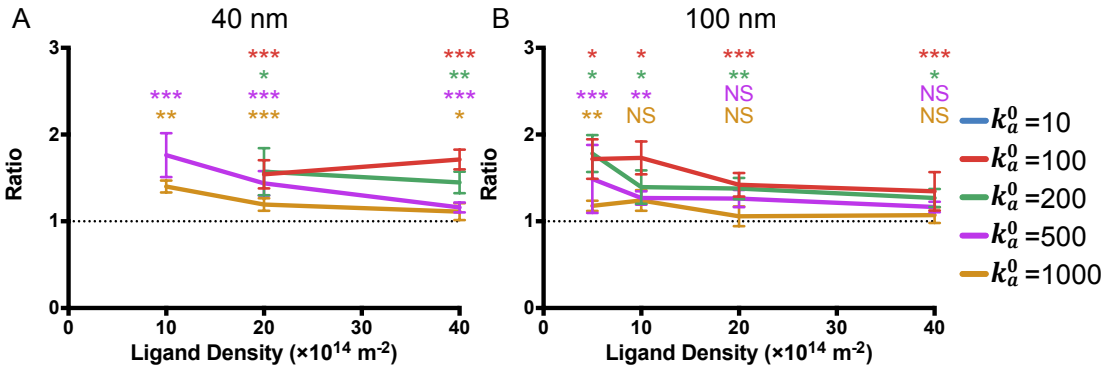

Figure 4.11: Specificity of Nanoparticle Binding in an *in silico* Transwell Model of the Blood Brain Barrier without Transport. The ratio of nanoparticles bound to the barrier with a receptor density of 10^{15} m^{-2} against binding to a barrier with a receptor density of 5×10^{14} m^{-2} for 40 nm (A) and 100 nm (B) nanoparticles. Data points with a percentage error of >30% were omitted. Each data point represents the mean ± standard deviation of three simulations (n=3). Significance calculated using the Holm-Sidak t-test, * $P < 0.05$, ** $P < 0.01$, *** $P < 0.005$

Figure 4.11A demonstrates that the greatest improvement for uptake by the higher receptor density occurs when the k_a^0 value is low and the ligand density is high or alternatively when the k_a^0 value is high but the ligand density is low. The Frenkel group have likewise demonstrated the latter, where a high ligand density with a low binding affinity gave super-selective behaviour for increased receptor expression (Gosk et al., 2004). However, their ligand densities were higher than in the simulations in this chapter, in order to guarantee that each available receptor can choose between multiple ligands, giving increased binding strength through entropy effects. The method presented here works in the limit of comparable ligand to receptor density, therefore it is difficult to replicate such findings with this method, even if there is broad agreement with their findings. Overall, this demonstrates that the binding specificity is dictated by the collective binding strength of a nanoparticle. *Figure 4.11B* demonstrates that a low k_a^0 value is consistently better for improving binding specificity, with a reduction in specificity as ligand

density is increased. It can be concluded from this that weakening the absolute binding affinity of nanoparticles improves specificity for a higher receptor expression. The increased receptor density may aid binding by increasing the likelihood of multiple receptor-bond formations, thus increasing stability of inherently weak interactions, or by simply improving the likelihood of an initial receptor-bond forming.

To investigate whether different nanoparticle compositions and receptor expression levels affected the bond density, the average number of bonds *per* particle was plotted (*Figure 4.12*). Simulations with less than 5 bound particles were omitted due to the high error attributed to these simulations. Increasing the ligand density increased the number of bonds per particle across all simulations. This effect was greater for larger particles (*Figures 4.12C and D*) as compared to smaller particles (*Figure 4.12A and C*). This demonstrates that the number of bonds is highly related to the absolute number of ligands that can form bonds, dictated by the contact surface area and the ligand density. An increased $\boldsymbol{k_a^0}$ also appeared to increase the number of bonds formed, although this effect is more negligible at 40 nm (*Figure 4.12A and B*), particularly for a high density of receptor (*Figure 4.12B*). Interestingly, the number of bonds *per* receptor is consistently lower with a higher receptor density. This suggests that the major route for the improved binding to the higher receptor density is caused by the increasing probability of forming an initial bond, as opposed to increasing the stability of the nanoparticle-cellular interaction through multiple bonds. However, it is likely that both contribute to the overall improved binding.

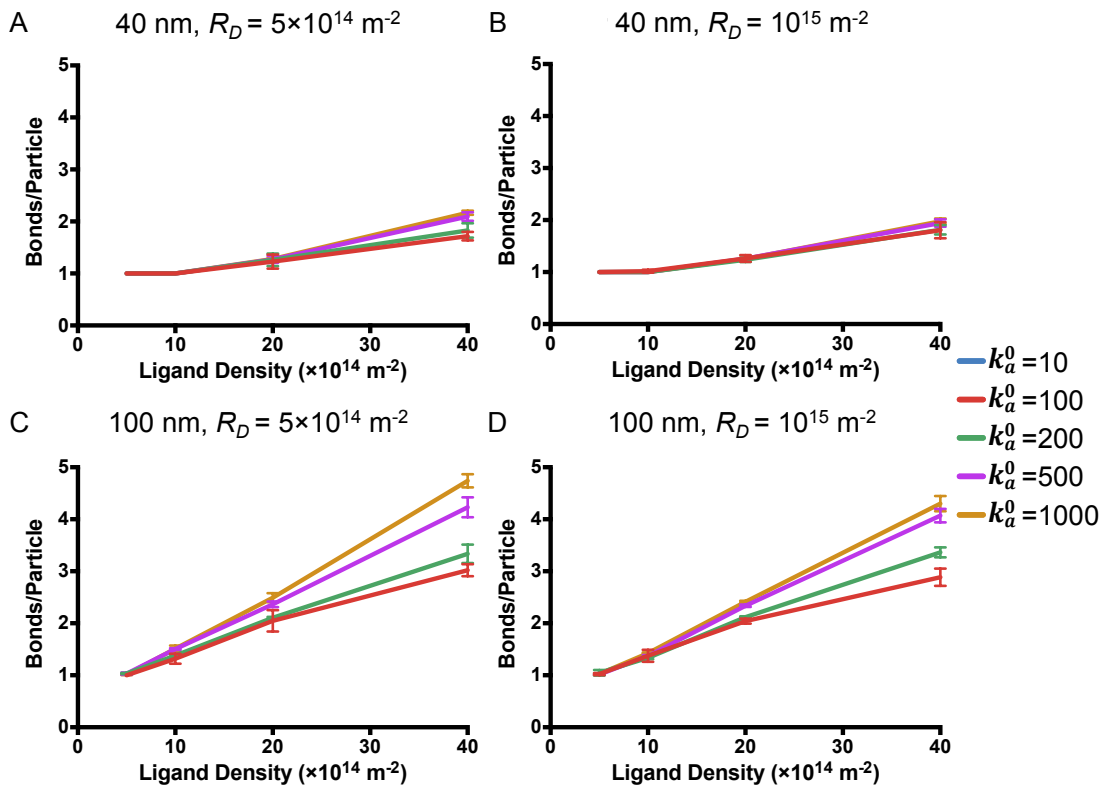

Figure 4.12 Number of Bonds *per* Nanoparticle for Binding in an *in silico* Transwell Model of the Blood Brain Barrier without Transport. The average number of bonds per nanoparticle bound to the barrier after 5 minutes for 40 nm particles with a receptor density of 5×10^{14} m^{-2} (A) or 10^{15} m^{-2} (B) and 100 nm particles with a receptor density of 5×10^{14} nm^{-2} (C) or 10^{15} nm^{-2} (D). Simulations with less than 5 bound particles were omitted. Each data point represents the mean ± standard deviation of three simulations (n=3).

4.3.3 Improving Transcytosis Efficiency by Adapting Nanoparticle Properties

To model transcytosis efficiency of nanoparticles, the same compositions of nanoparticle were modelled for 5 minutes, but with cell trafficking and unbinding into the basolateral compartment included. The percentage of particles that have successfully bound, undergone cell trafficking and been released on the basolateral side was plotted in *Figure 4.13*. 40 nm nanoparticles (*Figure 4.13A and B*) demonstrate that with strong overall binding, due to the collective influence of high ligand density and high $\boldsymbol{k_a^0}$, there is a reduction in the efficiency of transcytosis. Lower affinities ($\boldsymbol{k_a^0}$ = 10, 100 or 200) demonstrate improved transcytosis efficiency with increased

ligand density. A similar pattern is also observed for 100 nm nanoparticles (*Figure 4.13C and D*), but with the decline in efficiency occurring with lower ligand densities and with lower k_a^0 values. This reflects the steeper increase in the number of bonds *per* particle that occurs with larger nanoparticles, as observed in the previous section. The increased number of bonds increases the stability of the binding and provides a greater energetic barrier for release. Generally transcytosis efficiency was increased at the higher receptor density (*Figures 4.13B and D*) as compared to the lower density (*Figures 4.13A and C*). This reflects both the increased initial binding of the particles but also accounts for the reduction in the number of bonds *per* nanoparticle observed at the higher receptor densities in the previous section. Thus, more particles are present with lower energetic barriers to overcome for release.

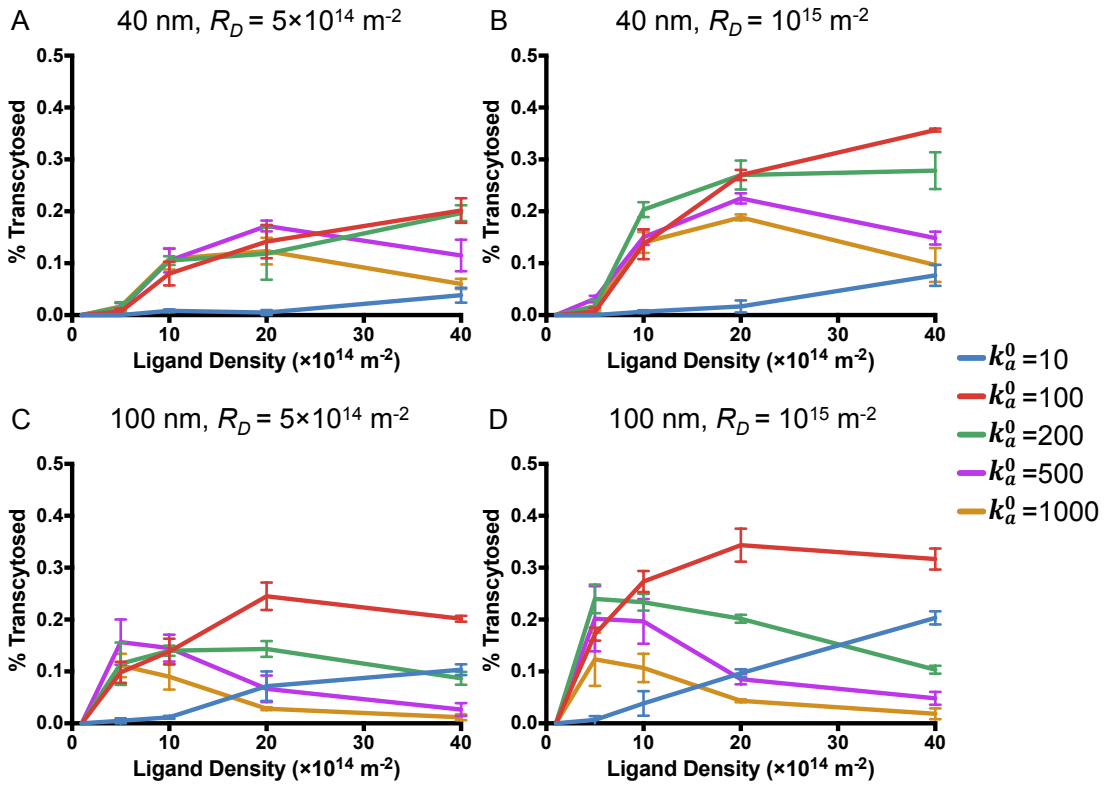

Figure 4.13: Nanoparticle Transcytosis in an *in silico* Transwell Model of the Blood Brain Barrier. The percentage of nanoparticles transcytosed across the transwell barrier after 5 minutes for 40 nm particles with a receptor density of 5×10^{14} m^{-2} (A) or 10^{15} m^{-2} (B) and 100 nm particles with a receptor density of 5×10^{14} nm^{-2} (C) or 10^{15} nm^{-2} (D). Each data point represents the mean ± standard deviation of three simulations (n=3).

In order to confirm that the lack of free basolateral nanoparticles at higher values of k_a^0 and ligand densities was due to failure to unbind the basolateral membrane, the percentage of basolaterally bound nanoparticles was plotted (*Figure 4.14*). *Figure 4.14* demonstrates that nanoparticles at high k_a^0 and ligand density are indeed sequestered on the basolateral membrane. Furthermore at low values of k_a^0 (k_a^0 = 10), there is virtually no binding to the basolateral membrane, suggesting that almost all transport results in rapid release on the basolateral side. Interestingly, the levels are much lower than that bound to the apical membrane without transport. This may reflect the lack of binding potential on the basolateral side of the simulations, suggesting apical binding is only maintained by rapid and dynamic bond formation and bond rupture, as opposed to forming more stable bonds.

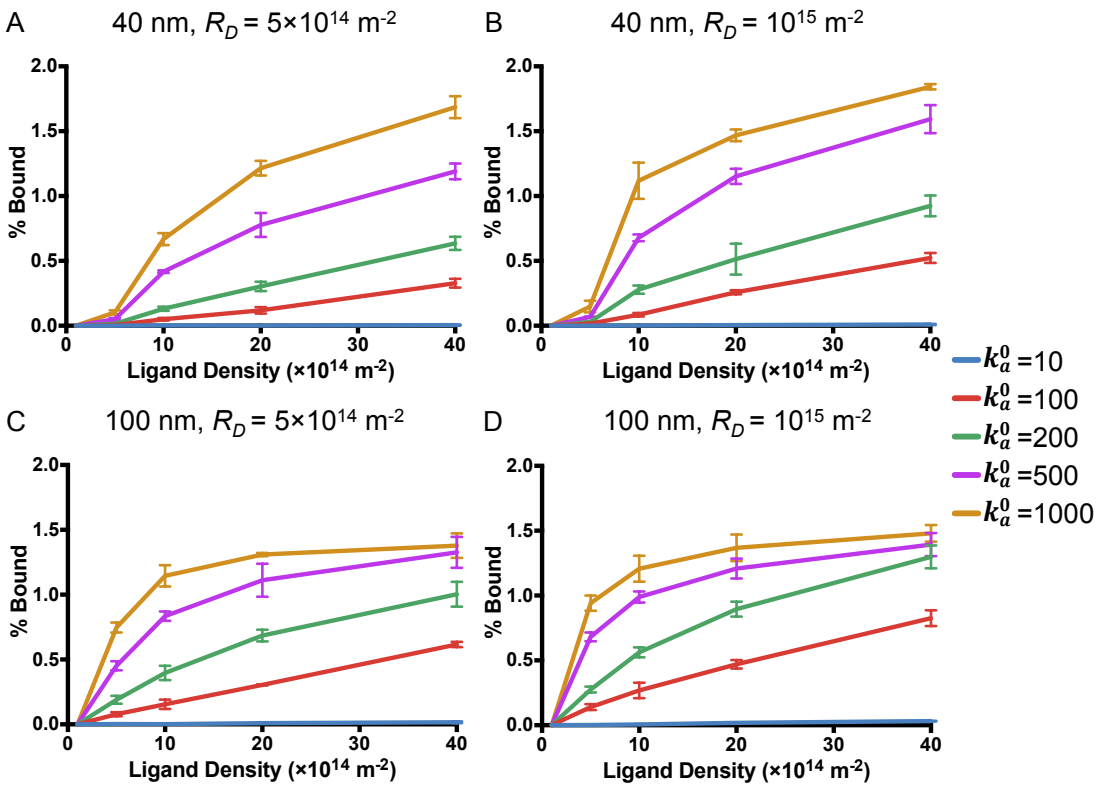

Figure 4.14: Nanoparticle Binding to the Basolateral Side of an *in silico* Transwell Model of the Blood Brain Barrier. The percentage of nanoparticles bound to the basolateral side of the barrier after 5 minutes for 40 nm particles with a receptor density of 5×10^{14} m^{-2} (A) or 10^{15} m^{-2} (B) and 100 nm particles with a receptor density of 5×10^{14} m^{-2} (C) or 10^{15} m^{-2} (D). Each data point represents the mean ± standard deviation of three simulations (n=3).

The relative unbinding efficiency of the different nanoparticle compositions was estimated by calculating the total number of unbound basolateral nanoparticles across three replicate simulations as a percentage of the total bound and unbound basolateral nanoparticles across the same three replicate simulations (*Figure 4.15*). A number of compositions had too few basolateral nanoparticles across all three replicate simulations to accurately calculate the unbinding efficiency, due to overall poor and unstable binding on the apical side, therefore these points were omitted from *Figure 4.15*. Nanoparticles with a $\boldsymbol{k_a^0}$ of 10 had an unbinding efficiency of >95%. Where as nanoparticles with a $\boldsymbol{k_a^0}$ of 1000 had an unbinding efficiency of <5% at higher ligand densities. As expected nanoparticle unbinding efficiency declined as the $\boldsymbol{k_a^0}$ or ligand density was increased.

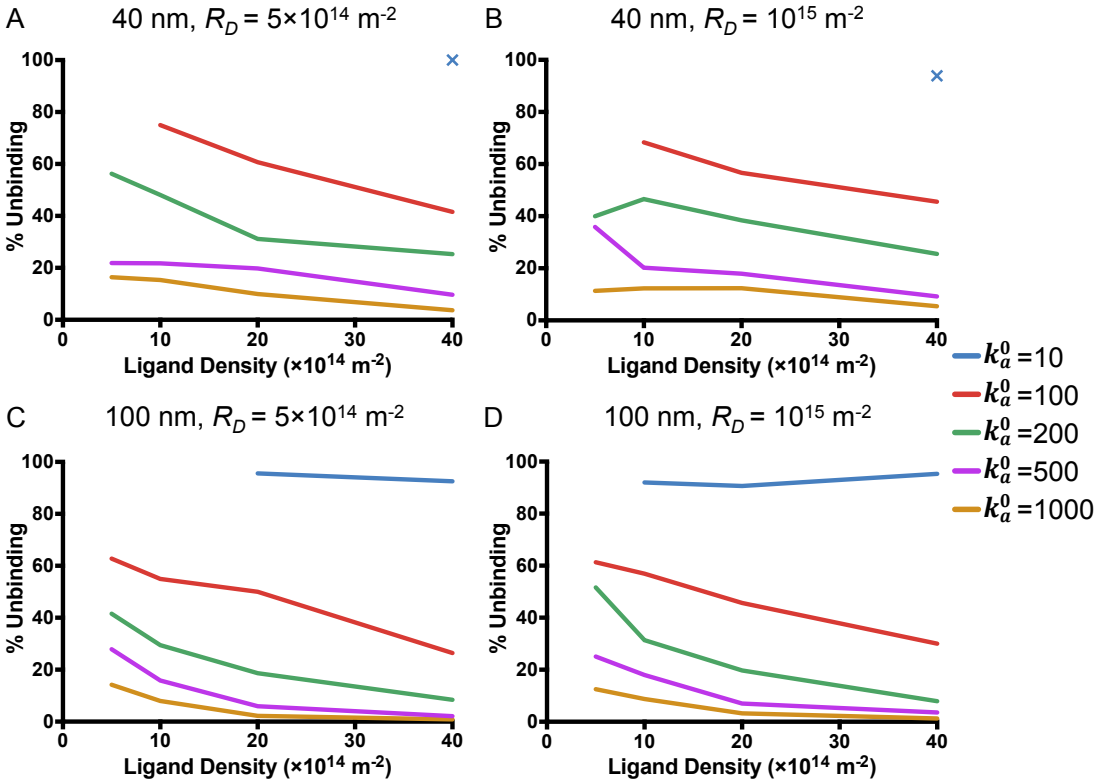

Figure 4.15: Nanoparticle Release in an *in silico* Transwell Model of the Blood Brain Barrier. The efficiency of nanoparticle release on the basolateral side of the barrier as a percentage of all transcytosed nanoparticles after 5 minutes for 40 nm particles with a receptor density of 5×10^{14} m^{-2} (A) or 1015 m-2 (B) and 100 nm particles with a receptor density of 5×10^{14} m^{-2} (C) or 10^{15} m^{-2} (D). Points with too few basolateral particles were omitted. Each data point represents the unbinding efficiency calculated from the total number of nanoparticles released across three simulations and the total number of nanoparticles transcytosed across three simulations.

4.3.4 Building a Capillary Model of Nanoparticle Binding

To give a simulation of nanoparticles binding under shear flow, the simulation of nanoparticles undergoing binding to the blood-brain barrier was combined with the simulation of blood flow from *Chapter 3*. Furthermore, the dislodging forces calculated from the drag and torque forces were integrated into *Equation 4.13*. The aspect ratio (γ) of spherical particles is equal to 1, therefore by applying this *Equation 4.4* and *Equation 4.6*, *Equation 4.3* reduces to:

$$F_D = 10\pi r l S_\mu \quad (4.14)$$

and *Equation 4.5* reduces to:

$$T = 3.78\pi r^3 S_\mu \quad (4.15).$$

The dislodging force (F_{dis}) is calculated as the force acting on the nanoparticle shared over the number of bonds (B_N). It can be assumed that whilst the drag force (*Equation 4.2*) affects all bonds equally, the torque force (*Equation 4.4*) will mainly affect bonds in the trailing half of the nanoparticle, therefore:

$$F_{dis} = F_d + \frac{T_q}{2} \quad (4.16) \text{ (Decuzzi and Ferrari, 2006).}$$

In the work of Decuzzi and Ferrari, the number of bonds was estimated as being related to the contact surface area and the receptor density. However, as the number of bonds is known in these simulations, the probability of bond breakage under shear flow can be given as:

$$P_{break} \simeq 1 - e^{-k_D \Delta t e^{\frac{B_L F dis}{K_B T B_N}}} \quad (4.17)$$

where k_B is the Boltzmann constant and T is the temperature. Cellular trafficking was omitted in these simulations. This is because a typical simulation of blood flow will simulate 0.5-2 s, much lower than the measured 20 s for transport. Moreover, it can be expected that cellular trafficking times will be reduced *in vivo* as endothelial cells in the blood-brain barrier can be as little as 500 nm in distance from the apical to basolateral side, compared to several microns in *in vitro* cultured cells. Nanoparticles in capillaries were

simulated with a time step of 0.00005 s for Brownian motion and 0.0001 s for laminar flow and receptor binding. The state graph and process order graph for parallel execution of the capillary model of nanoparticle binding is given in *Figure 4.16*.

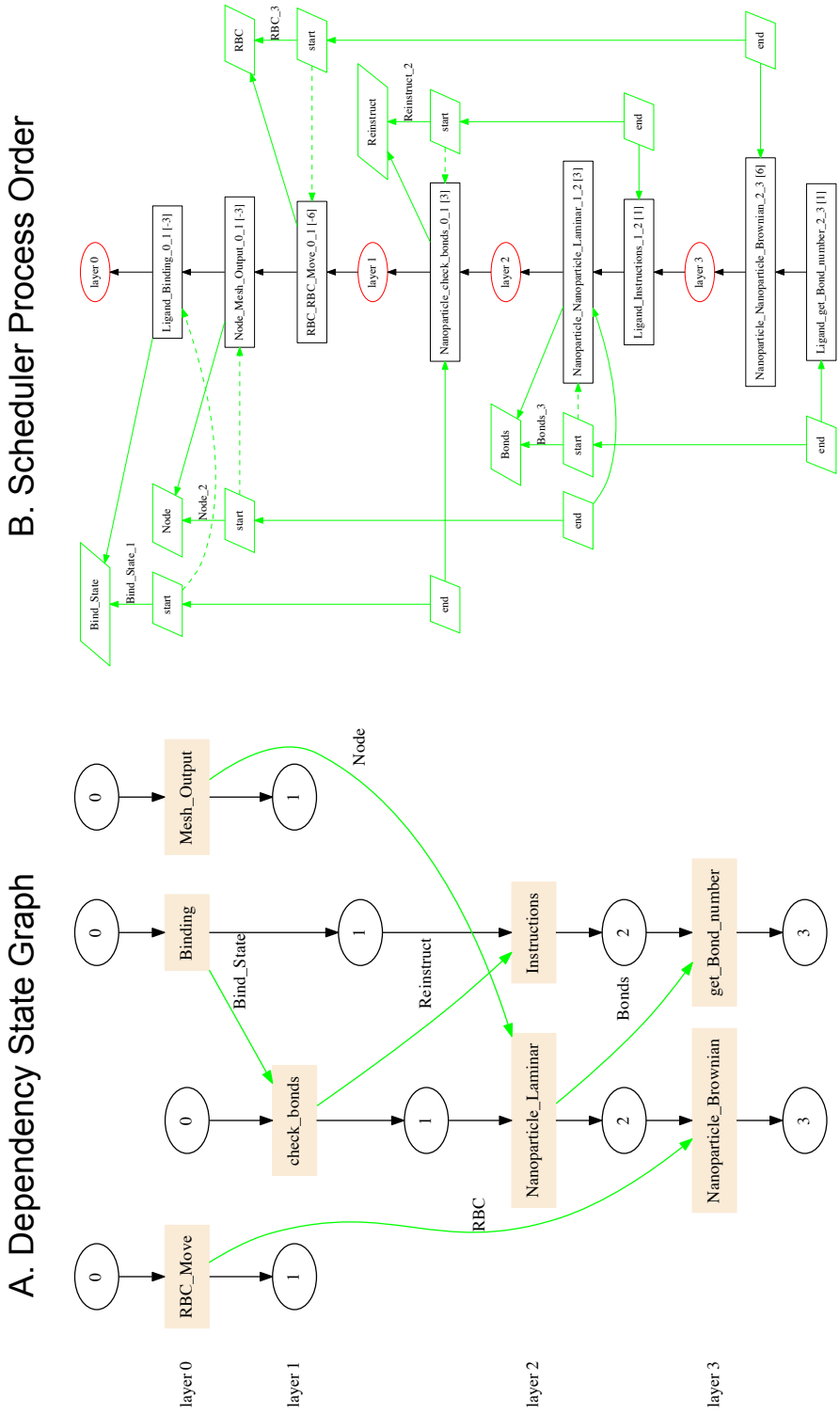

Figure 4.16: FLAME State and Process Order Graphs of the Capillary Receptor Binding Model. The state graph (A) demonstrates the dependency of functions on both previous functions and messages for parallelisation of the capillary receptor binding model. The process order graph (B) shows the order in which FLAME prioritises the functions to reduce the lag from using the message passing interface.

The dislodging force is dependent on particle size. In order to evaluate the relative dislodging force of different molecules under shear flow, the dislodging force was plotted against particle size (*Figure 4.17*). *Figure 4.17* demonstrates that the dislodging force increases with particle size in an exponential manner. Moreover, the size of key endogenous molecules including glucose, proteins and LDLs is indicated as a comparison to the size of nanoparticles. It is apparent that the relative size of nanoparticles compared to glucose leads to an increase in dislodging force by 150-1000 times. Furthermore, the dislodging force of nanoparticles is 2-13 times greater than LDL molecules, the typical substrate for the Lrp-1 receptor. Stronger binding to the vessel wall may therefore be required for nanoparticles to be transported. Forming more bonds and/or stronger individual bonds could provide this stronger binding. Therefore, it is important to find a nanoparticle composition that can bind under such conditions.

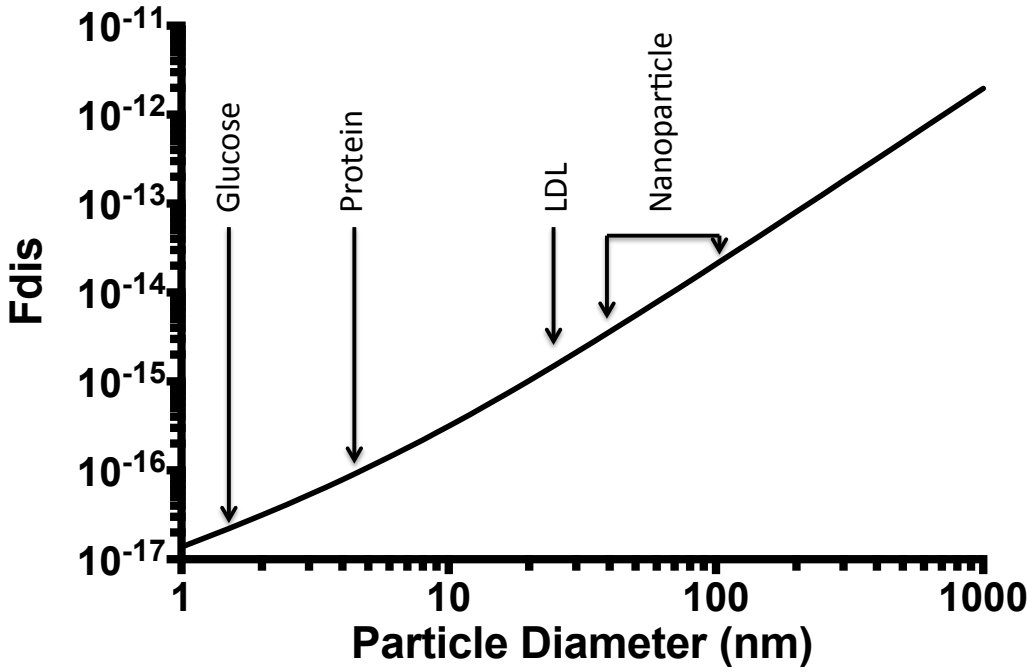

Figure 4.17: Dislodging Force as a Function of Particle Size. The dislodging force is demonstrated as function of particle size when $\boldsymbol{S_\mu = 0.25\ Pa}$ and $\boldsymbol{\delta_{eq} = 3\ nm}$.

4.3.5 The Effect of Functional Hyperaemia on Nanoparticle Binding

In order to evaluate whether functional hyperaemia negatively affects the efficiency of nanoparticle binding and transcytosis, the model presented in *Chapter 3* was adapted to model increasing shear flows. Functional hyperaemia can increase overall blood velocity by approximately 20-30% (Zheng et al., 2002). In order to model functional hyperaemia, RBC velocity was increased by one-third to 80 $\mu m \cdot s^{-1}$. Functional hyperaemia is, at least partially, mediated by an increase of blood flow through the arteriole. Therefore, blood flow velocity at the inlet was increased by one-third and then blood flow was resolved according to the methods in *Chapter 3*. The relative shear stress under normal and functional hyperaemia flow is shown in *Figure 4.18. Figure 4.18* demonstrates that shear stress is highest proximal to RBCs. The wall shear stress, distal to the RBCs, is higher under functional hyperaemia conditions (*Figure 4.18B*) than under normal flow (*Figure 4.18A*). Therefore, under functional hyperaemia the unbinding probability should be higher. The aim of this section is to establish what effects functional hyperaemia has on distribution and binding of nanoparticles to the endothelial blood-brain barrier.

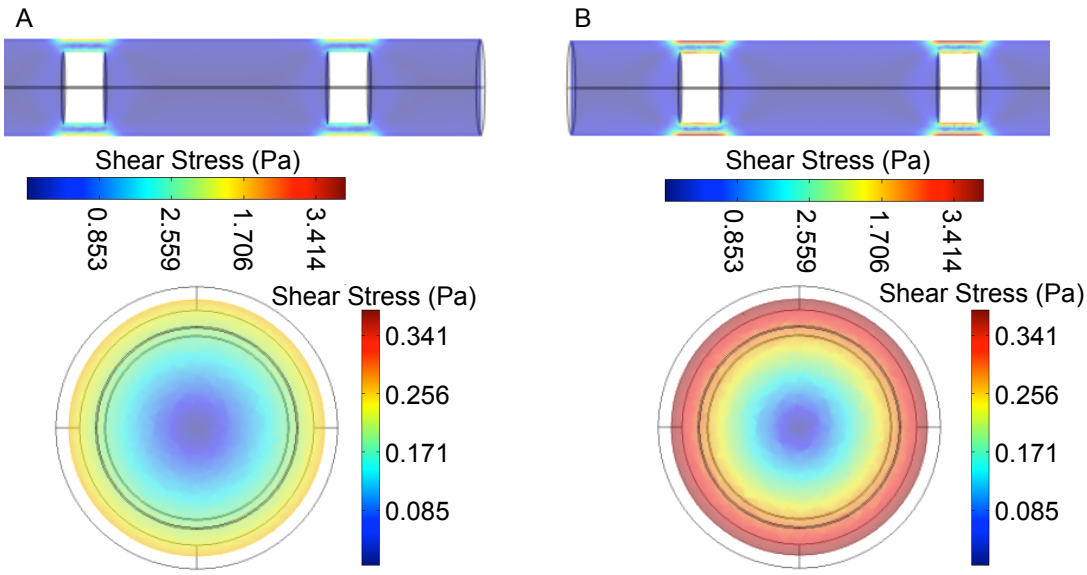

Figure 4.18: Shear Stress under Normal Flow and Functional Hyperaemia. The shear stress is demonstrated in longitudinal and latitudinal cross-sections of the vessel under normal flow (A) and functional hyperaemia (B). Latitudinal slices are taken distally from the RBCs.

Firstly, the number of nanoparticles that passaged through each vessel in 0.5 s was quantified. The normalised number of nanoparticles, in *Figure 4.19*, demonstrates that there is 1.3-fold increase in the number of nanoparticles that passes through a vessel under functional hyperaemia compared to normal flow.

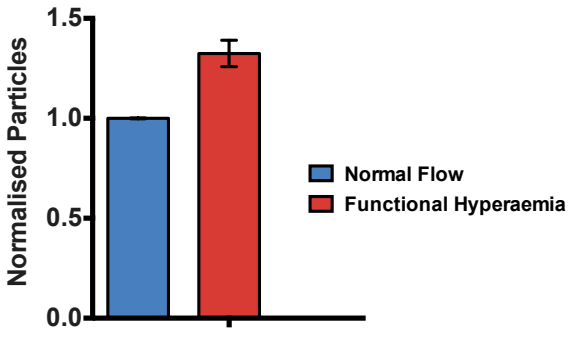

Figure 4.19: Normalised Number of Particles Transiting through a Vessel under Normal Flow and Functional Hyperaemia. The number of particles transiting through a vessel is normalised against normal flow. Each bar represents the mean ± standard deviation of three simulations (n=3).

Therefore if nanoparticle binding efficiency is maintained under functional hyperaemia, or is only marginally decreased, due to the increase access of nanoparticles to the area overall, delivery will be improved by inducing functional hyperaemia. Nanoparticle compositions used in the previous sections were placed within the two blood vessels with different receptor densities and their binding was analysed at 0.5 s (*Figure 4.20*). Generally, under flow in *Figure 4.20*, there appears to be a greater specificity for the higher density of receptor expression. This effect is observable even with higher levels of flow. The increased wall shear stress under functional hyperaemia does seem to reduce the percentage of nanoparticles bound in *Figure 4.20*, as expected. This difference appears greater at lower receptor densities, ligand densities, $\boldsymbol{k_a^0}$ values and sizes, likely reflecting both the decreased number of bonds and decreased stability of bonds compared with higher values.

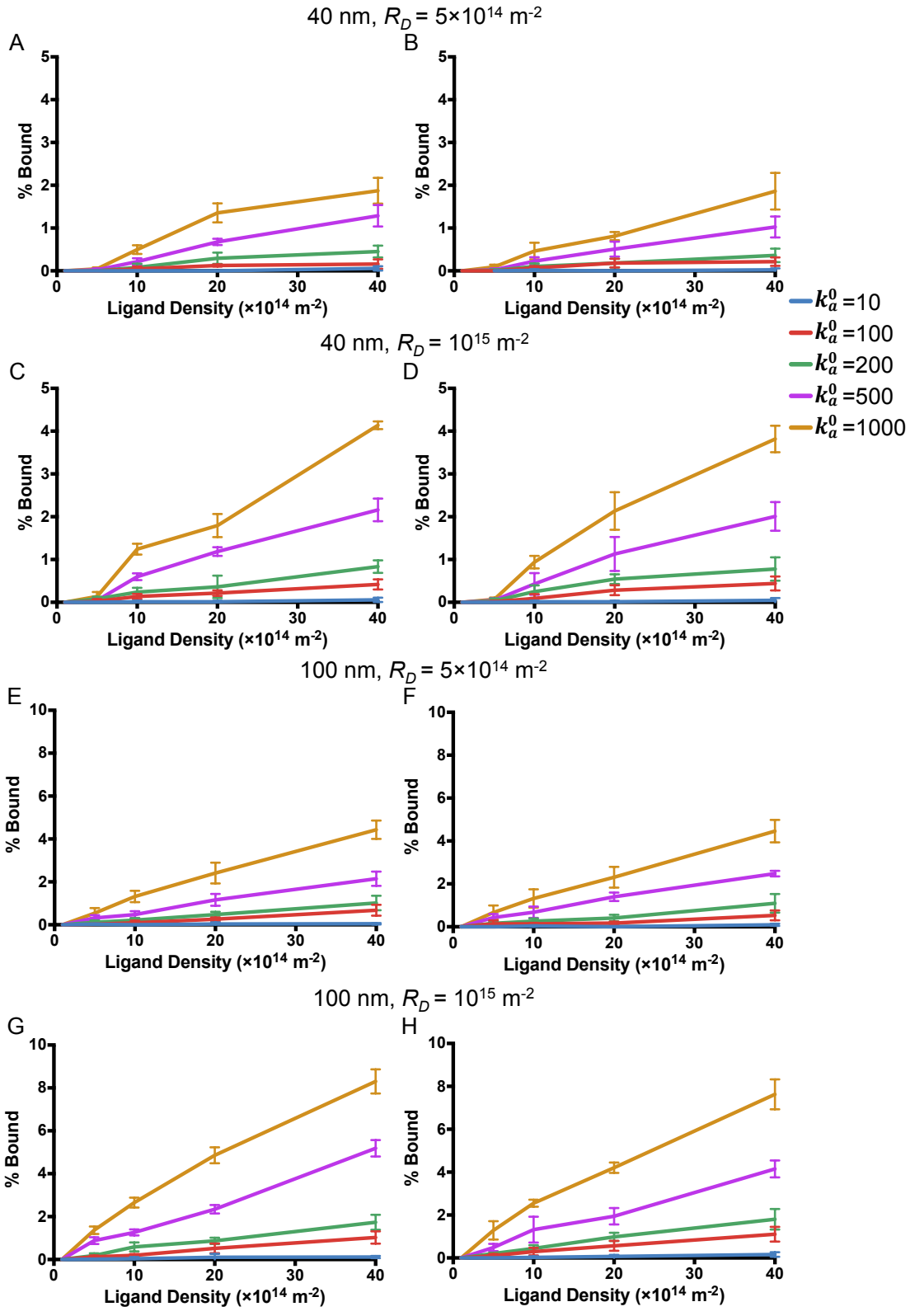

Figure 4.20: Efficiency of Nanoparticle Binding in a Capillary Model of Normal Flow and Functional Hyperaemia. Nanoparticles were simulated for 0.5 s under a normal flow (left, A, C, E and G) and functional hyperaemia (right, B, D, F and H). The percentage of nanoparticles bound to the apical side of the barrier was calculated for each composition of nanoparticle. Each data point represents the mean ± standard deviation of six simulations (n=6).

To investigate whether the lower binding efficiency was offset by the increased number of nanoparticles transiting the vessel, giving an increased number of bound particles under functional hyperaemia, the ratio of mean binding events under functional hyperaemia conditions compared to normal flow was compared after 0.05 s (*Figure 4.21*). Ratios with a cumulative error of >20% were excluded from these graphs. *Figure 4.21* demonstrates that for certain compositions of nanoparticle, there is an increased number of bound particles under functional hyperaemia. These compositions generally correlate with a higher overall binding affinity due to increased size, $\boldsymbol{k_a^0}$, ligand density and receptor density. Intriguingly, at 40 nm, several nanoparticle formulations bind at a ratio of <1 at a lower receptor density (*Figure 4.21A*), but above it at higher receptor density (*Figure 4.21B*). Therefore, induction of functional hyperaemia with these compositions should only give improved binding if the receptor density is increased. This may be a useful tool for specifically targeting the blood-brain barrier when the level of receptor expression can't be ascertained.

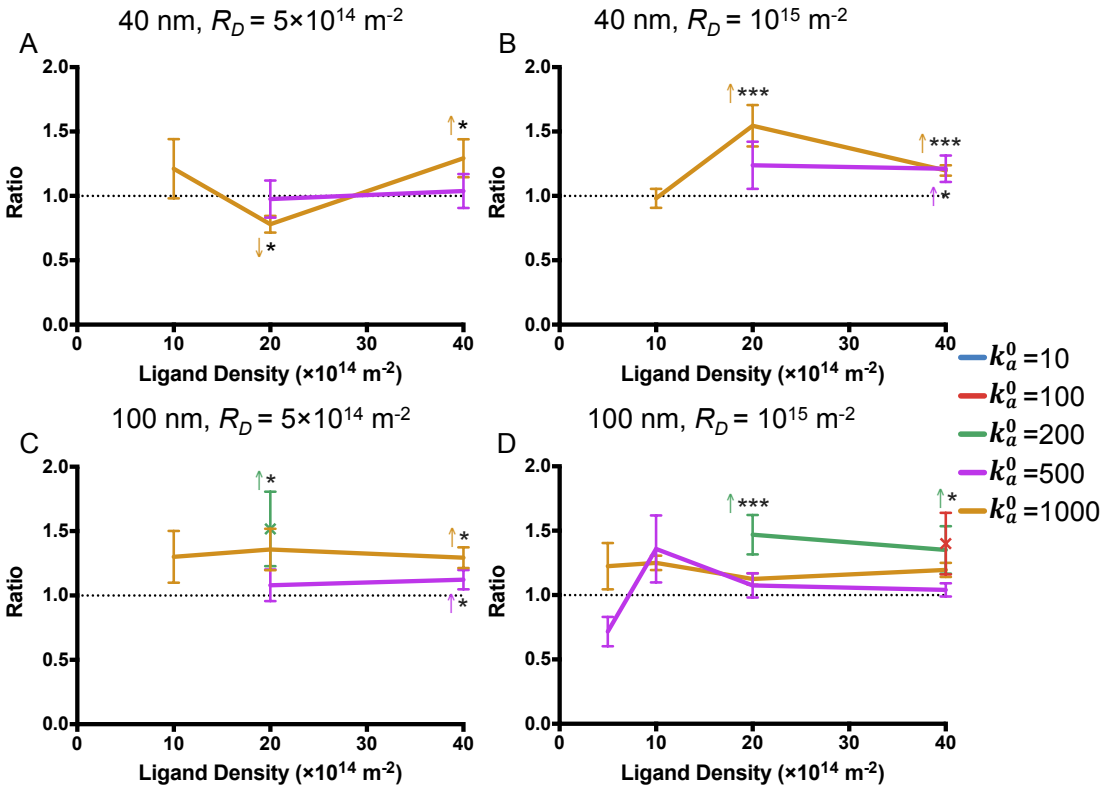

Figure 4.21: Effect of Functional Hyperaemia on Nanoparticle Binding. The ratio of nanoparticle binding under functional hyperaemia against normal flow for 40 nm (A and B) and 100 nm nanoparticles (C and D) with a receptor density of 5×10^{14} m^{-2} (A and C) or 10^{15} nm^{-2} (B and D). Points with a >20% error were excluded. Each data point is calculated from the mean ± standard error of the mean of binding under functional hyperaemia from six replicate simulations (n=6) and normal flow conditions conditions from six replicate simulations (n=6). Each point represents the ratio ± cumulative error. Significance calculated using the Holm-Sidak t-test, * P < 0.05, ** P < 0.01, *** P < 0.005, arrows represent a significant increase or decrease.

Next, the specificity for the higher receptor expression was studied. *Figure 4.22* demonstrates similar patterns to as seen in the transwell model, where specificity is generally increased with reduced overall binding affinity, either through low k_a^0 and high receptor density or high k_a^0 and low receptor density. The increases in specificity were generally slightly higher than in the transwell model. This may reflect the increased vulnerability under shear flow of nanoparticles that form fewer bonds.

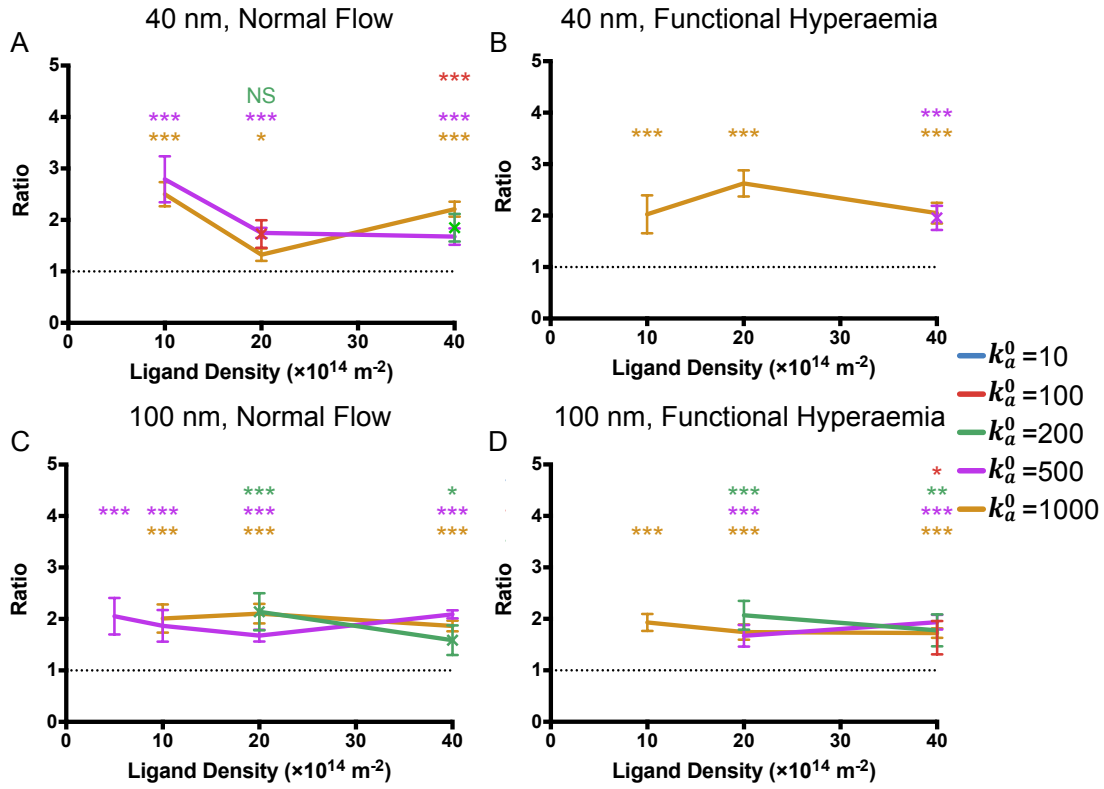

Figure 4.22: Specificity of Nanoparticles for increased Receptor Expression under Shear Flow. The ratio of binding between a receptor density of 10^{15} m^{-2} and 5×10^{14} m^{-2} for 40 nm (A and B) and 100 nm (C and D) nanoparticles under normal (A and C) or functional hyperaemia (B and D) flows. Points with a >20% error were excluded. Each data point is calculated from the mean ± standard error of the mean of binding under functional hyperaemia from six replicate simulations (n=6) and normal flow conditions conditions from six replicate simulations (n=6). Each point represents the ratio ± cumulative error. Significance calculated using the Holm-Sidak t-test, * $P < 0.05$, ** $P < 0.01$, *** $P < 0.005$

To investigate whether functional hyperaemia had an effect on the bond number, the average number of bonds *per* particle was plotted under normal flow and functional hyperaemia (*Figure 4.23*). *Figure 4.23* demonstrates that functional hyperaemia, on the whole, gives a marginal decrease in the number of receptor bonds. The increased shear stress is likely to make nanoparticles bound with very few bonds detach, which would give an overall increase in the average number of bonds *per* particle. However, it is also likely to uniformly increase the rate of bond rupture, thus giving an expected

decrease in the average number of bonds. These two effects working in tandem may result in making the difference in bond number smaller.

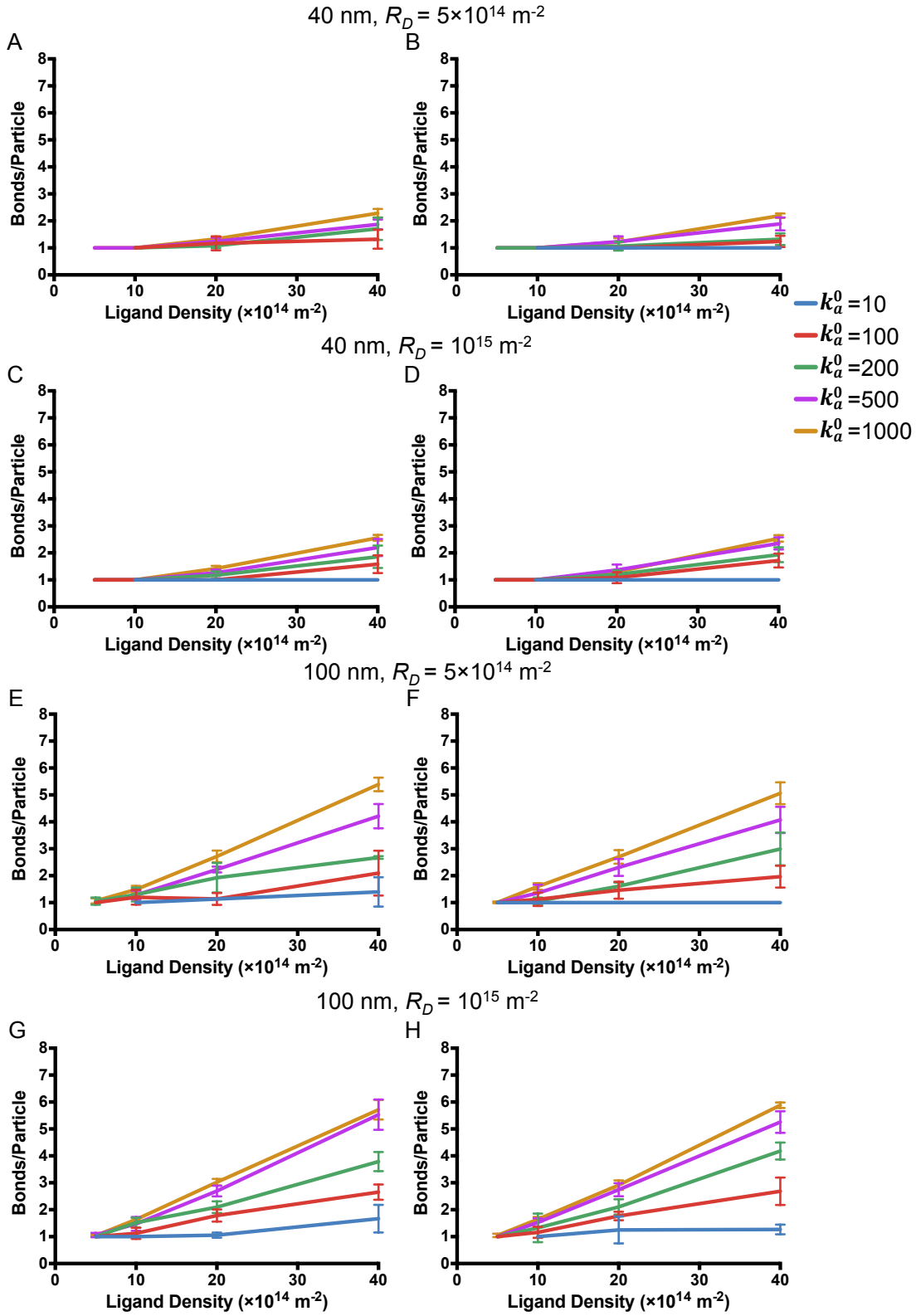

Figure 4.23: Average Number of Bonds per Nanoparticle in a Capillary Model of Normal Flow and Functional Hyperaemia. Nanoparticles were simulated for 0.5 s under a normal flow (left, A, C, E and G) and functional hyperaemia (right, B, D, F and H). The average number of bonds per bound nanoparticle was calculated for each composition of nanoparticle. Each data point represents the mean ± standard deviation of six simulations (n=6).

Finally, the ratio was calculated for nanoparticle binding under functional hyperaemia at receptor density of 10^{15} m^{-2} to normal flow with a density of 5×10^{14} m^{-2} (*Figure 4.24*). This demonstrated that combining the two methods to obtain specificity gave an improved targeting effect for some nanoparticle compositions than either method alone.

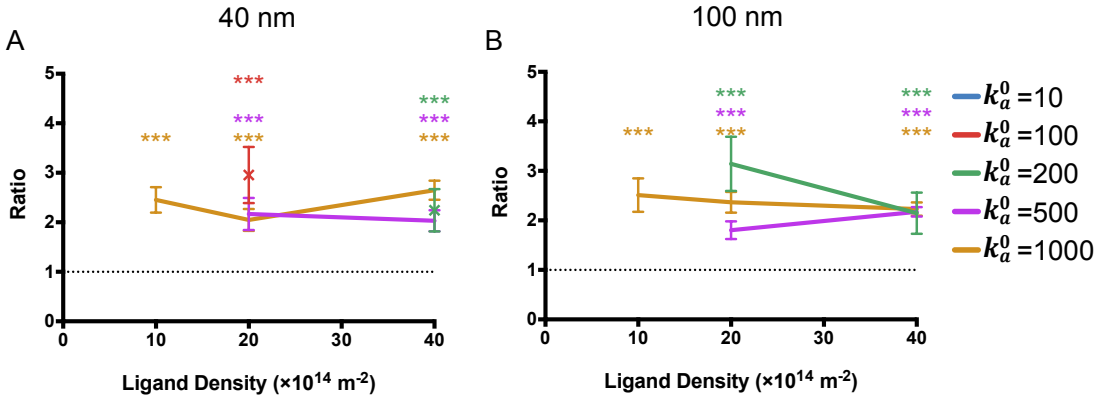

Figure 4.24: The Combined increased Specificity from induction of Functional Hyperaemia and increased Receptor Density. The ratio of binding under functional hyperaemia with a receptor density of 10^{15} m^{-2} compared to normal flow with a density of 5×10^{14} m^{-2} for 40 nm (A) and 100 nm particles (B). Points with a >20% error were excluded. Each data point is calculated from the mean ± standard error of the mean of binding under functional hyperaemia from six replicate simulations (n=6) and normal flow conditions conditions from six replicate simulations (n=6). Each point represents the ratio ± cumulative error. Significance calculated using the Holm-Sidak t-test, * $P < 0.05$, ** $P < 0.01$, *** $P < 0.005$

The models here are limited by the lack of cellular trafficking and release. In line with previous data, it can be expected that unbinding is less efficient with stronger overall binding of nanoparticles. However, there are several other factors, not considered here that may also impact unbinding efficiency. A key characteristic of these models is that binding and unbinding are related opposite processes. Cell intrinsic mechanisms to aid receptor-ligand detachment are excluded; these include changes in pH in the endosomal pathway, salt concentration and the presence of enzymes. Furthermore, a key function of the blood-brain barrier is to allow the CNS to have a different ionic composition compared to the blood (Abbott et al., 2010, Touitou and Barry, 2006); changes in ion concentration and pH can affect receptor-ligand

interactions, therefore altering the kinetics from one side of the barrier to the other. Furthermore, the impact of constituent molecules within culture media and blood are neglected in our simulations. As discussed in Chapter 3, protein fouling is often observed when nanoparticles come into contact with serum. This can cause particle swelling changing size parameters and potentially altering the binding dynamics of nanoparticles to the cell surface. Whilst a number of strategies may be employed to reduce this effect, such as PEGylation as discussed in Chapter 1, it can't be discounted that this would affect *in vitro* and *in vivo* validation of the data presented in this chapter.

The model is based on a number of previously unknown parameters, including the Lrp1-Angiopep-2 bond length, the $\boldsymbol{k_a^0}$ of the Lrp1-Angiopep-2 interaction and the receptor density of the Lrp-1 receptor on the blood-brain barrier. In their absence, a range of values from the literature and values calculated from existing data has been used. In studies of nanoparticles targeting the blood-brain barrier, size, receptor-ligand affinity and ligand density have not been considered together. However, ligand density has been considered alongside size in the work of Wiley and co-workers (Wiley et al., 2013). They used gold nanoparticles of different sizes and conjugated them to varying levels of transferrin. They demonstrated both a size and ligand density affect on the overall binding of the nanoparticles to Neuro2A cells. The overall $\boldsymbol{k_D}$ of their nanoparticles decreased with increasing size and increasing ligand density, representing a similar effect to that seen within this chapter. The ligand densities of their formulations varied from 0.001 nm^{-2} to 0.007 nm^{-2}, covering similar ranges to that covered in the simulations. The $\boldsymbol{k_D}$ of monoferric transferrin has previously been estimated to be 10^{-6} M, corresponding to a $\boldsymbol{k_a^0}$ of 100000, several orders of magnitude above that covered in the simulations (Sawyer and Krantz, 1986). Ligand densities for other nanoparticle formulations are available from the literature and also conform to the ranges investigated in this study. The Kreuter group used loperamide-loaded human serum albumin nanoparticles functionalised with the Ox26 or R17217 transferrin receptor antibodies, of ~166-168 nm, at ligand

densities of 0.003 nm^{-2} and 0.002 nm^{-2} to achieve anti-nociceptive effect in rats (Ulbrich et al., 2009).

The work by Yu and colleagues, did not directly calculate the $\boldsymbol{k_D}$ of their candidate antibodies, however they used Elisa inhibition studies to calculate IC50 values that can approximate the $\boldsymbol{k_D}$ (Yu et al., 2011). They created an anti-TfR antibody (TfR^A) and three variants of increasing IC50 value. This gave IC50 values of 1.7 nM (TfR^A), 6.9 nM (TfR^B), 65 nM (TfR^C) and 111 nM (TfR^D). When administered in trace doses, brain uptake was increased with increasing affinity. However, this trend was reversed with higher therapeutic doses with the lowest affinity performing best, hypothesised to be due to the rate-limiting step of unbinding. This demonstrates both the underlying importance of binding affinity but also blood concentration. The latter of which will be affected by blood clearance properties, underlying the need for consideration of properties including size and PEGylation on nanoparticle clearance.

A number of techniques exist to find the binding kinetics of proteins, including surface plasmon resonance (SPR), dual-polarisation interferometry (DPI), bio-layer interferometry (BLI), microscale thermophoresis (MT) and isothermal titration calorimetry (ITC). Surface Plasmon Resonance (SPR) and Dual-Polarisation Interferometry (DPI) both use an immobilised receptor and a flow system to calculate the association and dissociation properties. In SPR, binding of the receptor-ligand pair causes a change in the reflective angle, altering the signal (Pattnaik, 2005). DPI measures conformational changes that occur during a receptor-ligand interaction (Cross et al., 2008). Bio-layer interferometry is an optical technique that uses immobilised protein on a tip to detect binding and calculate binding properties (Rich and Myszka, 2007). ITC and MT do not require immobilising the receptor. ITC measures specific changes in temperature to follow the kinetics of a protein-protein interaction (Velázquez-Campoy et al., 2001). MT is able to detect changes in size, charge and hydration shell. It uses this data to follow the course of a reaction and ascertain the kinetics of the reaction (Wienken et al., 2010).

Whilst the literature does contain references to ligand density, receptor-ligand affinity and size, receptor density is rarely considered in blood-brain barrier delivery. In recent work, Chen and colleagues, established a technique to find the receptor density of live cells using fluorescence correlation spectroscopy and fluorescently labelled aptamers that bind specific cell surface receptors (Chen et al., 2009). They used this technique to look at the receptor density of protein tyrosine kinase 7 (PTK7) on two different cell lines and found densities of 5×10^{14} and 1.3×10^{15}, similar to the two values used in this study. It cannot be discounted also that differences in receptor expression will be found between species and different cell lines, which may affect the translation of results from *in vitro* to *in vivo* models.

Future work to ascertain these values would aid refinement of these methods. Furthermore, better integration of biological imaging techniques, such as fMRI, into more complex blood flow models may allow development of personalised treatment strategies. This could consider other aspects of changes in blood flow, including changes in neurovascular coupling and blood flow associated with disease.

One additional effect of nanoparticle binding strength that we have not studied is the effect of strong binding on nanoparticle penetration throughout the entire tissue. Frieboes and colleagues demonstrated that particles that bind rapidly and strongly to the vessel walls in tumour models gave a depletion effect throughout the remaining downstream vasculature network (Frieboes et al., 2013). This limits the potential for nanoparticles to penetrate throughout the entire tissue, potentially limiting therapeutic effect. This could be addressed by future work extrapolating these models to models of a vascular network.

The model only considers the binding of a single receptor on the blood brain barrier. However, nanoparticles have the potential to be decorated with multiple ligands; these are often used to target different cells. The wide-expression of Lrp-1 and the transferrin receptor in the CNS and in the periphery may cause off-target effects, multiple ligands could be used to give

better specificity. By using weak affinity ligands and a moderate ligand density, only the collective binding of different ligands would enable strong binding. This technique could be used to improve specificity to particular cell populations. However, whilst this would work in principle in terms of cellular binding, it is not possible to predict what the influence of binding different receptors will be on cellular transport. Further studies of the mechanism of transcytosis will enable better understanding of the routes through the cell and may lead to future improvements of the models presented in this chapter and better formulation of nanoparticles for optimal delivery across the blood-brain barrier and to cells of the CNS.

In the Battaglia laboratory, Angiopep-2 functionalised POEGMA-PDPA polymersomes have been used in the transwell model with a *B.End3* endothelial cell barrier. Varying the degree of polymer functionalisation altered the ligand density on the polymersomes. 1%, 2%, 3%, 4%, 5% and 6% Angiopep polymersomes were formulated giving ligand densities of 9.2×10^{14} m^{-2}, 1.8×10^{15} m^{-2}, 2.7×10^{15} m^{-2}, 3.6×10^{15} m^{-2}, 4.6×10^{15} m^{-2} and 5.5×10^{15} m^{-2} respectively. The transcytosis efficiency was measured at 30 minutes as seen in *Appendix IV*. This demonstrates that a higher ligand density can indeed reduce transcytosis efficiency. Whilst, the $\boldsymbol{k_a^0}$ of Angiopep-2-Lrp1 interaction and Lrp1 receptor density are unknown, this demonstrates a similar principle does occur *in vitro*.

4.4 CONCLUSIONS

In conclusion, agent-based models of nanoparticle binding to the blood-brain barrier in *in vitro* transwell and capillary models have been studied. It has been demonstrated that tailoring nanoparticle properties can control binding specificity for a higher level of receptor expression according to these models. Furthermore, an increase in blood flow velocity associated with functional hyperaemia improves overall nanoparticle delivery, for certain formulations, despite the reduced binding associated with increased shear stress. In the future, refinement of these models using biological data from the blood-brain

barrier and patients could enable personalised medicine for improved specific delivery to different regions of the CNS.

CHAPTER 5: RESULTS AND DISCUSSION III

MODELLING THE CHEMOTAXIS PROPERTIES OF NANOPARTICLES

5.1 INTRODUCTION

An important goal in the nanoparticle-mediated delivery of therapeutics is to improve their specificity, thus improving therapeutic load at target cells and reducing side-effects. The blood is a highly effective delivery system to all tissues of the body, particularly to the CNS. Nanoparticle properties such as size, shape, surface chemistry and active-targeting of desired tissues dictates their ability to penetrate into the target tissue and find target cells to release their cargo. In *Chapter 4*, receptor-mediated nanoparticle-cell binding was explored as a method to obtain specificity when nanoparticles interact with a potential target, with particular focus on transcytosis across the blood-brain barrier. However, another key aspect of successful delivery is in maximising the access of nanoparticles to the cells of interest. In order to reach their target cells within the CNS, nanoparticles in the blood must surpass a series of biological barriers. The first of which is the endothelial blood-brain barrier that regulates blood-tissue exchange. Nanoparticles that successfully reach the CNS must then penetrate through the parenchyma to reach the target cells. At the target cells, nanoparticles can be taken up and release their therapeutic cargo.

Recent work within the field of micro- and nano-scale technology has studied the introduction of chemotaxis properties into synthetic systems. Chemotaxis allows cells and bacteria to respond to chemical stimuli with changes in motility. In *Chapter 1*, the recent development of chemotactic polymersomes, within the Battaglia group, was discussed. These nanoparticles are able to follow glucose and hydrogen peroxide gradients by a combination of self-diffusiophoresis and self-osmophoresis. Chemotaxis to or from chemical stimuli within the body may be used to increase the distribution of

nanoparticles to their respective targets, ultimately improving both specificity and reducing off-target effects.

5.2 AIMS AND OBJECTIVES

In the work presented in this chapter, agent-based modelling is utilised to study nano- and micro- scale particles undergoing chemotaxis. The aim of this work is to investigate whether the introduction of non-substrate dependent directed motility, termed propulsion, properties can improve nanoparticle escape from the blood into the CNS and whether directed chemotaxis can aid distribution to targets. Furthermore, methods to better control chemotaxis efficiency for different gradients is explored.

5.3 RESULTS AND DISCUSSION

5.3.1 Building an Agent-based Model of Particle Propulsion

In order to effectively investigate the functions of chemotactic nanoparticles, a 3D model of nanoparticles undergoing propulsion was first developed using FLAME. This model initially makes the assumption that the substrate is homogenous and therefore the rate of propulsion is independent of substrate concentration. The characteristic random walk or Brownian motion of particles was generated by the methods of Andrews and Bray, as tested in *Chapter 3*, to give the movement vector for Brownian motion ($\boldsymbol{F_B}$) (Andrews and Bray, 2004). Rotational diffusion was modelled in a similar manner to the random walk, using the rotational diffusion coefficient ($\boldsymbol{D_r}$):

$$\boldsymbol{D_r} = \frac{\boldsymbol{k_B T}}{\boldsymbol{8\pi\eta r^3}} \qquad (5.1).$$

Three separate angles, ϑ, ι and κ were used for rotating around the x-, y- and z- axes respectively. The angles were rotated according to rotational diffusion by addition of $\Delta\vartheta$, $\Delta\iota$ and $\Delta\kappa$, generated through substituting $\boldsymbol{D_r}$ for $\boldsymbol{D_c}$ in the

Andrews and Bray method. A vector of propulsion ($\boldsymbol{F_P}$) was given as starting in the positive *y* direction:

$$\boldsymbol{F_P} = \begin{bmatrix} \mathbf{0} \\ \boldsymbol{\varphi \delta t} \\ \mathbf{0} \end{bmatrix} \qquad (5.2)$$

where φ is the velocity of propulsion and δt the time-step. This vector was then rotated according to the rotational diffusion, thus giving directional movement. The vector of propulsion was then added to the random movement vector generated for Brownian motion to give a total movement vector ($\boldsymbol{F_T}$) of:

$$\boldsymbol{F_T} = \boldsymbol{F_B} + \boldsymbol{F_P} \qquad (5.3).$$

Particles were propelled at velocities of 0 μm·s^{-1}, 10 μm·s^{-1}, 20 μm·s^{-1}, 50 μm·s^{-1} and 100 μm·s^{-1}. Particle motion was evaluated by calculating the mean squared displacement (MSD) of individual particles against time (t):

$$\boldsymbol{MSD(t)} = \langle \boldsymbol{q(t)} - \boldsymbol{q(0)} \rangle^2 \qquad (5.4)$$

where $\boldsymbol{q(t)}$ is the position of the particle at time $\boldsymbol{t}$ and $\boldsymbol{q(0)}$ is the position of the particle at time 0. The expected MSD for a particle of radius r is calculated through the diffusion coefficient ($\boldsymbol{D_c}$) and the relationship:

$$\boldsymbol{MSD} = \boldsymbol{kD_c} \qquad (5.5)$$

where $\boldsymbol{k}$ is a constant related to the number of dimensions, in 3D $\boldsymbol{k}$ is equal to 6.

Particles acting under directed propulsion should demonstrate a non-linear increase in MSD across short time-scales, reverting to a non-directed propulsion regime of a linear increase, albeit with an increased diffusion coefficient, over longer time-scales. The time it takes for this switch from a non-linear to a linear increase is dependent on the rotational diffusion coefficient, effectively how long it takes for particle to re-orientate (Howse et al., 2007, Palacci et al., 2010). The MSD, over time, was evaluated for four diameters of spherical particle, 100 nm, 200 nm, 500 nm and 1 μm. The translational and rotational diffusion coefficients for each particle, calculated through the Stokes-Einstein relations, are given in *Table 5.1*.

Diameter	D_c **(μm·s^{-1})**	D_r **(s^{-1})**
100 nm	2.671	801.4
200 nm	1.336	100.2
500 nm	0.534	6.411
1 μm	0.267	0.801

Table 5.1. Translational and Rotational Diffusion Coefficients for different Sized Particles. Temperature (T) = 310 K, viscosity (η) = 0.0017 Pa·s.

The average MSD over time for 20 individual particles (*Figure 5.1*) demonstrates that the 100 nm and 200 nm populations exhibit mainly linear increases in average MSD, albeit with an increased MSD with higher levels of propulsion (50 μm·s^{-1} and 100 μm·s^{-1}). However, 500 nm and 1 μm populations demonstrate non-linear increases in MSD over time when a propulsion velocity is applied.

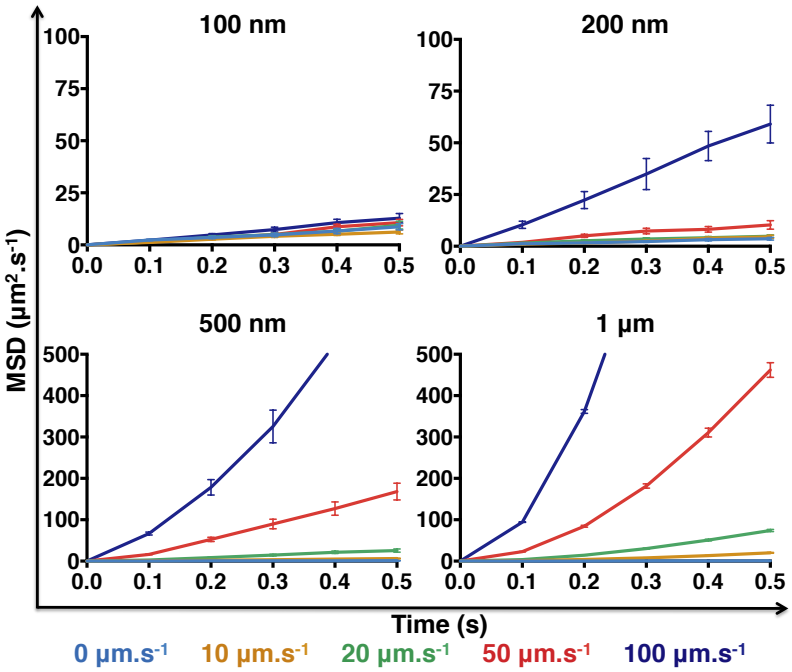

Figure 5.1: The Average Mean Squared Displacement of a Population of Nanoparticles *versus* Time. The average MSD of 100 nm, 200 nm, 500 nm and 1 µm nanoparticle populations is plotted at 0.1 s intervals for 0.5 s with propulsion velocities of 0 µm·s^{-1}, 10 µm·s^{-1}, 20 µm·s^{-1}, 50 µm·s^{-1} and 100 µm·s^{-1}. Each data point represents the mean ± standard deviation of 20 simulations (n=20).

Individual particle traces for MSD against time (*Figure 5.2*) show that for 100 nm and 200 nm populations, the rotational time is such that direction of motion is re-orientated over time periods shorter than the length of simulation.

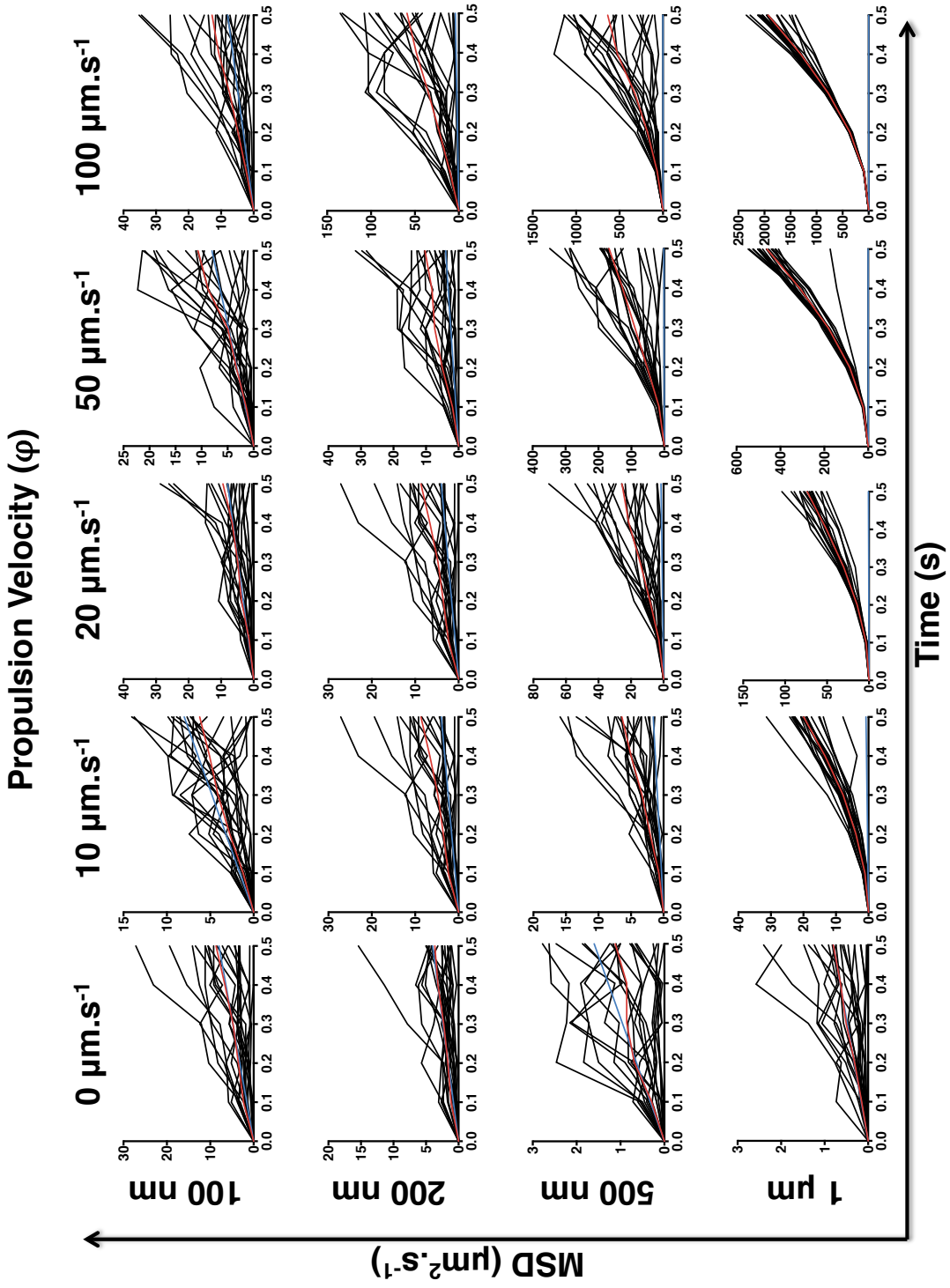

Figure 5.2: The Mean Squared Displacement of a Population of Nanoparticles versus Time. The individual MSDs of a population of 20 nanoparticles of size 100 nm, 200 nm, 500 nm or 1 µm are plotted at 0.1 s intervals for 0.5 s with propulsion velocities of 0 µm·s^{-1}, 10 µm·s^{-1}, 20 µm·s^{-1}, 50 µm·s^{-1} and 100 µm·s^{-1}. The red line indicates the average MSD for all particles, the blue line indicates the expected MSD when the propulsion velocity is equal to 0 µm·s^{-1}.

This is further demonstrated in the motion traces (*Figure 5.3*), where particles show an increased displacement with increased propulsion but lack orientational persistence across the whole simulation time, thus giving the linear increases observed in *Figure 5.1*.

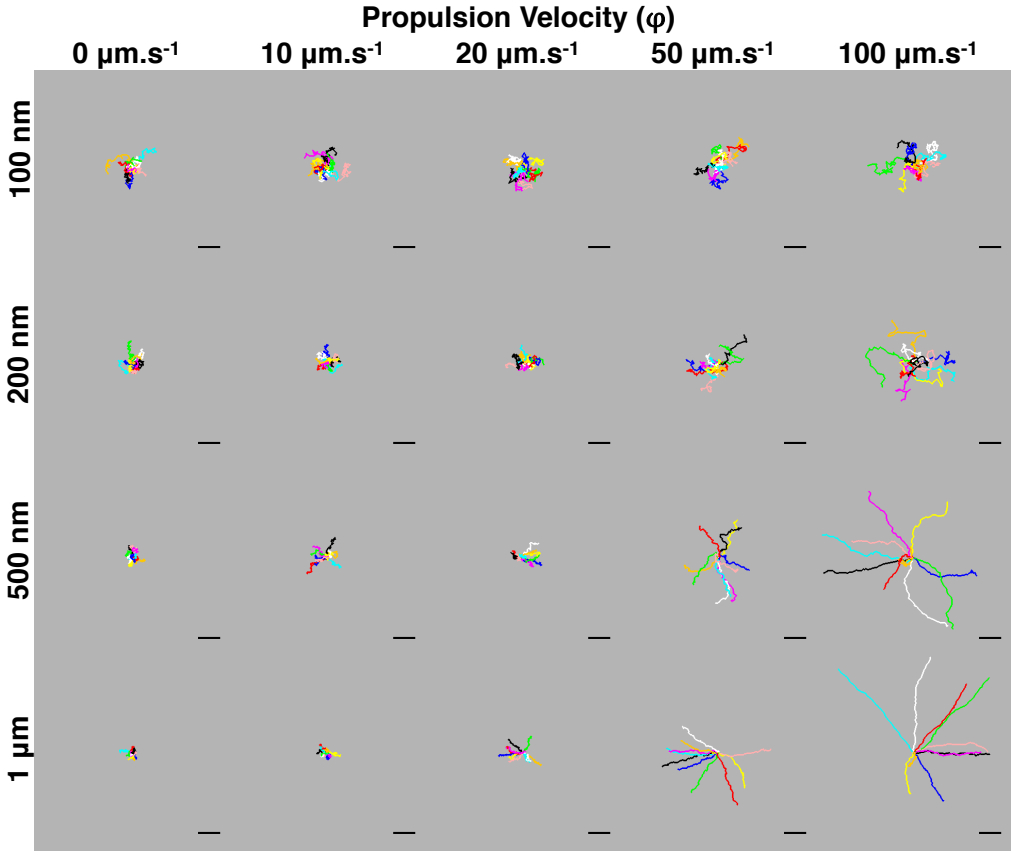

Figure 5.3: Nanoparticle Motion Traces with varying Size and Propulsion Velocity. The motion of 10 nanoparticles is tracked for 0.05 s at 0.001 s intervals. Nanoparticles start at a common origin in the centre of the simulation region. Separate colours indicate individual nanoparticles. Scale bar =1 µm.

Individual 500 nm and 1 µm particles demonstrate good orientational persistence in forming enhanced non-linear MSD curves (*Figure 5.2*) and motion traces where particles steadily move away from the common origin with a more linear trajectory (*Figure 5.3*). The whole population for 1 µm particles displays a highly uniform trend across 0.5 s, as compared to the 500 nm population, reflecting the small effect of rotational diffusion on 1 µm particles, thus enabling improved motility in a single direction over longer

periods of time. The result of this is that large particles are able to better follow a single trajectory over time.

5.3.2 Accumulation of Particles undergoing Propulsion at Interfaces

The increased displacement of particles acting under propulsion may aid distribution to the edges of a confined space, as would be expected in a biological system. In order to investigate this, 10 nanoparticles were simulated in a 2 μm box and their motion was traced across 0.05 s (*Figure 5.4*). The slow rotational times of the 500 nm and 1 μm populations allowed the nanoparticles to accumulate at the edges of the box, a phenomenon also observed with higher velocities for the 200 nm population. The motion traces for the 100 nm population show no such accumulation at the edge of the box, however as propulsion velocity increases, the particles appear to displace further, in accordance with the findings from *Figure 5.1*. Therefore they may interact with the edge more often than by Brownian motion alone. The accumulation at solid interfaces has previously been reported using a similar 2D model of propelled 1 μm particles (Volpe et al., 2011, Volpe et al., 2014). This principle may be used to aid accumulation of particles at cellular interfaces, thus stimulating improved transport.

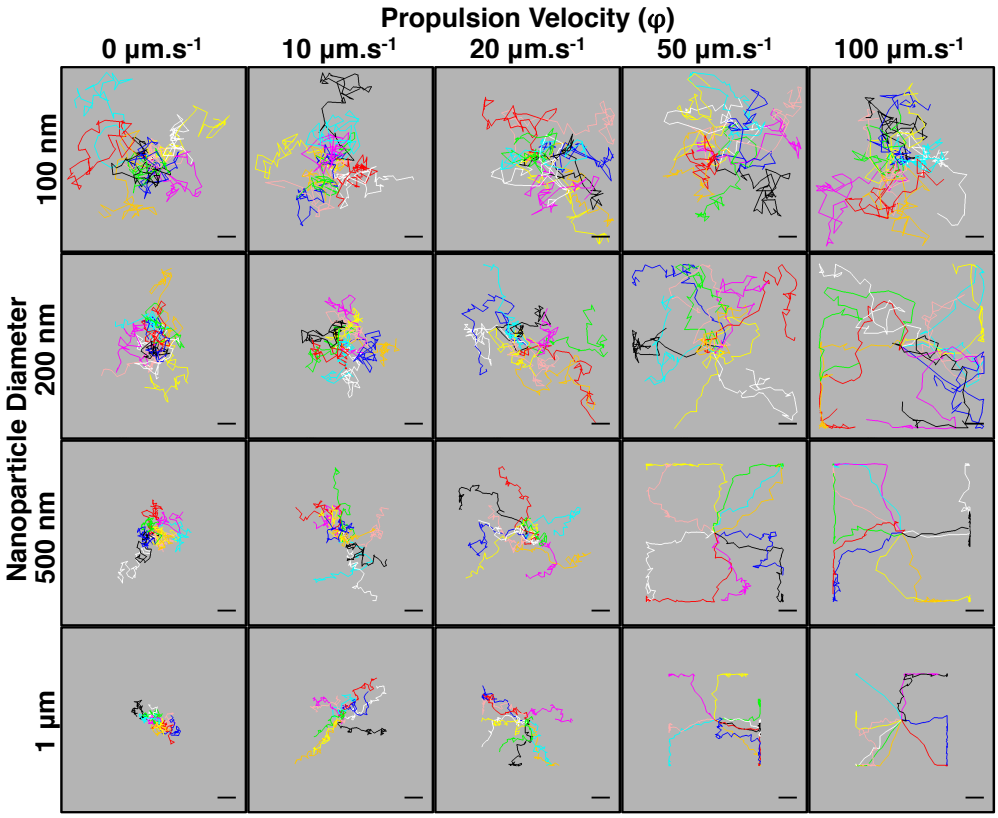

Figure 5.4: Nanoparticle Motion Traces with varying Size and Propulsion Velocity. The motion of 10 nanoparticles, confined in a 2×2×2 μm box, is tracked for 0.05 s at 0.001 s intervals. Nanoparticles start at a common origin in the centre of the box. Separate colours indicate individual nanoparticles. Scale bar = 200 nm.

5.3.3 Propulsion and Blood-Tissue Transport

The increased displacement and accumulation at interfaces of particles undergoing propulsion may aid dispersion within the blood to the vessel wall interfaces where transport occurs. In order to test the effect of placing propelled nanoparticles in the context of blood flow, two different models of laminar flow within a capillary were used, a simple Poiseuille's flow model and the model demonstrated in *Chapter 3*. This model incorporated both laminar and Brownian forces acting upon the nanoparticle by the relationship:

$$\boldsymbol{F_T} = \boldsymbol{F_B} + \boldsymbol{F_L} \qquad (5.6)$$

where $\boldsymbol{F_L}$ is the vector of movement generated from the laminar flow. To include laminar, Brownian and propulsion forces within a model of blood flow the vector for propulsion was therefore added to give:

$$\boldsymbol{F_T} = \boldsymbol{F_B} + \boldsymbol{F_L} + \boldsymbol{F_P} \qquad (5.7).$$

Particles undergoing propulsion were first simulated in the Poiseuille's model of blood flow. Nanoparticles were seeded randomly at the entrance of the vessel and allowed to passage through the vessel. The vessel walls were set as no-slip, sticky boundaries, so that the number of nanoparticles stuck to the vessel wall could be evaluated with different sized particles and velocities of propulsion. The motion of the nanoparticles was tracked through a latitudinal cross-section of the vessel and shows a similar effect to that seen in *Section 5.3.2*, where larger particles accumulate at the vessel walls and smaller particles demonstrate an overall increase in motility (*Figure 5.5*).

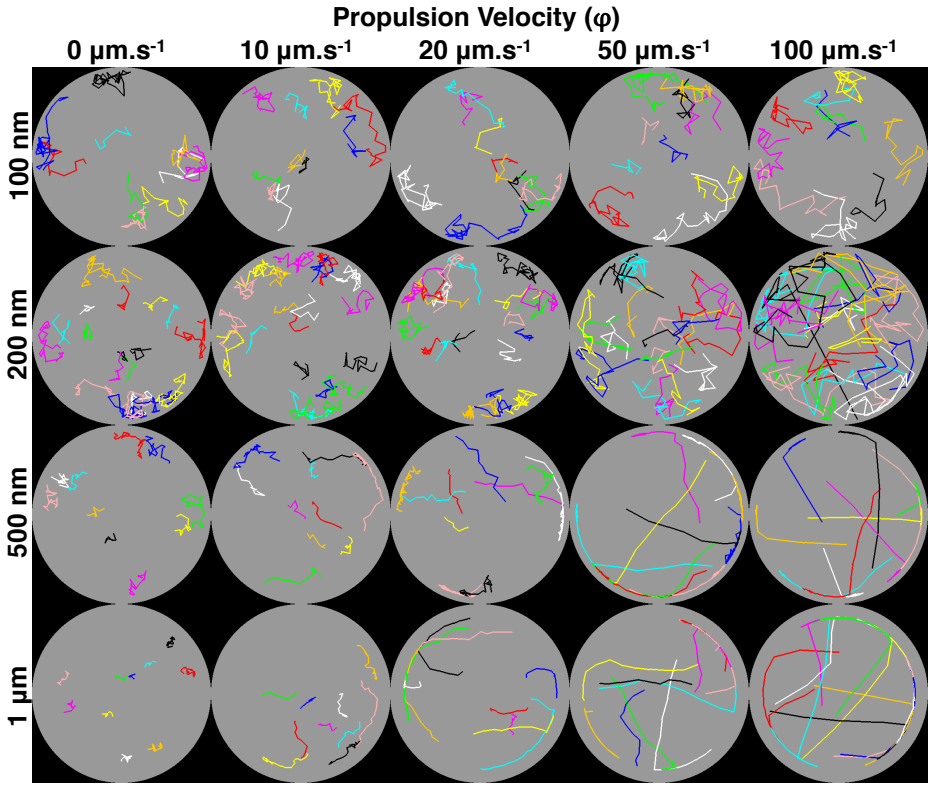

Figure 5.5: Nanoparticle Motion Traces with varying Size and Propulsion Velocity inside a Capillary. The motion of 10 nanoparticles is tracked for 0.05 s at 0.001 s intervals in a latitudinal cross-section of a Poiseuille's model of a capillary 8 μm in diameter. Nanoparticle traces that exit the vessel or bind to the wall are terminated. Separate colours indicate individual nanoparticles.

Figure 5.6 shows the percentage of particles that bind to the vessel wall during a single passage through the vessel. Binding to the vessel walls generally is improved by increasing the propulsion velocity in all samples. The naturally higher motility of 100 nm particles due to diffusion alone and lack of orientational persistence, makes this increase smaller in these groups, but it reaches significance at higher propulsion velocities ($P=0.0006$ for $\varphi=50$ μm·s^{-1} and $P=2.16\times10^{-9}$ for $\varphi=100$ μm·s^{-1}).

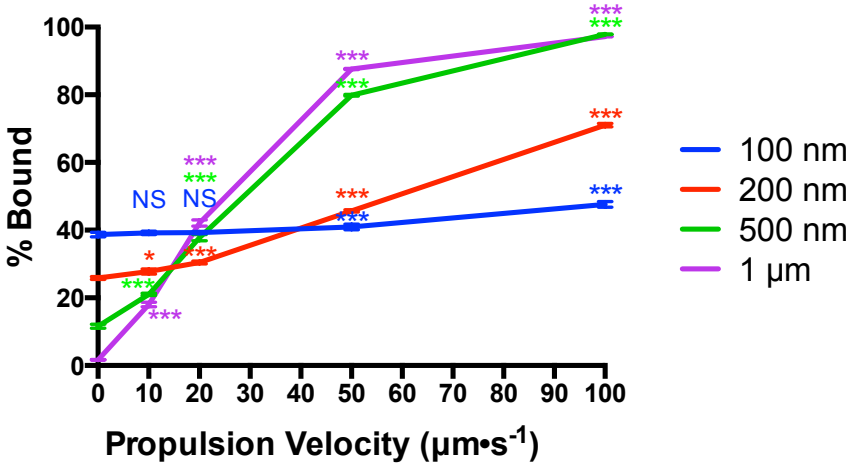

Figure 5.6: Binding of Nanoparticles undergoing Propulsion in a Simple Model of a Capillary. The percentage of nanoparticles bound when transiting through a Poiseuille flow model of a capillary with diameter of 8 µm, with different size particles and propulsion velocities of 0 µm·s^{-1}, 10 µm·s^{-1}, 20 µm·s^{-1}, 50 µm·s^{-1} and 100 µm·s^{-1}. Each data point represents the mean ± standard deviation of six simulations (n=6). Significance calculated using the Holm-Sidak t-test, points tested against nanoparticle populations of the same size but with a propulsion of 0 µm·s^{-1}, * $P < 0.05$, ** $P < 0.01$, *** $P < 0.005$

In order to see if this effect was maintained in a more realistic model of blood flow in a capillary, particles undergoing propulsion were tested in the model from *Chapter 3*. Particles were evenly distributed across the entire vessel, to minimise the effects from differences in their proximity to a RBC and simulated for 0.05 s. 500 nm and 1 µm populations were omitted from this experiment because their large size would likely significantly affect the blood flow in this model and their large sizes are well above the optimal range of nanoparticle size for *in vivo* application. *Figure 5.7* shows that whilst a similar conclusion can be made as to under Poiseuille's flow, where a higher propulsion velocity leads to higher uptake, the differences between samples are more pronounced and significance is reached for 100 nm particle at a propulsion velocity of 20 µm·s^{-1} (P=0.00088).

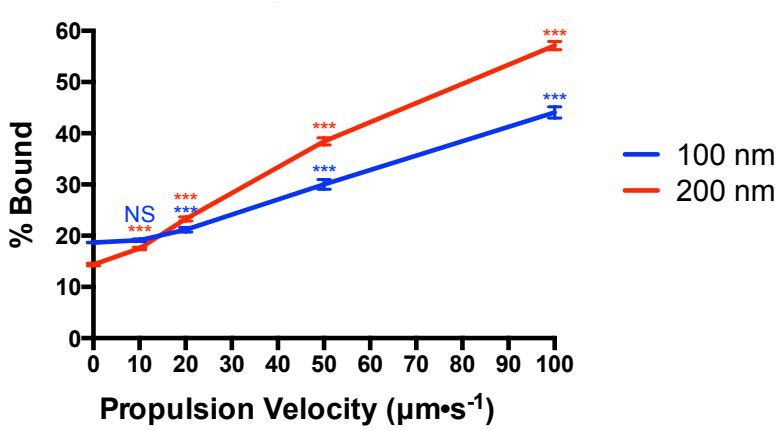

Figure 5.7: Binding of Chemotactic Nanoparticles in a Capillary. The percentage of nanoparticles bound when transiting through a complex model of capillary blood flow incorporating RBCs, with different size particles and propulsion velocities of 0 µm·s^{-1}, 10 µm·s^{-1}, 20 µm·s^{-1}, 50 µm·s^{-1} and 100 µm·s^{-1}. Each data point represents the mean ± standard deviation of three simulations (n=3). Significance calculated using the Holm-Sidak t-test, points tested against nanoparticle populations of the same size but with a propulsion of 0 µm·s^{-1}, * $P < 0.05$, ** $P < 0.01$, *** $P < 0.005$

Therefore, modelling would suggest that adding an element of propulsion to nanoparticle motion might increase overall uptake from the blood due to the improved distribution of nanoparticles to the endothelial wall interface. It should be noted that whilst improved distribution to the vessel walls is important for uptake, the increased motility might also alter the efficiency of nanoparticle binding. Moreover, the physical mechanisms underlying self-diffusiophoresis and self-osmophoresis will likely be affected by the laminar flow, a concept not addressed by the simulations.

In previous work within the Battaglia group, chemotactic polymersomes of 70-100 nm demonstrate orientational persistence that is far greater than expected from rotational diffusion. Therefore, it is hypothesised that the mechanism of self-diffusiophoresis/self-osmophoresis is able to reduce the angular velocity of these particles. The mechanism for this remains subject to further investigation, however it has been predicted in theoretical studies and demonstrated with microscale particles undergoing self-diffusiophoresis (Golestanian et al., 2007, Howse et al., 2007). The decreased angular velocity of these particles may enable the improved accumulation of 100 nm and 200

nm particles at interfaces in a similar manner to 500 nm and 1 μm particles, potentially increasing their uptake from the blood.

This effect was validated in *in vitro* and *in vivo* experiments with chemotactic polymersomes. Chemotactic polymersomes were able to migrate against a low flow through a 100 mm Petri dish towards a gradient of glucose. Furthermore, in polymersome uptake was enhanced by the addition of chemotactic properties in rat experiments studying delivery to the CNS using *in situ* perfusion of the rat brain. Chemotactic polymersomes, responsive to glucose and functionalised with Angiopep-2 (A-EP-EB), demonstrated a nearly 2-fold delivery increase into the parenchyma compared to non-chemotactic polymersome controls (*Appendix V*). The use of glucose as a substrate ensured that there would be a high level of substrate available within the blood, as blood glucose is maintained at ~4-7.8mM. However, in future, more specific and less ubiquitous stimuli may be used to improve specificity of this effect. The release of non-abundant stimulus into the blood by a tissue will create a local high concentration that will dissipate as it circulates the body, thus limiting this effect to the microvasculature of the tissue of release. Furthermore, similar principles could be used with particles that respond to non-chemical stimuli such as temperature (Jiang et al., 2010) or magnetic fields (Tierno et al., 2008). The use of magnetic nanoparticles has previously been demonstrated to improve uptake to the CNS across the blood-brain barrier (Pulfer et al., 1999, Pulfer and Gallo, 1998, Qiao et al., 2012).

5.3.4 Chemotaxis

To investigate whether chemotaxis could aid distribution to target cells, the model of particles undergoing propulsion was adapted to simulate substrate-dependent propulsion. Force of propulsion ($\boldsymbol{F_P}$) is given as proportional to the rate of reaction ($\boldsymbol{u}$), which for an enzyme following Michaelis-Menten kinetics is:

$$\boldsymbol{u} = \frac{\boldsymbol{u_{max}[S]}}{\boldsymbol{k_m + [S]}} \qquad (5.8)$$

where $\boldsymbol{k_m}$ is the concentration of substrate ($[\boldsymbol{S}]$) that gives a reaction rate equal to $\frac{\boldsymbol{u_{max}}}{\boldsymbol{2}}$. $\boldsymbol{u_{max}}$ is given by the enzymatic capacity of the enzyme, calculated from the conversion rate of a single enzyme ($\boldsymbol{k_{cat}}$) and the concentration of the enzyme ($[\boldsymbol{E}]$):

$$\boldsymbol{u_{max}} = \boldsymbol{k_{cat}}[\boldsymbol{E}] \qquad (5.9)$$

Therefore the rate of propulsion can be given:

$$\boldsymbol{F_P} \propto \frac{\boldsymbol{k_{cat}[E][S]}}{\boldsymbol{(k_m + [S])}} \qquad (5.10).$$

The size of particle, size of the enzyme and the method of encapsulation or attachment to the nanoparticle dictate the concentration of enzyme. The size data, encapsulation concentration based on data from Claudia Contini, $\boldsymbol{k_m}$ and $\boldsymbol{k_{cat}}$ for glucose oxidase from *Aspergillus niger* in a 100 nm polymersome are given in *Table 5.2*.

Property	Value
Molecular Weight	160 kDa
Encapsulation Efficiency (Molecules/ 100 nm Polymersome)	~18
$[E]$	0.135 mM
k_m	~30 mM
k_{cat}	920 s^{-1}

Table 5.2: Encapsulation and Enzyme Properties of Glucose Oxidase from *A. niger*. (Gibson et al., 1964, Swoboda and Massey, 1965).

Therefore the maximal reaction velocity (u_{max}) for polymersome encapsulated glucose oxidase is equal to 124.2 $mM \cdot s^{-1}$. The substrate dependent reaction velocity is given in *Figure 5.9*.

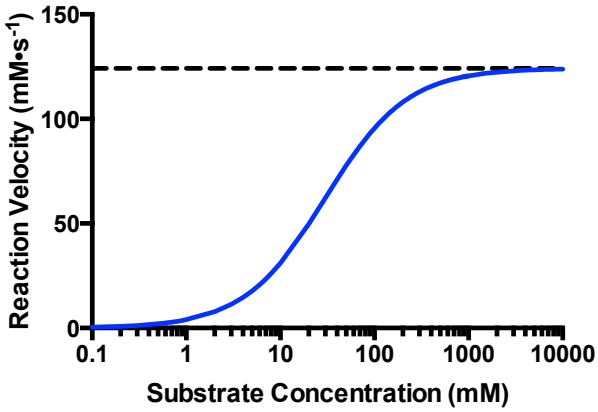

Figure 5.8: Substrate-dependent Reaction Velocity. The reaction rate of glucose oxidase, at a concentration of 0.135 mM, against substrate concentration.

It is assumed that the velocity of propulsion (φ) is related to the velocity of reaction. This relationship is complex, as demonstrated by the work of the Golestanian group (Golestanian et al., 2007). Therefore, a simplified relationship is used:

$$\varphi = \frac{u\varphi_{max}}{u_{max}} \qquad (6.8)$$

where φ_{max} is the maximal propulsion of velocity, given as 0 µm·s^{-1}, 10 µm·s^{-1}, 20 µm·s^{-1}, 50 µm·s^{-1} or 100 µm·s^{-1}, in accordance with previous rates of propulsion velocity.

Particles were placed in the centre of a simulated box and different gradients were applied across the box (*Figure 5.10*). The edges of the box were treated as reflective boundaries, except the top and bottom edges that were treated as sticky boundaries. The substrate concentration was given as linear gradients from 0 mM to 0 mM, 0 mM to 10 mM, 0 mM to 30 mM and 0 mM to 1000 mM (bottom to top), to reflect the different stages of the Michaelis-Menten profile. These were when the reaction rate is equal to 0 (0 mM), before the exponential phase (10 mM), during the exponential phase at the k_m (30 mM) and after the exponential phase (1000 mM) (*Figure 5.10*).

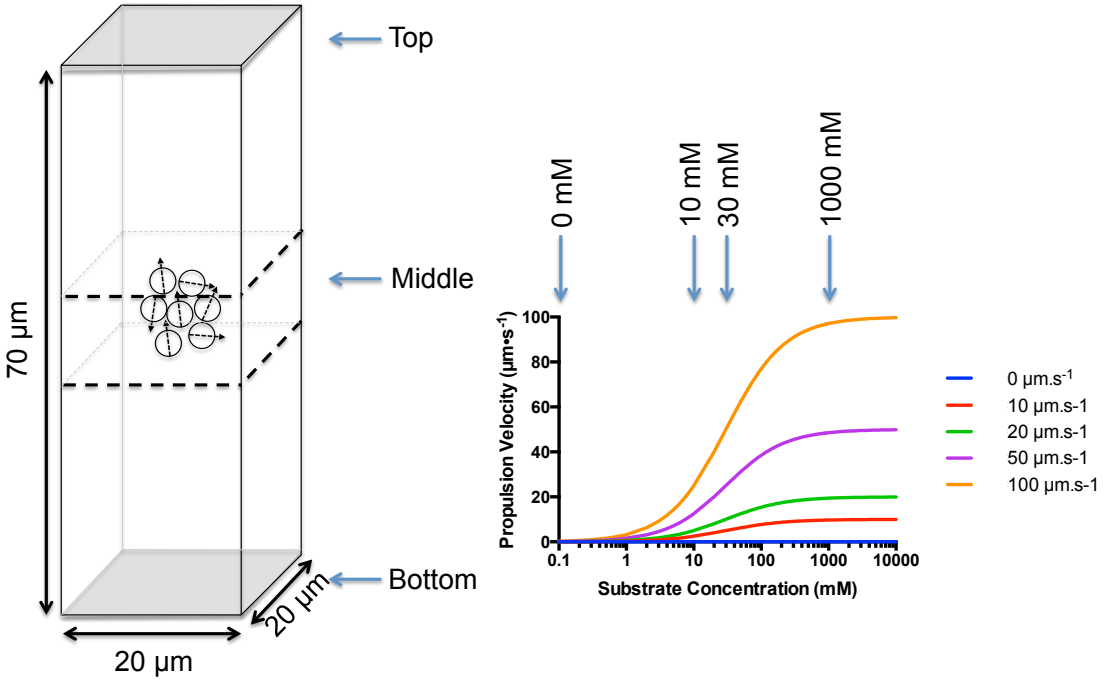

Figure 5.9: Chemotaxis Simulation Set up. Particles were placed in the centre of the simulation area and gradients were applied to the particles. The propulsion velocity was related to the substrate concentration by the Michaelis-Menten kinetics.

100 nm, 200 nm, 500 nm and 1 µm particles were simulated for 0.4 s and the chemotaxis efficiency scored by the ratio of particles bound to the top against the bottom (*Figure 5.11*). When no substrate concentration gradient is present, particle segregation is driven by diffusion, therefore the chemotaxis ratio should be equal to 1, as observed for all particle sizes in *Figure 5.11A*. However, when substrate is present, the segregation is driven by propulsion. In moderate gradients, 500 nm and 1 µm particles show a directional bias towards the source of substrate (*Figure 5.11B* and *C*). A weak but consistent chemotactic effect is also observed with 200 nm particles, but no directional biased is observed for 100 nm particles in any gradient applied (*Figure 5.11B, C* and *D*). This is in line with current opinion on nano-scale chemotactic systems, that the high rotational times of these particles is inhibitive to chemotaxis over long distances and time periods (Howse et al., 2007, Palacci et al., 2010). When the substrate concentration is steep and the reaction velocity tends towards u_{max}, chemotaxis is generally poor with only slight increases in chemotaxis scores (*Figure 5.11D*).

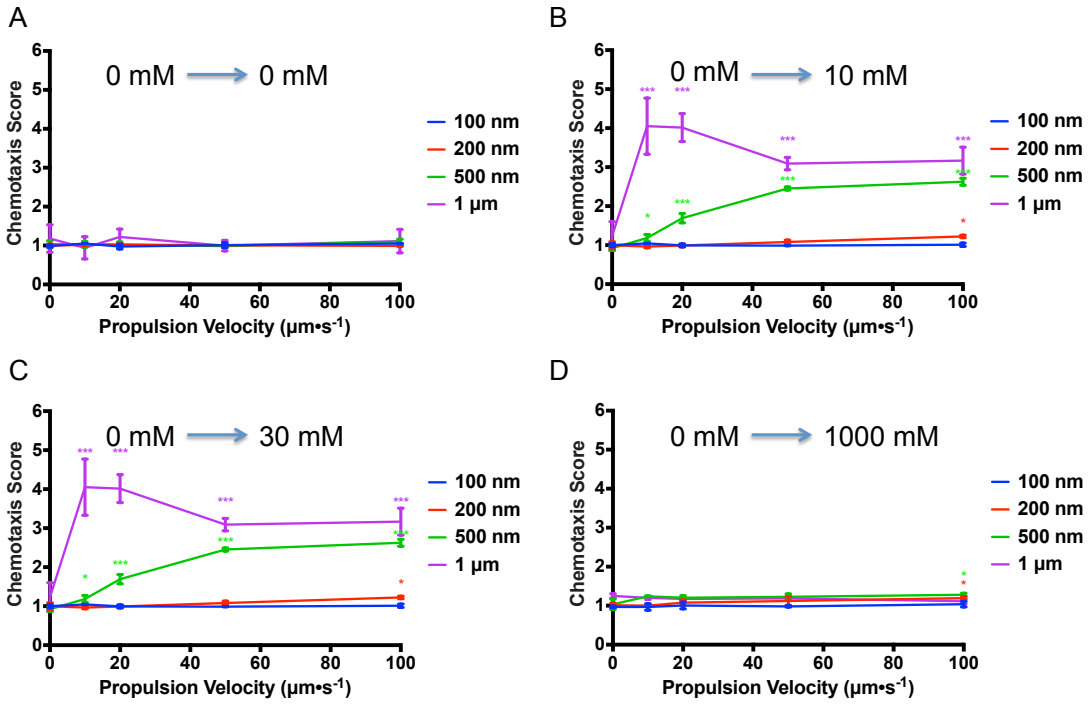

Figure 5.10: Chemotaxis Efficiency of Chemotactic Particles under different Gradients. Chemotaxis efficiency is measured against the velocity of propulsion, with four different sized particles, in four different gradients, 0 mM to 0 mM (A), 0 mM to 10 mM (B), 0mM to 30 mM (C) and 0 mM to 1000 mM (D) after 0.4 s. Each data point represents the mean ± standard deviation of three simulations (n=3). Significance calculated using the Holm-Sidak t-test, points tested against nanoparticle populations of the same size but with a propulsion of 0 $\mu m \cdot s^{-1}$, * $P < 0.05$, ** $P < 0.01$, *** $P < 0.005$

Interestingly, a lower velocity of propulsion appears to promote better chemotaxis for 1 μm particles. This may be a result of some particles being driven away from the substrate source due to the inability to reorientate themselves effectively, as a result of their slow rotational times. This is an example of the polar run and tumble, predicted by the work of Saha and colleagues (Saha et al., 2014). In order to demonstrate the relative influence of the polar run and tumble, particles were simulated with the maximum substrate gradient in the centre and the lowest concentration at the top and

bottom. The percentage of nanoparticles bound to the top or bottom after 0.05 s is given in *Figure 5.12*.

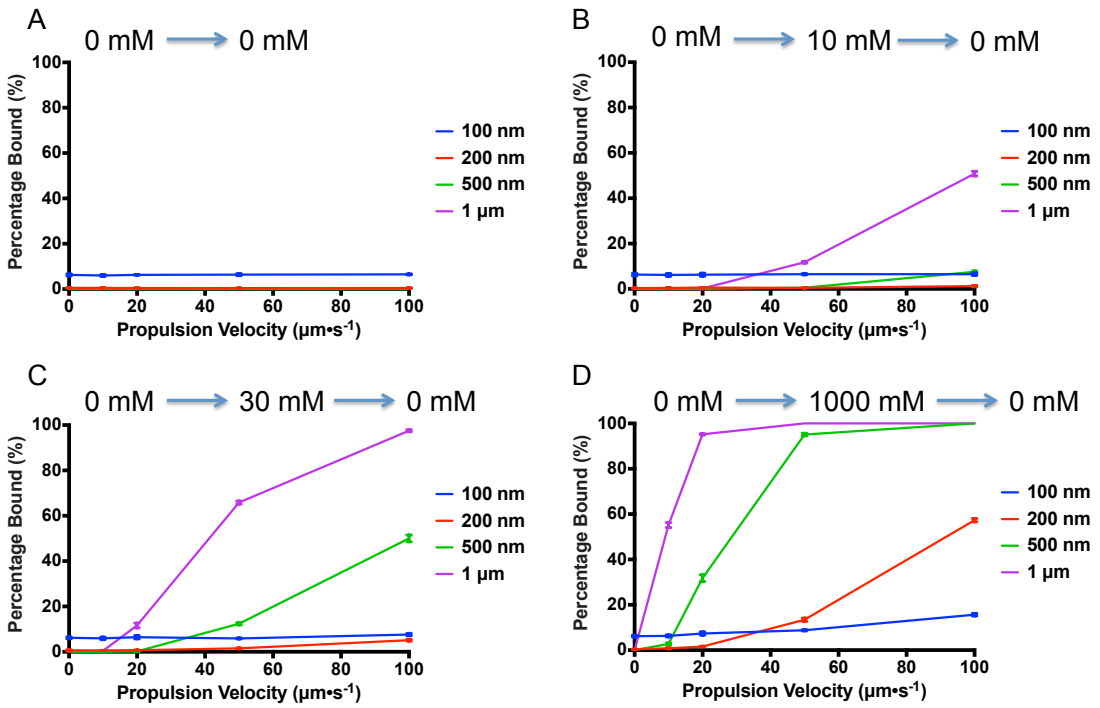

Figure 5.11: Polar Run and Tumble of different Particles. The percentage of particles bound after 0.05 s with different levels of propulsion, different particle sizes and different gradients of 0 mM to 0 mM to 0 mM (A), 0 mM to 10 mM to 0 mM (B), 0 mM to 30 mM to 0 mM (C), and 0 mM to 1000 mM to 0 mM (D). Each data point represents the mean ± standard deviation of three simulations (n=3). Significance calculated using the Holm-Sidak t-test, points tested against nanoparticle populations of the same size but with a propulsion of 0 $\mu m \cdot s^{-1}$, * $P < 0.05$, ** $P < 0.01$, *** $P < 0.005$

1 μm particles demonstrate a high level of polar run and tumble in all gradients, with the percentage bound ranging from ~50% to 100% (*Figure 5.12B-D*). 200 nm and 500 nm particles show polar chemotaxis that increases steadily with increasing gradient. However, 100 nm particles show little polar chemotaxis, with the only notable increase in binding occurring at high propulsion velocities (100 $\mu m \cdot s^{-1}$) and high gradients (0 mM → 1000 mM → 0 mM) in *Figure 5.12D*. This suggests that the high rotational time of small particles reduces the contribution of polar chemotaxis to net chemotactic

activity. The reduction of propulsion velocity also reduces the degree of polar chemotaxis exhibited by particles with a slow rotational diffusion. Therefore, obtaining a higher net chemotaxis towards a substrate requires tailoring the relative influence of polar and apolar run and tumble, by adjusting propulsion velocity relative to the rotational diffusion. Bacteria solve this issue by limiting their run time to ~1s before increasing their effective rotational time in a tumble. The sustained length of a run can be adjusted by changing the rotational time accordingly. Previously it had been considered that the only mechanism to do this was by altering the particle size. The work of the Battaglia group and the Golestanian group may open new avenues to control the length of the run according to substrate concentration-dependent changes in orientational persistence.

The propulsion velocity relative to a fixed rotational diffusion can also be adjusted by manipulation of the reaction rate. The reaction rate is reliant on the $\boldsymbol{k_{cat}}$, $\boldsymbol{k_m}$, $[\boldsymbol{S}]$ and $[\boldsymbol{E}]$. The $\boldsymbol{k_{cat}}$ and $\boldsymbol{k_m}$ are innate to the enzyme and $[\boldsymbol{S}]$ is a property determined by the biological system, therefore reduction of $[\boldsymbol{E}]$ represents the easiest way to manipulate the reaction rate. In parallel with the earlier experiments, maximal velocities of propulsion of 0 μm·s^{-1}, 10 μm·s^{-1}, 20 μm·s^{-1}, 50 μm·s^{-1} or 100 μm·s^{-1} were obtained by adjusting $[\boldsymbol{E}]$ to 0 mM, 0.0135 mM, 0.027 mM, 0.0675 mM and 0.135 mM respectively and maintaining $\boldsymbol{\varphi_{max}}$ at 100 μm·s^{-1} (*Figure 5.13*).

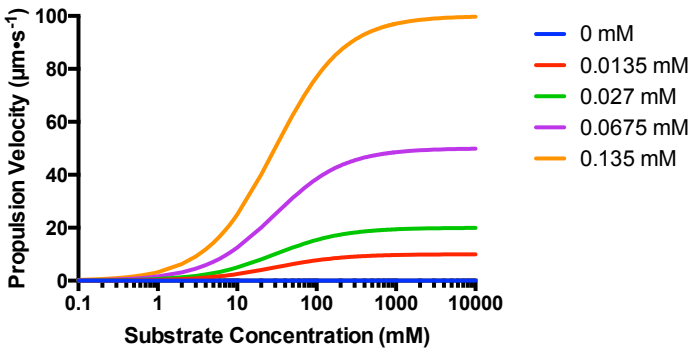

Figure 5.12: Enzyme and Substrate Concentration dependent Propulsion Velocity. The propulsion velocity is related to the Michaelis-Menten kinetics of different concentrations of enzyme and substrates.

Figure 5.14 and *Figure 5.15* demonstrate that a similar pattern of both net chemotaxis and polar run and tumble can be generated from reducing the enzyme concentration as opposed to reducing the propulsion velocity (*Figure 5.11* and *Figure 5.12*). In future better understanding of propulsion velocity and rotational diffusion coefficient changes may allow tailored design of nanoparticles to give the optimal chemotaxis along a specific gradient. Effective chemotaxis to a high concentration of a specific stimulus released by target cells/tissue may improve accumulation of particles in the region, thus improving delivery specificity.

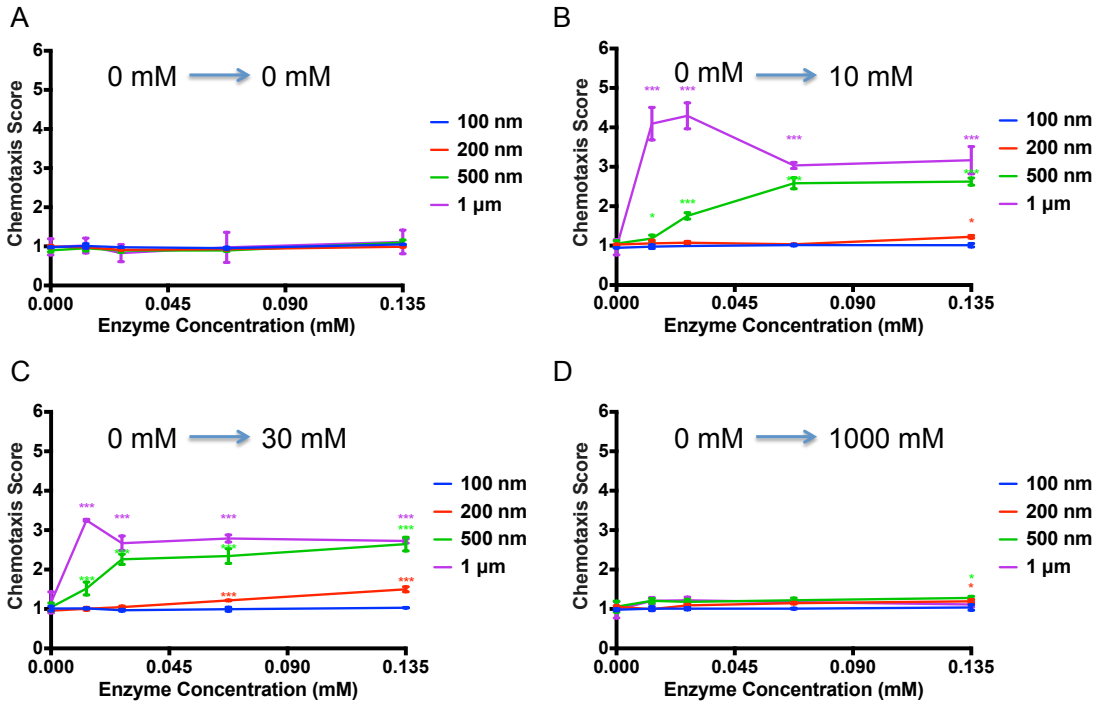

Figure 5.13: Chemotaxis Efficiency of Chemotactic Particles under different Gradients with different Enzyme Encapsulation. Chemotaxis efficiency is measured against the encapsulation of enzyme, with four different sized particles, in four different gradients, 0 mM to 0 mM (A), 0 mM to 10 mM (B), 0mM to 30 mM (C) and 0 mM to 1000 mM (D) after 0.4 s. Each data point represents the mean ± standard deviation of three simulations (n=3). Significance calculated using the Holm-Sidak t-test, points tested against nanoparticle populations of the same size but with a propulsion of 0 $\mu m \cdot s^{-1}$, * $P < 0.05$, ** $P < 0.01$, *** $P < 0.005$

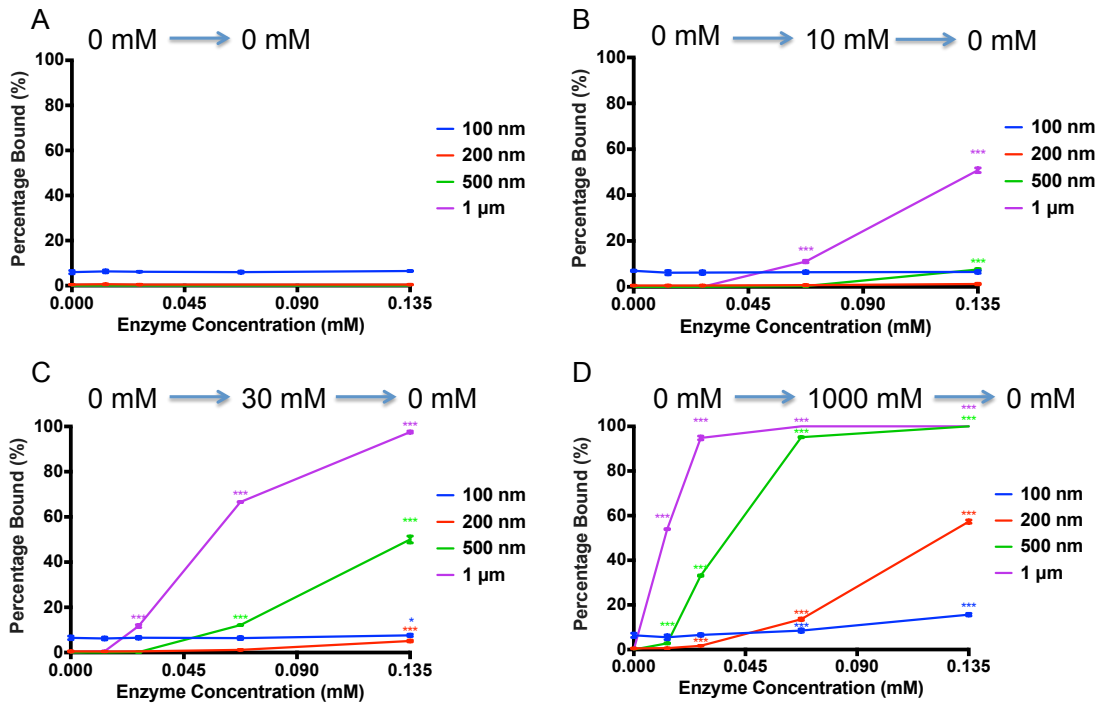

Figure 5.14: Polar Run and Tumble of different Particles with different Enzyme Encapsulation. The percentage of particles bound after 0.05 s with different levels of enzyme encapsulation, different particle sizes and different gradients of 0 mM to 0 mM to 0 mM (A), 0 mM to 10 mM to 0 mM (B), 0 mM to 30 mM to 0 mM (C), and 0 mM to 1000 mM to 0 mM (D). Each data point represents the mean ± standard deviation of three simulations (n=3). Significance calculated using the Holm-Sidak t-test, points tested against nanoparticle populations of the same size but with a propulsion of 0 $\mu m \cdot s^{-1}$, * $P < 0.05$, ** $P < 0.01$, *** $P < 0.005$

The simulations throughout this chapter model each nanoparticle as an independent agent. However, complex group behaviour of chemotactic micro-organisms has been demonstrated previously including effects such as swarming. It can be expected that group behaviour will also occur in nano-scale and micro-scale chemotactic particles. Particles that are side-by-side can form asymbiotic (*Figure 5.16A*) or symbiotic (*Figure 5.16B*) relationships with one another, depending on the particles orientation with respect to one another. Particles that are one behind the other can lead to blocking (*Figure 5.16C*) motion of one particle, repulsion (*Figure 5.16D*) or clumping (*Figure 5.16E*) of particles. At any particular point, many such interactions may occur simultaneously giving rise to clumps or asters of particles and patterns, as predicted by the work of Saha and colleagues (Saha et al., 2014). The

omission of these interactions may affect the translation from the simulations presented here to actual bulk behaviour of chemotactic nanoparticle populations.

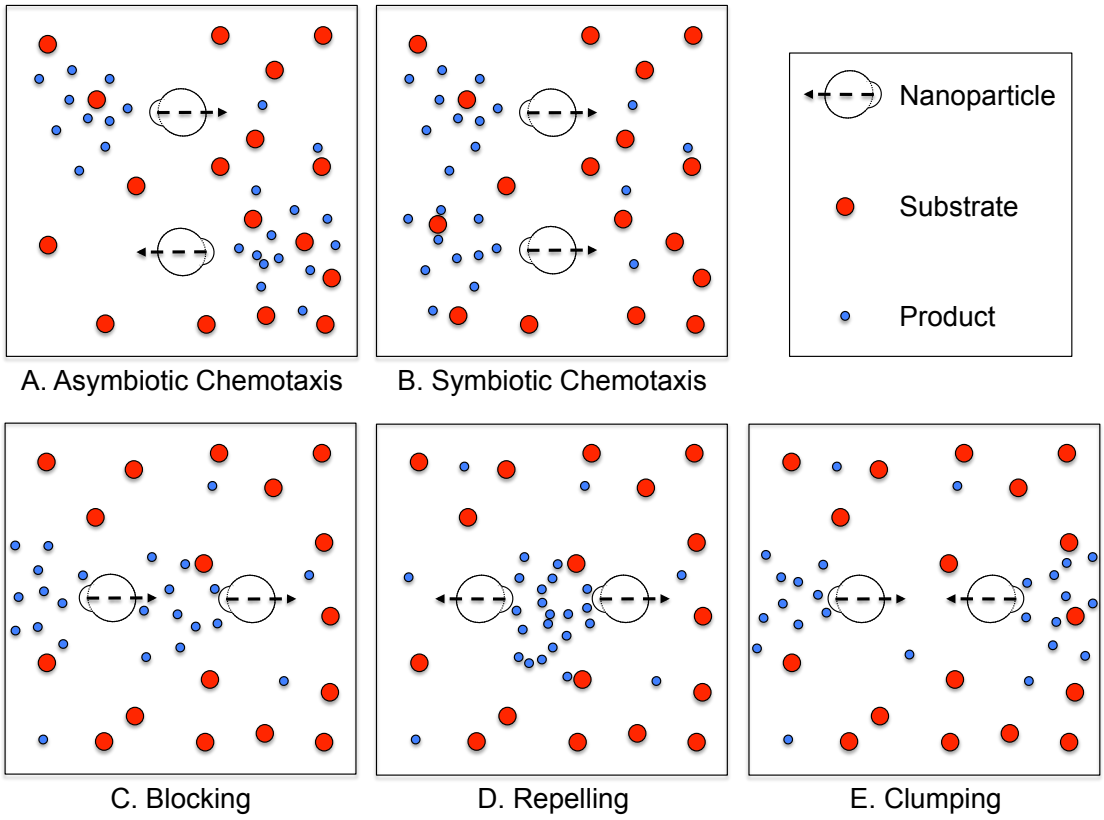

Figure 5.15: Group Behaviour of Self-Diffusiophoretic Particles. Two particles, in close proximity, both undertaking self-diffusiophoresis by converting a substrate into product(s) will interact in different ways according to their position and orientation of the site of product release relative to one another. Two particles, side-by-side, with orientation in opposing directions, will lead to little or no net movement of either particle (A). When the particles' orientation is aligned the cumulative concentration gradient will improve net motion of the particles (B). Particles one behind the other, with orientation in the same direction, leads to a blocking effect on the trailing, as no net concentration gradient is obtained (C). Particles in opposite orientation will either repel each other (D) or attract each other leading to clumping (E).

There have been many attempts to create artificial chemotactic particles in recent years. The first attempts concentrated on producing artificial flagella that responded to magnetic fields to produce thrust. Dreyfus and colleagues used magnetic particles, linked by DNA and attached to a red blood cell to

produce a propelled red blood cell (Dreyfus et al., 2005). Zhang and co-workers used a helical metal tail attached to a soft magnetic thin film of approximately 4.5 μm by 4.5 μm by 200 nm, to produce a magnetic responsive particle (Zhang et al., 2009). Snezhko and co-workers used 90 μm nickel spheres to self-assemble magnetic responsive snakes (Snezhko et al., 2009). Tierno and colleagues also demonstrated a magnetic responsive microswimmer, however this was achieved using the conjugation of a 2.8 μm Dynabead to 1 μm Dynabead using an 8 nm DNA linker, which was motile in close proximity to a solid surface (Tierno et al., 2008). In all of these studies, the use of artificial flagella, though effective, restricted the size of these swimmers to a micrometre size. This would limit their capacity to be used in biological *in vivo* applications as the particles would be both difficult to administer and rapidly cleared from body by the reticuloendothelial system. These methods rely on application of a magnetic field, this could allow guided uptake of nanoparticles into regions of interest by application of narrow magnetic fields.

Jiang and colleagues produced a thermophoretic Au-silica Janus particle of 1 μm that was able to follow temperature gradients created by an intense laser (Jiang et al., 2010). This method requires the existence of temperature gradients *in vivo* to be useful in targeting; while slight gradients may exist, they are likely to be too insignificant to exploit effectively. The ability of nanoparticles to follow chemical gradients *in vivo* represents a far more interesting prospect as they could follow natural gradients to find targets of interest. These gradients could be produced when a cell/tissue releases a particular molecule, creating a positive gradient towards the cell/tissue, or when it removes/consumes molecules leading to a negative gradient to the cell/tissue. Paxton and colleagues used 2 μm rods to catalyse the breakdown of hydrogen peroxide (Paxton et al., 2005). Mano and colleagues produced a 0.5 cm glucose responsive nanoswimmer using carbon fibres with glucose oxidase (Mano and Heller, 2005). A number of other groups have described micrometer scale swimmers that are responsive to hydrogen peroxide (Howse et al., 2007, Ke et al., 2010, Gibbs and Zhao, 2009). A recurrent theme in

these studies is that nanoscale motile particles remain elusive in the literature. In this chapter, particles covering nanometre to micrometre scales are used in simulations of chemotaxis. Some of the major challenges that have prevented the development of chemotactic nanoscale particles are demonstrated in these models. For example, when observing ability to follow chemical gradients, 100 nm nanoparticles displayed no directional bias and 200 nm nanoparticles only displayed directional bias at high propulsion (*Figure 4.11 B-C* and *Figure 4.14 B-C*). In *Chapter 1*, a chemotactic nanoparticle system designed in the Battaglia group is discussed. In testing of this particle, a reduced rotational time has been observed when subjected to glucose or hydrogen peroxide gradients, this would make the particle behave similar to micrometre particles in their ability to follow concentration gradients. Moreover, their natural rapid rotation times when there is low substrate would reduce the effect of the polar run and tumble effect demonstrated in *Figures 4.12 and 4.15*. Interestingly, even in the absence of chemotactic ability, propelled nanoscale particles may be able to distribute from the blood and through the CNS tissue more effectively than non-propelled systems, due to the increase mean squared displacement alone without directional bias.

In this Chapter, a simplified relationship between substrate concentration and nanoparticle propulsion has been used (*Equations 5.8-5.10*). These equations relate enzyme kinetics to a propulsion velocity. In future work, a more accurate relationship between substrate concentration and propulsion velocity could be found. For example, techniques such as NTA permit calculation of the drift velocity of nanoparticles when subjected to a chamber of a known substrate concentration. The work of the Golestanian group has previously described more complex theoretical relationships between particle mobility and enzymatic activity. This includes variables such as the diffusion coefficient of reactants and substrates in addition to enzyme kinetics (Saha et al., 2014). This could then be included to allow more accurate modelling in the future and better validation of the model results in experimental tests.

5.4 CONCLUSIONS

In conclusion, a model of substrate-independent and substrate-dependent propulsion of particles has been implemented using FLAME. This has been used to demonstrate how particles undergoing propulsion accumulate at solid interfaces, potentially improving cellular uptake. Furthermore, application of propulsion within the blood can aid distribution to the endothelial interface of the blood-brain barrier and other endothelial barriers, thus increasing potential uptake into tissues. Substrate-dependent propulsion has been demonstrated to produce net chemotaxis, if the propulsion and angular velocity are optimised for the given concentration gradient. In future, better understanding of how the angular velocity changes for particles undergoing propulsion will lead to higher levels of control over chemotaxis efficiency and will inform therapeutic nanoparticle design, giving improved specificity in delivery.

CHAPTER 6: CONCLUSIONS AND FUTURE DIRECTIONS

6.1 GENERAL CONCLUSIONS

In this thesis, a variety of modelling approaches have been used to explore methods to study and improve nanoparticle delivery to the CNS across the blood-brain barrier. A key aspect of this project was to apply the power of agent-based modelling to perform predictive simulations of nanoparticle behaviour. In order to model nanoparticle interaction with the blood-brain barrier, a core model of nanoparticle behaviour, under blood flow, in a capillary was created. This model incorporated RBCs at a physiological level. It was found by the inclusion of these cells, that the effect on fluid dynamics within a capillary was favourable for distribution of nanoparticles to the endothelial wall interface. The inclusion of RBCs in the simulations was important in improving the applicability of the *in silico* simulations to corresponding experiments *in vivo*. Furthermore, the core model gave considerable insight into how the fluid dynamics of blood flow in capillaries operates as a highly efficient delivery mechanism. This role of capillary blood flow, in the context of RBCs, in delivery had been relatively unexplored. Previous studies had focused on other aspects of capillary flow such as RBC morphology (Chambers and Mitragotri, 2007, Fedosov et al., 2014, Guest et al., 1963, Kaoui et al., 2009, McWhirter et al., 2009, McWhirter et al., 2011, Skalak and Branemar.Pi, 1969) or had used non-physiological haematocrits of 0% or 38% in delivery studies (Tan et al., 2012, Yu et al., 2011). The core model was designed to exploit the inherent parallelisation optimisation features in the FLAME framework. The structure of this model permitted facile manipulation of the model to answer different research questions, whilst maintaining the same basic core model.

It was demonstrated that this model could be used to aid considered nanoparticle design. Nanoparticle size was investigated in delivery through fenestrated endothelium and particularly in the enhanced permeability and retention effect. An important aspect of this work was to demonstrate the

importance of considering size in the context of polydispersity. These principles also apply to the work within the remainder of the thesis, but was omitted to reduce the number of variables to be considered. Moreover, whilst fenestrations are not present at the blood-brain barrier, they can be found at the choroid plexus and circumventricular organs. These present alternative potential entry routes into the CNS across the epithelial blood-cerebrospinal fluid barrier (Langlet, 2014, Langlet et al., 2013). Moreover, disruption of the endothelial tight junctions in the blood-brain can be found in a number of CNS diseases or is induced through deliberate disruption (Neuwelt et al., 1980, Dallasta et al., 1999, Bell et al., 2012). The fenestration model can be simply adjusted to model nanoparticle uptake across a disrupted blood-brain barrier.

The established model and another model based on *in vitro* transwell models of the blood-brain barrier were then used to screen nanoparticles with different properties, for their ability to bind to the blood-brain barrier and cross the blood-brain barrier by transcytosis. Previously, it has been demonstrated that transcytosis efficiency of antibodies was dependent on the binding strength, with low affinity antibodies unable to stably bind sufficiently to induce transcytosis and high affinity antibodies unable to unbind and be released into the parenchyma. This screening demonstrated that the overall affinity for nanoparticles could be controlled by manipulating a number of nanoparticle properties, including size, ligand density and receptor-ligand binding affinity. This demonstrates that nanoparticles have a greater flexibility in formulation than antibodies, as binding strength is controllable by the three different parameters studied and also quite probably by shape also. The effect of these properties on binding has been studied previously both theoretically and in biological studies (Decuzzi and Ferrari, 2006, Gosk et al., 2004, Fakhari et al., 2011, Takae et al., 2005, Chithrani et al., 2006). However the conversion into transcytosis efficiency, based on an emerging hypothesis in endothelial transcytosis, has been relatively unexplored (Gosk et al., 2004, Wiley et al., 2013, Yu et al., 2011, Yu et al., 2014). These parameters are often neglected in the literature on delivery to the CNS. Therefore, this work, in conjunction with the findings of Yu and colleagues, demonstrates that in future work on

nanoparticle delivery to the CNS, it is important to consider these parameters and the potential effect they may have on delivery efficiency. Overall, this work demonstrates that developing nanoparticles with an intermediate overall affinity could potentially improve transcytosis efficiency.

The nanoparticle binding models were also used to establish whether nanoparticle properties could improve uptake specificity when receptor expression is altered and/or when blood flow is changed. It was found that by altering nanoparticle properties, binding strength could be tuned to increase binding specificity to high receptor expression levels but not to low receptor expression. Furthermore, nanoparticle properties could be used to stabilise binding under the increased blood flow associated with functional hyperaemia. These two principles, used separately or in tandem, can improve the specificity of nanoparticle binding. Improving specificity of delivery to different regions of the CNS remains a highly unexplored area, with most studies to date focusing on general CNS delivery levels or therapeutic outcomes. Given the innate fragility of neural tissue, delivery in to the affected region of the CNS will require more attention if nanoparticle-mediated therapy for CNS disorders is going to become safe and effective. Thus far, only two methods have been published that address this issue. The first of these methods uses magnetic nanoparticles and a magnetic field to guide the nanoparticles into the region of interest (Pulfer et al., 1999, Pulfer and Gallo, 1998, Qiao et al., 2012). The second method uses transient site-specific disruption of the blood-brain barrier by ultrasound-mediated rupture of micro-bubbles in the blood (Hynynen et al., 2005, Kinoshita et al., 2006b, Kinoshita et al., 2006a, Mesiwala et al., 2002, Sheikov et al., 2004). The magnetic-guided approach is an interesting concept that should improve specificity of nanoparticles, however only a small selection of nanoparticles are responsive to magnetic fields. Furthermore, the use of such ‘hard’ nanoparticles gives an overall poorer interaction with biological material than ‘soft’ nanoparticles such as liposomes and polymersomes. Disruption of the blood-brain barrier, though effective in increasing drug penetrance, has inherent risks due to the integral role of the blood-brain barrier in maintaining CNS homeostasis. The blood

contains substances that within the CNS are neurotoxic, these include plasminogen, albumin and pro-thrombin (Nadal et al., 1995, Gingrich and Traynelis, 2000, Gingrich et al., 2000). Disruption, even if only transient, may therefore damage the underlying tissue. This damage can further trigger a cascade of events ultimately leading to progressive damage of the CNS. Further research on the effect of such a disruption is required before this method can be considered safe for long-term treatment strategies. Therefore, the design of new methods to improve delivery to specific regions of the CNS will be highly beneficial to future nanoparticle-mediated CNS therapy. In this thesis a number of methods have been suggested, that are used endogenously to improve delivery, notably increased receptor expression and functional hyperaemia. If they are realised in later experimental work, they may have considerable potential to aid CNS therapy whilst reducing potentially harmful off-target effects.

Finally chemotactic nanoparticles were explored as a method to increase accumulation at the blood-brain barrier interface and follow gradients to target cells. It was demonstrated that nanoparticles operating under propulsion had an increased displacement. Furthermore, when placed within the core model of capillary blood flow, propelled particles accumulated at the endothelial interface. It was predicted that this would lead to increased uptake across the blood-brain barrier into the CNS. This work directly led to corresponding experiments in rats, where a 2-fold increase in uptake to the CNS was observed with chemotactic, blood-brain barrier targeted nanoparticles compared to non-chemotactic controls (Nyberg and Battaglia, unpublished). Chemotactic nanoparticles were further demonstrated to be able to follow chemical gradients, a method that has potential to be harnessed to improve penetration through CNS tissue to target cells or regions. The chemotactic capability was dependent on the relationship between rotational time and propulsion velocity. It was demonstrated that the latter might be controlled by the enzyme concentration. The relationship between propulsion and rotational time appears to be complex and will require further study before any exact

relationship can be ascertained (Cecchin et al., Submitted, Golestanian et al., 2007, Howse et al., 2007).

The blood-brain barrier depicted in these simulations focuses on the role of the endothelium in both barrier function and transport into the CNS. However the endothelium is closely associated with other cells of the neurovascular unit, particularly pericytes and astrocytes. The density and organisation of these cells creates spatial limits that nanoparticles must migrate through. Furthermore, pericytes and astrocytes both possess phagocytic behaviour for the non-specific uptake of nanoparticles (Balabanov et al., 1996, van Deurs, 1976, al-Ali and al-Hussain, 1996, Nguyen et al., 2011). Additionally they express Lrp1, thus allowing the specific uptake of Lrp1-targeted nanoparticles (Wilhelmus et al., 2007, William Rebeck et al., 1993). Their close proximity to the barrier makes them the first cells the nanoparticles come across within the CNS. This may limit the ability of nanoparticles to be distributed and targeted to other cells in the CNS that are located more distally to the barrier, such as neurons and oligodendrocytes. Moreover, there is a basal laminar that separates the endothelium from the CNS parenchyma. This may prevent or slow the migration of large nanoparticles, as has been demonstrated in the basal laminar of neuromuscular junctions (Oldfors and Fardeau, 1983). It is evident that optimising nanoparticle transport across the blood-brain barrier is only part of the challenge in CNS delivery.

6.2: FUTURE PERSPECTIVES

The work within this thesis represents proof-of-concept studies into how nanoparticles can be adapted for improved general and specific uptake to the CNS across the blood-brain barrier. The models presented were deliberately simplistic to improve their flexibility to different research questions and to reduce the effect of complex interactions in the final analysis. The major drawback of such an approach is that direct comparison with experimental work from the Battaglia lab and the literature is complex. In future it is important to validate aspects of the methodology in biological systems and

refine the methodology to better reflect the situation in *in vitro* and *in vivo* systems. Once the methods are refined, they could be extrapolated to larger scale models of the cerebrovasculature and eventually towards patient-personalised medicine, as discussed later. The extrapolation to larger scale models is important to permit better *in silico* to *in vivo* translation, allowing the model to explain experimental observations and predict experimental outcomes.

6.2.1 Validation and Refinement

In any *in silico* study, the desire is to produce models that can be operated alongside traditional biological models. Ideally, each separate model improves the understanding of the other. *In silico* methods can be used to generate research hypotheses for *in vitro* or *in vivo* experimentation. The resulting data can then be used to improve the accuracy and complexity of the *in silico* modelling thus improving its power. Work within the Battaglia group has validated or informed some of the methodology used in this thesis, including, simulations of Brownian motion, timing of cellular trafficking in transcytosis, effect of ligand density on transcytosis efficiency and improved uptake of propelled particles under blood flow. However, future work will focus on validating concepts such as the increased specificity for higher levels of expression and increased specific uptake under functional hyperaemia conditions. Moreover, it is hoped that future work could identify specific values such as the $\boldsymbol{k_a^0}$ of Angiopep-2-Lrp-1 interaction, the receptor density of Lrp-1 at the blood-brain barrier and the propulsion-angular velocity relationship, that will improve the predictive aspects of the simulations.

6.2.2 Application to Large-scale Modelling

The main core model in this thesis focuses on uptake in a simulation of a single capillary. However, a network of capillaries is critical to blood-mediated delivery to the CNS, with variances in capillary morphology, branching and flow properties. Using image processing of *in vivo* vascular networks,

modelling has been undertaken at this scale (Groen et al., 2013, Mazzeo and Coveney, 2008, Torii et al., 2010). Integrating the methodology presented in this thesis can improve the *in silico* to *in vivo* translation. Furthermore, as computational power increases, these models can be made more and more complex. They can integrate dynamic changes that occur in the cerebrovasculature, such as arteriole vasodilation in functional hyperaemia, the role of pericytes in functional hyperaemia and regulation by the neurovascular unit. As greater complexity is integrated into simulations, it is hoped that the accuracy and predictive capabilities of the model improve.

6.2.3 Towards Personalised Medicine

One of the newest and most exciting potential avenues for treatment of many disorders is the idea of personalised medicine. The concept of personalised medicine is to design treatment strategies in a patient-specific manner using patient data such as genome sequences and proteomics (Barretina et al., 2012, Hamburg and Collins, 2010, Hood et al., 2004). A major advantage of large-scale modelling techniques, suggested in the previous section, is the ability to use patient data to tailor nanoparticle formulation accordingly. In a number of CNS diseases, changes to cerebrovasculature structures, blood flow alterations, neurovascular coupling deficiencies and blood-brain barrier dysfunction have been shown to occur, as discussed in Chapter 1. In recent years, progress in CNS imaging, such as MRI, fMRI, positron emission tomography (PET) and single photon emission` computed tomography (SPECT), has enabled the generation of high-quality data from patients. Integration of such primary data from patients into large-scale *in silico* models may allow rapid screening of delivery efficiency to give the best treatment strategies. This can include best methods of delivery to target sites, but also better understanding of the state of disease progression and therefore more accurate determination of therapeutic targets. Currently, several major projects and initiatives are being undertaken based on the principles of large-scale modelling of whole tissues, including the Human Brain Project

(https://www.humanbrainproject.eu) and the Virtual Physiological Human (http://www.vph-institute.org). Initiatives such as these are already creating organ level models encompassing patient-specific data, such as in the FUSIMO (http://www.fusimo.eu) or p-medicine (http://www.p-medicine.eu) projects. Moreover, the p-medicine project is beginning to integrate patient-specific data and the Virtual Physiological Human with the goal of achieving personalised medicine. Although modelling at this scale represent serious biological and computational challenges, the benefit of such initiatives has great potential to revolutionise therapeutic strategies towards the CNS.

BIBLIOGRAPHY

ABBOTT, N. J. 2004. Evidence for bulk flow of brain interstitial fluid: significance for physiology and pathology. *Neurochemistry International,* 45**,** 545-552.

ABBOTT, N. J. 2005. Dynamics of CNS barriers: Evolution, differentiation, and modulation. *Cellular and Molecular Neurobiology,* 25**,** 5-23.

ABBOTT, N. J., PATABENDIGE, A. A. K., DOLMAN, D. E. M., YUSOF, S. R. & BEGLEY, D. J. 2010. Structure and function of the blood-brain barrier. *Neurobiology of Disease,* 37**,** 13-25.

ABBOTT, N. J., RONNBACK, L. & HANSSON, E. 2006. Astrocyte-endothelial interactions at the blood-brain barrier. *Nature Reviews Neuroscience,* 7**,** 41-53.

ABHISHEK, C., GIUSEPPE, B. & RAMIN, G. 2011. The effect of interactions on the cellular uptake of nanoparticles. *Physical Biology,* 8**,** 046002.

ADLER, J. 1966. Chemotaxis in Bacteria. *Science,* 153**,** 708-716.

ADRA, S., SUN, T., MACNEIL, S., HOLCOMBE, M. & SMALLWOOD, R. 2010. Development of a Three Dimensional Multiscale Computational Model of the Human Epidermis. *Plos One,* 5**,** e8511.

AL-ALI, S. Y. & AL-HUSSAIN, S. M. 1996. An ultrastructural study of the phagocytic activity of astrocytes in adult rat brain. *Journal of Anatomy,* 188**,** 257-262.

ALBERTS, B., JOHNSON, A., LEWIS, J., RAFF, M., ROBERTS, K. & WALTER, P. 2002. *Molecular Biology of the Cell*, Garland Science.

ALEXIS, F., PRIDGEN, E., MOLNAR, L. K. & FAROKHZAD, O. C. 2008. Factors affecting the clearance and biodistribution of polymeric nanoparticles. *Molecular Pharmaceutics,* 5**,** 505-515.

ALYAUDTIN, R. N., REICHEL, A., LÖBENBERG, R., RAMGE, P., KREUTER, J. R. & BEGLEY, D. J. 2001. Interaction of Poly(butylcyanoacrylate) Nanoparticles with the Blood-Brain Barrier in vivo and in vitro. *Journal of Drug Targeting,* 9**,** 209-221.

ALYAUTDIN, R., PETROV, V., LANGER, K., BERTHOLD, A., KHARKEVICH, D. & KREUTER, J. R. 1997. Delivery of Loperamide Across the Blood-Brain Barrier with Polysorbate 80-Coated Polybutylcyanoacrylate Nanoparticles. *Pharmaceutical Research,* 14**,** 325-328.

AN, L., SHEN, T. T. & WANG, R. K. 2011. Using ultrahigh sensitive optical microangiography to achieve comprehensive depth resolved microvasculature mapping for human retina. *Journal of Biomedical Optics,* 16**,** 106013-106013-9.

ANDREWS, S. S. & BRAY, D. 2004. Stochastic simulation of chemical reactions with spatial resolution and single molecule detail. *Physical Biology,* 1**,** 137-151.

ARTALEJO, C. R., ELHAMDANI, A. & PALFREY, H. C. 2002. Sustained stimulation shifts the mechanism of endocytosis from dynamin-1-dependent rapid endocytosis to clathrin- and dynamin-2-mediated slow endocytosis in chromaffin cells. *Proceedings of the National Academy of Sciences,* 99**,** 6358-6363.

ATTWELL, D., BUCHAN, A. M., CHARPAK, S., LAURITZEN, M., MACVICAR, B. A. & NEWMAN, E. A. 2010. Glial and neuronal control of brain blood flow. *Nature,* 468**,** 232-243.

ATTWELL, D. & LAUGHLIN, S. B. 2001. An energy budget for signaling in the grey matter of the brain. *Journal of Cerebral Blood Flow and Metabolism,* 21**,** 1133-1145.

BACABAC, R. G., SMIT, T. H., COWIN, S. C., VAN LOON, J. J. W. A., NIEUWSTADT, F. T. M., HEETHAAR, R. & KLEIN-NULEND, J. 2005. Dynamic shear stress in parallel-plate flow chambers. *Journal of Biomechanics,* 38**,** 159-167.

BADHAN, R. K. S., CHENEL, M. & PENNY, J. I. 2014. Development of a physiologically-based pharmacokinetic model of the rat central nervous system. *Pharmaceutics,* 6**,** 97-136.

BAI, H., ROLFE, M. D., JIA, W., COAKLEY, S., POOLE, R. K., GREEN, J. & HOLCOMBE, M. 2014. Agent-Based Modeling of Oxygen-Responsive Transcription Factors in *Escherichia coli*. *PLoS Comput Biol,* 10**,** e1003595.

BALABANOV, R., WASHINGTON, R., WAGNEROVA, J. & DORE-DUFFY, P. 1996. CNS Microvascular Pericytes Express Macrophage-like Function, Cell Surface Integrin αM, and Macrophage Marker ED-2. *Microvascular Research,* 52**,** 127-142.

BAO, H., JIN, X., LI, L., LV, F. & LIU, T. 2012. OX26 modified hyperbranched polyglycerol-conjugated poly(lactic-co-glycolic acid) nanoparticles: synthesis, characterization and evaluation of its brain delivery ability. *Journal of Materials Science: Materials in Medicine,* 23**,** 1891-1901.

BARRETINA, J., CAPONIGRO, G., STRANSKY, N., VENKATESAN, K., MARGOLIN, A. A., KIM, S., WILSON, C. J., LEHAR, J., KRYUKOV, G. V., SONKIN, D., REDDY, A., LIU, M. W., MURRAY, L., BERGER, M. F., MONAHAN, J. E., MORAIS, P., MELTZER, J., KOREJWA, A., JANE-VALBUENA, J., MAPA, F. A., THIBAULT, J., BRIC-FURLONG, E., RAMAN, P., SHIPWAY, A., ENGELS, I. H., CHENG, J., YU, G. Y. K., YU, J. J., ASPESI, P., DE SILVA, M., JAGTAP, K., JONES, M. D., WANG, L., HATTON, C., PALESCANDOLO, E., GUPTA, S., MAHAN, S., SOUGNEZ, C., ONOFRIO, R. C., LIEFELD, T., MACCONAILL, L., WINCKLER, W., REICH, M., LI, N. X., MESIROV, J. P., GABRIEL, S. B., GETZ, G., ARDLIE, K., CHAN, V., MYER, V. E., WEBER, B. L., PORTER, J., WARMUTH, M., FINAN, P., HARRIS, J. L., MEYERSON, M., GOLUB, T. R., MORRISSEY, M. P., SELLERS, W. R., SCHLEGEL, R. & GARRAWAY, L. A. 2012. The Cancer Cell Line Encyclopedia enables predictive modelling of anticancer drug sensitivity. *Nature,* 483**,** 603-607.

BASKURT, O. K. & MEISELMAN, H. J. 2003. Blood rheology and hemodynamics. *Seminars in Thrombosis and Hemostasis,* 29**,** 435-450.

BATTAGLIA, G. & RYAN, A. J. 2005. Bilayers and Interdigitation in Block Copolymer Vesicles. *Journal of the American Chemical Society,* 127**,** 8757-8764.

BATTAGLIA, G., RYAN, A. J. & TOMAS, S. 2006. Polymeric Vesicle Permeability: A Facile Chemical Assay. *Langmuir,* 22**,** 4910-4913.

BELL, R. D., WINKLER, E. A., SINGH, I., SAGARE, A. P., DEANE, R., WU, Z., HOLTZMAN, D. M., BETSHOLTZ, C., ARMULIK, A., SALLSTROM, J., BERK, B. C. & ZLOKOVIC, B. V. 2012. Apolipoprotein E controls cerebrovascular integrity via cyclophilin A. *Nature,* 485**,** 512-516.

BENTLEY, K., GERHARDT, H. & BATES, P. A. 2008. Agent-based simulation of notch-mediated tip cell selection in angiogenic sprout initialisation. *Journal of Theoretical Biology,* 250**,** 25-36.

BERG, H. C. & BROWN, D. A. 1972. Chemotaxis in Escherichia coli analysed by Three-dimensional Tracking. *Nature,* 239**,** 500-504.

BERNABEU, M. O., JONES, M. L., NIELSEN, J. H., KRÜGER, T., NASH, R. W., GROEN, D., SCHMIESCHEK, S., HETHERINGTON, J., GERHARDT, H., FRANCO, C. A. & COVENEY, P. V. 2014. Computer simulations reveal complex distribution of haemodynamic forces in a mouse retina model of angiogenesis. *Journal of the Royal Society Interface,* 11, 20140543.

BOGDANOV, A., WRIGHT, S. C., MARECOS, E. M., BOGDANOVA, A., MARTIN, C., PETHERICK, P. & WEISSLEDER, R. 1997. A long-circulating co-polymer in "passive targeting" to solid tumors. *Journal of Drug Targeting,* 4**,** 321-330.

BOOKHEIMER, S. Y., STROJWAS, M. H., COHEN, M. S., SAUNDERS, A. M., PERICAK-VANCE, M. A., MAZZIOTTA, J. C. & SMALL, G. W. 2000. Patterns of brain activation in people at risk for Alzheimer's disease. *New England Journal of Medicine,* 343**,** 450-456.

BOX, G. E. P. & MULLER, M. E. 1958. A Note on the Generation of Random Normal Deviates. 610-611.

BROADWELL, R. D., BALIN, B. J. & SALCMAN, M. 1988. Transcytotic pathway for blood-borne protein through the blood-brain barrier. *Proceedings of the National Academy of Sciences of the United States of America,* 85**,** 632-636.

BUSIJA, D. W., BARI, F., DOMOKI, F. & LOUIS, T. 2007. Mechanisms involved in the cerebrovascular dilator effects of N-methyl-D-aspartate in cerebral cortex. *Brain Research Reviews,* 56**,** 89-100.

BUTLER, S. M. & CAMILLI, A. 2005. Going against the grain: chemotaxis and infection in Vibrio cholerae. *Nat Rev Micro,* 3**,** 611-620.

BUTT, A. M., JONES, H. C. & ABBOTT, N. J. 1990. ELECTRICAL-RESISTANCE ACROSS THE BLOOD-BRAIN-BARRIER IN ANESTHETIZED RATS - A DEVELOPMENTAL-STUDY. *Journal of Physiology-London,* 429**,** 47-62.

CAIN, C. C., SIPE, D. M. & MURPHY, R. F. 1989. Regulation of endocytic pH by the Na+,K+-ATPase in living cells. *Proceedings of the National Academy of Sciences of the United States of America,* 86**,** 544-548.

CARPENTER, M., STRONG, O. & TRUEX, R. c.1976. *Human neuroanatomy*, Baltimore: Williams & Wilkins.

CECCHIN, D., JOSEPH, A., CONTINI, C., NYBERG, S., RUIZ-PEREZ, L., FULLSTONE, G., AKHTAR, A., MADSEN, J., RYAN, A. J., FERNYHOUGH, C., ARMES, S. P., GOLESTANIAN, R. &

BATTAGLIA, G. Submitted. Enzyme-driven Chemotactic Synthetic Vesicles. *Nature Nanotechnology*.

CEDERVALL, T., LYNCH, I., LINDMAN, S., BERGGÅRD, T., THULIN, E., NILSSON, H., DAWSON, K. A. & LINSE, S. 2007. Understanding the nanoparticle–protein corona using methods to quantify exchange rates and affinities of proteins for nanoparticles. *Proceedings of the National Academy of Sciences,* 104**,** 2050-2055.

CHAMBERS, E. & MITRAGOTRI, S. 2007. Long circulating nanoparticles via adhesion on Red Blood Cells: Mechanism and extended circulation. *Experimental Biology and Medicine,* 232**,** 958-966.

CHEN, J., HESSLER, J. A., PUTCHAKAYALA, K., PANAMA, B. K., KHAN, D. P., HONG, S., MULLEN, D. G., DIMAGGIO, S. C., SOM, A., TEW, G. N., LOPATIN, A. N., BAKER, J. R., HOLL, M. M. B. & ORR, B. G. 2009. Cationic Nanoparticles Induce Nanoscale Disruption in Living Cell Plasma Membranes. *The Journal of Physical Chemistry B,* 113**,** 11179-11185.

CHEN, S. & DOOLEN, G. D. 1998. LATTICE BOLTZMANN METHOD FOR FLUID FLOWS. *Annual Review of Fluid Mechanics,* 30**,** 329-364.

CHEN, Y., MUNTEANU, A. C., HUANG, Y.-F., PHILLIPS, J., ZHU, Z., MAVROS, M. & TAN, W. 2009. Mapping Receptor Density on Live Cells by Using Fluorescence Correlation Spectroscopy. *Chemistry – A European Journal,* 15**,** 5327-5336.

CHIN, L. S., WORTH, D., GREENOUGH, C., COAKLEY, S., HOLCOMBE, M. & KIRAN, M. 2012. FLAME: an approach to the parallelisation of agent-based applications. *RAL Technical Reports,* RAL-TR-2008-022.

CHITHRANI, B. D., GHAZANI, A. A. & CHAN, W. C. W. 2006. Determining the size and shape dependence of gold nanoparticle uptake into mammalian cells. *Nano Letters,* 6**,** 662-668.

CHO, Y.-I. & CHO, D. J. 2011. Hemorheology and Microvascular Disorders. *Korean Circulation Journal,* 41**,** 287-295.

CHOI, H. S., LIU, W., MISRA, P., TANAKA, E., ZIMMER, J. P., IPE, B. I., BAWENDI, M. G. & FRANGIONI, J. V. 2007. Renal Clearance of Nanoparticles. *Nature biotechnology,* 25**,** 1165-1170.

CLARK, D. E. 2003. In silico prediction of blood-brain barrier permeation. *Drug Discovery Today,* 8**,** 927-933.

CLAUDIO, L., KRESS, Y., NORTON, W. T. & BROSNAN, C. F. 1989. INCREASED VESICULAR TRANSPORT AND DECREASED MITOCHONDRIAL CONTENT IN BLOOD-BRAIN-BARRIER ENDOTHELIAL-CELLS DURING EXPERIMENTAL AUTOIMMUNE ENCEPHALOMYELITIS. *American Journal of Pathology,* 135**,** 1157-1168.

CLEAVER, O. & MELTON, D. A. 2003. Endothelial signaling during development. *Nature Medicine,* 9**,** 661-668.

CONNER, S. D. & SCHMID, S. L. 2003. Regulated portals of entry into the cell. *Nature,* 422**,** 37-44.

CROSS, G. H., FREEMAN, N. J. & SWANN, M. J. 2008. Dual Polarization Interferometry: A Real-Time Optical Technique for Measuring (Bio)molecular Orientation, Structure and Function at the Solid/Liquid

Interface. *Handbook of Biosensors and Biochips.* John Wiley & Sons, Ltd.

CUCULLO, L., COURAUD, P.-O., WEKSLER, B., ROMERO, I.-A., HOSSAIN, M., RAPP, E. & JANIGRO, D. 2008. Immortalized human brain endothelial cells and flow-based vascular modeling: a marriage of convenience for rational neurovascular studies. *Journal of Cerebral Blood Flow and Metabolism,* 28**,** 312-328.

CUCULLO, L., HOSSAIN, M., TIERNEY, W. & JANIGRO, D. 2013. A new dynamic in vitro modular capillaries-venules modular system: Cerebrovascular physiology in a box. *Bmc Neuroscience,* 14.

DALLAIRE, L., TREMBLAY, L. & BELIVEAU, R. 1991. PURIFICATION AND CHARACTERIZATION OF METABOLICALLY ACTIVE CAPILLARIES OF THE BLOOD-BRAIN-BARRIER. *Biochemical Journal,* 276**,** 745-752.

DALLASTA, L. M., PISAROV, L. A., ESPLEN, J. E., WERLEY, J. V., MOSES, A. V., NELSON, J. A. & ACHIM, C. L. 1999. Blood-Brain Barrier Tight Junction Disruption in Human Immunodeficiency Virus-1 Encephalitis. *The American Journal of Pathology,* 155**,** 1915-1927.

DAVSON, H. & SEGAL, M. B. 1995. *Physiology of the CSF and Blood-Brain Barriers*, Taylor & Francis.

DE JONG, W. H., HAGENS, W. I., KRYSTEK, P., BURGER, M. C., SIPS, A. N. J. A. M. & GEERTSMA, R. E. 2008. Particle size-dependent organ distribution of gold nanoparticles after intravenous administration. *Biomaterials,* 29**,** 1912-1919.

DECUZZI, P. & FERRARI, M. 2006. The adhesive strength of non-spherical particles mediated by specific interactions. *Biomaterials,* 27**,** 5307-5314.

DECUZZI, P. & FERRARI, M. 2008. The Receptor-Mediated Endocytosis of Nonspherical Particles. *Biophysical Journal,* 94**,** 3790-3797.

DEISSENBERG, C., VAN DER HOOG, S. & DAWID, H. 2008. EURACE: A massively parallel agent-based model of the European economy. *Applied Mathematics and Computation,* 204**,** 541-552.

DEKOSKY, S. T. & MAREK, K. 2003. Looking backward to move forward: Early detection of neurodegenerative disorders. *Science,* 302**,** 830-834.

DEMEULE, M., CURRIE, J.-C., BERTRAND, Y., CHÉ, C., NGUYEN, T., RÉGINA, A., GABATHULER, R., CASTAIGNE, J.-P. & BÉLIVEAU, R. 2008a. Involvement of the low-density lipoprotein receptor-related protein in the transcytosis of the brain delivery vector Angiopep-2. *Journal of Neurochemistry,* 106**,** 1534-1544.

DEMEULE, M., RÉGINA, A., CHÉ, C., POIRIER, J., NGUYEN, T., GABATHULER, R., CASTAIGNE, J.-P. & BÉLIVEAU, R. 2008b. Identification and Design of Peptides as a New Drug Delivery System for the Brain. *Journal of Pharmacology and Experimental Therapeutics,* 324**,** 1064-1072.

DEREJKO, M., SLAWEK, J., WIECZOREK, D., BROCKHUIS, B., DUBANIEWICZ, M. & LASS, P. 2006. Regional cerebral blood flow in Parkinson's disease as an indicator of cognitive impairment. *Nuclear Medicine Communications,* 27**,** 945-951.

DERJAGUIN, B. V. 1987. Some results from 50 years' research on surface forces. *Surface Forces and Surfactant Systems.* Steinkopff.

DORE, S. E. 1923. On the contractility and nervous supply of the capillaries. *British Journal of Dermatology and Syphilis,* 35**,** 398-404.

DREYFUS, R., BAUDRY, J., ROPER, M. L., FERMIGIER, M., STONE, H. A. & BIBETTE, J. 2005. Microscopic artificial swimmers. *Nature,* 437**,** 862-865.

DVORAK, A. M., KOHN, S., MORGAN, E. S., FOX, P., NAGY, J. A. & DVORAK, H. F. 1996. The vesiculo-vacuolar organelle (VVO): a distinct endothelial cell structure that provides a transcellular pathway for macromolecular extravasation. *Journal of Leukocyte Biology,* 59**,** 100-15.

EBBENS, S. J. & HOWSE, J. R. 2010. In pursuit of propulsion at the nanoscale. *Soft Matter,* 6**,** 726-738.

EINSTEIN, A. 1905. The motion of elements suspended in static liquids as claimed in the molecular kinetic theory of heat. *Annalen Der Physik,* 17**,** 549-560.

ELICEIRI, B. P., GONZALEZ, A. M. & BAIRD, A. 2011. Zebrafish Model of the Blood-Brain Barrier: Morphological and Permeability Studies. *Blood-Brain and Other Neural Barriers: Reviews and Protocols,* 686**,** 371-378.

ERICKSON, H. P. 2009. Size and Shape of Protein Molecules at the Nanometer Level Determined by Sedimentation, Gel Filtration, and Electron Microscopy. *Biological Procedures Online,* 11**,** 32-51.

FAHRAEUS, R. & LINDQVIST, T. 1931. The viscosity of the blood in narrow capillary tubes. *American Journal of Physiology,* 96**,** 562-568.

FAKHARI, A., BAOUM, A., SIAHAAN, T. J., LE, K. B. & BERKLAND, C. 2011. Controlling ligand surface density optimizes nanoparticle binding to ICAM-1. *Journal of Pharmaceutical Sciences,* 100**,** 1045-1056.

FANG, J., NAKAMURA, H. & MAEDA, H. 2011. The EPR effect: Unique features of tumor blood vessels for drug delivery, factors involved, and limitations and augmentation of the effect. *Advanced Drug Delivery Reviews,* 63**,** 136-151.

FAWCETT, J. W. & ASHER, R. A. 1999. The glial scar and central nervous system repair. *Brain Research Bulletin,* 49**,** 377-391.

FEDOSOV, D. A., PELTOMAEKI, M. & GOMPPER, G. 2014. Deformation and dynamics of Red Blood Cells in flow through cylindrical microchannels. *Soft Matter,* 10**,** 4258-4267.

FERNANDEZ-KLETT, F., OFFENHAUSER, N., DIRNAGL, U., PRILLER, J. & LINDAUER, U. 2010. Pericytes in capillaries are contractile in vivo, but arterioles mediate functional hyperemia in the mouse brain. *Proceedings of the National Academy of Sciences of the United States of America,* 107**,** 22290-22295.

FERZIGER, J. H. & PERIĆ, M. 2002. *Computational methods for fluid dynamics*, Springer Berlin.

FEWEL, M. E., THOMPSON, B. G., JR. & HOFF, J. T. 2003. Spontaneous intracerebral hemorrhage: a review. *Neurosurgical focus,* 15**,** E1-E1.

FLEMING, A., DIEKMANN, H. & GOLDSMITH, P. 2013. Functional Characterisation of the Maturation of the Blood-Brain Barrier in Larval Zebrafish. *Plos One,* 8.

FRIDEN, P. M., WALUS, L. R., MUSSO, G. F., TAYLOR, M. A., MALFROY, B. & STARZYK, R. M. 1991. Anti-transferrin receptor antibody and antibody-drug conjugates cross the blood-brain barrier. *Proceedings of the National Academy of Sciences of the United States of America,* 88**,** 4771-4775.

FRIEBOES, H. B., WU, M., LOWENGRUB, J., DECUZZI, P. & CRISTINI, V. 2013. A Computational Model for Predicting Nanoparticle Accumulation in Tumor Vasculature. *Plos One,* 8**,** e56876.

GANTA, S., DEVALAPALLY, H., SHAHIWALA, A. & AMIJI, M. 2008. A review of stimuli-responsive nanocarriers for drug and gene delivery. *Journal of Controlled Release,* 126**,** 187-204.

GAO, H., SHI, W. & FREUND, L. B. 2005. Mechanics of receptor-mediated endocytosis. *Proceedings of the National Academy of Sciences of the United States of America,* 102**,** 9469-9474.

GAO, H., ZHANG, S., CAO, S., YANG, Z., PANG, Z. & JIANG, X. 2014. Angiopep-2 and Activatable Cell-Penetrating Peptide Dual-Functionalized Nanoparticles for Systemic Glioma-Targeting Delivery. *Molecular Pharmaceutics,* 11**,** 2755-2763.

GAO, K. & JIANG, X. 2006. Influence of particle size on transport of methotrexate across blood brain barrier by polysorbate 80-coated polybutylcyanoacrylate nanoparticles. *International Journal of Pharmaceutics,* 310**,** 213-219.

GARAY, R. P., EL-GEWELY, R., ARMSTRONG, J. K., GARRATTY, G. & RICHETTE, P. 2012. Antibodies against polyethylene glycol in healthy subjects and in patients treated with PEG-conjugated agents. *Expert Opinion on Drug Delivery,* 9**,** 1319-1323.

GAULTIER, A., WU, X., LE MOAN, N., TAKIMOTO, S., MUKANDALA, G., AKASSOGLOU, K., CAMPANA, W. M. & GONIAS, S. L. 2009. Low-density lipoprotein receptor-related protein 1 is an essential receptor for myelin phagocytosis. *Journal of Cell Science,* 122**,** 1155-1162.

GENG, Y. A. N., DALHAIMER, P., CAI, S., TSAI, R., TEWARI, M., MINKO, T. & DISCHER, D. E. 2007. Shape effects of filaments versus spherical particles in flow and drug delivery. *Nature Nanotechnology,* 2**,** 249-255.

GERWECK, L. E. & SEETHARAMAN, K. 1996. Cellular pH Gradient in Tumor versus Normal Tissue: Potential Exploitation for the Treatment of Cancer. *Cancer Research,* 56**,** 1194-1198.

GIBBS, J. G. & ZHAO, Y.-P. 2009. Autonomously motile catalytic nanomotors by bubble propulsion. *Applied Physics Letters,* 94**,** 163104.

GIBSON, Q. H., SWOBODA, B. E. P. & MASSEY, V. 1964. Kinetics and Mechanism of Action of Glucose Oxidase. *Journal of Biological Chemistry,* 239**,** 3927-3934.

GINGRICH, M. B., JUNGE, C. E., LYUBOSLAVSKY, P. & TRAYNELIS, S. F. 2000. Potentiation of NMDA Receptor Function by the Serine Protease Thrombin. *The Journal of Neuroscience,* 20**,** 4582-4595.

GINGRICH, M. B. & TRAYNELIS, S. F. 2000. Serine proteases and brain damage – is there a link? *Trends in Neurosciences,* 23**,** 399-407.

GOLESTANIAN, R., LIVERPOOL, T. B. & AJDARI, A. 2005. Propulsion of a Molecular Machine by Asymmetric Distribution of Reaction Products. *Physical Review Letters,* 94**,** 220801.

GOLESTANIAN, R., LIVERPOOL, T. B. & AJDARI, A. 2007. Designing phoretic micro- and nano-swimmers. *New Journal of Physics,* 9**,** 126.

GOODMAN, C. M., MCCUSKER, C. D., YILMAZ, T. & ROTELLO, V. M. 2004. Toxicity of Gold Nanoparticles Functionalized with Cationic and Anionic Side Chains. *Bioconjugate Chemistry,* 15**,** 897-900.

GORDON, G. R. J., CHOI, H. B., RUNGTA, R. L., ELLIS-DAVIES, G. C. R. & MACVICAR, B. A. 2008. Brain metabolism dictates the polarity of astrocyte control over arterioles. *Nature,* 456**,** 745-U45.

GORDON, L. G. M. 1981. Osmophoresis. *The Journal of Physical Chemistry,* 85**,** 1753-1755.

GOSK, S., VERMEHREN, C., STORM, G. & MOOS, T. 2004. Targeting Anti-Transferrin Receptor Antibody (OX26) and OX26-Conjugated Liposomes to Brain Capillary Endothelial Cells Using In Situ Perfusion. *J Cereb Blood Flow Metab,* 24**,** 1193-1204.

GRADISHAR, W. J., TJULANDIN, S., DAVIDSON, N., SHAW, H., DESAI, N., BHAR, P., HAWKINS, M. & O'SHAUGHNESSY, J. 2005. Phase III Trial of Nanoparticle Albumin-Bound Paclitaxel Compared With Polyethylated Castor Oil–Based Paclitaxel in Women With Breast Cancer. *Journal of Clinical Oncology,* 23**,** 7794-7803.

GREF, R., LÜCK, M., QUELLEC, P., MARCHAND, M., DELLACHERIE, E., HARNISCH, S., BLUNK, T. & MÜLLER, R. H. 2000. 'Stealth' corona-core nanoparticles surface modified by polyethylene glycol (PEG): influences of the corona (PEG chain length and surface density) and of the core composition on phagocytic uptake and plasma protein adsorption. *Colloids and Surfaces B: Biointerfaces,* 18**,** 301-313.

GRIEP, L. M., WOLBERS, F., DE WAGENAAR, B., TER BRAAK, P. M., WEKSLER, B. B., ROMERO, I. A., COURAUD, P. O., VERMES, I., VAN DER MEER, A. D. & VAN DEN BERG, A. 2013. BBB ON CHIP: microfluidic platform to mechanically and biochemically modulate blood-brain barrier function. *Biomedical Microdevices,* 15**,** 145-150.

GROEN, D., HETHERINGTON, J., CARVER, H. B., NASH, R. W., BERNABEU, M. O. & COVENEY, P. V. 2013. Analysing and modelling the performance of the HemeLB lattice-Boltzmann simulation environment. *Journal of Computational Science,* 4**,** 412-422.

GROMNICOVA, R., DAVIES, H. A., SREEKANTHREDDY, P., ROMERO, I. A., LUND, T., ROITT, I. M., PHILLIPS, J. B. & MALE, D. K. 2013. Glucose-Coated Gold Nanoparticles Transfer across Human Brain Endothelium and Enter Astrocytes *In Vitro*. *Plos One,* 8**,** e81043.

GUAN, J., PAVLOVIC, D., DALKIE, N., WALDVOGEL, H. J., O'CARROLL, S. J., GREEN, C. R. & NICHOLSON, L. F. B. 2013. Vascular Degeneration in Parkinson's Disease. *Brain Pathology,* 23**,** 154-164.

GUEST, M. M., DERRICK, J. R., COOPER, R. G. & BOND, T. P. 1963. RED BLOOD CELLS - CHANGE IN SHAPE IN CAPILLARIES. *Science,* 142**,** 1319-&.

GUPTA, S., SOELLINGER, M., GRZYBOWSKI, D. M., BOESIGER, P., BIDDISCOMBE, J., POULIKAKOS, D. & KURTCUOGLU, V. 2010. Cerebrospinal fluid dynamics in the human cranial subarachnoid space: an overlooked mediator of cerebral disease. I. Computational model. *Journal of the Royal Society Interface,* 7**,** 1195-1204.

HALL, C. N., REYNELL, C., GESSLEIN, B., HAMILTON, N. B., MISHRA, A., SUTHERLAND, B. A., O'FARRELL, F. M., BUCHAN, A. M., LAURITZEN, M. & ATTWELL, D. 2014. Capillary pericytes regulate cerebral blood flow in health and disease. *Nature,* 508**,** 55-+.

HAMAD, I., HUNTER, A. C., SZEBENI, J. & MOGHIMI, S. M. 2008. Poly(ethylene glycol)s generate complement activation products in human serum through increased alternative pathway turnover and a MASP-2-dependent process. *Molecular Immunology,* 46**,** 225-232.

ISHIDA, T., WANG, X., SHIMIZU, T., NAWATA, K. & KIWADA, H. 2007. PEGylated liposomes elicit an anti-PEG IgM response in a T cell-independent manner. *Journal of Controlled Release,* 122**,** 349-355.

HAMBURG, M. A. & COLLINS, F. S. 2010. The Path to Personalized Medicine. *New England Journal of Medicine,* 363**,** 301-304.

HAMILTON, N. B., ATTWELL, D. & HALL, C. N. 2010. Pericyte-mediated regulation of capillary diameter: a component of neurovascular coupling in health and disease. *Frontiers in neuroenergetics,* 2.

HAMMER, D. A. & APTE, S. M. 1992. Simulation of cell rolling and adhesion on surfaces in shear flow: general results and analysis of selectin-mediated neutrophil adhesion. *Biophysical Journal,* 63**,** 35-57.

HANISCH, U.-K. & KETTENMANN, H. 2007. Microglia: active sensor and versatile effector cells in the normal and pathologic brain. *Nature Neuroscience,* 10**,** 1387-1394.

HARDER, D. R. 1987. PRESSURE-INDUCED MYOGENIC ACTIVATION OF CAT CEREBRAL-ARTERIES IS DEPENDENT ON INTACT ENDOTHELIUM. *Circulation Research,* 60**,** 102-107.

HARUTA, M. 2003. When Gold Is Not Noble: Catalysis by Nanoparticles. *The Chemical Record,* 3**,** 75-87.

HAUN, J. B. & HAMMER, D. A. 2008. Quantifying Nanoparticle Adhesion Mediated by Specific Molecular Interactions. *Langmuir,* 24**,** 8821-8832.

HELDIN, C.-H., RUBIN, K., PIETRAS, K. & OSTMAN, A. 2004. High interstitial fluid pressure [mdash] an obstacle in cancer therapy. *Nat Rev Cancer,* 4**,** 806-813.

HERVÉ, F., GHINEA, N. & SCHERRMANN, J.-M. 2008. CNS Delivery Via Adsorptive Transcytosis. *The AAPS Journal,* 10**,** 455-472.

HERZ, J. & MARSCHANG, P. 2003. Coaxing the LDL receptor family into the fold. *Cell,* 112**,** 289-292.

HICKEY, W. F., HSU, B. L. & KIMURA, H. 1991. LYMPHOCYTE-T ENTRY INTO THE CENTRAL-NERVOUS-SYSTEM. *Journal of Neuroscience Research,* 28**,** 254-260.

HOBBS, S. K., MONSKY, W. L., YUAN, F., ROBERTS, W. G., GRIFFITH, L., TORCHILIN, V. P. & JAIN, R. K. 1998. Regulation of transport pathways in tumor vessels: Role of tumor type and microenvironment. *Proceedings of the National Academy of Sciences,* 95**,** 4607-4612.

HOOD, L., HEATH, J. R., PHELPS, M. E. & LIN, B. Y. 2004. Systems biology and new technologies enable predictive and preventative medicine. *Science,* 306**,** 640-643.

HOPKINS, C. R. 1983. Intracellular routing of transferrin and transferrin receptors in epidermoid carcinoma A431 cells. *Cell,* 35**,** 321-330.

HOWSE, J. R., JONES, R. A. L., RYAN, A. J., GOUGH, T., VAFABAKHSH, R. & GOLESTANIAN, R. 2007. Self-Motile Colloidal Particles: From Directed Propulsion to Random Walk. *Physical Review Letters,* 99**,** 048102.

HUANG, S., LI, J., HAN, L., LIU, S., MA, H., HUANG, R. & JIANG, C. 2011. Dual targeting effect of Angiopep-2-modified, DNA-loaded nanoparticles for glioma. *Biomaterials,* 32**,** 6832-6838.

HUGHES, S., GARDINER, T., HU, P., BAXTER, L., ROSINOVA, E. & CHAN-LING, T. 2006. Altered pericyte-endothelial relations in the rat retina during aging: Implications for vessel stability. *Neurobiology of Aging,* 27**,** 1838-1847.

HYNYNEN, K., MCDANNOLD, N., SHEIKOV, N. A., JOLESZ, F. A. & VYKHODTSEVA, N. 2005. Local and reversible blood–brain barrier disruption by noninvasive focused ultrasound at frequencies suitable for trans-skull sonications. *Neuroimage,* 24**,** 12-20.

ILIFF, J. J., LEE, H., YU, M., FENG, T., LOGAN, J., NEDERGAARD, M. & BENVENISTE, H. 2013. Brain-wide pathway for waste clearance captured by contrast-enhanced MRI. *Journal of Clinical Investigation,* 123**,** 1299-1309.

IYER, A. K., KHALED, G., FANG, J. & MAEDA, H. 2006. Exploiting the enhanced permeability and retention effect for tumor targeting. *Drug Discovery Today,* 11**,** 812-818.

JACKSON, D. E., HOLCOMBE, M. & RATNIEKS, F. L. W. 2004. Trail geometry gives polarity to ant foraging networks. *Nature,* 432**,** 907-909.

JACKSON, D. E., MARTIN, S. J., RATNIEKS, F. L. W. & HOLCOMBE, M. 2007. Spatial and temporal variation in pheromone composition of ant foraging trails. *Behavioral Ecology,* 18**,** 444-450.

JAIN, R. K. & STYLIANOPOULOS, T. 2010. Delivering nanomedicine to solid tumors. *Nature reviews. Clinical oncology,* 7**,** 653-664.

JAKOBSSON, L., FRANCO, C. A., BENTLEY, K., COLLINS, R. T., PONSIOEN, B., ASPALTER, I. M., ROSEWELL, I., BUSSE, M., THURSTON, G., MEDVINSKY, A., SCHULTE-MERKER, S. & GERHARDT, H. 2010. Endothelial cells dynamically compete for the tip cell position during angiogenic sprouting. *Nat Cell Biol,* 12**,** 943-953.

JEONG HUN, K., JIN HYOUNG, K., KYU-WON, K., MYUNG HUN, K. & YOUNG SUK, Y. 2009. Intravenously administered gold nanoparticles pass through the blood,Äìretinal barrier depending on the particle size, and induce no retinal toxicity. *Nanotechnology,* 20**,** 505101.

JEONG, J.-Y., KWON, H.-B., AHN, J.-C., KANG, D., KWON, S.-H., PARK, J. A. & KIM, K.-W. 2008. Functional and developmental analysis of the blood-brain barrier in zebrafish. *Brain Research Bulletin,* 75**,** 619-628.

JIANG, H.-R., YOSHINAGA, N. & SANO, M. 2010. Active Motion of a Janus Particle by Self-Thermophoresis in a Defocused Laser Beam. *Physical Review Letters,* 105**,** 268302.

JOO, F. & KARNUSHI.I 1973. PROCEDURE FOR ISOLATION OF CAPILLARIES FROM RAT-BRAIN. *Cytobios,* 8**,** 41-48.

KAOUI, B., BIROS, G. & MISBAH, C. 2009. Why Do Red Blood Cells Have Asymmetric Shapes Even in a Symmetric Flow? *Physical Review Letters,* 103.

KE, H., YE, S., CARROLL, R. L. & SHOWALTER, K. 2010. Motion Analysis of Self-Propelled Pt–Silica Particles in Hydrogen Peroxide Solutions. *The Journal of Physical Chemistry A,* 114**,** 5462-5467.

KEIDING, S., VILSTRUP, H. & HANSEN, L. 1980. Importance of flow and haematocrit for metabolic function of perfused rat liver. *Scandinavian Journal of Clinical and Laboratory Investigation,* 40**,** 355-359.

KIBBEY, R. G., RIZO, J., GIERASCH, L. M. & ANDERSON, R. G. W. 1998. The LDL Receptor Clustering Motif Interacts with the Clathrin Terminal Domain in a Reverse Turn Conformation. *The Journal of Cell Biology,* 142**,** 59-67.

KINOSHITA, M., MCDANNOLD, N., JOLESZ, F. A. & HYNYNEN, K. 2006a. Noninvasive localized delivery of Herceptin to the mouse brain by MRI-guided focused ultrasound-induced blood–brain barrier disruption. *Proceedings of the National Academy of Sciences,* 103**,** 11719-11723.

KINOSHITA, M., MCDANNOLD, N., JOLESZ, F. A. & HYNYNEN, K. 2006b. Targeted delivery of antibodies through the blood–brain barrier by MRI-guided focused ultrasound. *Biochemical and Biophysical Research Communications,* 340**,** 1085-1090.

KIRAN, M., BICAK, M., MALEKI-DIZAJI, S. & HOLCOMBE, M. 2011. Flame: A Platform for High Performance Computing of Complex Systems, Applied for Three Case Studies. *Acta Physica Polonica B Proceedings Supplement,* 4**,** 201-216.

KNOP, R. 1969. Remark on algorithm 334 [G5]: normal random deviates. *Commun. ACM,* 12**,** 281.

KORIN, N., KANAPATHIPILLAI, M., MATTHEWS, B. D., CRESCENTE, M., BRILL, A., MAMMOTO, T., GHOSH, K., JUREK, S., BENCHERIF, S. A., BHATTA, D., COSKUN, A. U., FELDMAN, C. L., WAGNER, D. D. & INGBER, D. E. 2012. Shear-Activated Nanotherapeutics for Drug Targeting to Obstructed Blood Vessels. *Science,* 337**,** 738-742.

KRAMS, R., WENTZEL, J. J., OOMEN, J. A. F., VINKE, R., SCHUURBIERS, J. C. H., DE FEYTER, P. J., SERRUYS, P. W. & SLAGER, C. J. 1997. Evaluation of Endothelial Shear Stress and 3D Geometry as Factors Determining the Development of Atherosclerosis and Remodeling in Human Coronary Arteries in Vivo: Combining 3D Reconstruction from Angiography and IVUS (ANGUS) with Computational Fluid Dynamics. *Arteriosclerosis, Thrombosis, and Vascular Biology,* 17**,** 2061-2065.

KREUTER, J. R., ALYAUTDIN, R. N., KHARKEVICH, D. A. & IVANOV, A. A. 1995. Passage of peptides through the blood-brain barrier with colloidal polymer particles (nanoparticles). *Brain Research,* 674**,** 171-174.

KREUTER, J. R., SHAMENKOV, D., PETROV, V., RAMGE, P., CYCHUTEK, K., KOCH-BRANDT, C. & ALYAUTDIN, R. 2002. Apolipoprotein-mediated Transport of Nanoparticle-bound Drugs Across the Blood-Brain Barrier. *Journal of Drug Targeting,* 10**,** 317-325.

KREUTZBERG, G. W. 1996. Microglia: A sensor for pathological events in the CNS. *Trends in Neurosciences,* 19**,** 312-318.

KURTCUOGLU, V., SOELLINGER, M., SUMMERS, P., POULIKAKOS, D. & BOESIGER, P. 2007. Mixing and modes of mass transfer in the third cerebral ventricle: A computational analysis. *Journal of Biomechanical Engineering-Transactions of the Asme,* 129**,** 695-702.

LANGLET, F. 2014. Tanycytes: a gateway to the metabolic hypothalamus. *Journal of neuroendocrinology,* 2**6,** 753-60.

LANGLET, F., MULLIER, A., BOURET, S. G., PREVOT, V. & DEHOUCK, B. 2013. Tanycyte-like cells form a blood–cerebrospinal fluid barrier in the circumventricular organs of the mouse brain. *Journal of Comparative Neurology,* 521**,** spc1-spc1.

LI, B. & FREEMAN, R. D. 2010. Neurometabolic Coupling in the Lateral Geniculate Nucleus Changes With Extended Age. *Journal of Neurophysiology,* 104**,** 414-425.

LI, X., UPADHYAY, A. K., BULLOCK, A. J., DICOLANDREA, T., XU, J., BINDER, R. L., ROBINSON, M. K., FINLAY, D. R., MILLS, K. J., BASCOM, C. C., KELLING, C. K., ISFORT, R. J., HAYCOCK, J. W., MACNEIL, S. & SMALLWOOD, R. H. 2013. Skin Stem Cell Hypotheses and Long Term Clone Survival – Explored Using Agent-based Modelling. *Scientific Reports,* 3**,** 1904.

LIPTON, P. 1999. Ischemic cell death in brain neurons. *Physiological Reviews,* 79**,** 1431-1568.

LIU, Y., SHAH, S. & TAN, J. 2012. Computational Modeling of Nanoparticle Targeted Drug Delivery. *Reviews in Nanoscience and Nanotechnology,* 1**,** 66-83.

LOMAS, H., CANTON, I., MACNEIL, S., DU, J., ARMES, S. P., RYAN, A. J., LEWIS, A. L. & BATTAGLIA, G. 2007. Biomimetic pH sensitive polymersomes for efficient DNA encapsulation and delivery. *Advanced Materials,* 19**,** 4238-+.

LOMAS, H., MASSIGNANI, M., ABDULLAH, K. A., CANTON, I., LO PRESTI, C., MACNEIL, S., DU, J. Z., BLANAZS, A., MADSEN, J., ARMES, S. P., LEWIS, A. L. & BATTAGLIA, G. 2008. Non-cytotoxic polymer vesicles for rapid and efficient intracellular delivery. *Faraday Discussions,* 139**,** 143-159.

LOPRESTI, C., MASSIGNANI, M., FERNYHOUGH, C., BLANAZS, A., RYAN, A. J., MADSEN, J., WARREN, N. J., ARMES, S. P., LEWIS, A. L., CHIRASATITSIN, S., ENGLER, A. J. & BATTAGLIA, G. 2011. Controlling Polymersome Surface Topology at the Nanoscale by Membrane Confined Polymer/Polymer Phase Separation. *Acs Nano,* 5**,** 1775-1784.

LOUVEAU, A., SMIRNOV, I., KEYES, T. J., ECCLES, J. D., ROUHANI, S. J., PESKE, J. D., DERECKI, N. C., CASTLE, D., MANDELL, J. W., LEE, K. S., HARRIS, T. H. & KIPNIS, J. 2015. Structural and functional features of central nervous system lymphatic vessels. *Nature,* 523**,** 337-341.

LUNDQVIST, M., STIGLER, J., ELIA, G., LYNCH, I., CEDERVALL, T. & DAWSON, K. A. 2008. Nanoparticle size and surface properties determine the protein corona with possible implications for biological impacts. *Proceedings of the National Academy of Sciences,* 105**,** 14265-14270.

MA, J. Y., AYATA, C., HUANG, P. L., FISHMAN, M. C. & MOSKOWITZ, M. A. 1996. Regional cerebral blood flow response to vibrissal stimulation in mice lacking type I NOS gene expression. *American Journal of Physiology-Heart and Circulatory Physiology,* 270**,** H1085-H1090.

MAEDA, H., WU, J., SAWA, T., MATSUMURA, Y. & HORI, K. 2000. Tumor vascular permeability and the EPR effect in macromolecular therapeutics: a review. *Journal of Controlled Release,* 65**,** 271-284.

MANO, N. & HELLER, A. 2005. Bioelectrochemical Propulsion. *Journal of the American Chemical Society,* 127**,** 11574-11575.

MARKOU, A., CHIAMULERA, C., GEYER, M. A., TRICKLEBANK, M. & STECKLER, T. 2009. Removing Obstacles in Neuroscience Drug Discovery: The Future Path for Animal Models. *Neuropsychopharmacology,* 34**,** 74-89.

MARTIN, A. J., FRISTON, K. J., COLEBATCH, J. G. & FRACKOWIAK, R. S. J. 1991. DECREASES IN REGIONAL CEREBRAL BLOOD-FLOW WITH NORMAL AGING. *Journal of Cerebral Blood Flow and Metabolism,* 11**,** 684-689.

MARTIN, A. M., KUHLMANN, C., TROSSBACH, S., JAEGER, S., WALDRON, E., ROEBROEK, A., LUHMANN, H. J., LAATSCH, A., WEGGEN, S., LESSMANN, V. & PIETRZIK, C. U. 2008. The Functional Role of the Second NPXY Motif of the LRP1 Œ≤-Chain in Tissue-type Plasminogen Activator-mediated Activation of N-Methyl-D-aspartate Receptors. *Journal of Biological Chemistry,* 283**,** 12004-12013.

MARTINEZ-VERACOECHEA, F. J. & FRENKEL, D. 2011. Designing super selectivity in multivalent nano-particle binding. *Proceedings of the National Academy of Sciences,* 108**,** 10963-10968.

MASSIGNANI, M., LOPRESTI, C., BLANAZS, A., MADSEN, J., ARMES, S. P., LEWIS, A. L. & BATTAGLIA, G. 2009. Controlling Cellular Uptake by Surface Chemistry, Size, and Surface Topology at the Nanoscale. *Small,* 5**,** 2424-2432.

MASSIGNANI, M., CANTON, I., SUN, T., HEARNDEN, V., MACNEIL, S., BLANAZS, A., ARMES, S. P., LEWIS, A. & BATTAGLIA, G. 2010. Enhanced Fluorescence Imaging of Live Cells by Effective Cytosolic Delivery of Probes. *Plos One,* 5**,** e10459.

MAXFIELD, F. R. & MCGRAW, T. E. 2004. Endocytic recycling. *Nat Rev Mol Cell Biol,* 5**,** 121-132.

MAYER, U., WAGENAAR, E., BEIJNEN, J. H., SMIT, J. W., MEIJER, D. K. F., VANASPEREN, J., BORST, P. & SCHINKEL, A. H. 1996. Substantial excretion of digoxin via the intestinal mucosa and prevention of long-term digoxin accumulation in the brain by the mdr1a P-glycoprotein. *British Journal of Pharmacology,* 119**,** 1038-1044.

MAZZEO, M. D. & COVENEY, P. V. 2008. HemeLB: A high performance parallel lattice-Boltzmann code for large scale fluid flow in complex geometries. *Computer Physics Communications,* 178**,** 894-914.

MCWHIRTER, J. L., NOGUCHI, H. & GOMPPER, G. 2009. Flow-induced clustering and alignment of vesicles and Red Blood Cells in microcapillaries. *Proceedings of the National Academy of Sciences of the United States of America,* 106**,** 6039-6043.

MCWHIRTER, J. L., NOGUCHI, H. & GOMPPER, G. 2011. Deformation and clustering of Red Blood Cells in microcapillary flows. *Soft Matter,* 7**,** 10967-10977.

MEHTA, P., CUMMINGS, R. D. & MCEVER, R. P. 1998. Affinity and Kinetic Analysis of P-selectin Binding to P-selectin Glycoprotein Ligand-1. *Journal of Biological Chemistry,* 273**,** 32506-32513.

MELLMAN, I. 1996. ENDOCYTOSIS AND MOLECULAR SORTING. *Annual Review of Cell and Developmental Biology,* 12**,** 575-625.

MENDELSOHN, A. R. & LARRICK, J. W. 2013. Sleep Facilitates Clearance of Metabolites from the Brain: Glymphatic Function in Aging and Neurodegenerative Diseases. *Rejuvenation Research,* 16**,** 518-523.

MESIWALA, A. H., FARRELL, L., WENZEL, H. J., SILBERGELD, D. L., CRUM, L. A., WINN, H. R. & MOURAD, P. D. 2002. High-intensity focused ultrasound selectively disrupts the blood-brain barrier in vivo. *Ultrasound in Medicine & Biology,* 28**,** 389-400.

METEA, M. R., KOFUJI, P. & NEWMAN, E. A. 2007. Neurovascular coupling is not mediated by potassium siphoning from glial cells. *Journal of Neuroscience,* 27**,** 2468-2471.

MICHEL, R., PASCHE, S., TEXTOR, M. & CASTNER, D. G. 2005. Influence of PEG Architecture on Protein Adsorption and Conformation. *Langmuir,* 21**,** 12327-12332.

MILHORAT, T. & HAMMOCK, M. K. 1983. Cerebrospinal Fluid as Reflection of Internal Milieu of Brain. *In:* WOOD, J. (ed.) *Neurobiology of Cerebrospinal Fluid 2.* Springer US.

MILICI, A. J., L'HERNAULT, N. & PALADE, G. E. 1985. Surface densities of diaphragmed fenestrae and transendothelial channels in different murine capillary beds. *Circulation Research,* 56**,** 709-17.

MILLER, G. 2002. Drug targteting - Breaking down barriers. *Science,* 297**,** 1116-1118.

MONTEROS, A. E. D. L., HUANG, A., KUMAR, S., ZHAO, R. P., NAZARIAN, R., PAN, T., CHANG, R. & DE VELLIS, J. 1999. Transferrin is an essential factor for myelination. *Journal of Neurochemistry,* 72**,** S5-S5.

NADAL, A., FUENTES, E., PASTOR, J. & MCNAUGHTON, P. A. 1995. Plasma albumin is a potent trigger of calcium signals and DNA synthesis in astrocytes. *Proceedings of the National Academy of Sciences of the United States of America,* 92**,** 1426-1430.

NEDERGAARD, M. 2013. Garbage Truck of the Brain. *Science (New York, N.Y.),* 340**,** 1529-1530.

NEUHAUS, W., LAUER, R., OELZANT, S., FRINGELI, U. P., ECKER, G. F. & NOE, C. R. 2006. A novel flow based hollow-fiber blood-brain barrier in vitro model with immortalised cell line PBMEC/C1-2. *Journal of Biotechnology,* 125**,** 127-141.

NEUWELT, E. A., FRENKEL, E. P., DIEHL, J., VU, L. H., RAPOPORT, S. & HILL, S. 1980. Reversible osmotic blood-brain barrier disruption in humans: implications for the chemotherapy of malignant brain tumors. *Neurosurgery,* 7**,** 44-52.

NGUYEN, J. V., SOTO, I., KIM, K.-Y., BUSHONG, E. A., OGLESBY, E., VALIENTE-SORIANO, F. J., YANG, Z., DAVIS, C.-H. O., BEDONT, J. L., SON, J. L., WEI, J. O., BUCHMAN, V. L., ZACK, D. J., VIDAL-SANZ, M., ELLISMAN, M. H. & MARSH-ARMSTRONG, N. 2011. Myelination transition zone astrocytes are constitutively phagocytic and have synuclein dependent reactivity in glaucoma. *Proceedings of the National Academy of Sciences,* 108**,** 1176-1181.

NIEWOEHNER, J., BOHRMANN, B., COLLIN, L., URICH, E., SADE, H., MAIER, P., RUEGER, P., STRACKE, J. O., LAU, W., TISSOT, A. C., LOETSCHER, H., GHOSH, A. & FRESKGÅRD, P.-O. 2014. Increased Brain Penetration and Potency of a Therapeutic Antibody Using a Monovalent Molecular Shuttle. *Neuron,* 81**,** 49-60.

OLDFORS, A. & FARDEAU, M. 1983. THE PERMEABILITY OF THE BASAL LAMINA AT THE NEUROMUSCULAR JUNCTION. AN ULTRASTRUCTURAL STUDY OF RAT SKELETAL MUSCLE USING PARTICULATE TRACERS. *Neuropathology and Applied Neurobiology,* 9**,** 419-432.

OTSUKA, H., NAGASAKI, Y. & KATAOKA, K. 2003. PEGylated nanoparticles for biological and pharmaceutical applications. *Advanced Drug Delivery Reviews,* 55**,** 403-419.

OWENS, D. E. & PEPPAS, N. A. 2006. Opsonization, biodistribution, and pharmacokinetics of polymeric nanoparticles. *International Journal of Pharmaceutics,* 307**,** 93-102.

PALACCI, J. R. M., COTTIN-BIZONNE, C. C., YBERT, C. & BOCQUET, L. R. 2010. Sedimentation and Effective Temperature of Active Colloidal Suspensions. *Physical Review Letters,* 105**,** 88304.

PARDRIDGE, W. M. 2005. The blood-brain barrier: bottleneck in brain drug development. *NeuroRx : the journal of the American Society for Experimental NeuroTherapeutics,* 2**,** 3-14.

PARDRIDGE, W. M., BUCIAK, J. L. & FRIDEN, P. M. 1991. Selective transport of an anti-transferrin receptor antibody through the blood-brain barrier in vivo. *Journal of Pharmacology and Experimental Therapeutics,* 259**,** 66-70.

PATABENDIGE, A., SKINNER, R. A. & ABBOTT, N. J. 2013. Establishment of a simplified in vitro porcine blood-brain barrier model with high transendothelial electrical resistance. *Brain Research,* 1521**,** 1-15.

PATTNAIK, P. 2005. Surface plasmon resonance. *Applied Biochemistry and Biotechnology,* 126**,** 79-92.

PAVELKA, M. & ROTH, J. 2010. Glycocalyx Changes in Tumours. *Functional Ultrastructure.* Springer Vienna.

PAXTON, W. F., SEN, A. & MALLOUK, T. E. 2005. Motility of catalytic nanoparticles through self‐generated forces. *Chemistry-A European Journal,* 11**,** 6462-6470.

PEARSON, R. T., WARREN, N. J., LEWIS, A. L., ARMES, S. P. & BATTAGLIA, G. 2013. Effect of pH and Temperature on PMPC‚ÄìPDPA Copolymer Self-Assembly. *Macromolecules,* 46**,** 1400-1407.

PENG, X. Q., CARHUAPOMA, J. R., BHARDWAJ, A., ALKAYED, N. J., FALCK, J. R., HARDER, D. R., TRAYSTMAN, R. J. & KOEHLER, R. C. 2002. Suppression of cortical functional hyperemia to vibrissal stimulation in the rat by epoxygenase inhibitors. *American Journal of Physiology-Heart and Circulatory Physiology,* 283**,** H2029-H2037.

PENG, X. Q., ZHANG, C. Y., ALKAYED, N. J., HARDER, D. R. & KOEHLER, R. C. 2004. Dependency of cortical functional hyperemia to forepaw stimulation on epoxygenase and nitric oxide synthase activities in rats. *Journal of Cerebral Blood Flow and Metabolism,* 24**,** 509-517.

PENNISI, M., RUSSO, G., MOTTA, S. & PAPPALARDO, F. Agent based modeling of the effects of potential treatments over the blood–brain barrier in multiple sclerosis. *Journal of Immunological Methods*.

PEPPIATT, C. M., HOWARTH, C., MOBBS, P. & ATTWELL, D. 2006. Bidirectional control of CNS capillary diameter by pericytes. *Nature,* 443**,** 700-704.

PETERSON, E. C., WANG, Z. & BRITZ, G. 2011. Regulation of cerebral blood flow. *International journal of vascular medicine,* 2011**,** 823525-823525.

POGSON, M., HOLCOMBE, M., SMALLWOOD, R. & QWARNSTROM, E. 2008. Introducing Spatial Information into Predictive NF-κB Modelling – An Agent-Based Approach. *Plos One,* 3**,** e2367.

POLLER, B., GUTMANN, H., KRAHENBUHL, S., WEKSLER, B., ROMERO, I., COURAUD, P. O., TUFFIN, G., DREWE, J. & HUWYLER, J. 2008. The human brain endothelial cell line hCMEC/D3 as a human blood-brain barrier model for drug transport studies. *Journal of Neurochemistry,* 107**,** 1358-1368.

PORTER, J. T. & MCCARTHY, K. D. 1996. Hippocampal astrocytes in situ respond to glutamate released from synaptic terminals. *Journal of Neuroscience,* 16**,** 5073-5081.

POZRIKIDIS, C. 1994. The motion of particles in the Hele-Shaw cell. *Journal of Fluid Mechanics,* 261**,** 199-222.

PULFER, S., CICCOTTO, S. & GALLO, J. 1999. Distribution of Small Magnetic Particles in Brain Tumor-bearing Rats. *Journal of Neuro-Oncology,* 41**,** 99-105.

PULFER, S. K. & GALLO, J. M. 1998. Enhanced Brain Tumor Selectivity of Cationic Magnetic Polysaccharide Microspheres. *Journal of Drug Targeting,* 6**,** 215-227.

QIAO, R., JIA, Q., HÜWEL, S., XIA, R., LIU, T., GAO, F., GALLA, H.-J. & GAO, M. 2012. Receptor-Mediated Delivery of Magnetic Nanoparticles across the Blood–Brain Barrier. *Acs Nano,* 6**,** 3304-3310.

RANSOHOFF, R. M., KIVISAKK, P. & KIDD, G. 2003. Three or more routes for leukocyte migration into the central nervous system. *Nature Reviews Immunology,* 3**,** 569-581.

RAPOPORT, S. I. 1976. *Blood-brain barrier in physiology and medicine*, Raven Press.

REESE, T. S. & KARNOVSKY, M. J. 1967. FINE STRUCTURAL LOCALIZATION OF A BLOOD-BRAIN BARRIER TO EXOGENOUS PEROXIDASE. *The Journal of Cell Biology,* 34**,** 207-217.

REN, J., SHEN, S., WANG, D., XI, Z., GUO, L., PANG, Z., QIAN, Y., SUN, X. & JIANG, X. 2012. The targeted delivery of anticancer drugs to brain glioma by PEGylated oxidized multi-walled carbon nanotubes modified with angiopep-2. *Biomaterials,* 33**,** 3324-3333.

RICH, R. L. & MYSZKA, D. G. 2007. Higher-throughput, label-free, real-time molecular interaction analysis. *Analytical Biochemistry,* 361**,** 1-6.

ROBINSON, E. J. H., JACKSON, D. E., HOLCOMBE, M. & RATNIEKS, F. L. W. 2005. Insect communication: `No entry' signal in ant foraging. *Nature,* 438**,** 442-442.

ROY, C. S. & SHERRINGTON, C. S. 1890. On the Regulation of the Blood-supply of the Brain. *The Journal of physiology,* 11**,** 85-158.17.

RUBANYI, G. M., FREAY, A. D., KAUSER, K., JOHNS, A. & HARDER, D. R. 1990. MECHANORECEPTION BY THE ENDOTHELIUM - MEDIATORS AND MECHANISMS OF PRESSURE-INDUCED AND FLOW-INDUCED VASCULAR-RESPONSES. *Blood Vessels,* 27**,** 246-257.

RUITENBERG, A., DEN HEIJER, T., BAKKER, S. L. M., VAN SWIETEN, J. C., KOUDSTAAL, P. J., HOFTNAN, A. & BRETELER, M. M. B. 2005. Cerebral hypoperfusion and clinical onset of dementia: The Rotterdam study. *Annals of Neurology,* 57**,** 789-794.

SABBATINI, P., AGHAJANIAN, C., DIZON, D., ANDERSON, S., DUPONT, J., BROWN, J. V., PETERS, W. A., JACOBS, A., MEHDI, A., RIVKIN, S., EISENFELD, A. J. & SPRIGGS, D. 2004. Phase II Study of CT-2103 in Patients With Recurrent Epithelial Ovarian, Fallopian Tube, or Primary Peritoneal Carcinoma. *Journal of Clinical Oncology,* 22**,** 4523-4531.

SADEQUE, A. J. M., WANDEL, C., HE, H., SHAH, S. & WOOD, A. J. J. 2000. Increased drug delivery to the brain by P-glycoprotein inhibition[ast]. *Clin Pharmacol Ther,* 68**,** 231-237.

SAHA, S., GOLESTANIAN, R. & RAMASWAMY, S. 2014. Clusters, asters, and collective oscillations in chemotactic colloids. *Physical Review E,* 89**,** 062316.

SARIN, H. 2010. Physiologic upper limits of pore size of different blood capillary types and another perspective on the dual pore theory of microvascular permeability. *Journal of Angiogenesis Research,* 2**,** 14-14.

SAWYER, S. T. & KRANTZ, S. B. 1986. Transferrin receptor number, synthesis, and endocytosis during erythropoietin-induced maturation of Friend virus-infected erythroid cells. *Journal of Biological Chemistry,* 261**,** 9187-9195.

SCHINKEL, A. H., MOL, C., WAGENAAR, E., VANDEEMTER, L., SMIT, J. J. M. & BORST, P. 1995. MULTIDRUG-RESISTANCE AND THE ROLE OF P-GLYCOPROTEIN KNOCKOUT MICE. *European Journal of Cancer,* 31A**,** 1295-1298.

SCHINKEL, A. H., SMIT, J. J. M., VANTELLINGEN, O., BEIJNEN, J. H., WAGENAAR, E., VANDEEMTER, L., MOL, C., VANDERVALK, M. A., ROBANUSMAANDAG, E. C., TERIELE, H. P. J., BERNS, A. J. M. & BORST, P. 1994. DISRUPTION OF THE MOUSE MDR1A P-GLYCOPROTEIN GENE LEADS TO A DEFICIENCY IN THE BLOOD-BRAIN-BARRIER AND TO INCREASED SENSITIVITY TO DRUGS. *Cell,* 77**,** 491-502.

SCHMID-SCHÖNBEIN, H., WELLS, R. & GOLDSTON, J. 1969. Influence of Deformability of Human Red Cells upon Blood Viscosity. *Circulation Research,* 25**,** 131-&.

SCHMID, S. L. 1997. CLATHRIN-COATED VESICLE FORMATION AND PROTEIN SORTING:An Integrated Process. *Annual Review of Biochemistry,* 66**,** 511-548.

SCHRÖDER, U. & SABEL, B. A. 1996. Nanoparticles, a drug carrier system to pass the blood-brain barrier, permit central analgesic effects of i.v. dalargin injections. *Brain Research,* 710**,** 121-124.

SHEIKOV, N., MCDANNOLD, N., VYKHODTSEVA, N., JOLESZ, F. & HYNYNEN, K. 2004. Cellular mechanisms of the blood-brain barrier opening induced by ultrasound in presence of microbubbles. *Ultrasound in Medicine & Biology,* 30**,** 979-989.

SHELINE, Y. I., MORRIS, J. C., SNYDER, A. Z., PRICE, J. L., YAN, Z., D'ANGELO, G., LIU, C., DIXIT, S., BENZINGER, T., FAGAN, A., GOATE, A. & MINTUN, M. A. 2010. APOE4 Allele Disrupts Resting State fMRI Connectivity in the Absence of Amyloid Plaques or Decreased CSF A beta 42. *Journal of Neuroscience,* 30**,** 17035-17040.

SILVERMAN, M. & SIMON, M. 1974. Flagellar rotation and the mechanism of bacterial motility. *Nature,* 249**,** 73-74.

SIMIONESCU, M., SIMIONESCU, N. & PALADE, G. E. 1974. MORPHOMETRIC DATA ON THE ENDOTHELIUM OF BLOOD CAPILLARIES. *The Journal of Cell Biology,* 60**,** 128-152.

SKALAK, R. & BRANEMAR.PI 1969. DEFORMATION OF RED BLOOD CELLS IN CAPILLARIES. *Science,* 164**,** 717-&.

SMART, T. P., MYKHAYLYK, O. O., RYAN, A. J. & BATTAGLIA, G. 2009. Polymersomes hydrophilic brush scaling relations. *Soft Matter,* 5**,** 3607-3610.

SMITH, C. D., ANDERSEN, A. H., KRYSCIO, R. J., SCHMITT, F. A., KINDY, M. S., BLONDER, L. X. & AVISON, M. J. 1999a. Altered brain activation in cognitively intact individuals at high risk for Alzheimer's disease. *Neurology,* 53**,** 1391-1396.

SMITH, M. J., BERG, E. L. & LAWRENCE, M. B. 1999b. A direct comparison of selectin-mediated transient, adhesive events using high temporal resolution. *Biophysical Journal,* 77**,** 3371-3383.

SNEZHKO, A., BELKIN, M., ARANSON, I. S. & KWOK, W. K. 2009. Self-Assembled Magnetic Surface Swimmers. *Physical Review Letters,* 102**,** 118103.

SOUNDARARAJAN, A., BAO, A., PHILLIPS, W. T., PEREZ, R. & GOINS, B. A. 2009. (186)Re-Liposomal Doxorubicin (Doxil): In Vitro Stability, Pharmacokinetics, Imaging and Biodistribution in a Head and Neck Squamous Cell Carcinoma Xenograft Model. *Nuclear medicine and biology,* 36**,** 515-524.

SQUIRE, J. M., CHEW, M., NNEJI, G., NEAL, C., BARRY, J. & MICHEL, C. 2001. Quasi-Periodic Substructure in the Microvessel Endothelial Glycocalyx: A Possible Explanation for Molecular Filtering? *Journal of Structural Biology,* 136**,** 239-255.

ŚRODA, K., RYDLEWSKI, J., LNAGNER, M., KOZUBEK, A., GRZYBEK, M. & SIKORSKI, A. F. 2005. Repeated injections of PEG-PE liposomes generate anti-PEG antibodies. *Cell. Mol. Biol. Lett,* 10**,** 37-47.

STEFANOVIC, B., HUTCHINSON, E., YAKOVLEVA, V., SCHRAM, V., RUSSELL, J. T., BELLUSCIO, L., KORETSKY, A. P. & SILVA, A. C. 2008. Functional reactivity of cerebral capillaries. *Journal of Cerebral Blood Flow and Metabolism,* 28**,** 961-972.

STEINMAN, D. A., THOMAS, J. B., LADAK, H. M., MILNER, J. S., RUTT, B. K. & SPENCE, J. D. 2002. Reconstruction of carotid bifurcation hemodynamics and wall thickness using computational fluid dynamics and MRI. *Magnetic Resonance in Medicine,* 47**,** 149-159.

STORM, G., BELLIOT, S. O., DAEMEN, T. & LASIC, D. D. 1995. Surface modification of nanoparticles to oppose uptake by the mononuclear phagocyte system. *Advanced Drug Delivery Reviews,* 17**,** 31-48.

SUN, T., ADRA, S., SMALLWOOD, R., HOLCOMBE, M. & MACNEIL, S. 2009. Exploring Hypotheses of the Actions of TGF-β1 in Epidermal Wound Healing Using a 3D Computational Multiscale Model of the Human Epidermis. *Plos One,* 4**,** e8515.

SUN, T., MCMINN, P., COAKLEY, S., HOLCOMBE, M., SMALLWOOD, R. & MACNEIL, S. 2007. An integrated systems biology approach to understanding the rules of keratinocyte colony formation. *Journal of the Royal Society Interface,* 4**,** 1077-1092.

SUN, T., MCMINN, P., HOLCOMBE, M., SMALLWOOD, R. & MACNEIL, S. 2008. Agent Based Modelling Helps in Understanding the Rules by Which Fibroblasts Support Keratinocyte Colony Formation. *Plos One,* 3**,** e2129.

SWOBODA, B. E. P. & MASSEY, V. 1965. Purification and Properties of the Glucose Oxidase from Aspergillus niger. *Journal of Biological Chemistry,* 240**,** 2209-2215.

TAKAE, S., AKIYAMA, Y., OTSUKA, H., NAKAMURA, T., NAGASAKI, Y. & KATAOKA, K. 2005. Ligand Density Effect on Biorecognition by PEGylated Gold Nanoparticles: Regulated Interaction of RCA120 Lectin with Lactose Installed to the Distal End of Tethered PEG Strands on Gold Surface. *Biomacromolecules,* 6**,** 818-824.

TAN, J., THOMAS, A. & LIU, Y. 2012. Influence of Red Blood Cells on nanoparticle targeted delivery in microcirculation. *Soft Matter,* 8**,** 1934-1946.

TAN, J., WANG, S., YANG, J. & LIU, Y. 2013. Coupled Particulate and Continuum Model for Nanoparticle Targeted Delivery. *Computers & structures,* 122**,** 128-134.

TIAN, X., NYBERG, S., SHARP, P. S., MADSEN, J., DANESHPOUR, N., ARMES, S. P., BERWICK, J., AZZOUZ, M., SHAW, P., ABBOTT, N. J. & BATTAGLIA, G. 2015. LRP-1-mediated intracellular antibody delivery to the Central Nervous System. *Scientific Reports,* 5**,** 11990.

TIERNO, P., GOLESTANIAN, R., PAGONABARRAGA, I. & SAGUÉS, F. 2008. Magnetically Actuated Colloidal Microswimmers. *The Journal of Physical Chemistry B,* 112**,** 16525-16528.

TODORICH, B., PASQUINI, J. M., GARCIA, C. I., PAEZ, P. M. & CONNOR, J. R. 2009. Oligodendrocytes and Myelination: The Role of Iron. *Glia,* 57**,** 467-478.

TORII, R., KEEGAN, J., WOOD, N., DOWSEY, A., HUGHES, A., YANG, G.-Z., FIRMIN, D., THOM, S. M. & XU, X. Y. 2010. MR Image-Based Geometric and Hemodynamic Investigation of the Right Coronary Artery with Dynamic Vessel Motion. *Annals of Biomedical Engineering,* 38**,** 2606-2620.

TOUITOU, E. & BARRY, B. 2006. *Enhancement in Drug Delivery*, CRC Press.

ULBRICH, K., HEKMATARA, T., HERBERT, E. & KREUTER, J. 2009. Transferrin- and transferrin-receptor-antibody-modified nanoparticles enable drug delivery across the blood–brain barrier (BBB). *European Journal of Pharmaceutics and Biopharmaceutics,* 71**,** 251-256.

URMONEIT, B., PRIKULIS, I., WIHL, G., DURSO, D., FRANK, R., HEEREN, J., BEISIEGEL, U. & PRIOR, R. 1997. Cerebrovascular smooth muscle cells internalize Alzheimer amyloid beta protein via a lipoprotein pathway: Implications for cerebral amyloid angiopathy. *Laboratory Investigation,* 77**,** 157-166.

VAN BEEK, A. H. E. A., CLAASSEN, J. A. H. R., RIKKERT, M. G. M. O. & JANSEN, R. W. M. M. 2008. Cerebral autoregulation: an overview of current concepts and methodology with special focus on the elderly. *Journal of Cerebral Blood Flow and Metabolism,* 28**,** 1071-1085.

VAN DEN BERG, B. M., VINK, H. & SPAAN, J. A. E. 2003. The endothelial glycocalyx protects against myocardial edema. *Circulation Research,* 92**,** 592-594.

VAN DEURS, B. 1976. Observations on the blood-brain barrier in hypertensive rats, with particular reference to phagocytic pericytes. *Journal of Ultrastructure Research,* 56**,** 65-77.

VAN FURTH, R. 1982. Current View on the Mononuclear Phagocyte System. *Immunobiology,* 161**,** 178-185.

VASEY, P. A., KAYE, S. B., MORRISON, R., TWELVES, C., WILSON, P., DUNCAN, R., THOMSON, A. H., MURRAY, L. S., HILDITCH, T. E., MURRAY, T., BURTLES, S., FRAIER, D., FRIGERIO, E. & CASSIDY, J. 1999. Phase I Clinical and Pharmacokinetic Study of PK1 [N-(2-

Hydroxypropyl)methacrylamide Copolymer Doxorubicin]: First Member of a New Class of Chemotherapeutic Agents—Drug-Polymer Conjugates. *Clinical Cancer Research,* 5**,** 83-94.

VELÁZQUEZ-CAMPOY, A., OHTAKA, H., NEZAMI, A., MUZAMMIL, S. & FREIRE, E. 2001. Isothermal Titration Calorimetry. *Current Protocols in Cell Biology.* John Wiley & Sons, Inc.

VILLRINGER, A. & DIRNAGL, U. 1995. COUPLING OF BRAIN ACTIVITY AND CEREBRAL BLOOD-FLOW - BASIS OF FUNCTIONAL NEUROIMAGING. *Cerebrovascular and Brain Metabolism Reviews,* 7**,** 240-276.

VITTAZ, M., BAZILE, D., SPENLEHAUER, G., VERRECCHIA, T., VEILLARD, M., PUISIEUX, F. & LABARRE, D. 1996. Effect of PEO surface density on long-circulating PLA-PEO nanoparticles which are very low complement activators. *Biomaterials,* 17**,** 1575-1581.

VOLPE, G., BUTTINONI, I., VOGT, D., KUMMERER, H.-J. & BECHINGER, C. 2011. Microswimmers in patterned environments. *Soft Matter,* 7**,** 8810-8815.

VOLPE, G., GIGAN, S. & VOLPE, G. 2014. Simulation of the active Brownian motion of a microswimmer. *American Journal of Physics,* 82**,** 659-664.

WANG, X., ISHIDA, T. & KIWADA, H. 2007. Anti-PEG IgM elicited by injection of liposomes is involved in the enhanced blood clearance of a subsequent dose of PEGylated liposomes. *Journal of Controlled Release,* 119**,** 236-244.

WANG, L., CHIERICO, L., LITTLE, D., PATIKARNMONTHON, N., YANG, Z., AZZOUZ, M., MADSEN, J., ARMES, S. P. & BATTAGLIA, G. 2012. Encapsulation of Biomacromolecules within Polymersomes by Electroporation. *Angewandte Chemie International Edition,* 51**,** 11122-11125.

WATANABE, S., ROST, B. R., CAMACHO-PEREZ, M., DAVIS, M. W., SOHL-KIELCZYNSKI, B., ROSENMUND, C. & JORGENSEN, E. M. 2013. Ultrafast endocytosis at mouse hippocampal synapses. *Nature,* 504**,** 242-247.

WEINBAUM, S., ZHANG, X., HAN, Y., VINK, H. & COWIN, S. C. 2003. Mechanotransduction and flow across the endothelial glycocalyx. *Proceedings of the National Academy of Sciences,* 100**,** 7988-7995.

WELLS, R. E. & MERRILL, E. W. 1962. INFLUENCE OF FLOW PROPERTIES OF BLOOD UPON VISCOSITY-HEMATOCRIT RELATIONSHIPS. *Journal of Clinical Investigation,* 41**,** 1591-&.

WESTERHOUT, J., PLOEGER, B., SMEETS, J., DANHOF, M. & DE LANGE, E. C. M. 2012. Physiologically Based Pharmacokinetic Modeling to Investigate Regional Brain Distribution Kinetics in Rats. *Aaps Journal,* 14**,** 543-553.

WHO 2007. *Neurological Disorders: Public health challenges*, WHO Press.

WIENKEN, C. J., BAASKE, P., ROTHBAUER, U., BRAUN, D. & DUHR, S. 2010. Protein-binding assays in biological liquids using microscale thermophoresis. *Nat Commun,* 1**,** 100.

WIIG, H. & SWARTZ, M. A. 2012. Interstitial Fluid and Lymph Formation and Transport: Physiological Regulation and Roles in Inflammation and Cancer. *Physiological Reviews,* 92**,** 1005-1060.

WILEY, D. T., WEBSTER, P., GALE, A. & DAVIS, M. E. 2013. Transcytosis and brain uptake of transferrin-containing nanoparticles by tuning avidity to transferrin receptor. *Proceedings of the National Academy of Sciences,* 110**,** 8662-8667.

WILHELMUS, M. M. M., OTTE-HÖLLER, I., VAN TRIEL, J. J. J., VEERHUIS, R., MAAT-SCHIEMAN, M. L. C., BU, G., DE WAAL, R. M. W. & VERBEEK, M. M. 2007. Lipoprotein Receptor-Related Protein-1 Mediates Amyloid-β-Mediated Cell Death of Cerebrovascular Cells. *The American Journal of Pathology,* 171**,** 1989-1999.

WILLIAM REBECK, G., REITER, J. S., STRICKLAND, D. K. & HYMAN, B. T. 1993. Apolipoprotein E in sporadic Alzheimer's disease: Allelic variation and receptor interactions. *Neuron,* 11**,** 575-580.

WONG, A. D., YE, M., LEVY, A. F., ROTHSTEIN, J. D., BERGLES, D. E. & SEARSON, P. C. 2013. The blood-brain barrier: an engineering perspective. *Frontiers in neuroengineering,* 6**,** 7-7.

XIE, L., KANG, H., XU, Q., CHEN, M. J., LIAO, Y., THIYAGARAJAN, M., O,ÄÔDONNELL, J., CHRISTENSEN, D. J., NICHOLSON, C., ILIFF, J. J., TAKANO, T., DEANE, R. & NEDERGAARD, M. 2013. Sleep Drives Metabolite Clearance from the Adult Brain. *Science,* 342**,** 373-377.

YAMASHIRO, D. J., TYCKO, B., FLUSS, S. R. & MAXFIELD, F. R. 1984. Segregation of transferrin to a mildly acidic (pH 6.5) para-golgi compartment in the recycling pathway. *Cell,* 37**,** 789-800.

YANG, L., KRESS, B. T., WEBER, H. J., THIYAGARAJAN, M., WANG, B., DEANE, R., BENVENISTE, H., ILIFF, J. J. & NEDERGAARD, M. 2013. Evaluating glymphatic pathway function utilizing clinically relevant intrathecal infusion of CSF tracer. *Journal of Translational Medicine,* 11**,** 107-107.

YU, Y. J., ATWAL, J. K., ZHANG, Y., TONG, R. K., WILDSMITH, K. R., TAN, C., BIEN-LY, N., HERSOM, M., MALONEY, J. A., MEILANDT, W. J., BUMBACA, D., GADKAR, K., HOYTE, K., LUK, W., LU, Y., ERNST, J. A., SCEARCE-LEVIE, K., COUCH, J. A., DENNIS, M. S. & WATTS, R. J. 2014. Therapeutic bispecific antibodies cross the blood-brain barrier in nonhuman primates. *Science Translational Medicine,* 6**,** 261ra154.

YU, Y. J., ZHANG, Y., KENRICK, M., HOYTE, K., LUK, W., LU, Y., ATWAL, J., ELLIOTT, J. M., PRABHU, S., WATTS, R. J. & DENNIS, M. S. 2011. Boosting Brain Uptake of a Therapeutic Antibody by Reducing Its Affinity for a Transcytosis Target. *Science Translational Medicine,* 3**,** 84ra44-84ra44.

ZHANG, L., ABBOTT, J. J., DONG, L., PEYER, K. E., KRATOCHVIL, B. E., ZHANG, H., BERGELES, C. & NELSON, B. J. 2009. Characterizing the Swimming Properties of Artificial Bacterial Flagella. *Nano Letters,* 9**,** 3663-3667.

ZHANG, J., JOHNSON, P. C. & POPEL, A. S. 2008a. Red Blood Cell aggregation and dissociation in shear flows simulated by lattice Boltzmann method. *Journal of Biomechanics,* 41**,** 47-55.

ZHANG, L., ZHU, H., OPREA, T., GOLBRAIKH, A. & TROPSHA, A. 2008b. QSAR Modeling of the Blood,ÄìBrain Barrier Permeability for Diverse Organic Compounds. *Pharmaceutical Research,* 25**,** 1902-1914.

ZHENG, Y., MARTINDALE, J., JOHNSTON, D., JONES, M., BERWICK, J. & MAYHEW, J. 2002. A Model of the Hemodynamic Response and Oxygen Delivery to Brain. *Neuroimage,* 16**,** 617-637.

ZIGMOND, S. H. 1977. Ability of polymorphonuclear leukocytes to orient in gradients of chemotactic factors. *The Journal of Cell Biology,* 75**,** 606-616.

ZLOKOVIC, B. V. 2008. The blood-brain barrier in health and chronic neurodegenerative disorders. *Neuron,* 57**,** 178-201.

APPENDIX

APPENDIX I

APLEY PRIZE SUBMISSION

INTRODUCTION

The central nervous system (CNS) includes the brain and spinal cord and is involved in processing, co-ordinating and dissipating information to/from the rest of the body. Diseases affecting the CNS will account for an estimated 11.84% of all deaths by 2015. Despite the high burden of disease, few effective treatment options exist for CNS disorders. One of the major reasons for this is the poor penetration of potential therapeutics into the CNS tissue. This is due to the formation of a blood-brain barrier, between the CNS tissue and the blood, by the endothelial cells that constitute blood vessel walls. This barrier prevents almost all unregulated exchange across the endothelial walls into the CNS tissue. Whilst this effectively blocks many potential therapeutic molecules, the natural entry of specific large macromolecules may provide a gateway to access the CNS.

A specific transport system known as receptor-mediated transcytosis (RMT) has gained recent interest for CNS delivery. RMT involves a cargo molecule binding a specific receptor on the blood side (apical side) of an endothelial cell that initiates uptake into the cell in a membrane bound structure called a vesicle, transport across the cell and release, unaltered, on the CNS side (basolateral side) of the cell. Recent developments have utilised nanoparticles that can carry a vast array of potential cargo and be decorated with specific ligands for RMT receptors to increase CNS penetrance. However, whilst these systems have been successful in increasing CNS penetrance, further optimisation is required to maximise therapeutic delivery. Moreover, new methods to deliver to specific regions of the CNS are required to avoid potentially catastrophic off-target effects.

Agent-based modelling is a type of specifically designed for systems analysis. It deconstructs a system into components, known as agents, and assigns mathematical expressions to describe their behaviour. Subsequently, by combining the different agent together in simulations, through agent-agent and agent-environment interactions, emerging systems behaviour can be observed.

AIM

This work sets out to use agent-based modelling of blood flow within the CNS vasculature to investigate physical, physiological and biological parameters that effect uptake of nanoparticles across the blood-brain barrier.

RESULTS

Developing Agent-based Models of Blood Flow

First an agent-based model of blood flow in a single microvessel was developed by integrating finite element methods for fluid flow with agent-based simulations of nanoparticle behaviour in the blood. Incorporated in this is the inclusion of RBCs that constitute ~40% (v/v) of the blood but are reduced to 10% in the microvessels where transport occurs. The effect of these RBCs on blood flow was investigated by varying the volume of RBCs from 0% to 40%. It was found that physiologically relevant concentrations of RBCs (10-12%) produced fluid dynamics effects that maximised the number of molecules that come into close proximity contact with the vessel wall and consequently receptors.

Modulating Nanoparticle-Endothelial Interactions

The interaction of a nanoparticle with the endothelium is a key property for determining effective uptake of the particle into the CNS. This interaction for RMT is propagated through the binding of ligand(s) on the nanoparticle to receptor(s) on the endothelium. Therefore, the nanoparticle-endothelial

interaction is governed by, the density of the receptor, the density of the ligand, the strength of receptor-ligand association, the contact surface area of the nanoparticle-endothelial interface and the shear forces acting at the endothelial-nanoparticle interface. Previous equations have been adapted to study these interactions to look at various phenomena of transport across the BBB.

Previously, it has been demonstrated that RMT efficiency can be controlled through the strength of interaction between the ligand and receptor, with intermediate association strengths more favourable for efficient transcytosis. This is because transcytosis involves the effective binding on the apical membrane but also unbinding on the basolateral membrane. In this work a similar effect with nanoparticles is demonstrated, where the overall RMT efficiency can be modulated by the ligand-receptor affinity, ligand density and particle size.

Achieving Specific Delivery

The flexibility of the parameters that influence transcytosis means different formulations can be designed for optimal transport in particular conditions. One of the major goals of this project is to elucidate methods where specific delivery in different regions of the CNS can be achieved. One area that has been previously studied for specific delivery is receptor expression level. In this work it has been demonstrated that using a higher density of a lower specificity ligand will specifically target regions of the vessel wall where receptor expression is higher. This is because without forming multiple bonds, the binding is unstable and will be broken. However if the receptor and ligand density are both increased more bonds will be formed that collectively stabilise the interaction.

Another area that could be exploited is differences in blood flow, as a result of natural variation between vascular beds, disease abnormalities or inducible flow regulation mechanisms. In this work a particular flow regulation mechanism specific to the CNS, called neurovascular coupling, is

investigated. Neurovascular coupling refers to the local increase in blood flow rates when part of the neural system of the CNS is stimulated, called functional hyperaemia. We have looked at optimising uptake under conditions representing normal and functional hyperaemia conditions. The aim of this would be to design a formulation that undertakes efficient RMT under functional hyperaemia such that we can control uptake into a set region by inducing local functional hyperaemia.

Chemotaxis

Many cells are able to follow chemical stimuli to find improved conditions or desirable targets. Recently, translational work has looked at developing these properties in nanoparticles. Using agent-based simulations, the important considerations for the design of chemotactic systems at the nanoscale are demonstrated. Furthermore this work demonstrates how such particles can be used to follow biological signals to target cells; accrue at interfaces where uptake is more likely to occur and how this can be used to maximise the availability of nanoparticles at vessel walls.

CONCLUSIONS

In this work an agent-based model of blood flow at the blood-brain barrier is produced and used to study strategies for improving general and specific uptake of nanoparticles into the CNS.

APPENDIX II

MODEL OF BROWNIAN MOTION

```
#include <stdio.h>
#include <stdlib.h>
#include <math.h>
#include <time.h>

/************************** Definitions ***************************/
#define dt 0.001                                /*** Time Step in s ***/
#define Kb 0.00000000000000000000013806488 /* Boltzmann Constant */
#define T 310                                   /** Temperature (K) ***/
#define viscosity 0.0017                        /*** Viscosity H20 ****/

/********************* Box-Muller Transformation ******************/

double BoxMuller()
{
/* Create Stored Variables */
    static double n2 = 0.0;
    static int n2_cached = 0;
/* If no stored value */
if (!n2_cached) {
/* Create Random Values between -1 and 1 */
double x, y, r;
        do {
            x = 2.0*rand()/RAND_MAX - 1;
            y = 2.0*rand()/RAND_MAX - 1;
            r = x*x + y*y;
        } while (r == 0.0 || r > 1.0); /* If x^2 + y^2 < 1 */
        {
```

```
            double d = sqrt(-2.0*log(r)/r);
            double n1 = x*d;
/* Store 2nd value */
            n2 = y*d;
            n2_cached = 1;
/* Return result */
            return n1;
        }
/* If stored value */
} else {
        n2_cached = 0;
/* Return stored value */
return n2;
    }
}

/****************************** Main ******************************/
int main ()
{
/* Initialise Random Number Generator */
    srand (time (NULL));
/* Initiate Particle Variables */
    double x = 0.0;
    double y = 0.0;
    double z = 0.0;
    double radius = 0.00000005;
    double Dc = (Kb * T)/(6 * M_PI * viscosity * radius);
/* Calculate Standard Deviation (Andrews and Bray) */
double SD_Dc = sqrt (2.0 * dt * Dc);
/* Start Iteration Loop */
    int iteration;
```

```
    for (iteration = 1; iteration < 1001; iteration++)
    {
/* Display Iteration Number */
printf ("%d\n", iteration);
/* Assign deltax, deltay and deltaz (in nm) */
double deltax = 1000000000.0 * Std_Dev * BoxMuller();
        double deltay = 1000000000.0 * Std_Dev * BoxMuller();
        double deltaz = 1000000000.0 * Std_Dev * BoxMuller();
/* Update x, y and z Variables */
        x += deltax;
        y += deltay;
        z += deltaz;
}
/* Print Results */
    printf ("(%f, %f, %f)\n", x, y, z);
return 0;
}
```

APPENDIX III

FLAME MODEL OF BROWNIAN MOTION

BROWNIAN.xml

```
<xmodel                                                version="2"
xmlns:xsi="http://www.w3.org/2001/XMLSchema-instance"

xsi:noNamespaceSchemaLocation='http://flame.ac.uk/schema/xmml_
v2.xsd'>
<name>Model of Brownian Motion</name>
<author>Gavin Fullstone</author>

<!--********************** Environment **********************-->
<environment>
    <functionFiles><file>FUNCTIONS.c</file></functionFiles>
</environment>

<!--************************ Agents ************************-->
<agents>
<xagent>
<name>Nanoparticle</name>
  <memory>
   <variable><type>int</type><name>id</name></variable>
   <variable><type>double</type><name>x</name></variable>
   <variable><type>double</type><name>y</name></variable>
   <variable><type>double</type><name>z</name></variable>
   <variable><type>double</type><name>radius</name></variable>
   <variable><type>double</type><name>Dc</name></variable>
```

```
   <variable><type>double</type><name>SD_Dc</name></variable>
  </memory>
<!--** Functions **-->
    <functions>
        <function>
          <name>Brownian</name>
            <currentState>0</currentState>
            <nextState>1</nextState>
      </function>
    </functions>
</xagent>
</agents>

<!--********************** Messages **********************-->
<messages>
</messages>
</xmodel>
```

FUNCTIONS.c

```
#include <stdio.h>
#include <stdlib.h>
#include <math.h>
#include <time.h>

/******************* Box-Muller Transformation ******************/
double BoxMuller()
{
/* Create Stored Variables */
```

```
    static double n2 = 0.0;
    static int n2_cached = 0;
/* If no stored value */
if (!n2_cached) {
/* Create Random Values between -1 and 1 */
double x, y, r;
        do {
            x = 2.0*rand()/RAND_MAX - 1;
            y = 2.0*rand()/RAND_MAX - 1;
            r = x*x + y*y;
        } while (r == 0.0 || r > 1.0); /* Check that x^2 + y^2
is less than 1 */
        {
            double d = sqrt(-2.0*log(r)/r);
            double n1 = x*d;
/* Store 2nd value */
            n2 = y*d;
            n2_cached = 1;
/* Return result */
            return n1;
        }
/* If stored value */
    } else {
        n2_cached = 0;
/* Return stored value */
        return n2;
    }
}
```

```
/********************** Nanoparticle Functions ********************/
int Brownian ()
{
/* Initiate Access to Memory Variables */
    xmachine_memory_Nanoparticle * xmemory = current_xmachine->xmachine_Nanoparticle;
/* Assign deltax, deltay and deltaz (in nm) */
    double deltax = 1000000000.0 * xmemory->SD_Dc * BoxMuller();
    double deltay = 1000000000.0 * xmemory->SD_Dc * BoxMuller();
    double deltaz = 1000000000.0 * xmemory->SD_Dc * BoxMuller();
/* Update x, y and z Variables */
    xmemory->x += deltax;
    xmemory->y += deltay;
    xmemory->z += deltaz;
/* Print Results */
    printf ("(%f, %f, %f)\n", x, y, z);
    return 0;
}
```

APPENDIX IV

TRANSCYTOSIS EFFICIENCY OF ANGIOPEP-2 FUNCTIONALISED POLYMERSOMES

This experiment, performed by Sophie Nyberg from the Battaglia group, used angiopep-2 functionalised polymersomes with different degrees of functionalisation (1%, 2%, 3%, 4%, 5% and 6% functionalised polymer). The percentage transcytosed was measured by fluorescence intensity in the basolateral compartment of an *in vitro* transwell seeded with *B. End 3* cells after 30 minutes.

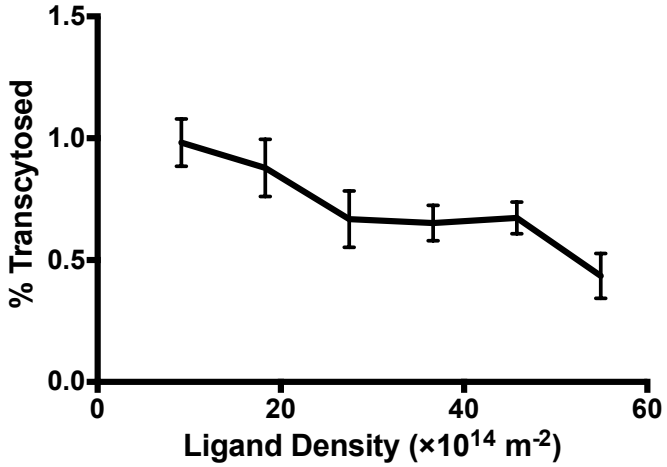

Transcytosis Efficiency of Angiopep-2 Functionalised Polymersomes. Transcytosis efficiency of polymersomes functionalised with different densities of Angiopep-2, after 30 minutes, in a transwell model of the blood brain barrier. Data provided by Sophie Nyberg. Mean ± standard deviation, n=3.

APPENDIX V

DELIVERY OF CHEMOTACTIC NANOPARTICLES INTO THE CNS OF RATS

This data, obtained by Sophie Nyberg from the Battaglia group, demonstrates the percentage of the total injected dose of polymersomes entering the CNS in rats after 10 minutes of *in situ* perfusion. In this experiment, the carotid arteries were isolated and perfused at a set flow perfusion rate with an artificial blood mix containing a known quantity of polymersomes. After 10 minutes, the rats were euthanised and the brain separated into the capillary fraction and the capillary depleted fraction corresponding to the parenchyma. The data below represents the percentage of polymersomes in the parenchyma as measured by the fluorescence microscopy.

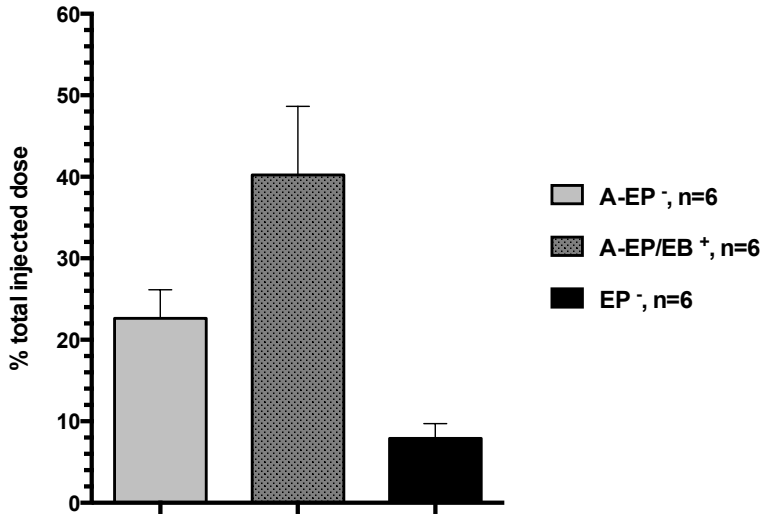

Delivery of Chemotactic Nanoparticles into the CNS of Rats. Fluorescence quantification of polymersome uptake into the rat brain parenchyma after 10 minutes of *in situ* perfusion. Polymersome formulations are chemotactic Angiopep-2-POEGMA-PDPA/PEO-PBO (A-EP-EB^{+}), non-chemotactic Angiopep-2-POEGMA-PDPA (A-EP) and non-CNS-targeting POEGMA-PDPA (EP). *P<0.05, **P<0.01, ***P<0.001, ****P<0.0001. Mean ± standard error of the mean. Provided by Sophie Nyberg.